



**University of  
Nottingham**  
UK | CHINA | MALAYSIA

Unravelling the underpinning mechanisms  
associated with the microwave treatment of electric  
arc furnace dust with polyvinyl chloride: An  
electromagnetic and kinetic investigation

Thesis submitted to the University of Nottingham for the  
degree of Doctor of Philosophy

Sanad Altarawneh

June 2023

*This thesis is dedicated to my parents*

## Abstract

Herein, the underpinning mechanisms associated with the microwave thermal treatment of electric arc furnace dust (EAFD) with polyvinyl chloride (PVC) in terms of their response to the electromagnetic radiation in the microwave frequency band and the effect of EAFD pure constituents on the thermal degradation kinetics of PVC have been studied. Such data provide a foundation based on which the co-thermal treatment of EAFD and PVC can be realised using microwave energy as an alternative disposal strategy for these wastes.

The separation of the microwave electromagnetic fields was achieved in a TE<sub>10</sub> cavity by means of using small cylindrical samples with a 4 mm diameter along with the correct positioning of the sliding short circuit such that the electric or magnetic field was solely passed through the sample. Heating experiments suggests that ZnO, ZnFe<sub>2</sub>O<sub>4</sub>, Fe<sub>3</sub>O<sub>4</sub>, and graphite are the major phases that contribute to the microwave heating of EAFD with ZnO having the highest heating rate (~ 37 °C/s) among zinc and iron bearing oxides. Moreover, only Fe<sub>3</sub>O<sub>4</sub> and graphite heated in the magnetic field suggesting the possibility of selective heating of these phases by the microwave magnetic field maxima.

The non-isothermal kinetic analysis performed on the thermogravimetric scans of metal oxides/PVC mixtures suggests a catalytic activity for both ZnO and ZnFe<sub>2</sub>O<sub>4</sub> in which both were found to react directly with the PVC monomer resulting in a drop in the dehydrochlorination onset temperature from 272 to 214 and 235 °C, respectively. The resulting products from this interaction is majorly zinc in its water soluble chloride form (ZnCl<sub>2</sub>) which suggests that PVC can be utilised as a potential additive for the recycling of metallurgical waste (e.g., EAFD). To provide a selective chlorination of zinc in

ZnFe<sub>2</sub>O<sub>4</sub> while leaving iron in its stable oxide form (Fe<sub>2</sub>O<sub>3</sub>), the pyrolysis should be performed at temperatures as low as 235 °C. This is because the presence of parallel reactions with different energy barriers results in reaction channelling favouring the chlorination of zinc while the resulting Fe<sub>2</sub>O<sub>3</sub> remains untouched due to its slow reaction kinetics with H<sub>2</sub> in that temperature range (i.e., iron remains as stable Fe<sub>2</sub>O<sub>3</sub> instead of transforming to active Fe<sub>3</sub>O<sub>4</sub>).

The reaction of Fe<sub>3</sub>O<sub>4</sub> and Fe<sub>2</sub>O<sub>3</sub> (after reduction to Fe<sub>3</sub>O<sub>4</sub>) with PVC was found to occur by reacting with gaseous emitted HCl, contrary to ZnO and ZnFe<sub>2</sub>O<sub>4</sub> which react directly with the PVC monomer. The onset de-hydrochlorination temperature of PVC was thus not affected when PVC was mixed with Fe<sub>3</sub>O<sub>4</sub> and Fe<sub>2</sub>O<sub>3</sub>. The capturing of the emitted gaseous HCl resulted, however, in slowing the rate of the de-hydrochlorination stage since HCl is a known catalyst for PVC de-hydrochlorination which was seen in the form of an increase in the activation energy associated with that stage.

Combining the observations from both an electromagnetic and kinetic perspective, it is believed that utilising microwave energy can result in a fast selective heating of zinc bearing oxides over iron bearing compounds. This, in turn, would allow PVC in contact with ZnO and ZnFe<sub>2</sub>O<sub>4</sub> to heat at a faster rate leading to channelling the chlorination reactions towards zinc oxides, which enhances the chlorinating selectivity, especially that all the chlorine will be abstracted by “high temperature” ZnO and ZnFe<sub>2</sub>O<sub>4</sub> before PVC decomposes normally into gaseous HCl and solid polyene.

**Declaration:**

I declare that the published papers presented in this thesis were generated from the work done by the author (Sanad Altarawneh) and that this thesis is not submitted in support of an application for any other qualification or degree in this institution or any other institution.

Signed:

Sanad Altarawneh

The four manuscripts attached to appendices 1, 2, 3, and 4 were published by Elsevier.

The following statement is presented in the publisher's sharing policies section:

“Theses and dissertations which contain embedded PJAs as part of the formal submission can be posted publicly by the awarding institution with DOI links back to the formal publications on ScienceDirect”

<https://www.elsevier.com/about/policies/sharing> Accessed on January 10<sup>th</sup>, 2023

## **Acknowledgements**

I would like to express my deepest gratitude to my supervisors Prof. Mohammad Al-Harashah, Prof. Chris Dodds, Dr. Adam Buttress, and Prof. Sam Kingman for their continuous guidance and support.

## List of publications:

### Published:

**Altarawneh S**, Al-Harashsheh M, Buttress A, Dodds C, Rodriguez J, Kingman S. Microwave selective heating of electric arc furnace dust constituents toward sustainable recycling: Contribution of electric and magnetic fields. *Journal of Industrial and Engineering Chemistry*. 2021;104:521-8. doi: <https://doi.org/10.1016/j.jiec.2021.09.001>.

**Altarawneh S**, Al-Harashsheh M, Dodds C, Buttress A, Kingman S. Thermal degradation kinetics of polyvinyl chloride in presence of zinc oxide. *Thermochimica Acta*. 2021:179105. doi: <https://doi.org/10.1016/j.tca.2021.179105>.

**Altarawneh S**, Al-Harashsheh M, Dodds C, Buttress A, Kingman S. Thermodynamic, pyrolytic, and kinetic investigation on the thermal decomposition of polyvinyl chloride in the presence of franklinite. *Process Safety and Environmental Protection*. 2022. doi: <https://doi.org/10.1016/j.psep.2022.10.028>.

**Altarawneh S**, Al-Harashsheh M, Buttress A, Dodds C, Kingman S. A thermo-kinetic investigation on the thermal degradation of polyvinyl chloride in the presence of magnetite and hematite. *Thermochimica Acta*. 2022:179390. doi: <https://doi.org/10.1016/j.tca.2022.179390>.

## Table of Content

Abstract .....	i
Declaration: .....	iii
Acknowledgements .....	iv
List of publications: .....	v
List of Figures .....	xi
List of Tables .....	xiv
CHAPTER ONE .....	15
Introduction .....	15
1.1 Background .....	15
1.2 Aims and objectives .....	18
CHAPTER TWO .....	20
Introduction to microwave heating principles .....	20
2.1 Overview .....	20
2.2 Microwave heating mechanisms .....	21
2.2.1 Dipolar polarisation loss .....	22
2.2.2 Dielectric properties and the Debye equations .....	23
2.2.3 Electric conduction loss .....	25
2.2.4 Magnetic loss .....	26
2.2.4.1 Magnetic hysteresis loss .....	26
2.2.4.2 Eddy currents loss .....	27
2.3 The power equation and volumetric heating .....	28
2.4 Microwave measurement and heating equipment .....	29
2.4.1 Microwave measurement technique .....	29
2.4.2 Microwave heating equipment .....	30
2.4.2.1 Magnetrons .....	30
2.4.2.2 Solid state generators .....	31
2.4.2.3 Waveguides .....	32
2.4.2.4 Waveguide terminations .....	33
2.4.2.5 Load termination .....	33
2.4.2.6 Short circuit termination .....	33
2.4.2.7 Microwave cavities (applicators) .....	34
2.5 Some engineering challenges of microwaves .....	35
2.5.1 Penetration depth .....	35
2.5.2 Heating homogeneity .....	36

2.5.3 Thermal runaway .....	37
CHAPTER THREE .....	39
An overview of electric arc furnaces, electric arc furnace dust and polyvinyl chloride .....	39
3.1 Overview .....	39
3.2 Electric arc furnaces.....	39
3.2.1 Types of EAFs .....	40
3.2.2 Construction of an EAF .....	41
3.2.3 Raw materials.....	42
3.3 Electric arc furnace dust (EAFD) .....	43
3.3.1 Formation of EAFD .....	44
3.3.2 Minimisation of EAFD formation .....	45
3.3.3 Conventional treatment routes .....	45
3.3.4 Characteristics and properties of EAFD .....	47
3.3.4.1 Particle size .....	47
3.3.4.2 Density .....	48
3.3.4.3 Chemical composition .....	48
3.3.4.4 Mineralogical composition .....	51
3.3.4.5 Morphology of EAFD .....	52
3.3.5 Pyrometallurgical treatment of EAFD .....	53
3.3.5.1 The Waelz kiln process .....	53
3.3.5.2 Primus process .....	54
3.3.5.3 Rotary Hearth Furnace (RHF) .....	55
3.3.5.4 Challenges and obstacles of pyrometallurgical treatment of EAFD....	56
3.3.5.4.1 Energy requirements .....	56
3.3.5.4.2 The final product and process economics.....	56
3.3.5.4.3 Requirements of the feeding material .....	57
3.3.5.4.4 The environmental impact .....	57
3.3.6 Hydrometallurgical treatment of EAFD .....	57
3.3.6.1 Acidic leaching .....	58
3.3.6.1.1 Sulphuric acid .....	58
3.3.6.1.2 Hydrochloric acid.....	59
3.3.6.1.3 Nitric acid.....	60
3.3.6.2 Alkaline leaching .....	61
3.3.6.3 Salt leaching.....	62
3.3.6.3.1 Hexahydrate ferric chloride ( $\text{FeCl}_3 \cdot 6\text{H}_2\text{O}$ ) .....	62
3.3.6.3.2 Ammonium chloride $\text{NH}_4\text{Cl}$ .....	62
3.3.6.3.3 Ammonium Carbonate $(\text{NH}_4)_2\text{CO}_3$ .....	63
3.3.7 Challenges and opportunities of hydrometallurgical treatment of EAFD ..	63
3.3.7.1 Process economics .....	64
3.3.7.1.1 The extent of zinc extraction.....	64
3.3.7.1.2 The material of construction .....	64
3.3.7.1.3 Process selectivity .....	65
3.3.7.1.4 The concentration of the leaching reagent .....	65

3.3.7.2 The variability of EAFD composition .....	65
3.3.8 Carbothermic reduction of EAFD using microwave energy .....	66
3.4 Polyvinyl Chloride plastic.....	67
3.4.1 Overview.....	67
3.4.2 Alternative treatment methods of PVC.....	67
3.4.2.1 Vinyloop PVC recycling process.....	68
3.4.2.2 The NKT pyrolysis process .....	68
3.4.2.3 Stignæs PVC recycling process.....	69
3.4.2.4 MVR Hamburg (municipal solid waste incineration).....	69
3.4.3 The thermal degradation of PVC .....	70
3.4.3.1 Reaction mechanism of PVC de-hydrochlorination .....	70
3.4.3.1.1 Unimolecular de-hydrochlorination mechanism.....	72
3.4.3.1.2 Free radical de-hydrochlorination mechanism.....	73
3.4.3.1.3 Ionic de-hydrochlorination mechanism .....	74
3.4.3.2 Polyene thermal cracking stage .....	74
3.4.3.3 Kinetics of PVC degradation .....	75
3.4.3.4 Interaction of PVC with metal oxides.....	76
3.4.3.4.1 PVC and ZnO.....	77
3.4.3.4.2 PVC and PbO .....	77
3.4.3.4.3 PVC and Fe <sub>2</sub> O <sub>3</sub> .....	78
3.4.3.4.4 PVC and ZnFe <sub>2</sub> O <sub>4</sub> .....	78
3.4.3.4.5 PVC and Fe <sub>3</sub> O <sub>4</sub> .....	79
3.5 Literature on the co-thermal treatment of EAFD with PVC.....	79
3.5.1 The kinetics of PVC degradation in the presence of EAFD .....	79
3.5.2 The thermodynamics of the chlorination of EAFD constituents .....	82
3.5.3 Metal extraction from EAFD in the presence of PVC .....	84
3.5.3.1 Metal extraction under pyrolytic conditions .....	84
3.5.3.1.1 Conventional energy as the heating source.....	84
3.5.3.1.2 Microwave energy as the heating source .....	86
3.5.3.2 Oxidative thermal treatment of EAFD-PVC blends .....	87
3.6 Summary .....	88
 CHAPTER FOUR.....	 90
 Microwave selective heating of electric arc furnace dust constituents toward sustainable recycling: Contribution of electric and magnetic fields (paper 1)	 90
4.1 Overview.....	90
4.2 Dielectric characterisation .....	91
4.3 Heating in separated electric (E) and magnetic (H) microwave fields .....	94
4.3.1 Electromagnetic simulation and the experimental setup .....	94
4.3.2 Microwave heating profiles of metal oxides exposed to separated electric and magnetic fields .....	97
4.4 Summary .....	98

CHAPTER FIVE .....	100
The effect of zincite (ZnO) and franklinite (ZnFe <sub>2</sub> O <sub>4</sub> ) as major zinc bearing oxides in EAFD on the thermal decomposition kinetics of polyvinyl chloride (papers 2 and 3).....	100
5.1 Overview.....	100
5.2 Pyrolysis and thermal stability.....	101
5.3 The kinetics of PVC de-hydrochlorination in the presence of ZnO and ZnFe <sub>2</sub> O <sub>4</sub> .....	104
5.4 Summary .....	111
CHAPTER SIX.....	112
A thermo-kinetic investigation on the thermal degradation of polyvinyl chloride in the presence of magnetite and hematite (paper 4) .....	112
6.1 Overview.....	112
6.2 Pyrolysis and thermal stability.....	113
6.3 The kinetics of PVC de-hydrochlorination in the presence of Fe <sub>3</sub> O <sub>4</sub> and Fe <sub>2</sub> O <sub>3</sub> .....	117
6.4 Kinetics of the carbothermic reduction of Fe <sub>3</sub> O <sub>4</sub> and FeO by the char generated from PVC degradation .....	123
6.5 Summary .....	127
CHAPTER SEVEN .....	128
Conclusions and future work .....	128
7.1 Conclusions.....	128
7.2 Future work.....	131
7.2.1 Microwave electromagnetic interaction with EAFD and PVC – selective heating using separated microwave fields .....	131
7.2.2 The effect of different EAFD components on the degradation kinetics of PVC.....	132
References.....	134
Appendix 1: Microwave selective heating of electric arc furnace dust constituents toward sustainable recycling: contribution of electric and magnetic fields .....	144
Appendix 2: Thermal degradation kinetics of polyvinyl chloride in presence of zinc oxide .....	174
Appendix 3: Thermodynamic, pyrolytic, and kinetic investigation on the thermal decomposition of polyvinyl chloride in the presence of franklinite.....	210

Appendix 4: A thermo-kinetic investigation on the thermal degradation of polyvinyl chloride in the presence of magnetite and hematite .....246

## List of Figures

Figure 1: A schematic illustration showing the research gap, thesis objectives and thesis output. ....	19
Figure 2: Electromagnetic spectrum from low (radio) frequency to high (gamma-ray) frequency [38]. ....	20
Figure 3: Interaction of microwaves with different types of materials [42]. ....	21
Figure 4: Movement of a permanent dipole when exposed to an external electric field (adapted from [45]). ....	22
Figure 5: The dispersion of the real and imaginary permittivities with electromagnetic frequency (adapted from [44]). ....	24
Figure 6: Magnetisation hysteresis loop for a magnetic material inside an alternating magnetic field where M and H are magnetisation and magnetic field intensity, respectively (adapted from [55]). ....	26
Figure 7: Formation of eddy currents in an electrically conducting disk positioned in an alternating magnetic field (B(t) time dependent alternating magnetic field). ....	27
Figure 8: Schematic diagram of a magnetron (adapted from [61]). ....	31
Figure 9: A typical rectangular waveguide with co-ordination system [62]. ....	32
Figure 10: A graphite sample in a single mode TE <sub>10</sub> cavity before (A) and after (B) heating at a power of ~ 118 W and a frequency of 2.47 GHz showing localised heating (OD and ID are outer and inner diameter, respectively). ....	37
Figure 11: (A) DC electric arc furnace with a single electrode [68] and (B) AC electric arc furnace with 3 electrodes [71]. ....	41
Figure 12: Main components of a typical AC electric arc furnace: 1. Furnace body, 2. Furnace roof, 3.sledge, 4. Purging cradle, 5. Operating door, 6. Electrodes, 7. Water cooled copper rings, and 8. Rocker [73]. ....	41
Figure 13: Mechanisms of EAFD emission in electric arc furnaces [80]. ....	45
Figure 14: SEM micrograph of spinel ferrite spherical particles with particle size - 270/+400 mesh [77]. ....	52
Figure 15: An example of an irregular shape particle in EAFD [80]. ....	53
Figure 16: A schematic illustration of the Waelz kiln process [117]. ....	54
Figure 17: A flowchart of PRIMUS process for the treatment of EAFD [118]. ....	55
Figure 18: RHF process used for the recycling of EAFD [123]. ....	56
Figure 19: A schematic diagram of the Vinyloop process; (A) PVC waste collection, (B) PVC selective dissolution, (C) contamination filtration, (D) steam distillation, (E) solvent recovery, and (F) recycled PVC [146]. ....	68
Figure 20: Thermogravimetric analysis of PE, PP [149], PET [150], PS and PVC [149] at a heating rate of 10 °C/min (data collected and presented in [17]). ....	70
Figure 21: Schematic showing the formation of a benzene ring from PVC degradation [161]. ....	72
Figure 22: Schematic illustration of the unimolecular mechanism for PVC dehydrochlorination (adapted from [162]). ....	73
Figure 23: Free radical mechanism for the dehydrochlorination of PVC. ....	74
Figure 24: Total thermal degradation of PVC [27]. ....	75
Figure 25: Activation energy of PVC dehydrochlorination (first stage) and backbone cracking (second stage) in the presence of EAFD at different ratios and heating rates [9]. ....	81

Figure 26: Gibbs free energy of the chlorination (A) and non-chlorination (B) reactions (FactSage 7.0) [15].	83
Figure 27: The complex relative permittivities (real and imaginary) of EAFD against temperature at the two frequencies 911 MHz and 2.47 GHz reported in Al-Harashsheh et al. [20].	86
Figure 28: The complex relative permittivities (real and imaginary) of PVC against temperature at the two frequencies 911 MHz and 2.47 GHz reported in Al-Harashsheh et al. [20].	86
Figure 29: The loss tangent of the major EAFD components against temperature at a frequency of 2.47 GHz.	92
Figure 30: The dielectric properties of pure PVC (A) and waste unplasticized PVC (B) in the temperature window 25 – 700 °C.	94
Figure 31: A photo of the experimental setup used to perform the electric/magnetic microwave heating.	95
Figure 32: A top view of the waveguide showing the position of a ZnO sample in the maximum electric (A) and maximum magnetic (B) fields with a power input of 118 W.	96
Figure 33: Response of ZnO (A) and Fe <sub>3</sub> O <sub>4</sub> (B) to pure electric and pure magnetic microwave fields in a single mode TE <sub>10</sub> cavity under a microwave power of 118 ± 12 W (E is electric field and H is magnetic field).	98
Figure 34: The thermal behaviour of pure PVC, ZnO-PVC (39.4 wt% ZnO), and ZnFe <sub>2</sub> O <sub>4</sub> -PVC (32.5 wt% ZnFe <sub>2</sub> O <sub>4</sub> ) under a nitrogen flow of 100 mL/min and a heating rate of 10 °C/min.	102
Figure 35: Chemistry and morphology of a particle in the pyrolysis residue of ZnO-PVC mixture at a temperature of 370 °C.	103
Figure 36: The activation energy (A), the natural logarithm of the frequency factor (unit of A is min <sup>-1</sup> ) (B), and the rate constant at a temperature of 200 °C (C) associated with the de-hydrochlorination of PVC, ZnO-PVC, and ZnFe <sub>2</sub> O <sub>4</sub> -PVC under a nitrogen flow of 100 mL/min (kinetic parameters reported using Friedman method) [168].	106
Figure 37: The morphology and chemistry of formed FeCl <sub>2</sub> during the pyrolysis of ZnFe <sub>2</sub> O <sub>4</sub> -PVC (32.5 wt% ZnFe <sub>2</sub> O <sub>4</sub> ) at a temperature of 650 °C and under a nitrogen flow of ~ 5 mL/min.	108
Figure 38: A comparison between experimental and model based de-hydrochlorination rate of (A) PVC, (B) ZnO-PVC mixture (39.4 wt% ZnO) and (C) ZnFe <sub>2</sub> O <sub>4</sub> -PVC mixture (32.5 wt% ZnFe <sub>2</sub> O <sub>4</sub> ) using data extracted from Friedman model.	110
Figure 39: The thermal behaviour of pure PVC, Fe <sub>3</sub> O <sub>4</sub> -PVC (31.6 wt% Fe <sub>3</sub> O <sub>4</sub> ), and Fe <sub>2</sub> O <sub>3</sub> -PVC (29.9 wt% Fe <sub>2</sub> O <sub>3</sub> ) under a nitrogen flow of 100 mL/min and a heating rate of 10 °C/min.	114
Figure 40: The morphology and chemistry of a crystal obtained from the pyrolysis of Fe <sub>2</sub> O <sub>3</sub> -PVC mixture at a temperature of 600 °C which is potentially related to FeCl <sub>2</sub> ·2H <sub>2</sub> O.	116
Figure 41: The morphology and chemistry of FeCl <sub>2</sub> obtained from the pyrolysis of Fe <sub>2</sub> O <sub>3</sub> -PVC mixture at a temperature of 600 °C.	117

Figure 42: The kinetic parameters (A) activation energy and (B) frequency factor (units $\text{min}^{-1}$ ) associated with PVC de-hydrochlorination alone and in the presence of stoichiometric quantities of $\text{Fe}_3\text{O}_4$ (31.6 wt% $\text{Fe}_3\text{O}_4$ ) and $\text{Fe}_2\text{O}_3$ (29.9 wt% $\text{Fe}_2\text{O}_3$ ).	119
Figure 43: The rate constant at temperatures of 200 (A) and 300 °C (B) for the de-hydrochlorination of PVC alone and in the presence of stoichiometric quantities of $\text{Fe}_3\text{O}_4$ (31.6 wt% $\text{Fe}_3\text{O}_4$ ) and $\text{Fe}_2\text{O}_3$ (29.9 wt% $\text{Fe}_2\text{O}_3$ ).	121
Figure 44: A comparison between experimental and model based de-hydrochlorination rate of (A) $\text{Fe}_3\text{O}_4$ -PVC (31.6 wt% $\text{Fe}_3\text{O}_4$ ) and (B) $\text{Fe}_2\text{O}_3$ -PVC (29.9 wt% $\text{Fe}_2\text{O}_3$ ) mixtures using data extracted from Friedman model.	122
Figure 45: The kinetic parameters (A) activation energy and (B) frequency factor (unit is $\text{min}^{-1}$ ) associated with the carbothermic reduction of $\text{Fe}_3\text{O}_4$ to $\text{FeO}$ by the char generated from PVC degradation.	124
Figure 46: The kinetic parameters ((A) activation energy and (B) frequency factor) associated with the carbothermic reduction of $\text{FeO}$ to $\alpha$ -Fe by the char generated from PVC degradation.	125
Figure 47: A comparison between experimental and model based carbothermic reduction rate of (A) $\text{Fe}_3\text{O}_4$ to $\text{FeO}$ and (B) $\text{FeO}$ to $\alpha$ -Fe using data extracted from Friedman model.	126

\*The figures in the manuscripts attached to appendices 1, 2, 3, and 4 have their own numbering and are not mentioned in the table above.

## List of Tables

Table 1: Particle size distribution of EAFD from different references.....	48
Table 2: True density of EAFD from different references. ....	48
Table 3: Chemical composition as a weight% of EAFD from different references. ...	49
Table 4: Mineralogical content of EAFD from different references. ....	51
Table 5: Kinetics parameters of PVC degradation from different references. ....	76
Table 6: Permittivity and permeability data for ZnO and Fe <sub>3</sub> O <sub>4</sub> at room temperature and a frequency of 2.47 GHz. ....	97

\*The tables in the manuscripts attached to appendices 1, 2, 3, and 4 have their own numbering and are not mentioned in the table above.

# CHAPTER ONE

## Introduction

### 1.1 Background

Electric arc furnace dust (EAFD) is one of the major waste materials generated from the steelmaking industry. Currently, electric arc furnaces (EAFs) account for more than 30% of steel manufactured globally [1]. From these furnaces, quantities of 10 – 20 kg of EAFD is generated for every 1 ton of produced steel [2]. The huge production volume of steel results in the generation of EAFD at an alarming rate. EAFD is considered a hazardous material due to the presence of toxic heavy metals such as Pb and Cd [3]. Hence, the disposal/storage of this waste material in landfill has become an undesirable option. For example, according to the Environmental permitting (England and Wales) Regulations 2010 ([legislation.gov.uk](http://legislation.gov.uk)), the stored amount of EAFD in a secure place should not exceed 2500 tonnes (at any one time) for a period that does not exceed three months. This storage is also subject to the following conditions:

1. EAFD should be stored indoors.
2. It should be stored at a dock prior to being exported or after being imported.
3. EAFD should arrive at the storage place in bags and must be stored there in bags or drums.

The storage of this material in accordance with country legislation is a costly practice, which makes finding a sustainable recycling route necessary. Recycling of EAFD back into EAFs on the other hand, can be considered a reliable practice only if EAFD is rich with ferrous oxides and lean with other non-ferrous species. In the case of excess levels of non-ferrous species, recycling can induce many problems such as [4]:

1. Increasing energy input requirements for reduction reactions.
2. Formation of slag that can attack the furnace refractory lining.
3. Some of the non-ferrous elements can be retained in the molten steel bath which results in the formation of steel of undesirable chemistry with mechanical and physical properties that do not meet specifications.

Pyrometallurgical treatment of EAFD relies on the difference in the vapour pressure of ferrous and non-ferrous species resulting in the selective volatilisation of non-ferrous species, leaving iron in the residue. The most commonly applied pyrometallurgical technique for the treatment of EAFD is the Waelz process [5-7]. In this process, metal oxides in EAFD are reduced at high temperatures (1100-1200 °C) to their elemental forms resulting in a selective evaporation of non-ferrous metals, principally zinc, which is then oxidised and collected as ZnO. Despite the industrial applicability of this process, it still has some limitations. In order for the process to be economically justified, the concentration of zinc in EAFD should be at least 16% [8]. Moreover, the process is extremely energy intensive, and it requires complicated and expensive dust/gas filtration systems [9].

Much research has been devoted to the extraction of zinc from EAFD using hydrometallurgical techniques [10-14]. The main forms in which zinc is present in EAFD are zincite (ZnO) and franklinite ( $\text{ZnFe}_2\text{O}_4$ ) [15]. The extraction of zinc from ZnO is not problematic by any of the hydrometallurgical techniques.  $\text{ZnFe}_2\text{O}_4$ , in contrast, showed a refractory behaviour when leached [14, 16] which results in low zinc extraction. The hydrometallurgical approach, in general, suffers from either low extraction yield or the contamination of the leaching liquor with other impurities which complicates the extraction of zinc at a high purity.

Plastic waste materials are accumulated in large amounts around the globe. Among all plastic types, polyvinyl chloride (PVC) is one of the most widely used halogenated plastic with a

production and consumption amounts of 61 and 38.5 million tons, respectively in 2013 [17]. In 2020, the plastic converters demand of PVC in Europe was 4.7 million tons [18]. A simulation study [19] estimated that in China alone, the amount of accumulated PVC will reach up to 600 million tons by the end of 2050. The abundance of this material at the end of useful life makes its disposal a significant challenge [20]. In the past, the landfilling and incineration of PVC were the most prevalent disposal routes. In recent years, however, landfilling has become increasingly difficult due to the strict regulations imposed by the Environmental Protection Agency (EPA) and the scarcity of landfill sites [21]. Incineration, is also deemed an unsuitable disposal method due to the harmful emissions during pyrolysis, such as hydrogen chloride and chlorinated hydrocarbons (dioxins) [22, 23].

The thermal treatment of EAFD with halogenated plastics has gained an increased attention [9, 15, 21, 24, 25]. This is because the metal oxides present in EAFD are able to capture emitted HCl from the pyrolysis of PVC, as well as their ability to suppress some of the organic emissions resulting from the thermal cracking of the polymer [26-32]. Aside to the fact that EAFD is able to capture acidic emissions from halogenated plastics, it was also reported by Al-Harashseh et al. [20, 24, 25] that valuable metals such as zinc and lead can be extracted by the leaching of the post pyrolysis residues of EAFD and PVC. This, in turn, makes the co-thermal treatment option of EAFD with PVC an excellent candidate to mitigate their environmental footprint, while simultaneously enabling the extraction of valuable metals; the co-thermal treatment of EAFD with halogenated plastics have been done using both conventional [24, 25, 33-35] and microwave energy [20, 36].

Evidence in literature (sections 3.3.4.3 and 3.3.4.4) shows a significant variation in the chemistry and mineralogy of EAFD from one country to another and from one plant to another. This means, the response of EAFDs from different sources to microwave energy will vary appreciably depending on its chemical components. Moreover, the effect of EAFD on the

kinetics and the thermal degradation behaviour of PVC will also vary greatly based on the mineralogy of EAFD. Hence, sound predictions of the microwave response of EAFDs from different sources can only be made when detailed knowledge of the dielectric properties of the main EAFD components and their heating behaviour in different electromagnetic fields is established. Moreover, the effect of different EAFDs with different chemistries on the thermal decomposition behaviour and pyrolysis kinetics of PVC can only be made with the existence of a database which reports the effect of the major EAFD constituents on the kinetics of PVC degradation along with the thermal behaviour at different pyrolysis temperatures.

## **1.2 Aims and objectives**

The aim of this research is to provide a greater understanding of the fundamental interaction of microwave energy with EAFD and PVC during their thermal co-treatment. The thesis also aims to establish a kinetic database for the thermal degradation of PVC in the presence of the major constituents of EAFD. To achieve these aims, the following research objectives were set:

1. Extract the dielectric properties of the major EAFD constituents and PVC under a broad temperature range to use them in an electromagnetic model. This model was then used to be able to introduce the samples to separated microwave electric and magnetic microwave fields.
2. Study the interaction of the major EAFD constituents presented by ZnO, ZnFe<sub>2</sub>O<sub>4</sub>, Fe<sub>2</sub>O<sub>3</sub>, Fe<sub>3</sub>O<sub>4</sub>, PbO, CaCO<sub>3</sub>, SiO<sub>2</sub> and Graphite with separated electromagnetic microwave fields (electric and magnetic) to test the possibility for selectively heating magnetic components such as Fe<sub>3</sub>O<sub>4</sub> in the microwave magnetic maxima. This, in turn, can potentially contribute towards improving the chlorination selectivity by oxidising Fe<sub>3</sub>O<sub>4</sub> back to stable Fe<sub>2</sub>O<sub>3</sub>.

- Extract the temperature independent kinetic parameters (activation energy, frequency factor and reaction model) associated with the thermal degradation of PVC in the presence of zinc and iron bearing compounds present in EAFD: ZnO, ZnFe<sub>2</sub>O<sub>4</sub>, Fe<sub>2</sub>O<sub>3</sub>, and Fe<sub>3</sub>O<sub>4</sub>. These parameters allow predicting reaction rates associated with the degradation of PVC at any temperature and helped in understanding the reaction mechanisms of the zinc and iron bearing oxides with PVC, which ultimately affects the choice of the optimum temperature for highest chlorination selectivity towards zinc.

Below, a summary is provided showing how this thesis approached the gaps present in literature and how it implemented the objectives to produce an output which meets the project aims:

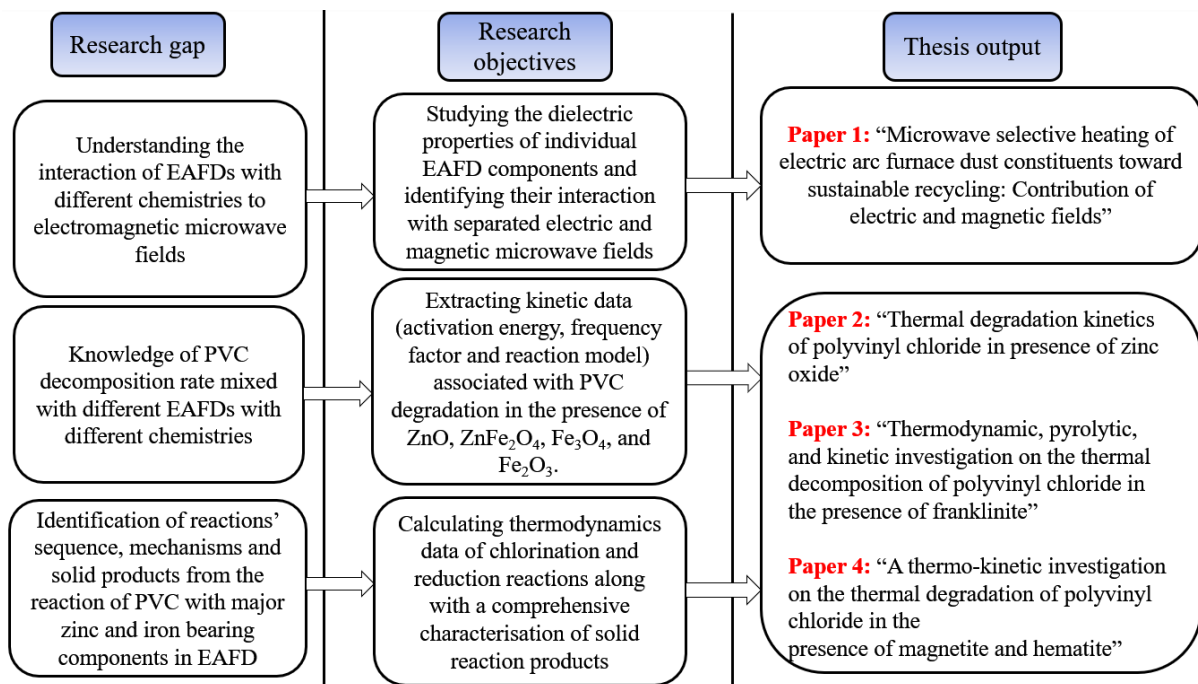


Figure 1: A schematic illustration showing the research gap, thesis objectives and thesis output.

# CHAPTER TWO

## Introduction to microwave heating principles

### 2.1 Overview

Microwave radiation is considered a part of the electromagnetic spectrum occupying its lower frequency end with frequencies ranging from 300 MHz to 300 GHz [37]. This range of frequencies is divided into three main bands: ultra-high frequency UHF (300 MHz – 3 GHz), super-high frequency SHF (3 – 30 GHz) and extremely high frequency EHF (30 – 300 GHz) [38]. An image showing the electromagnetic spectrum is presented in Figure 2.

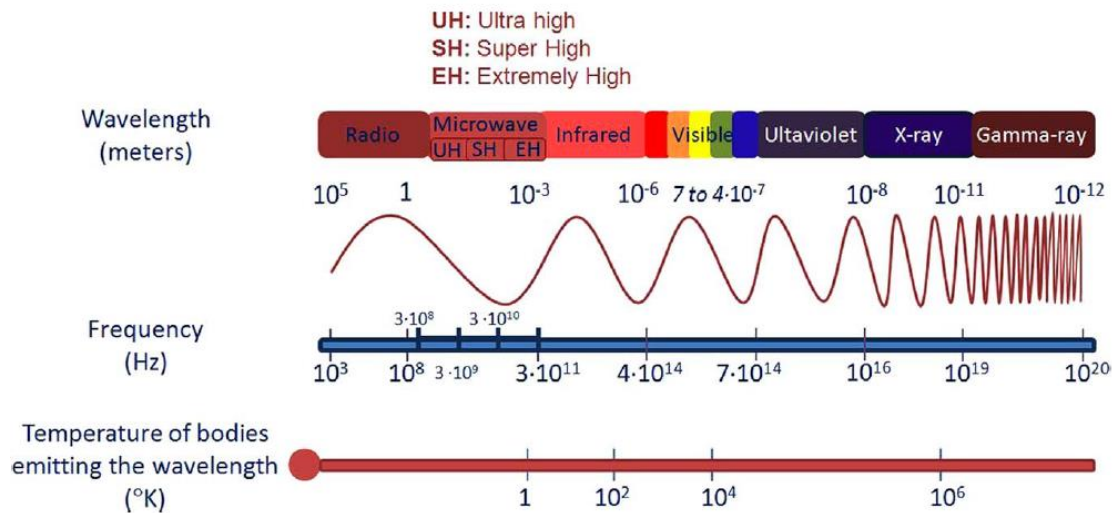


Figure 2: Electromagnetic spectrum from low (radio) frequency to high (gamma-ray) frequency [38].

There are a set of frequencies allocated for industrial, scientific, and medical (ISM) purposes. This is due to the versatile usages of microwave radiation in different applications such as power transmission, radar, and communication which can be affected by the waves generated in the ISM region [39]. Microwaves can be utilised for heating in many industrial sectors such as food processing, wood drying, treatment of plastics and rubbers, and ceramic pre-heating [40]. It has many advantages over conventional heating, such as providing higher heating rates, uniform heating, reduction in harmful emissions, smaller equipment size, and selective heating [37, 40, 41].

There are three types of materials according to their interaction with microwaves (Figure 3) [42]. Transparent materials, also known as low loss materials, allow microwaves to pass through without absorbing energy [43]. Conductors are materials which prevent microwaves from penetrating through causing them to reflect off the external surface [43], while absorbing materials are those which dissipate microwave energy as heat [43].

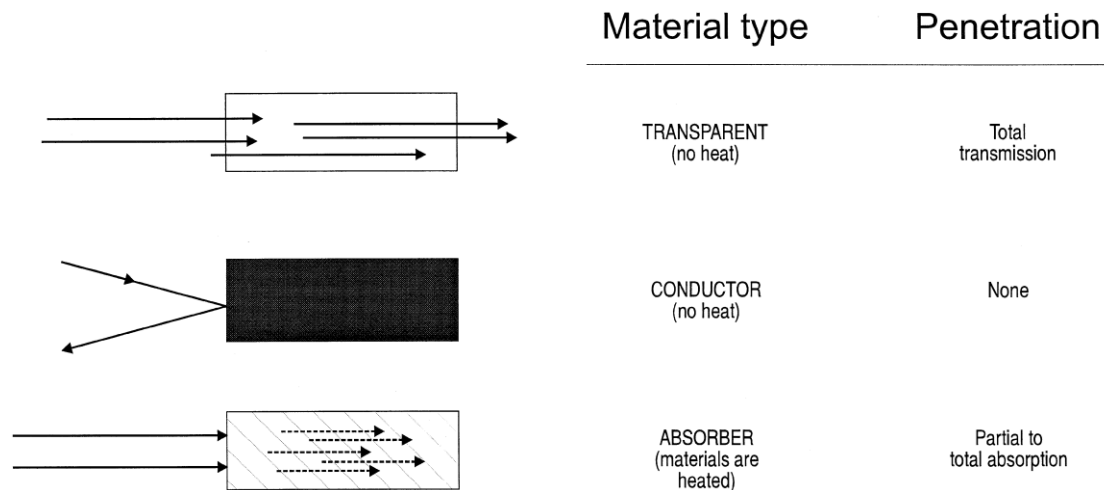


Figure 3: Interaction of microwaves with different types of materials [42].

In the following sections, microwave heating mechanisms, dielectric properties and their measurement techniques, and microwave equipment are discussed.

## 2.2 Microwave heating mechanisms

The heating action of microwaves depends on the type of the material and the frequency of the electromagnetic radiation. Materials which respond to the electric component of the electromagnetic wave are either dielectrics or electrically conducting materials. In the former, charged particles in the material polarise (charge displacement from equilibrium position to another) in response to an external electric field resulting in the formation of what is called induced dipoles [44]. Induced dipoles are a result of electronic and atomic polarisation [44]. Here, we will focus on polar dielectrics; materials containing permanent dipoles such as water. These materials have an asymmetric charge distribution on their molecules making them

responsive to external alternating electric fields in a process called reorientation polarisation [44] which sometimes referred to as dipolar polarisation.

### 2.2.1 Dipolar polarisation loss

In this mechanism, when an external electric field is applied, permanent dipoles try to align themselves with that field by rotation [37]. The alignment of the molecules (dipoles) with the field is called the polarisation and is denoted as  $P$  which is a measure of the displacement of charge inside the material (Figure 4).

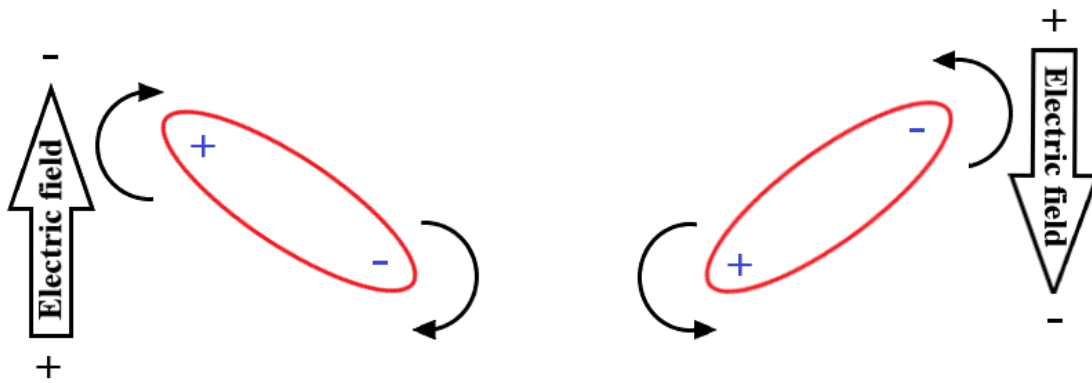


Figure 4: Movement of a permanent dipole when exposed to an external electric field (adapted from [45]).

The molecular alignment does not occur instantaneously, instead, molecules show some inertia which is a function of the molecular size, temperature and viscosity of the medium [46]. Because of this inertia, the polarisation vector  $P$  lags the external electric field  $E$  which makes the polarisation current  $\frac{dP}{dt}$  have a component with the electric field, thus generating heat in the material. The power dissipated in the material from this mechanism is given as [44]:

$$P_{av} = \frac{1}{2} E_{max} P_{max} \omega \cos \theta_0 \quad (1)$$

Such that,  $P_{av}$  is the average power dissipated in the material,  $E_{max}$  is the amplitude of the electric field,  $P_{max}$  is the amplitude of the polarisation vector,  $\omega$  is the angular frequency, and  $\theta_0$  is the phase angle between  $\frac{dP}{dt}$  and  $E$ . Hence, if  $P$  is in phase with  $E$ , the value of  $\theta_0$  will be  $90^\circ$  leading to zero power dissipation.

### 2.2.2 Dielectric properties and the Debye equations

The degree of a material's response to a microwave's electric field can be quantified by its dielectric permittivity: real permittivity ( $\epsilon'$ ) and imaginary permittivity ( $\epsilon''$ ) [47]. The real permittivity represents the charge polarisation ability of the material, while the imaginary permittivity represent how much of the stored energy is dissipated as heat [44, 48, 49]. These two parameters are linked together through the complex permittivity as follows [50]:

$$\epsilon = \epsilon' - j\epsilon'' \quad (2)$$

Where  $j = \sqrt{-1}$ .

For a liquid medium with permanent dipoles, the Debye model [46] was able to describe the real and imaginary parts of Equation 2 mathematically as follows:

$$\epsilon' = \epsilon'_{\infty} + \frac{\epsilon'_s - \epsilon'_{\infty}}{1 + \omega^2 \tau^2} \quad (3)$$

$$\epsilon'' = \frac{(\epsilon'_s - \epsilon'_{\infty})\omega\tau}{1 + \omega^2 \tau^2} \quad (4)$$

Where  $\epsilon_s$  is the permittivity at low frequency,  $\epsilon_{\infty}$  is the permittivity at high frequency, and  $\tau$  is the relaxation time, defined as the time needed for a molecule to change orientation from one equilibrium position to another. The relaxation time was described by Debye's model [46] and was given as follows:

$$\tau = \frac{4\pi r^3 n}{k_b T} \quad (5)$$

Where:  $n$  is the viscosity of the medium,  $r$  is the radius of rotating dipole,  $k_b$  is Boltzmann's constant, and  $T$  is the temperature in Kelvin (K).

Equations 3 and 4 show that the real and imaginary permittivities depend on the frequency of microwaves and the type of material. For a certain material with fixed properties, the behaviour of  $\epsilon'$  and  $\epsilon''$  with frequency of an electromagnetic wave is shown qualitatively in Figure 5.

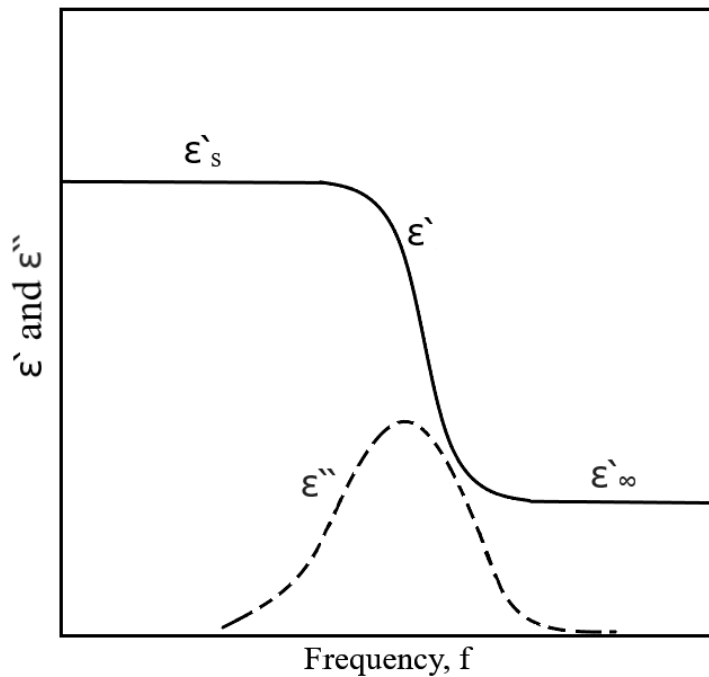


Figure 5: The dispersion of the real and imaginary permittivities with electromagnetic frequency (adapted from [44]).

To find the frequency at which the imaginary permittivity shows a maximum value, we take the derivative of  $\epsilon''$  with respect to  $\omega$  and equate it with zero [51]:

$$\frac{d\epsilon''}{d\omega} = 0 \quad (6)$$

Applying the derivative in Equation 6 to Equation 4, we obtain the frequency at which maximum loss factor is obtained [51]:

$$\omega^* = \frac{1}{\tau} \quad (7)$$

Equation 7 suggests that maximum  $\epsilon''$  is obtained in the material when the frequency of a microwave equals the reciprocal of the relaxation time of the permanent dipoles of this

material. Substituting Equation 7 in Equations 3 and 4 we obtain the values of  $\varepsilon'$  and  $\varepsilon''$  at a maximum loss factor [51]:

$$\varepsilon'(\omega^*) = \frac{\varepsilon'_s + \varepsilon'_\infty}{2} \quad (8)$$

$$\varepsilon''(\omega^*) = \frac{\varepsilon'_s - \varepsilon'_\infty}{2} \quad (9)$$

At a maximum imaginary permittivity, the real permittivity has a value equals the average value of  $\varepsilon'_s$  and  $\varepsilon'_\infty$ .

### 2.2.3 Electric conduction loss

When a material is exposed to a microwave field, translational motion of charge in the form of electrons or ions also contribute significantly to microwave heating due to electrical resistance. Such heating effect can be seen in metallic powders, ionic solutions, and ceramics. For metallic powders and ionic solutions, heating may occur from room temperature since the electrical conductivity of these materials is high. Most ceramics, in contrast, heat by this mechanism only at high temperatures [47]. This is because, at elevated temperatures, atoms in the lattice become thermally excited obtaining sufficient amount of energy to leave the lattice in the form of ions [52, 53]. The imaginary permittivity associated with conduction loss mechanism is given as follows [50]:

$$\varepsilon''_{conduction} = \frac{\sigma}{\varepsilon_0 \omega} \quad (10)$$

Where,  $\sigma$  is the electrical conductivity of the material and  $\varepsilon_0$  is the permittivity of free space. Equation 10 suggests that the imaginary permittivity from the conduction effect is directly related to the electrical conductivity of the material and inversely related to the frequency of the microwave field.

## 2.2.4 Magnetic loss

In addition to the electric component of a microwave, the magnetic component also contributes significantly to the heating. In order for a material to heat in a magnetic field, it has to be either electrically conductive or magnetic [47]. The two main mechanisms associated with microwave magnetic heating are magnetic hysteresis and eddy currents.

### 2.2.4.1 Magnetic hysteresis loss

Electricity and magnetism are related to one another. The spinning of electrons around their own axis and around the atomic nuclei is equivalent to an electric current which, in turn, produces a magnetic moment [54]. In magnetic materials, these magnetic moments are aligned in the same direction in zones called magnetic domains. The magnetic domains are randomly oriented, cancelling each other's magnetic moment, resulting in a zero net magnetisation [55]. When exposed to an external magnetic field, the magnetic moments in these domains align to the same direction and the material becomes magnetised [55]. In order to demagnetise the material, an opposite direction magnetic field is needed and a magnetisation hysteresis loop is formed [47]. The magnetisation hysteresis loop is shown in Figure 6.

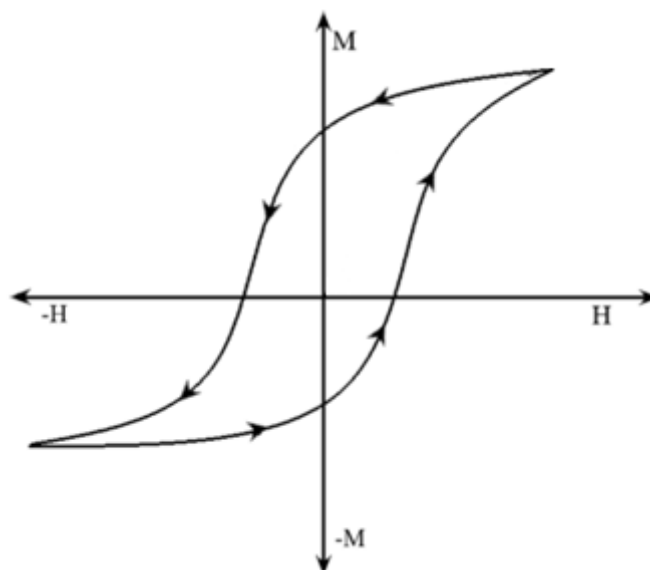


Figure 6: Magnetisation hysteresis loop for a magnetic material inside an alternating magnetic field where  $M$  and  $H$  are magnetisation and magnetic field intensity, respectively (adapted from [55]).

The amount of heat released in the material is proportional to the area inside the hysteresis loop [56]. For magnetic materials, a complex permeability is defined as [50]:

$$\mu = \mu' - j\mu'' \quad (11)$$

Such that the real permeability ( $\mu'$ ) represents the material's ability to store magnetic energy as magnetisation, while the imaginary permeability ( $\mu''$ ) is the ability to release this energy as heat [47].

#### 2.2.4.2 Eddy currents loss

According to Faraday's law, whenever a changing magnetic field passes through a conducting loop, an electromotive force is formed around this loop resulting in the formation of an electric current. Hence, for a solid conducting material positioned in an alternating microwave magnetic field, circular densely packed currents are formed in the material which are referred to as eddy currents (Figure 7).

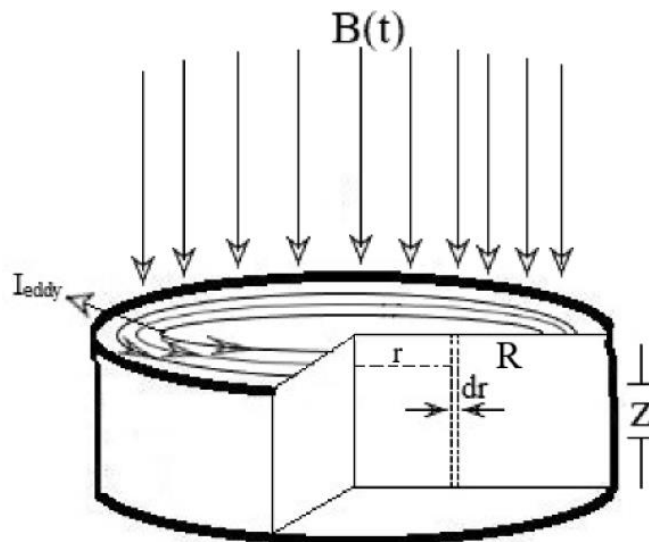


Figure 7: Formation of eddy currents in an electrically conducting disk positioned in an alternating magnetic field ( $B(t)$  time dependent alternating magnetic field).

The power dissipated per unit volume due to eddy currents can be given according to the following equation:

$$P = \frac{\sigma B_0^2 \omega R^2}{16} \quad (12)$$

Where  $P$  is the power dissipated per unit volume,  $R$  is the radius of the disk, and  $B_0$  is the intensity of the magnetic flux.

### 2.3 The power equation and volumetric heating

The equation used to describe the power dissipation in materials originates from the Poynting vector, which is defined as the power carried with an electromagnetic wave per unit area and is given by the cross product of the electric and magnetic fields:

$$\rho = \vec{E} \times \vec{H} \quad (\text{W/m}^2) \quad (13)$$

The power through a closed surface area can be given by integrating the Poynting vector over the surface area [44] which may be written as [57]:

$$P = \oint (\vec{E} \times \vec{H}) d\vec{S} \quad (14)$$

Where  $d\vec{S}$  is an infinitesimally small area. Equation 14 coupled with Maxwell's equations lead to the final equation describing the power dissipation in the material [44]:

$$P = \omega \epsilon_0 \epsilon''_{eff} E^2_{rms} V \quad (15)$$

Where  $E_{rms}$  is the root mean square of the intensity of the electric field,  $V$  is the volume of the material, and  $\epsilon''_{eff}$  is the effective loss factor which accounts for the contribution of different heating mechanism together [47]:

$$\epsilon''_{eff} = \epsilon''_{conduction} + \epsilon''_{polarisation} \quad (16)$$

In case of magnetic dielectric materials, Equation 15 should be modified to the following form given in [44]:

$$P = \omega \epsilon_0 \epsilon''_{eff} E^2_{rms} V + \omega \mu_0 \mu''_{eff} H^2_{rms} V \quad (17)$$

Where  $\mu''_{eff}$  is the effective permeability loss factor,  $\mu_0$  is the permeability of free space, and  $H_{rms}$  is the root mean square of the intensity of the magnetic field.

The equations above, show that the main parameter affecting the power dissipation in materials is the value of the imaginary part of permittivity (dielectric materials) and permeability (magnetic materials).

## 2.4 Microwave measurement and heating equipment

### 2.4.1 Microwave measurement technique

Here, only the cavity perturbation measurement technique will be discussed. This technique relies on measuring an electromagnetic signal in a resonant cavity with and without a sample inside it. The main advantages of this technique are the non-contact measurement type and the requirement of a very small power input (power level of approximately 1 mW) [58]. Other advantages of this technique are the requirements of a very small sample size and the possibility to perform the measurements at high temperatures above 1000 °C [47, 50]. Most cavity perturbation systems are composed of cylindrical cavities containing a  $TM_{0n0}$  standing electromagnetic wave used for the measurements. The resonant frequency and the Q-factor inside the cavity are initially measured with an empty sample holder. The Q-factor is given as [44]:

$$Q = 2\pi \frac{\text{Energy stored}}{\text{Energy lost per cycle}} \quad (18)$$

This means, the smaller the Q-factor is, the more energy is dissipated in the sample. Afterwards, the sample is loaded in the sample holder and then the sample holder and the sample are inserted into the resonant cavity. The shift in the resonant frequency ( $\Delta f$ ) and the change in the Q-factor value are used to calculate the complex relative permittivity according to the following equations [59]:

$$\varepsilon' = 1 + 2J_1^2(X_{l,m}) \frac{V_0}{V_1} \frac{f_0 - f_s}{f_0} \quad (19)$$

$$\varepsilon'' = J_1^2(X_{l,m}) \frac{V_0}{V_1} \left( \frac{1}{Q_s} - \frac{1}{Q_0} \right) \quad (20)$$

Such that,  $J_1$  is the 1<sup>st</sup> order Bessel function,  $X_{l,m}$  is the root m<sup>th</sup> of the 1<sup>st</sup> order Bessel function,  $V_0$  is the volume of the cylindrical cavity,  $V_s$  is the volume of the cylindrical sample,  $f_0$  is the resonant frequency of the unloaded cavity,  $f_s$  is the resonant frequency of the loaded cavity,  $Q_s$  and  $Q_0$  are the Q-factor of loaded and unloaded cavity, respectively. The main limitation of this technique is that it requires small sample size to maintain the electromagnetic configuration of the fields inside the cavity [60], it requires certain sample shape in order for the derived equations to be usable [60] and it is only accurate for low loss materials, typically with loss tangent not higher than 0.1 (loss tangent is  $\frac{\varepsilon''}{\varepsilon'}$ ).

#### 2.4.2 Microwave heating equipment

A microwave heating setup is composed of many pieces each perform a different task. The most basic components of a microwave heating setup are microwave generators, waveguides, waveguide termination, and microwave applicators.

##### 2.4.2.1 Magnetrons

A schematic diagram of a typical magnetron oscillator is shown in Figure 8 [61]. A magnetron consists of a cylindrical cathode in the centre, surrounded by an anode containing several cavities that are spread around in circular fashion. In this device, an electron beam is generated inside vacuum tubes and is directed using a combination of electric and magnetic fields [61]. A voltage is applied between the electrodes (anode and cathode) along with a simultaneous magnetic field such that the electric and magnetic fields are perpendicular to one another [61]. The presence of the magnetic field makes the electrons emitted from the cathode follow a spiral trajectory in their way towards the anode [62]. With high enough magnetic fields, electrons do not reach the anode, instead they form a “rotating space charge” [61]. Rotating electrons

interact with the resonant cavities in the anode resulting in increasing or decreasing their velocity, leading to the formation of electron bunches moving around at microwave frequencies [61]. This, in turn, results in self-sustaining oscillations in the cavities where a portion of the microwave power is extracted using a coupling loop (Figure 8) [61]. Magnetrons were first invented in 1921, allowing the generation of a continuous or pulsed microwave signal with powers up to a few megawatts, a frequency span 1 to 40 GHz, efficiency of around 80%, and a life span of approximately 5000 hours [61].

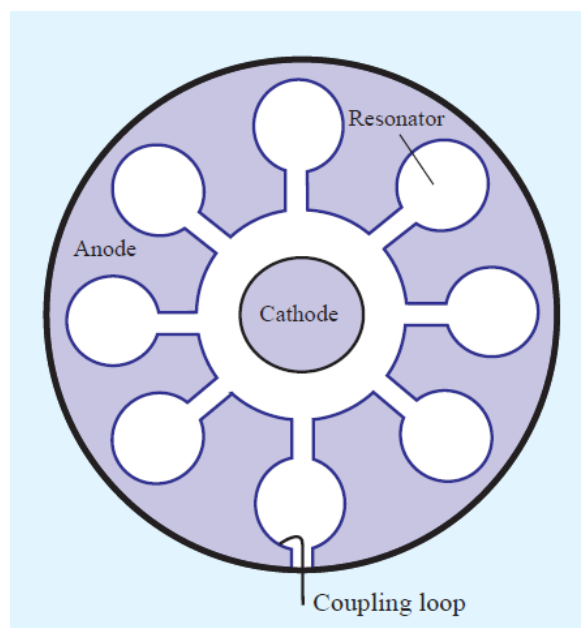


Figure 8: Schematic diagram of a magnetron (adapted from [61]).

#### 2.4.2.2 Solid state generators

A solid state microwave generator is a transistor based amplifier which augments the input power in steps [63]. This means, lower voltages need to be used compared to magnetrons making them safer to operate. However, this type of generator is an evolving technology and to this point is still limited to low powers compared to magnetrons. The major advantages of solid-state generators over magnetrons is their stable power output, ability to produce microwaves with precise frequency, and a longer life-span.

### 2.4.2.3 Waveguides

The generated microwave power needs to be directed towards the material of interest for heating. This can be done using waveguides which are considered an important component of a microwave setup. Waveguides, most of the time, are rectangular ducts made of a highly electrically conductive material (usually aluminium or copper) through which microwaves travel from the microwave source to the processed sample. A typical rectangular waveguide is shown in Figure 9.

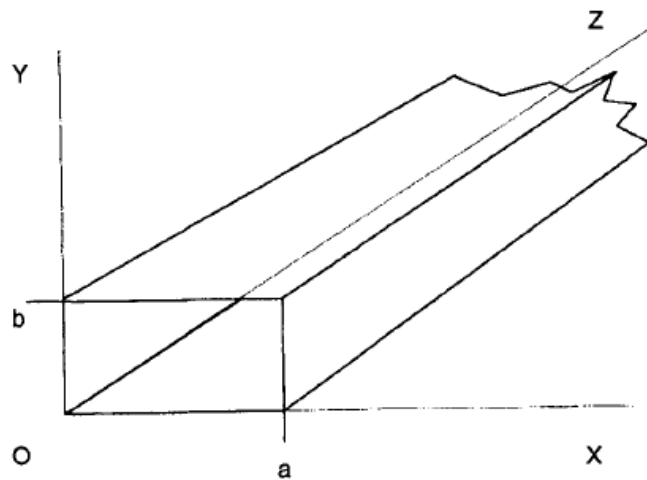


Figure 9: A typical rectangular waveguide with co-ordination system [62].

One of the most important factors to be taken into account when deciding to transfer a microwave signal through a waveguide, is the value of the cut-off wavelength. A cut-off wavelength is the maximum wavelength an electromagnetic wave can propagate with without attenuation. For the commonly used mode transverse electric  $TE_{10}$ , the cut-off wavelength in a rectangular waveguide can be given as follows [62]:

$$\lambda_c = 2a \quad (21)$$

Where,  $\lambda_c$  is the cut-off wavelength and “ $a$ ” is the width of the waveguide (see Figure 9). It is also important to point out that waves propagating inside a waveguide have a larger wavelength than its corresponding free-space wave. The relation between the two can be given for a  $TE_{10}$  as follows [62]:

$$\frac{1}{\lambda_g^2} = \frac{1}{\lambda_0^2} - \frac{1}{\lambda_c^2} \quad (22)$$

Where,  $\lambda_g$  is the guided wavelength and  $\lambda_0$  is the wavelength in free space.

#### 2.4.2.4 Waveguide terminations

Before proceeding to microwave applicators, it would be useful to first consider the last piece connected to a microwave setup (terminal piece). The last piece connected to a waveguide could either be a perfect load (dummy load) or a metallic wall (short circuit).

#### 2.4.2.5 Load termination

In this type of termination, all the microwave power pushed through the waveguide is absorbed and none of it is reflected. This, in turn, affects the electromagnetic configuration inside the waveguide, such that the electromagnetic field inside the waveguide corresponds to a travelling wave type of field distribution. Such configuration allows the sample to be exposed to both the electric and magnetic fields simultaneously, which could be useful for the heating of dielectric magnetic materials. The equations describing a travelling electromagnetic wave can be written as [64]:

$$E(z, t) = E_{max} \sin \left[ 2\pi \left( \frac{z}{\lambda} - \frac{t}{T} \right) \right] \quad (23)$$

$$H(z, t) = H_{max} \sin \left[ 2\pi \left( \frac{z}{\lambda} - \frac{t}{T} \right) \right] \quad (24)$$

Such that  $z$  is the direction of propagation,  $t$  is the time, and  $T$  is the period. Equations 23 and 24 suggest that a sample located in the direction of propagation of a travelling wave will be simultaneously exposed to both the electric and the magnetic fields.

#### 2.4.2.6 Short circuit termination

In this type, the last piece connected to the waveguide is a highly conductive metallic wall (aluminium or copper) which is used to reflect microwaves. Usually, this wall is adjusted within the waveguide with a plunger, such that it can be moved forward and backward inside

the waveguide which essentially helps in positioning the correct electromagnetic field (electric or magnetic) on the sample of interest, and thus greatly enhancing impedance matching for a better power absorption. Since microwaves are reflected off this wall, the waveguide in such configuration contains two travelling waves in opposite directions (forward and backward). The interference of these two waves yields a standing wave which can be described by the following equations [64]:

$$E = 2E_{max} \cos \left[ \frac{2\pi z}{\lambda} \right] \sin \left[ \frac{2\pi t}{T} \right] \quad (25)$$

$$H = 2H_{max} \sin \left[ \frac{2\pi z}{\lambda} \right] \cos \left[ \frac{2\pi t}{T} \right] \quad (26)$$

In Equations 25 and 26, it can be seen that when the electric field is maximum, the value of the magnetic field is zero and vice versa. Hence, in a standing wave, when the sample is positioned correctly, it will be exposed to one field at a time. For the simple case of a  $TE_{10}$ , a boundary condition exists on the metallic wall of the short circuit where the value of the electric field at the wall is zero and that of the magnetic field is maximum. Thus, by moving the plunger (outwards or inwards), the positions of the fields is displaced by the same amount of displacement of the plunger. This, in turn, helps in maximising the intensity of the electric/magnetic field at the sample position.

#### 2.4.2.7 Microwave cavities (applicators)

There are two types of microwave applicators:

1. Single mode applicators.
2. Multi-mode applicators.

A single mode resonant applicator is a microwave reflective metal enclosure into which the electromagnetic wave is exposed to many reflections in preferred directions [44]. The interference of the forward and reflected power, as mentioned earlier, will yield a standing

wave of a known configuration. Samples are then introduced into this cavity using an opening in the applicator which is referred to as “choke”. A choke is usually a circular opening on the top of the waveguide (applicator) which extends through a circular waveguide. The diameter of this choke must be significantly smaller than the cut-off wavelength which allows introducing the sample into the system without microwave leakage.

The best example of a multi-mode microwave cavity is the domestic microwave oven. A multi-mode microwave cavity is an enclosed metallic box the dimensions of which should be several wavelengths long in at least two co-ordinates [44]. The name of such configuration comes from the fact that such cavities are capable of providing several resonant modes in a certain frequency range. The formation of different modes is produced from the constructive/destructive interference of the reflected electromagnetic waves from all directions which yields a standing wave pattern carrying different microwave resonant modes. The main disadvantage that might be encountered in such a setup is the heating homogeneity. For this, samples to be heated can be placed on microwave transparent rotating tables which helps in exposing the same part of the material to different microwave modes which maximises the heating.

## **2.5 Some engineering challenges of microwaves**

### **2.5.1 Penetration depth**

In microwave processing, one of the main challenges faced by engineers is the penetration depth of microwaves into materials. A penetration depth  $D_p$  is defined as the distance from the surface of the material at which the power drops to a value of  $\frac{1}{e}$  of that measured at the surface [44]. Usually, the effect of the magnetic part is neglected and the penetration depth maybe written as follows [65]:

$$D_p = \frac{\lambda_0}{2\pi(2\varepsilon')^{\frac{1}{2}}} \left[ \left[ 1 + \left( \frac{\varepsilon''}{\varepsilon'} \right)^2 \right]^{\frac{1}{2}} - 1 \right]^{-\frac{1}{2}} \quad (27)$$

Where  $\lambda_0$  is the wavelength of the free space propagating wave. In a study conducted by Peng et al. [65], it was concluded that in some magnetic materials, the penetration depth can even be smaller due to heat dissipation from the magnetic part of the electromagnetic field. The general penetration depth which accounts for all electromagnetic fields was given as [65]:

$$D_p = \frac{\lambda_0}{2\sqrt{2}\pi} \left[ \varepsilon''\mu'' - \varepsilon'\mu' + [(\varepsilon'\mu')^2 + (\varepsilon''\mu'')^2 + (\varepsilon'\mu'')^2 + (\varepsilon''\mu')^2]^{\frac{1}{2}} \right]^{-\frac{1}{2}} \quad (28)$$

In general, whether the magnetic effect is taken into account or not, it can be seen from Equations 27 and 28 that the penetration depth increases with an increase in the wavelength  $\lambda_0$ . Hence, usually, at an industrial scale, the used frequency is 915 MHz instead of 2.45 GHz which is needed to achieve higher penetration depths.

### 2.5.2 Heating homogeneity

Since the essence of microwave heating relies on the direct interaction between the electric field carried by the microwaves and the material in question, in some cases, the electric field passes through a certain portion of the material resulting in heating a specific part while leaving the rest unheated. An example of such a phenomenon can be seen in Figure 10.

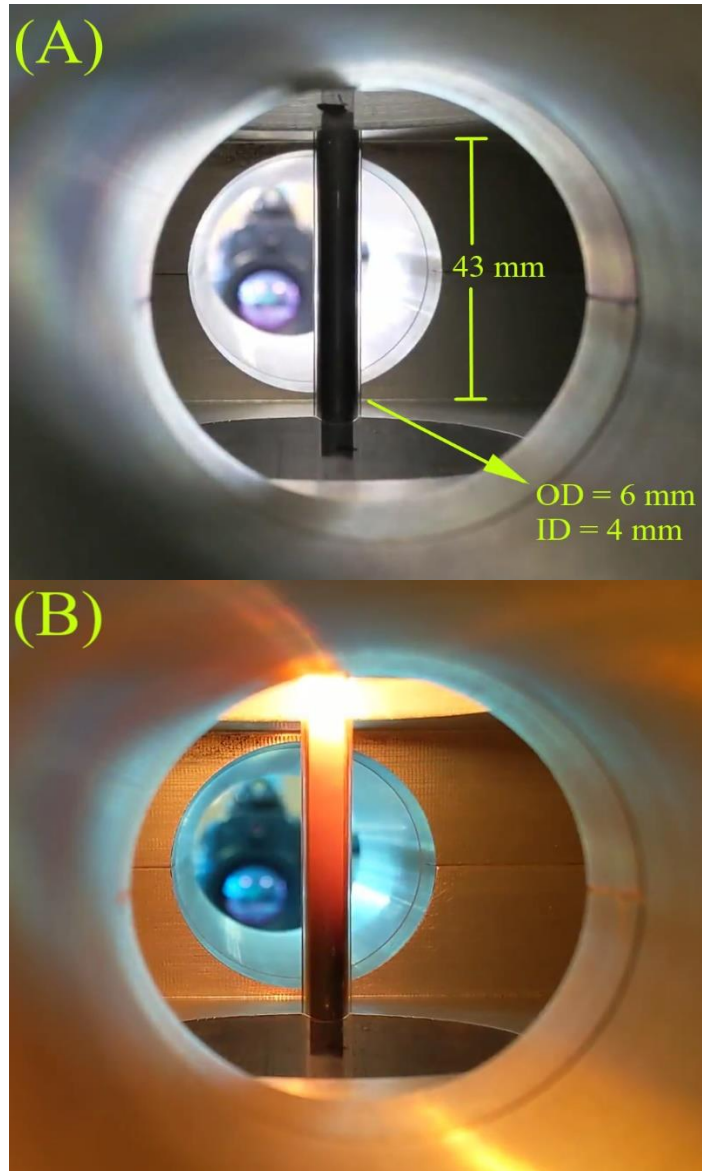


Figure 10: A graphite sample in a single mode TE<sub>10</sub> cavity before (A) and after (B) heating at a power of ~ 118 W and a frequency of 2.47 GHz showing localised heating (OD and ID are outer and inner diameter, respectively).

It is seen in Figure 10 that the heating was localised at the upper portion of the sample while the rest was heated by thermal conduction resulting in a thermal gradient.

### 2.5.3 Thermal runaway

The volumetric heating power equation shown in section 2.3 shows a direct relation between the amount of power dissipated and the loss factor (imaginary part of permittivity) of the material. As an example, when applying microwaves as an energy source for metallurgical processing, one might encounter a thermal runaway problem. This is because, the imaginary permittivity (loss factor) associated with ceramic materials contained in ores (e.g., metal

oxides/sulphides) increases rapidly after a certain temperature usually referred to as “critical temperature” [50]. At the critical temperature, the permittivity of the material rises rapidly [50] which makes controlling the temperature in that range quite challenging when the sample is exposed to microwave energy. An example of this phenomenon can be seen in Bobicki et al. [50] and in the manuscript attached to Appendix 1.

# CHAPTER THREE

## **An overview of electric arc furnaces, electric arc furnace dust and polyvinyl chloride**

### **3.1 Overview**

Understanding the factors affecting the formation and the chemistry of EAFD is important to assess the current practices followed for its treatment and to make sound proposals for mitigating its environmental impact. Hence, a brief introduction to EAFs, EAFD and PVC is presented. Types and construction of EAFs are presented and the raw materials used in EAFs are listed. For EAFD, the material is defined, and its hazard nature is shown. The formation mechanisms and the minimisation of EAFD formation is mentioned. The characteristics and the treatment methods of EAFD are also summarised. Finally, alternative treatment methods of PVC are summarised, along with the mechanisms reported in literature for its thermal decomposition. All researches tackling the co-thermal treatment of EAFD and PVC are presented, assessed, and summarised at the end of this chapter.

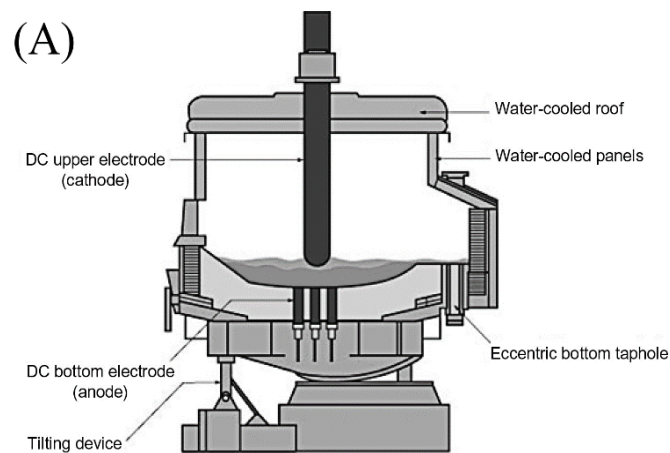
### **3.2 Electric arc furnaces**

EAFs are used for the production of special steels by means of heating using electrical energy. Chemical energy, however, also contributes significantly to heating during the process of controlling the chemical composition, where oxygen is injected and result in exothermic oxidation reactions [66]. One of the principal advantages of EAFs is that the feedstock consists mainly of scrap and cold pig iron. This makes the amount of needed reducing agents much smaller in contrast to when iron ores are used [67]. EAFs have many advantages including the ability to process a wide variety of feed stock, good control of heat generation by controlling the electric currents, and smaller emissions, since heat is supplied by electricity. In contrast, it still has some limitations, where the usage of these furnaces become economically unjustified

in regions where electricity is expensive. A preview of electric arc furnaces types, construction, and raw materials will be summarised in the following sections.

### 3.2.1 Types of EAFs

There are two types of electric arc furnaces: Alternating current (AC) and Direct current (DC) furnaces. The interest in the development of DC furnaces began in the 1990s [68]. Most of EAFs are of AC type [68], however, some DC installations can be seen in Europe, North America, and Japan [69]. This interest in the development of DC furnaces was manifested because of the advantages shown by this type such as the lower energy and electrode consumption, as well as less flickering [68]. According to Elizarov et al. [70] small to medium capacity DC furnaces can show less electrode consumption in the order of 5 – 6 kg/ton of molten steel. In their work, it was also stated that the usage of DC furnaces results in a decrease of charge losses, ferroalloys consumption, and the amounts of emitted dust at 5 – 7%, 15 – 20%, and 6 – 8 times, respectively [70]. Figure 11 (A) and (B) show typical DC and AC electric arc furnaces, respectively.



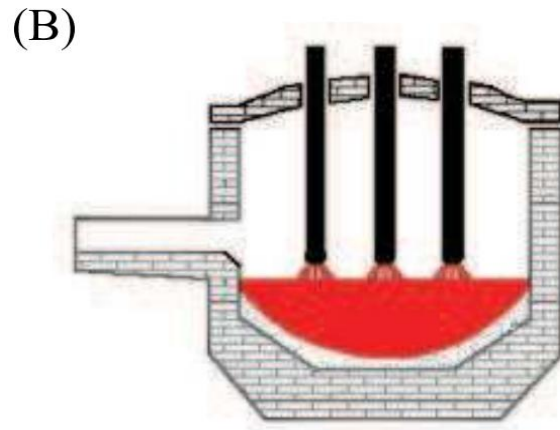


Figure 11: (A) DC electric arc furnace with a single electrode [68] and (B) AC electric arc furnace with 3 electrodes [71].

### 3.2.2 Construction of an EAF

Discussion in this section will be limited to the common type of EAFs which operates in the AC mode and comprises of three electrodes. A typical EAF mainly consists of a refractory lined shell which acts as the body of the furnace, a water cooled retractable roof which has three holes and from which electrodes are introduced, and a rocker which is used to adjust the tilt of the furnace [68, 72, 73]. Figure 12 shows the main constituents of an AC electric arc furnace.

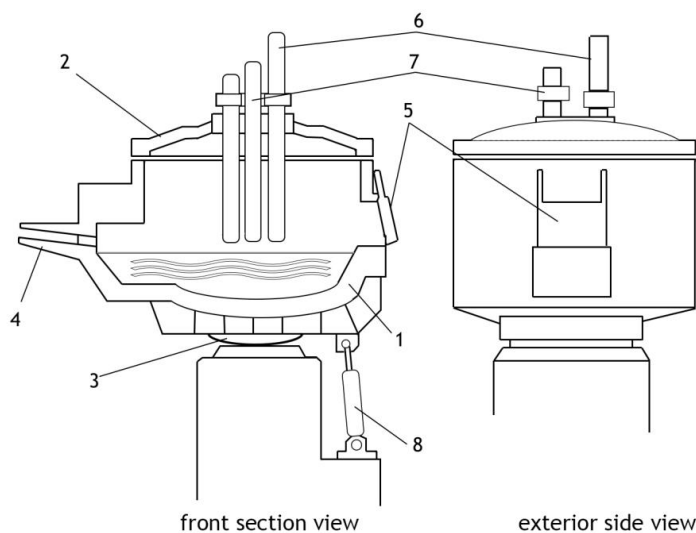


Figure 12: Main components of a typical AC electric arc furnace: 1. Furnace body, 2. Furnace roof, 3.sledge, 4. Purging cradle, 5. Operating door, 6. Electrodes, 7. Water cooled copper rings, and 8. Rocker [73].

The shell which contains the molten bath is made from steel and is lined with a refractory material to withstand the high temperatures inside and to minimise heat losses. The material of

construction of the refractory lining is either magnesite or stabilised dolomite and in some cases silica brick [73]. The second main part of an EAF is the roof; it is retractable so that charged scrap and other additives can be added to the furnace. The roof is important to reduce the heat losses during the smelting process. In some furnaces, roofs are protected by silica bricks or chrome magnesite [73]. In other furnaces, however, roofs are protected by cooling using water panels which reduce refractory lining consumption [68, 74].

Electric current, which is considered the largest contributor to heating in EAFs (aside to chemical energy from combustion reactions), is supplied via graphite electrodes [74]. Graphite is well-known for its high electrical and thermal conductivity, which makes it suitable for this purpose. Typically, the size of an electrode range from 38 to 76 cm in diameter and the length of the electrode is in the order of 3 meters [74]. The diameter of electrodes in large DC furnaces are in the upper range of diameters up to 80 cm [68].

### 3.2.3 Raw materials

EAFs can take all sort of feed stock such as ferrous scrap, hot briquetted iron (HBI), direct reduced iron (DRI), and pig iron. However, the choice of the feeding material to the furnace is mainly controlled by two factors [68, 74]:

- 1- The grade and the desired chemistry of the produced steel.
- 2- The region where the smelting process is taking place which has an effect on the abundance of recycled scrap.

The composition of the scrap metal used specifies the chemistry of the final product. For instance, when ductile steel production is of concern, the content of residual metallic materials such as Cu, Cr, Ni, and Mo should not exceed 0.2% [75]. The problem with these elements is that during the refining process, they do not oxidise and do not go to slag, but instead they remain in the molten bath and carried over to the final product [75]. Hence, when specific

concentration of tramp elements should not be exceeded, scrap of well-known chemistry or virgin materials, such as iron from blast furnaces or DRI should be used [75, 76].

The second factor which affects the type of the charged materials is the region of origin. In developed countries, steel scrap accounts for 100% of the raw materials charged to EAFs [68]. In other countries, however, this is not the case. The quantities of scrap in these countries is less than the required amount for the smelting batch, and hence, the disparity is compensated by direct reduced iron (DRI), hot briquetted iron (HBI), and pig iron [68].

From the discussion above, it can be seen that the chemistry of EAFD generated from EAFs in different countries can vary greatly due to the variation in the type of the raw materials used as a feedstock.

### **3.3 Electric arc furnace dust (EAFD)**

Among many of the hazardous wastes accumulated worldwide, EAFD is considered one of the most troubling due to the severe toxicity of its constituents to human health and the wider environment. Currently no sustainable disposal method is available for this material which either does not leave negative environmental footprint or is economically feasible. The number of studies devoted for the understanding of the mechanisms involved in the formation of EAFD is limited [77-81]. The lack of a mechanistic understanding of EAFD formation limited the adoption of suitable practices in the steel industry to minimise its formation [80]. The amount of formed EAFD can reach up to 1 – 2% of the charge which is collected in dust baghouses [82]. Consequently, this waste material will continue to accumulate becoming a major issue to steel manufacturers. In this section, the formation mechanisms of EAFD, the minimisation of its emission, conventional disposal routes, its characteristics, and the methods used for its treatment will be discussed in detail.

### 3.3.1 Formation of EAFD

Limited studies were devoted for the identification of the mechanisms associated with the formation of EAFD. According to Birat et al. [78] the main mechanisms behind the formation of EAFD are:

1. The volatilisation of metallic species.
2. The formation of liquid droplets from the bursting of CO bubbles on the surface of the molten bath inside the EAF.

These two mechanisms account for 27% and 60% of formed EAFD, respectively [78]. Müller et al. [79] studied the formation of particles from the “gas bubbling mechanism” using a bench scale model steel bath. It was concluded that the main factors that affect the formation of dusts from metallurgical processes in general are the velocity of the bubbling gas, the size of the bubbles, the surface tension and the viscosity of the liquid steel [79]. More recently, a detailed study was conducted by Guézennec et al. [80] to specify the main mechanisms involved in the formation of EAFD. Their study was based on observations using a high speed camera of a molten steel bath, which resembles the conditions in a typical EAF and in which argon gas was bubbled through and burst at the surface [80]. The morphology of the collected particles in the filters was studied which helped in the interpretation of the causing mechanism. The following EAFD formation mechanisms were suggested (see Figure 13) [80]:

- 1) Volatilisation close to the arc (point 1) and close to the oxygen jet (point 1') which represent the hottest spots in the bath.
- 2) Formation of liquid droplets at the impact points between the arc (point 2) and the oxygen lance (point 2').
- 3) Emerging of fine liquid drops from the bursting of CO bubbles (point 3) produced from the decarburisation process.
- 4) Bursting of the liquid droplets in the oxidising environment above the steel bath.

- 5) Finally, the direct fly-off of solid particles from the charging stream (point 5) such as coal (for slag foaming), scrap and fluxing agents.

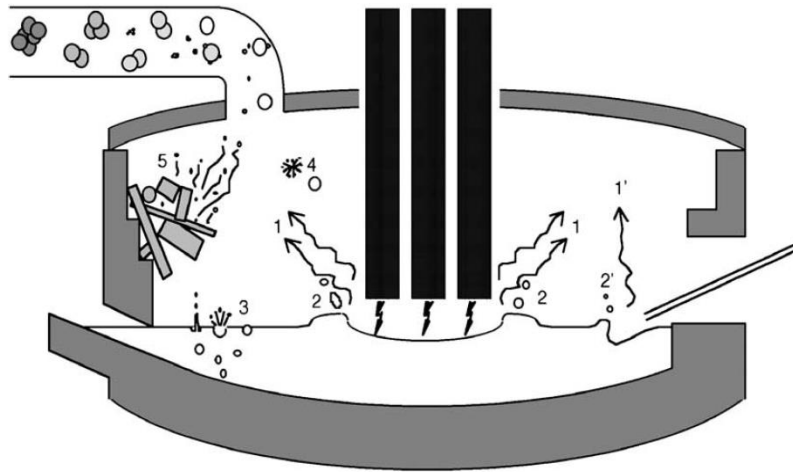


Figure 13: Mechanisms of EAFD emission in electric arc furnaces [80].

Based on the morphological analysis of the collected particles, it was concluded that CO bubble bursting (3<sup>rd</sup> mechanism) on the surface of the bath is the main mechanism for the formation of EAFD [80].

### 3.3.2 Minimisation of EAFD formation

Several studies suggested suitable practices for the reduction of EAFD formation [80, 83, 84].

It was suggested that decreasing the CO bubble size in the range 1 – 4 mm would strongly reduce the amount of formed EAFD [80]. It was also stated that the same level of decarburisation can still be achieved by favouring the nucleation of bubbles over their growth. Huber et al. [83] suggested to limit adding the additives (coal and fluxes) from the top of the furnace, but instead, introduce them from the bottom which would reduce the amounts of the large irregular particles seen in EAFDs.

### 3.3.3 Conventional treatment routes

A number of potential disposal routes for EAFD have been investigated, which some were applied at a large scale. Current practices for the disposal of EAFD are: pyrometallurgical treatment, recycling back to the furnace, and disposal in landfills. In pyrometallurgical

treatment, the Waelz process is the most commonly applied method for the treatment of EAFD [85]. According to Suetens et al., 80% of recycled EAFD is treated in the Waelz kiln [7]. Some nascent pyrometallurgical methods such as the Rotary Hearth Furnace (RHF) and Primus process are also able to treat EAFD for the production of enriched zinc oxide (ZnO) and hot metal (Fe) which has a grade similar to the one produced from conventional blast furnaces (BFs) [7, 86]. More details about these methods are mentioned in section 3.3.5.

Recycling EAFD back to EAFs is another route for its disposal. The main purposes of recycling EAFD back to EAFs are [67]:

1. Lowering the overall amount of EAFD generated from the process.
2. Increasing the zinc content in generated EAFD.

Despite the significant decrease in the amount of emitted EAFD by using this technique, the main potential benefit for recycling EAFD back to EAFs is the enrichment of the produced dust with zinc which in some references was referred to as “Secondary Dust” [4]. Increasing the zinc content in EAFD is important to the Waelz process and provides zinc-rich EAFD to other potential recycling techniques such as hydrometallurgical processing.

In Mantovani et al. [4] the concentration of zinc ranged from 3.54 to 19.76% in the EAFD samples collected from EAFs in which only scrap was used as the feeding material. However, when EAFD was recycled back to the furnace, the collected EAFD sample contained zinc with a percentage up to 27.07% [4]. According to Yang and Gustafsson [87] recycling EAFD back to EAFs resulted in the increase of the zinc content by 11%. López and López-Delgado [88] reported that increasing the zinc content in EAFD from 26 to 51% can be achieved by mixing EAFD with a reducing agent followed by briquetting and recycling back in EAFs.

The landfill strategy is one of the most commonly used options for the disposal of EAFD. There are two types of landfilling sites [21]:

1. Conventional municipal landfills.
2. Secure landfills.

Both these types of landfills follow the Environmental Protection Agency (EPA) standards in landfilling in which the former requires EAFD to be stabilised before its disposal [21, 88]. In the past, the disposal of EAFD in landfills was the cheapest option [67]. However, with time, the legislative specifications of the disposed materials are becoming stricter, and the prices of landfilling are rising [67]. Such strict regulations render the landfill strategy a non-sustainable option for the disposal of EAFD.

### 3.3.4 Characteristics and properties of EAFD

The physical and chemical properties of EAFD are strongly affected by the practices followed in the steel manufacturing process. The quality of the produced and recycled steel, the feeding procedure to EAFs, the power input to the furnace, the characteristics of the gas flow in the extraction system, and the procedures followed in controlling the melting process and the chemistry of the bath are the major process aspects affecting the properties of EAFD [80, 84, 86, 89]. In literature, the most important studied properties were particle size, density, chemical composition, mineralogical composition, and morphology of EAFD. This section will include a brief survey of the properties of EAFD from different sources worldwide.

#### *3.3.4.1 Particle size*

The particle size of EAFD is an important parameter since it affects how the material should be handled. Many EAFD characterisation papers reported the particle size distribution of EAFD [4, 12, 90-92]. In general, the size of EAFD particles ranges from lower than 20  $\mu\text{m}$  (fine particles) to thousand microns (large particles) [80]. Table 1 shows the reported particle size of EAFD from different references.

Table 1: Particle size distribution of EAFD from different references.

Reference	Particle size, $\mu\text{m}$
Li and Tsai [77]	0.3 – 1.0 which agglomerate to 3.0 – 20
Sekula et al. [93]	0.75 – 4.7
Menad et al. [94]	More than 70% < 15
Mantovani et al. [4]	< 10 and 20 – 80
Sofilić et al. [90]	From “< 50” to “> 125”
Guézennec et al. [80]	< 0.2 to few thousand microns
Machado et al. [91]	0.04 – 36
Lee and Song [33]	0.1 – 22
Da Silva et al. [92]	0.04 – 40
Oustadakis et al. [12]	0.06 – 0.8, 0.8 – 120 and 200 – 550
Rizescu et al. [95]	< 2 and 10 – 100

#### 3.3.4.2 Density

EAFD has a powder form, and hence, its density is reported in literature as either bulk or true (skeletal) density. The true density of EAFD is relatively high due to the presence of heavy metals. Table 2 shows the true density of EAFD from different references.

Table 2: True density of EAFD from different references.

Reference	True density, $\text{g/cm}^3$
Mantovani et al. [4]	2.96 – 4.12 for six different samples
de Vargas et al. [96]	4.23
Barreneche et al. [97]	4.93
Lanzerstorfer [98]	3.91

The bulk density was reported by Nyirenda [99] at 1.1 – 2.5  $\text{g/cm}^3$ .

#### 3.3.4.3 Chemical composition

The most important property for the proper handling, disposal, or recycling of EAFD, is its chemical composition. The chemical composition of EAFD is strongly affected by the chemistry of the feeding material, the type of the steel produced, the operating conditions, and the extent of EAFD recycling back to EAFs [86, 90, 100, 101]. The feeding material to EAFs

is affected by the region in which the furnace is operating [68]. In developed countries, scrap alone can meet the requirements of the melting batch. In emerging countries, due to scrap deficiency, the required amount for the heat is met by supplying hot briquetted iron (HBI), direct reduced iron (DRI), and pig iron in addition to the scrap [68]. In view of these variations of the feed stock from one country to another, the chemical composition of EAFD is expected to vary greatly based on the region of its production. Table 3 shows the chemical composition of EAFD from different references from different countries.

Table 3: Chemical composition as a weight% of EAFD from different references.

Reference	Country	Element									
		Zn	Fe	Pb	Ca	Si	Mn	Mg	Al	Na	K
Mantovani et al. [4] <sup>a</sup>	Brazil	12.16	43.04	1.49	-	-	-	-	-	0.81	1.02
Machado et al. [91]		9.24	48.96	-	3.28	-	-	1.65	-	-	-
Da Silva et al. [92]		13.4	42	1.3	4.3	1.3	1.9	1.6	0.3	0.7	1.6
Dutra et al. [102]		12.2	37.08	1.72	2.19	-	-	-	0.41	-	-
Xia and Pickles [16] <sup>b</sup>	Canada	24.93	12.81	2.28	-	-	-	-	-	-	-
Sofilić et al. [90] <sup>c</sup>	Croatia	5.51	44.79	1.31	4.09	2.02	5.53	2.38	0.23	0.53	0.81

Oustadak is et al. [12]	Greece	20.32	-	5.58	-	-	-	-	-	-	-
Montene gro et al. [103]		27.05	14.40	3.81	13.3 2	1.44	1.00	1.30	-	1.30	1.62
Al- Harahshe h et al. [34] <sup>b</sup>	Jordan	32.4	23.0	3.5	5.6	2.4	1.3	8.1	1.0	3.3	1.5
Sekula et al. [93]	Poland	20	30	6.8	2.1	-	2.5	-	-	-	-
Li and Tsai [77] <sup>e</sup>	Taiwan	23.8	22.7	2.14	2.64	1.49	2.94	1.38	n.r	2.32	1.36
Salihoglu and Pinarli [104]	Turkey	19.05	11.58	2.48	6.65	1.62	-	4.09	0.22	0.2	0.48
Keyser et al. [105] <sup>e</sup>	USA	18.3	31.3	2.02	4.19	1.81	3.29	1.68	0.25	0.99	0.66
Tsubouchi et al. [106] <sup>f</sup>	Japan	26.83	30.51	0.49	2.02	2.08	1.05	0.65	1.72	1.63	1.32
Havlik et al. [107]	Luxem bourg	20.9	27.8	2.7	4.3	2.1	3.2	-	-	-	-

Zhang et al. [108]	China	31.4	27.6	0.16	2.4	10.1	0.88	-	-	-	1.8
--------------------	-------	------	------	------	-----	------	------	---	---	---	-----

a: Concentrations are averaged from four different samples.

b: Concentrations are from washed EAFD.

c: Reported concentration is averaged from 12 different samples collected over a year.

d: Concentrations are averaged from nine carbon steel manufacturing mills in Taiwan.

e: Mean concentration from seven plants in the USA.

f: Mean concentration from 6 collected samples.

#### 3.3.4.4 Mineralogical composition

The mineralogy of the major elements in EAFD was reported in many references in literature [15, 33, 91, 92]. Knowing the mineralogical phases in which a certain element is present is very important since it determines how EAFD will behave under different treatment procedures. For instance, it was reported in literature that zinc can easily be extracted from EAFD using acidic and basic leaching when present in EAFD as ZnO, while its extraction from ZnFe<sub>2</sub>O<sub>4</sub> is difficult [14, 16, 109, 110]. Another example on the importance of knowing the mineralogy can be seen in pyrometallurgical treatment procedures. For example, the required stoichiometric amount of carbon used to reduce the iron bearing oxides would vary appreciably based on the oxidation state (FeO, Fe<sub>3</sub>O<sub>4</sub>, or Fe<sub>2</sub>O<sub>3</sub>) of iron. Finally, it was reported by Al-Harashseh [15], that the chlorination of Fe<sub>3</sub>O<sub>4</sub> by HCl is thermodynamically favourable, while the chlorination of Fe<sub>2</sub>O<sub>3</sub> is thermodynamically not possible. Table 4 summarises the main phases in which the major elements are present in EAFD.

Table 4: Mineralogical content of EAFD from different references.

Fe	Zn	Pb	Mg	Ca	Mn	Source
Fe <sub>2</sub> O <sub>3</sub> Fe <sub>3</sub> O <sub>4</sub> ZnFe <sub>2</sub> O <sub>4</sub> MgFe <sub>2</sub> O <sub>4</sub> CrFe <sub>2</sub> O <sub>4</sub>	ZnO, ZnFe <sub>2</sub> O <sub>4</sub>	Not reported	MgFe <sub>2</sub> O <sub>4</sub>	Not reported	MnO	Da Silva et al. [92]
Fe <sub>2</sub> O <sub>3</sub>	ZnO	PbO	MgO	CaO	Not reported	Lee and Song [33]
Fe <sub>3</sub> O <sub>4</sub> ZnFe <sub>2</sub> O <sub>4</sub> FeCr <sub>2</sub> O <sub>4</sub> Ca <sub>0.15</sub> Fe <sub>2.85</sub> O <sub>4</sub>	ZnO, ZnFe <sub>2</sub> O <sub>4</sub>	Not reported	Not reported	Ca <sub>0.15</sub> Fe <sub>2.85</sub> O <sub>4</sub>	Not reported	Machado et al. [91]

Fe <sub>2</sub> O <sub>3</sub>	ZnFe <sub>2</sub> O <sub>4</sub>	PbO	MgO	CaO	MnO	Oustadakis et al. [12]
Fe <sub>2</sub> O <sub>3</sub>	ZnO ZnFe <sub>2</sub> O <sub>4</sub>	PbO	MgO	CaO	MnO	Xia and Pickles [16]
Fe <sub>2</sub> O <sub>3</sub> Fe <sub>3</sub> O <sub>4</sub> ZnFe <sub>2</sub> O <sub>4</sub>	ZnO ZnFe <sub>2</sub> O <sub>4</sub>	PbO	MgO	CaCO <sub>3</sub> CaSO <sub>4</sub>	MnO <sub>2</sub>	Al-Harashsheh [15]
Fe <sub>3</sub> O <sub>4</sub> ZnFe <sub>2</sub> O <sub>4</sub>	ZnO ZnFe <sub>2</sub> O <sub>4</sub>	Pb <sub>3</sub> SiO <sub>5</sub>	Not reported	CaCO <sub>3</sub> CaO CaSO <sub>4</sub> .0.5H <sub>2</sub> O	(Zn,Mn,Fe) (Fe,Mn) <sub>2</sub> O <sub>4</sub>	Havlik et al. [111]

### 3.3.4.5 Morphology of EAFD

Different particle morphologies were reported in the literature. A fraction of EAFD appears as spherical particles and the other fraction has irregular shapes [80]. The spherical particles can be divided mainly into three types:

1. Spinel ferrite [77].
2. Zinc oxide (ZnO) monocrystals [80].
3. Slag droplets [80].

An example of spherical particles is presented in Figure 14 which was reported in Li and Tsai [77].

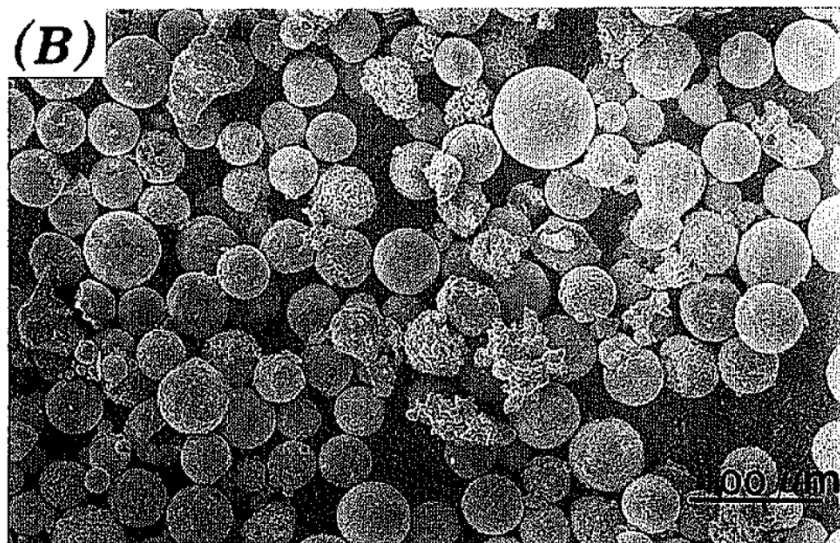


Figure 14: SEM micrograph of spinel ferrite spherical particles with particle size -270/+400 mesh [77].

Guézennec et al. [80] reported the presence of spherical particles in the form of extremely fine zincite monocrystals and large sized (20 – 200  $\mu\text{m}$ ) particles which contains slag components (Ca, Al, Fe, Si...).

Irregular particles were also observed [80] and their presence was attributed to “direct dust fly-off”. The chemistry of these particles indicate that they are formed from coal and lime [80].

Figure 15 shows a SEM micrograph of these particles [80].

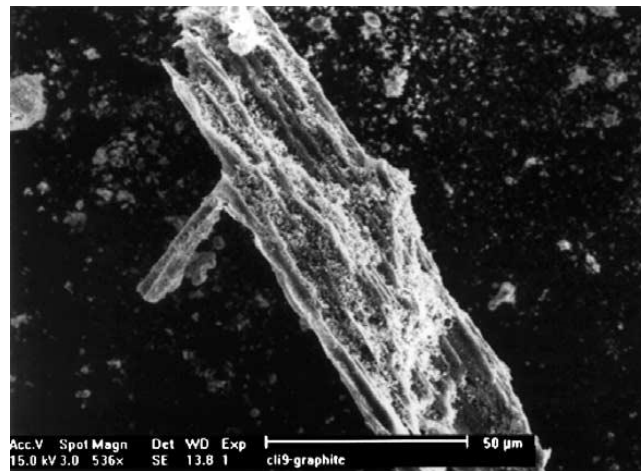


Figure 15: An example of an irregular shape particle in EAFD [80].

### 3.3.5 Pyrometallurgical treatment of EAFD

The pyrometallurgical treatment of EAFD relies on the carbothermic reduction of non-ferrous components, namely zinc oxides ( $\text{ZnO}$  and  $\text{ZnFe}_2\text{O}_4$ ), followed by the selective evaporation of their elemental components over iron. Unlike hydrometallurgical processes, pyrometallurgical techniques witnessed commercial application such as the Waelz process, Primus process, and the Rotary Hearth Furnace (RHF) [112]. All these techniques rely on the principle of the carbothermic reduction; however, they vary only regarding the used facilities and the applied techniques [113, 114].

#### 3.3.5.1 The Waelz kiln process

Among many pyrometallurgical techniques, the Waelz kiln process accounts for 80% of the recycled EAFD [7]. In this process, EAFD is homogeneously mixed with reducing and fluxing

agents and the mixture is then made into pellets [115]. These pellets are then heated to a temperature of 1100 – 1200 °C resulting in the reduction and volatilisation of zinc and lead separating them from the charge [115]. These vapours are then oxidised and collected in their oxide forms (Waelz oxide). While metallic iron is oxidised in the charge forming what is called Waelz slag [116]. A schematic illustration of the Waelz kiln process is shown in Figure 16.

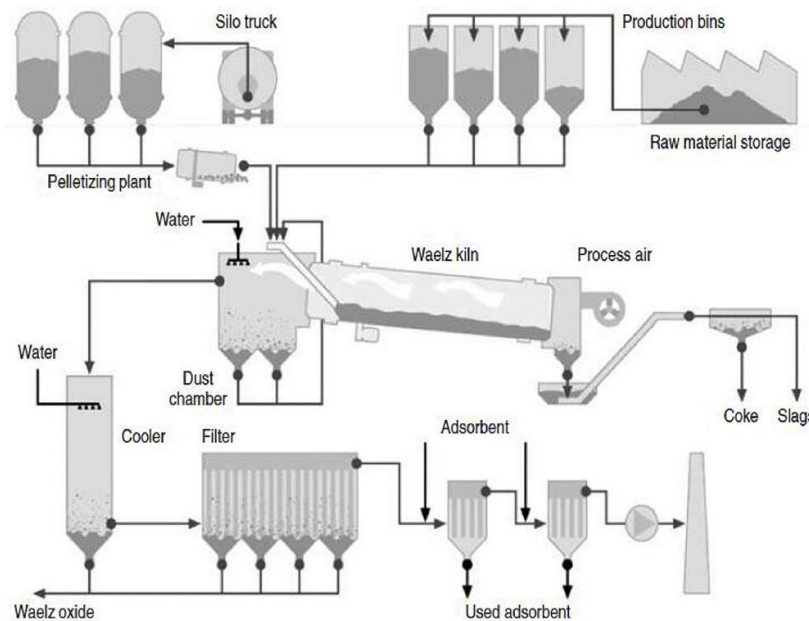


Figure 16: A schematic illustration of the Waelz kiln process [117].

### 3.3.5.2 Primus process

In this process, a multi-hearth-furnace is utilised for the metallisation of fine EAFD [118]. The furnace in this process is different from that of the Waelz process. The furnace is composed of a cylindrical chamber fixed on a vertical axis and contains several circular compartments that are stacked on top of each other [115]. Pulverised EAFD and coal are mixed and loaded from the top (upper most hearth) and then transported to the next hearth by means of scrapers [115]. The temperature of this furnace reaches 1100 °C by means of coal burning and the burning of generated CO gas from reduction reactions [115]. At these high temperatures, zinc and lead oxides are reduced into their elemental forms. The elemental zinc and lead are then oxidised inside the furnace and removed through the exhaust to the bag filter with a recovery up to 95%. At the bottom, direct reduced iron or iron rich residue with a metallisation level of 90 – 95%

are discharged and cooled which can then be used in Blast Furnaces (BF) or EAFs for steel making [119]. A flowchart of this process is shown in Figure 17.

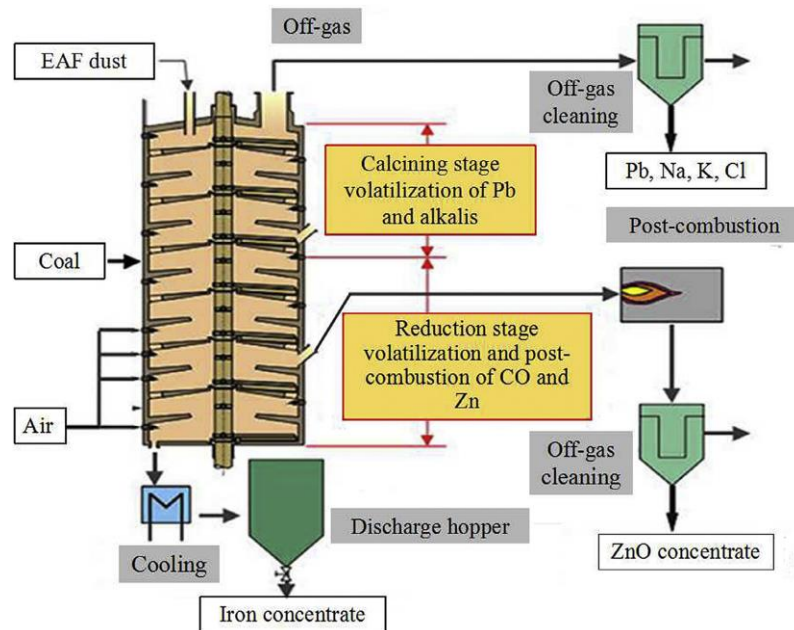


Figure 17: A flowchart of PRIMUS process for the treatment of EAFD [118].

### 3.3.5.3 Rotary Hearth Furnace (RHF)

The RHF is a coal based reduction method for the recycling of EAFD [120]. Initially, EAFD, additives, and reducing agents are mixed and pelletised [121]. These pellets are then moved to the heating zone inside the RHF where the mixture is heated up to 1000 °C after which the pellets are transported to the reaction zone having a temperature of 1300 °C where series of chemical reactions take place [115]; metal oxides are reduced into their elemental forms. Elemental zinc and lead are then separated by vaporisation and are then collected through the exhaust pipe [115]. These vapours are then oxidised and are eventually collected in the dust collector as soot [115]. The iron oxides are reduced to DRI with a reduction percentage of up to 90% in 15 – 20 mins [122]. A flow diagram of the RHF process is shown in Figure 18.

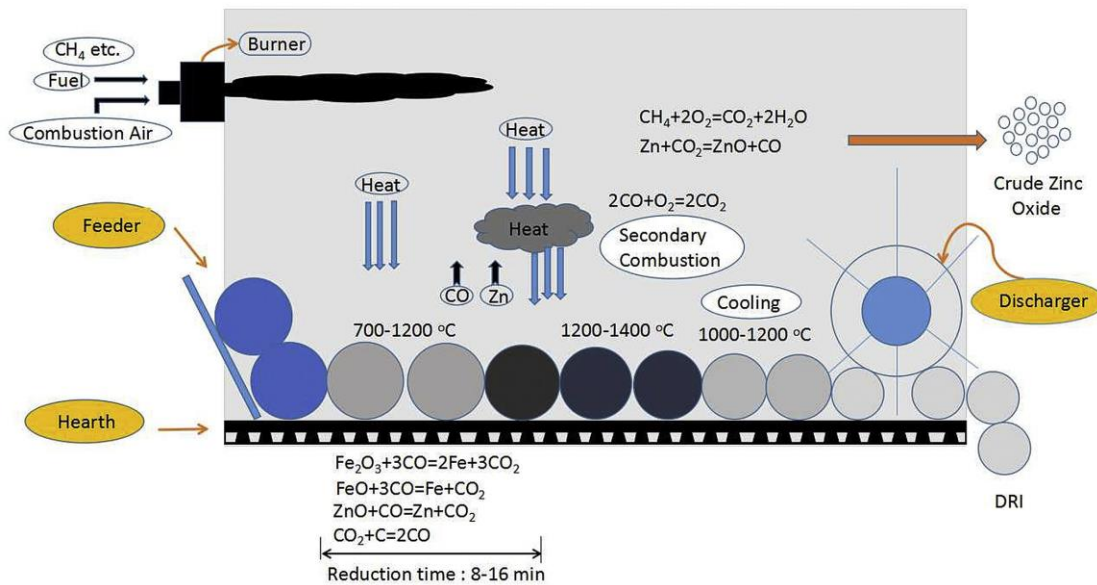


Figure 18: RHF process used for the recycling of EAFD [123].

### 3.3.5.4 Challenges and obstacles of pyrometallurgical treatment of EAFD

While this technique showed a good potential for EAFD recycling and was in fact applied at an industrial scale, the pyrometallurgical approach still suffers from many problems/complications.

#### 3.3.5.4.1 Energy requirements

One of the major limitations of the pyrometallurgical approach for the recycling of EAFD is the energy consumption. Furnaces, in general, operate in the temperature range 1000 – 1300 °C to improve the kinetics of the reactions which is needed to achieve certain metallisation levels. Also, a significant portion of the energy is consumed to compensate for the endothermic nature of the reduction reactions whereby metallic oxides are transformed into their elemental counterparts. All these factors combined, render the pyrometallurgical approach energy intensive.

#### 3.3.5.4.2 The final product and process economics

Unlike hydrometallurgical methods, the products generated from the pyrometallurgical methods are in their oxide forms. These oxides need further processing in hydrometallurgical techniques followed by electrowinning to produce metals in their pure form. This, in turn, can

affect the economics of the process giving the relatively low price of the product along with the high energy consumption.

#### *3.3.5.4.3 Requirements of the feeding material*

In some pyrometallurgical processes such as the Waelz kiln, the concentration of zinc should not be less than 16 wt% in order for the process to be economically justified [124]. In newer installations such as the RHF, low zinc EAFD (< 5 wt%) can be used as a the feeding material, however, zinc oxide blockage can be encountered when high zinc content is used [1].

#### *3.3.5.4.4 The environmental impact*

Finally, one of the major drawbacks of the pyrometallurgical approach is the emission of the greenhouse gases. Since these processes rely on the carbothermic reduction of metal oxides, large amounts of CO and CO<sub>2</sub> are emitted from these processes, with associated detrimental environmental impacts.

### 3.3.6 Hydrometallurgical treatment of EAFD

The high zinc content and the small particle size of EAFD are the most attractive features for exploiting it as a source of zinc using hydrometallurgical techniques. The hydrometallurgical approach, in general, is not energy intensive [13] and makes it possible to recycle the leaching residue back to EAFs due to the reduction in the amount of non-ferrous species it contains [125]. However, despite these advantages, this treatment technique still has many limitations such as incomplete zinc recovery under ambient conditions, contamination of the pregnant solution with iron, and the requirement for costly equipment to resist the harsh acidic and basic medias [14, 103, 126]. In this section, a brief review of hydrometallurgical research conducted on the extraction of zinc from EAFD is presented.

### 3.3.6.1 Acidic leaching

Generally, acidic leaching is known to have faster kinetics generating solutions that are easier to recycle, and the need to use less concentration solutions compared to alkaline solutions [126]. The most common acidic leaching reagents are sulphuric acid ( $\text{H}_2\text{SO}_4$ ), hydrochloric acid ( $\text{HCl}$ ), and nitric acid ( $\text{HNO}_3$ ).

#### 3.3.6.1.1 Sulphuric acid

Much research has been conducted on the extraction of zinc from EAFD using sulphuric acid as a leaching reagent. Kukurugya et al. [126] studied the response of zinc, calcium, and iron containing species upon the treatment of EAFD with sulphuric acid solutions. The highest zinc extraction achieved was 87% using a solution of 1 M  $\text{H}_2\text{SO}_4$ , a temperature of 80 °C and a liquid to solid ratio of 50. Also, they concluded that the dissolution of zinc from  $\text{ZnO}$  was controlled by diffusion, while the dissolution from  $\text{ZnFe}_2\text{O}_4$  was controlled by the rate of the chemical reaction [126]. This result was also mentioned in a work done by Cruells et al. [127]. In that work [127], the non-magnetic part of EAFD was leached at different temperatures, solid to liquid ratios and acid concentrations. They observed that zinc can be extracted up to 80% under optimal conditions [127]. Montenegro et al. [103], used a multistage leaching approach in which the last stage used was a pressurised leaching to maximise the extraction of zinc by attacking the zinc ferrite mineral ( $\text{ZnFe}_2\text{O}_4$ ). It was stated that the maximum possible extraction of zinc was 99% achieved after exposing EAFD to two ambient leaching stages followed by pressure leaching at 200 °C [103]. Hence, it was concluded that the optimal leaching conditions for an iron-free solution with zinc extraction of 60% are: room temperature, 1 M  $\text{H}_2\text{SO}_4$  acid concentration, and a leaching time of 20 minutes [103]. Havlik et al., published three different researches on the extraction of zinc from EAFD using sulphuric acid [10, 107, 109]. In the first work [107], they investigated hydrothermal extraction of zinc from EAFD (i.e., high temperature/pressure leaching); it was found that the maximum possible extraction of zinc was

84% which was obtained at a temperature of 150 °C, a pressure of 4.1 bar, leaching time of 10 minutes, and a concentration of 0.4 M [107]. In the subsequent studies, the leaching of EAFD was done under atmospheric pressure conditions; the maximum zinc extraction achieved was 67% leading to the conclusion that operating up to a pressure of 4.1 bar positively affects the zinc yield, yet it adversely affected the leaching selectivity due to the increased iron dissolution [10, 109]. Oustadakis et al. [12] tested three different parameters on sulphuric acid leaching of EAFD: acid concentration, temperature, and solid to liquid ratio. It was reported that zinc can be extracted up to a percentage of 80% under the following conditions: acid concentration of 1.5 M, temperature of 60 °C and solid to liquid ratio of 10% [12]. Under these conditions, however, iron was extracted at 44.55% [12]. From this work, it can be seen that sulphuric acid is capable of extracting zinc to fairly high percentages. An advantage which discriminates sulphuric acid from other leaching reagents is that the acid is inherently capable of precipitating calcium and lead in the form of lead and calcium sulphates which positively affects the selectivity [10, 12, 103, 107, 109]. Nonetheless, iron is significantly leached from EAFD in all the aforementioned works if high zinc recovery is of concern.

#### *3.3.6.1.2 Hydrochloric acid*

Studies on the extraction of valuable metals from EAFD using HCl leaching are quite scarce. Teo et al. [128] studied the possibility to extract zinc and iron from EAFD using aqueous solutions of HCl under different temperatures, acid concentrations and EAFD to acid ratio. The highest zinc and iron extraction achieved in that work were 70% and 60% respectively using 5 M HCl solution, EAFD to acid ratio of 3 g to 100 mL, temperature of 70 °C and leaching time of 15 minutes [128]. It was evident from the X-Ray diffraction pattern of the leaching residue that zinc ferrite ( $\text{ZnFe}_2\text{O}_4$ ) persisted leaching even under optimum conditions, while ZnO was completely dissolved [128]. Earlier to that work, Langová et al. [11] studied the extraction of zinc from tandem furnace sludge (TFS) and from synthetic  $\text{ZnFe}_2\text{O}_4$  under atmospheric and

hydrothermal leaching conditions. It was concluded from that work that  $\text{ZnFe}_2\text{O}_4$  can be dissolved using 0.3 M  $\text{HCl}$  solution, when operating at a temperature and pressure of 250 °C and 85 bar [11]. The maximum zinc recovery obtained from synthetic  $\text{ZnFe}_2\text{O}_4$  and TFS were 90% and 99% respectively, hence, concluding that atmospheric leaching is insufficient to extract zinc from  $\text{ZnFe}_2\text{O}_4$ , which is in agreement with the data published by Teo et al. [128].

#### *3.3.6.1.3 Nitric acid*

The usage of nitric acid for metal extraction is very limited due to the high cost and the danger associated with the nitrous oxide emission [21]. The only two studies were conducted on the extraction of valuable metals from EAFD using  $\text{HNO}_3$  are those performed by Shawabkeh et al. [129] and Yücel et al. [130]. Shawabkeh et al. [129] studied different acids ( $\text{H}_2\text{SO}_4$ ,  $\text{HCl}$ ,  $\text{HNO}_3$ ) for the extraction of zinc from EAFD. It was shown that zinc can be extracted at 21.3% g Zn/g EAFD which translates to 73% Zn/Total zinc in EAFD in a  $\text{HNO}_3$  solution with a concentration of 5 M and a temperature of  $50 \pm 2$  °C [129]. In the same study, zinc was extracted at 74.9% in  $\text{H}_2\text{SO}_4$  at the same conditions except at a concentration of 2 M [129]. Under the same conditions of  $\text{HNO}_3$  mentioned above,  $\text{HCl}$  extracted zinc with a recovery of 79.4% [129].

Yücel et al. [130] studied the effect of  $\text{HNO}_3$  concentration, leaching temperature, and the stirring speed on the extraction of both zinc and iron. It was concluded that increasing the temperature and  $\text{HNO}_3$  concentration led to an increase in the extraction of zinc [130]. The maximum extraction achieved was 97% when using a concentration of 4 M  $\text{HNO}_3$ , a temperature of 80 °C and a stirring speed of 300 [130]. Under these conditions, however, ~93% of iron was extracted. It was concluded that the optimal leaching conditions are: 0.5 M  $\text{HNO}_3$  and 60-80 °C to minimise iron dissolution and to obtain zinc at 85-93% [130].

### 3.3.6.2 Alkaline leaching

A number of studies have reported the extraction of valuable metals from EAFD using alkaline solutions [14, 16, 131-133]. The main advantage of alkaline leaching is its superior selectivity for zinc over acidic leaching [133]. In the work done by Al-Makhadmeh et al. [14] the leaching of zinc from EAFD using NaOH as a leaching reagent was studied. NaOH concentration, contact time, temperature, and the Solid to Liquid Ratio (SLR) were the studied parameters [14]. It was reported that both temperature and NaOH concentration significantly affect zinc recovery [14]. From the XRD results, it was confirmed that the extraction of zinc from  $\text{ZnFe}_2\text{O}_4$  is very difficult and therefore the recovery of zinc was calculated based on the reactive zinc mineral ( $\text{ZnO}$ ) [14]. The maximum zinc recovery obtained in that work was 92.9% using 6 M NaOH, SLR = 20 mg/mL, 60 °C, and 3 h leaching time [14]. Zhang et al. [108] attempted to totally extract zinc from EAFD using two stages leaching with NaOH. In the first stage, leaching was performed under atmospheric pressure and the following parameters were investigated: temperature, NaOH concentration, time, and Liquid to Solid ratio (L/S ratio) [108]. Only  $\text{ZnO}$  was dissolved in the first stage and the highest recovery was achieved at a temperature of 70 °C, 5 M NaOH concentration, 15 mL/g liquid to solid, and 2 h leaching [108]. The residue from the first stage (mainly  $\text{ZnFe}_2\text{O}_4$ ) was exposed to pressure leaching in presence of starch as a reducing agent. When the residue from the first leaching stage was subjected to pressure leaching, the total extraction of zinc reached 89.7% and the final leaching residue was rich with magnetite ( $\text{Fe}_3\text{O}_4$ ) which was confirmed by both XRD and Vibrating Sample Magnetometer (VSM). Dutra et al. [102] studied the extraction of zinc from EAFD using different leaching conditions: 1) conventional agitation leaching, 2) pressure leaching, 3) microwave treatment followed by leaching and 4) leaching aided with ultra-sonic agitation. The aim of the microwave pre-treatment and the ultra-sonic agitation was to form cracks and break up agglomerates, which can enhance the leaching efficiency [102]. However, it was

reported that no enhancement on the zinc recovery was achieved when these methods were followed and the maximum zinc recovery of 74% was achieved under these conditions: 6 M NaOH, 90 °C and 4 h leaching time [102].

From the discussion above, while the alkaline leaching showed a high selectivity towards zinc extraction (i.e., leaving iron in the solid residue) it was not efficient enough due to the chemically resistive nature of  $ZnFe_2O_4$ .

### 3.3.6.3 Salt leaching

#### 3.3.6.3.1 Hexahydrate ferric chloride ( $FeCl_3 \cdot 6H_2O$ )

In the previous section, it was shown that  $ZnFe_2O_4$  showed a refractory behaviour when leached in alkaline medias. Hence, attempts have been made utilising salt solutions to dissolve  $ZnFe_2O_4$  for higher zinc recovery [8, 124, 134]. Leclerc et al. [8] used a solution of  $FeCl_3 \cdot 6H_2O$  to extract zinc from synthetic  $ZnFe_2O_4$ . The effects of temperature, leaching time and the molar ratio of  $FeCl_3 \cdot 6H_2O/ZnFe_2O_4$  were the studied parameters [8]. It was concluded that zinc can be completely extracted when the leaching was done at a temperature of 150 °C, time of 8 h, with a molar ratio of 10 [8]. Wang et al. [134] produced a similar work in which it was confirmed that using  $FeCl_3 \cdot 6H_2O$  solution at a temperature of 150 °C with leaching time of 2 h and  $FeCl_3 \cdot 6H_2O/ZnFe_2O_4$  mass ratio of 15:20 can result in a zinc extraction efficiency of 97.2% and a leaching liquor almost completely free of  $Fe^{3+}$  ions [134].

#### 3.3.6.3.2 Ammonium chloride $NH_4Cl$

Miki et al. [110] studied the behaviour of zinc, calcium, and iron in raw EAFD and a “CaO pre-treated EAFD” upon leaching using  $NH_4Cl$  solutions. It was shown in another work [135] that  $ZnFe_2O_4$  can be converted to ZnO and  $Ca_2Fe_2O_5$  upon the thermal treatment of EAFD with CaO at temperature of 1100 °C for 5 h under air. This, in turn, can improve the leaching selectivity since ZnO is amenable to leaching while  $ZnFe_2O_4$  is impervious. Hence, a comparison was established between the leaching of raw EAFD and CaO treated EAFD for the

extraction of zinc [110]. It was reported that the leaching of raw EAFD and the CaO pre-treated EAFD using 2 M  $\text{NH}_4\text{Cl}$  solution, at a temperature of 70 °C, and a leaching time of 2 h results in the extraction of zinc at < 50% and ~ 97%, respectively [110]. This result was attributed to the resisting behaviour of  $\text{ZnFe}_2\text{O}_4$  present in the raw EAFD which was absent in the “CaO pre-treated EAFD” [110]. Moreover, it was reported that almost all of the iron was retained in the leaching residue rendering this process to be superior in terms of selectivity for zinc over iron. However, the pre-treatment step is very energy intensive which might affect the justification of applying this process at a larger scale.

#### 3.3.6.3.3 Ammonium Carbonate $(\text{NH}_4)_2\text{CO}_3$

The applicability of ammonium carbonate  $(\text{NH}_4)_2\text{CO}_3$  leaching of EAFD was mentioned in two works [111, 136]. Nyirenda et al. [136] studied the behaviour of three different EAFD samples from different suppliers. It was reported that the extraction efficiency of zinc ranged from 60-80% based on the type of EAFD [136]. This result is mainly attributed to the different mineralogical forms in which zinc is present in one EAFD sample to another (i.e., different  $\text{ZnFe}_2\text{O}_4$  content).  $\text{ZnFe}_2\text{O}_4$  was reported to be refractory to leaching using ammonium carbonate solutions [136]. Following that statement, Havlik et al. [111] utilised this idea for the quantification of ZnO mineral in EAFD. In that work [111], the leaching efficiency of zinc was reported to be 65%. This amount of leached zinc is believed to be solely from ZnO making this leaching procedure a powerful method in determining the percentage of ZnO and  $\text{ZnFe}_2\text{O}_4$  in any EAFD sample.

#### 3.3.7 Challenges and opportunities of hydrometallurgical treatment of EAFD

The application of hydrometallurgical treatment methods is still limited to laboratory scale and has not yet been scaled up to an industrial level. Nonetheless, hydrometallurgical treatment of EAFD has high potential of being applied at a larger scale. This can be attributed to the fact that hydrometallurgy, in general, is less energy intensive and more environmentally sound

compared to the pyrometallurgical approach. However, several challenges need to be addressed in order to realise this approach commercially.

#### *3.3.7.1 Process economics*

The process economics for a hydrometallurgical process can be governed by many aspects including the degree of metal extraction, the possibility to operate under ambient conditions, the material of construction for the leaching reactors, selectivity towards the metal of interest, and the concentration of the leaching reagent.

##### *3.3.7.1.1 The extent of zinc extraction*

From the summary of previous hydrometallurgical studies presented in the sections above, it is clear that obtaining a high zinc recovery required a pre-treatment (high temperature) step such as that reported by Miki et al. [110] where EAFD was pre-calcined with CaO at a high temperature of 1100 °C to transform  $ZnFe_2O_4$  into ZnO before being leached in  $NH_4Cl$ . The other approach followed to maximise the extraction of zinc was to operate under hydrothermal conditions, whereby the leaching solution is heated to a temperature higher than its normal boiling temperature by means of pressurising it [8, 11, 107]. In other ambient condition studies shown above, a significant portion of zinc presented in the form of  $ZnFe_2O_4$  was not leached out due to its chemically resistive nature.

These techniques suffer from either large energy consumption during the calcination process in the pre-treatment approach or the contamination of the leaching liquor with undesirable elements such as iron.

##### *3.3.7.1.2 The material of construction*

High zinc extraction can only be achieved by the aid of hydrothermal approach [8, 11, 107] where the leaching reagent is superheated above its normal boiling point by performing the reaction in high pressure chambers. This method if applied at a large scale, will require special

and expensive equipment. Moreover, the hydrometallurgical approach relies on acidic, basic, or salt based leaching reagents. All these mediums are chemically reactive and would require special alloys or clad reactors to withstand their high reactivity. Most of the resistive materials are expensive which can affect the process economics.

#### *3.3.7.1.3 Process selectivity*

The extraction of zinc at a high percentage can be achieved at the expense of extracting other undesirable metallic species such as iron. Iron can act as an impurity during the electrowinning processes, especially that it has a higher reduction potential making the selective deposition of zinc a real challenge. Moreover, one of the major beneficial side products of the hydrometallurgical processing of EAFD is the iron-rich post processed EAFD. However, when the selectivity towards zinc is lacking, the solid residue will not have much iron left, making its recycling back to EAFs not useful.

#### *3.3.7.1.4 The concentration of the leaching reagent*

One of the parameters which can greatly affect the process economics is the concentration of the leaching reagent. High concentrations are sometimes required to achieve a high zinc extraction. This, in turn, can negatively affect the economics of the hydrometallurgical process.

#### *3.3.7.2 The variability of EAFD composition*

As mentioned earlier (section 3.2.3) , steel production plants in various regions/countries follow different smelting practices. This then introduces a great variation in the chemical composition of EAFD. Hence, one of the major obstacles facing the hydrometallurgical treatment procedure is the variation of the mineralogical composition of EAFD from different plants/countries which can affect decisions in the hydrometallurgical extraction procedure such as the SLR, the controlling mechanism of dissolution which subsequently affect the optimum operating temperature. Moreover, the absence of sufficient amount of data for the

standardisation of the treatment of EAFD from different sources makes it challenging to adopt the hydrometallurgical approach at least internationally where different EAFDs with different qualities are imported.

### 3.3.8 Carbothermic reduction of EAFD using microwave energy

Several studies were conducted on the carbothermic reduction of EAFD using microwave energy as the heating source [137-140]. In the study conducted by Zhou et al. [137] EAFD from stainless steel and carbon steel industries were carbothermally reduced by graphite using microwave energy. The removal efficiency of zinc oxide was about 95%, while the reduction efficiency of iron oxide was 80% for a mixture containing 84 wt% EAFD and 16 wt% graphite heated under microwaves with power of 10 kW for 20 minutes [137]. Ye et al. [139] studied the carbothermic reduction of EAFD with biochar using microwave irradiation. In the same study, a comparison was made between the reduction efficiency with microwaves and with conventional heating [139]. It was concluded that for a mixture of 1:4 Biochar to EAFD heated to 1050 °C for 15 minutes with a microwave power of 1.5 kW, the metallisation degree of iron was 94.7% compared to 67.6% obtained from conventional heating [139]. Additionally, the volatilisation degree of zinc and lead under microwave irradiation was 99.6 and 92.9%, respectively [139]. In conclusion, the reduction efficiency obtained with microwave heating was found to be higher and was attributed to the volumetric heating effect of microwaves preventing the formation of a “cold centre” present in conventional heating [139]. A study conducted by Omran et al. [138] addressed the possibility of the selective separation of zinc from EAFD by means of carbothermic reduction with graphite under a microwave field. A microwave generator with a power of 1.1 kW and a frequency of 2.45 GHz was used to thermally treat pellets of EAFD and graphite at temperatures of 750, 850, and 950 °C [138]. Results from that work suggest that a temperature of 750 °C was not enough to evaporate zinc while a temperature of 950 °C resulted in a high zinc removal percentage of 94% [138]. The

residue from the thermal treatment mainly contained metallic iron and calcium ferrite which can be recycled to steelmaking furnaces [138].

### **3.4 Polyvinyl Chloride plastic**

#### **3.4.1 Overview**

Polyvinyl chloride (PVC) is one of the most used thermoplastics and is ranked the third (after polypropylene and high and low density polyethylene) in terms of plastic demand from converters in Europe at 4.7 million tons in 2020 [18]. A study conducted by Zhou et al. [19] suggested that up to 600 million tons of PVC will be accumulated in China alone before the year 2050. These high numbers can be attributed to the versatile usages of PVC in many applications such as pressure piping, packaging, simulated wood house siding, and disposable gloves [141]. The disposal of this material is considered a principal challenge faced by environmental engineers. Landfilling and incineration of PVC are the most prevalent disposal routes [17, 142]. Recently, however, landfilling has become an unsustainable option since PVC does not decompose and can cause soil undermining [143]. Moreover, the high stability of PVC results in vast dump areas with a consequential increase in landfill cost, rendering this disposal route economically unjustified. Incineration, on the other hand, was deemed unsustainable solution due to the harmful emissions such as hydrogen chloride and chlorinated hydrocarbons (dioxins) [144]. Moreover, during the thermal degradation of PVC, significant amount of Cl containing oils are evolved which were reported to be corrosive to handling equipment [17].

#### **3.4.2 Alternative treatment methods of PVC**

Some alternative nascent technologies were developed for the treatment of waste PVC. Despite the existence of these alternative treatment methods, none of these processes is mature enough to be applied worldwide. This section will include a brief summary of the alternative treatment methods and a detailed discussion on the thermal degradation of PVC including reaction mechanism and kinetics.

### 3.4.2.1 Vinyloop PVC recycling process

While this method involves the dissolution of PVC and its additives, it is classified as a mechanical recycling method since it does not involve the cracking of the polymer [145]. In this process, PVC contaminated with other materials is selectively extracted using an organic solvent [146]. The solvent used by the vinyloop process was the Methyl Ethyl Ketone (MEK) with n-Hexane as a co-solvent [147]. After the dissolution, PVC is then precipitated by means of evaporation using steam [146]. The PVC is also filtered and dried while the organic solvent is recovered and returned to the process [148]. Since the process was unable to separate PVC completely from the other additives such as phthalate ester plasticiser [146], the plant established in Ferrara, Italy in 2002 was shut down in 2018 [146]. A schematic diagram of the Vinyloop process is presented in Figure 19 [146].

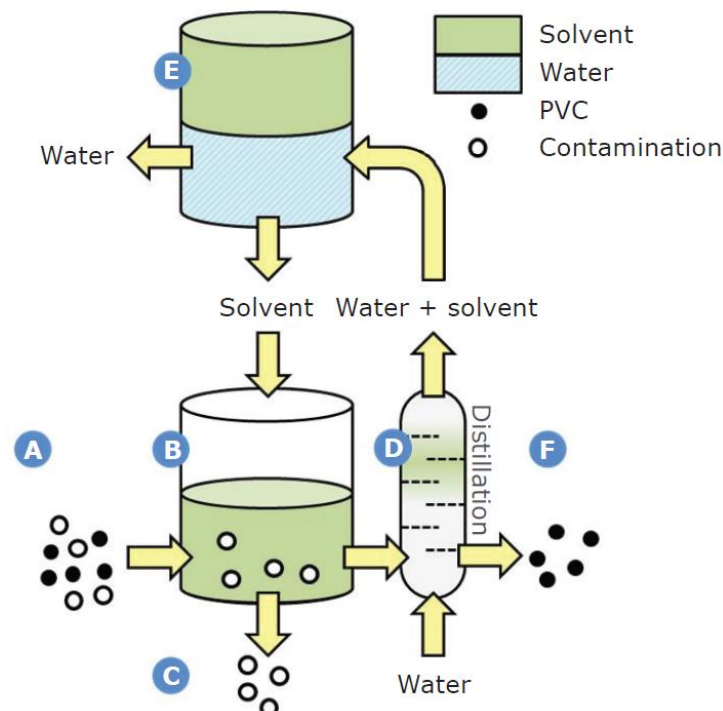


Figure 19: A schematic diagram of the Vinyloop process; (A) PVC waste collection, (B) PVC selective dissolution, (C) contamination filtration, (D) steam distillation, (E) solvent recovery, and (F) recycled PVC [146].

### 3.4.2.2 The NKT pyrolysis process

This process was financed by the Danish environmental protection agency and the NKT holding, ECVN and the Norwegian company Norsk Hydro [145]. Initially, other materials

such as polyethylene, polypropylene, wood, sand, iron, brass, copper are separated from PVC [145]. The thermal decomposition of PVC takes place in a reactor at a pressure and temperature of 2 – 3 bar and 375 °C (max), respectively [145]. The filler added with PVC during the thermal degradation is limestone ( $\text{CaCO}_3$ ) [148]. The PVC reacts with the filler producing calcium chloride [148]. After the separation of the gas, liquid, and solid phases, the major products are [145]: Calcium chloride ( $< 1$  ppm lead), Coke, Metal concentrate (up to 60 wt% lead) and Organic condensate. The metal concentrate and the presence of lead can be attributed to the presence of stabilisers in the original recycled PVC.

#### *3.4.2.3 Stignæs PVC recycling process*

In this process, PVC cables are exposed to leaching using spent caustic soda solution [148]. After the course of the reaction, PVC is completely dechlorinated and a solution of  $\text{NaCl}_{(\text{aq})}$  is obtained. The product is then neutralised using hydrochloric acid and evaporated to concentrate the solution [148]. The organic solid residue is then subjected to four post heating stages to produce gaseous and oil organic fractions which can be used for energy extraction [148].

#### *3.4.2.4 MVR Hamburg (municipal solid waste incineration)*

This plant is able to treat PVC with municipal waste and chlorine is eventually recovered as hydrochloric acid to a quality that meets industrial specifications [148]. In this process, two incineration lines are present each fitted with a grate and a steam generator [148]. The flue gas is then passed through an acid scrubber to capture halogen compounds ( $\text{HCl}$ ,  $\text{HF}$ ,  $\text{HBr}$ ,  $\text{HI}$ ) [148]. 10 – 12%  $\text{HCl}$  solution is produced from passing the flue gas through the acid scrubber [148]. The major products generated from this process are [148]: Electricity, Steam, Hydrochloric acid, Metals (steel (major) and non-ferrous metal), Gypsum, and Slag. More information on this process is presented in detail in Kreißig et al. [148].

### 3.4.3 The thermal degradation of PVC

Knowledge of how PVC behaves under thermal excitation is important for its recycling. Here, the reaction mechanism, pyrolysis products, and previous literature on the kinetics of PVC degradation will be presented. Literature on the effect of the major oxides present in EAFD on the thermal degradation of PVC will also be covered.

#### 3.4.3.1 Reaction mechanism of PVC de-hydrochlorination

The precise mechanism of the thermal dissociation of PVC is still a subject of debate. PVC is known to have a lower dissociation temperature when compared to the other plastics such as polyethylene (PE), polyethylene terephthalate (PET), polystyrene (PS), and polypropylene (PP) (Figure 20) [17].

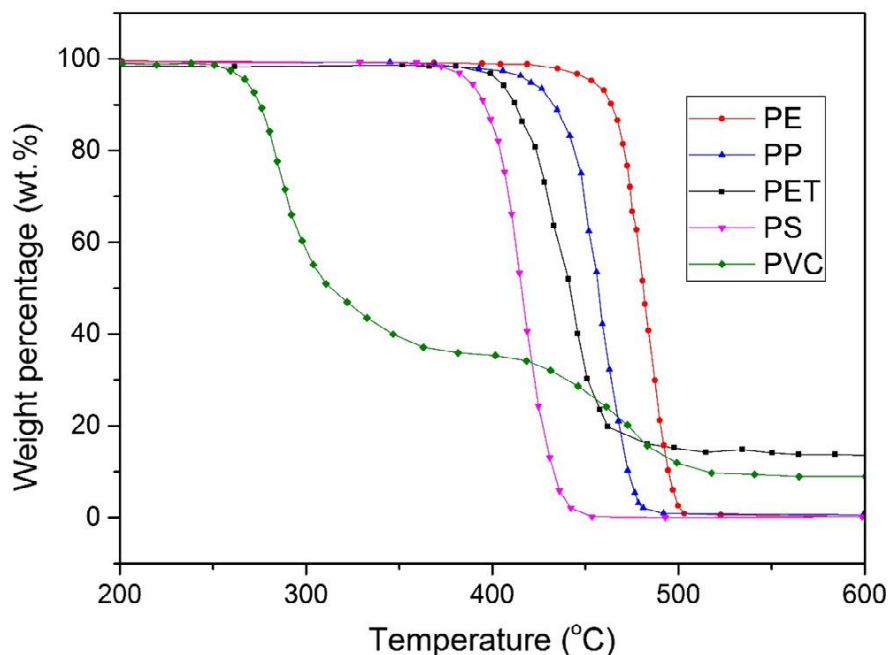
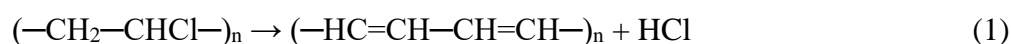


Figure 20: Thermogravimetric analysis of PE, PP [149], PET [150], PS and PVC [149] at a heating rate of 10 °C/min (data collected and presented in [17]).

This thermal instability of PVC was mainly attributed to the presence of thermally labile-sites/defects in the polymer chain [151, 152]. According to Iván [153] and Starnes [151], the thermal dissociation of PVC starts from sites that contain allylic and tertiary chloride atoms generated during the polymerisation process. Minsker [154], in contrast, attributed the poor thermal stability of PVC to the presence of ketoallylic chlorine atoms ( $-\text{CO}(\text{CH}=\text{CH})_n\text{CHCl}-$ )

produced from incidental oxidation during the plastic production. Crawley McNeill [155] suggested that the instability can be associated to the head to head structure in the polymer chain. Despite the absence of consensus on the initiator of the thermal decomposition of PVC, allylic and tertiary chlorine were considered the most important suggested causes [156]. Based on the suggested reasons of the thermal instability, many mechanisms were proposed for the degradation of PVC. The thermal degradation of PVC, in general, involves the dehydrochlorination of the polymer chain by the emission of hydrogen chloride (HCl) gas, followed by thermal cracking of the PVC backbone into low molecular weight organic compounds and the formation of char [9]. Some debate within the literature concerns the number of stages involved in the dissociation of PVC under an inert environment (pyrolysis). Miranda et al. [157] reported three dissociation stages of PVC under nitrogen, which was apparent from the presence of three derivative thermogravimetric (DTG) peaks. Other researchers, in contrast, reported the presence of only two degradation stages [9, 142, 158]. It was reported by Miranda et al. [157] that this contradiction can be assigned to the variation of experimental conditions, such as sample mass and heating rate. There is an agreement, however, on the mechanistic steps occurring during the degradation. In the first (two overlapped) stage, it was reported that the mass loss is between 63-65% and it extends from ~200 °C to ~375 °C [9, 30, 142, 157]. The reported mass loss is higher than the stoichiometric amount of HCl (58.3%) in PVC. Hence, in the first stage, it is believed that all HCl is removed from the PVC chain along with low molecular weight organics, mainly aromatics [27, 159]. The solid residue from the first stage, on the other hand, consists mainly of conjugated double bonds chain (polyene structure) and a cross-linked hydrocarbon structure [9]. The chemical reaction in the first stage is represented as follows [160]:



The formed alternating single and double bond structure then dissociates partially to form aromatics, such as benzene (Figure 21).

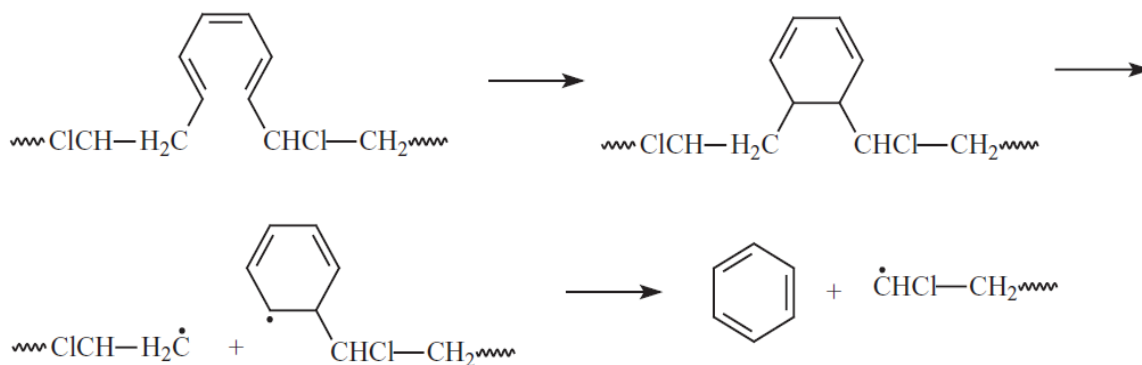


Figure 21: Schematic showing the formation of a benzene ring from PVC degradation [161].

The above reactions describe the overall events happening in the first stage at a macroscopic level. In literature, however, the discussion is more detailed. Three initiation mechanisms are reported for the de-hydrochlorination of PVC [162]:

1. Unimolecular de-hydrochlorination mechanism [163].
2. Free radical de-hydrochlorination mechanism [164].
3. Ionic de-hydrochlorination mechanism [165].

#### 3.4.3.1.1 Unimolecular de-hydrochlorination mechanism

This mechanism was introduced by Braun and Bender [163]. The mechanism suggests that transition states with cyclic forms in the PVC chain can result in its de-hydrochlorination [162, 163]. This de-hydrochlorination then yields HCl as a gaseous emission. A schematic showing the mechanism is presented in Figure 22.

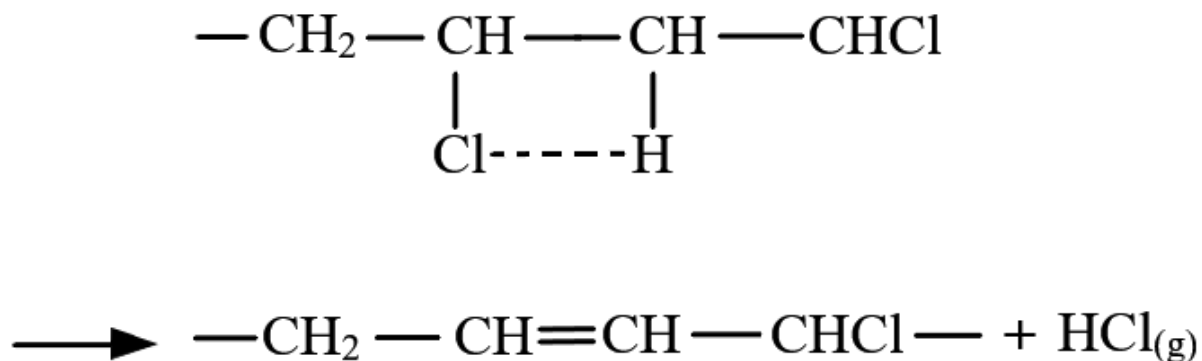


Figure 22: Schematic illustration of the unimolecular mechanism for PVC de-hydrochlorination (adapted from [162]).

It was also suggested that the formation of allylic chlorine positions in the PVC chain can promote this mechanism leading to the “zipper elimination” effect which generates polyene sequences (alternating single-double bonds) at the end [162, 163].

#### 3.4.3.1.2 Free radical de-hydrochlorination mechanism

This mechanism was proposed by Winkler [164] and Stromberg et al. [166]. The mechanism suggests that a chlorine free radical ( $\text{Cl}\cdot$ ) abstracts a hydrogen atom from a methylenic position in an intact PVC chain forming HCl and leaving behind an active radical site on the carbon atom [162, 164, 166]. A chlorine atom adjacent to the carbon free radical then dissociates forming a new chlorine free radical and a carbon-carbon double bond on the PVC chain [162, 164, 166]. The newly formed ( $\text{Cl}\cdot$ ) then attacks another hydrogen atom and the sequence continues. A schematic showing how the free radical mechanism works is presented in Figure 23.

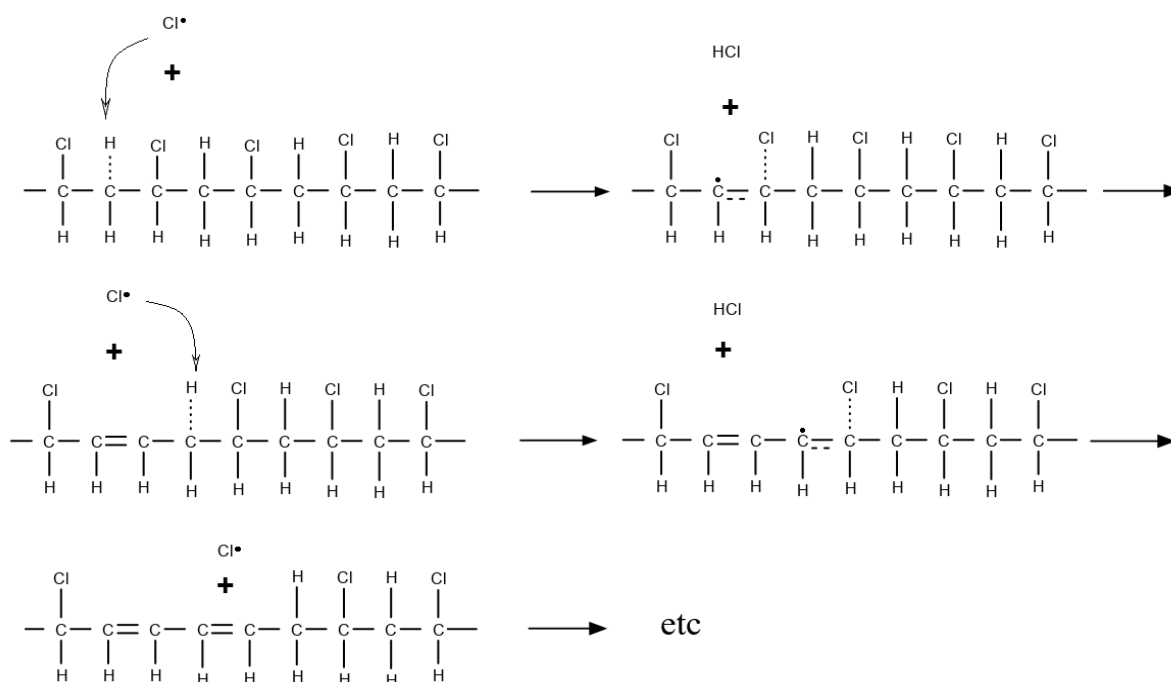


Figure 23: Free radical mechanism for the de-hydrochlorination of PVC.

The de-hydrochlorination in a PVC chain terminates when the formed  $\text{Cl}\cdot$  attacks another PVC chain.

#### 3.4.3.1.3 Ionic de-hydrochlorination mechanism

The mechanism proposed by Rieche et al. [165] suggests that the charge separation in the chlorine-carbon bonds intensifies when certain allylic sites are formed relative to the chlorine atom [162, 165]. This, in turn, results in the loss of chloride ( $\text{Cl}^-$ ) and hydrogen ( $\text{H}^+$ ) ions which then react together to form  $\text{HCl}$ , leaving behind carbon-carbon double bonds [162, 165]. The formed double bond then results in the activation of a new allylic chlorine site, which then allows the mechanism to proceed to completion.

#### 3.4.3.2 Polyene thermal cracking stage

The second decomposition stage of PVC extends from  $325\text{ }^\circ\text{C}$  to  $520\text{ }^\circ\text{C}$  [9]. During this stage, the formed polyene structure from the first stage decomposes further to low molecular weight organics; mainly unsubstituted and alkyl aromatics [27]. The final mass% after the two degradation stages was reported to be  $\sim 9\%$ , which mainly consists of char [142]. The total dissociation of PVC is shown in Figure 24.

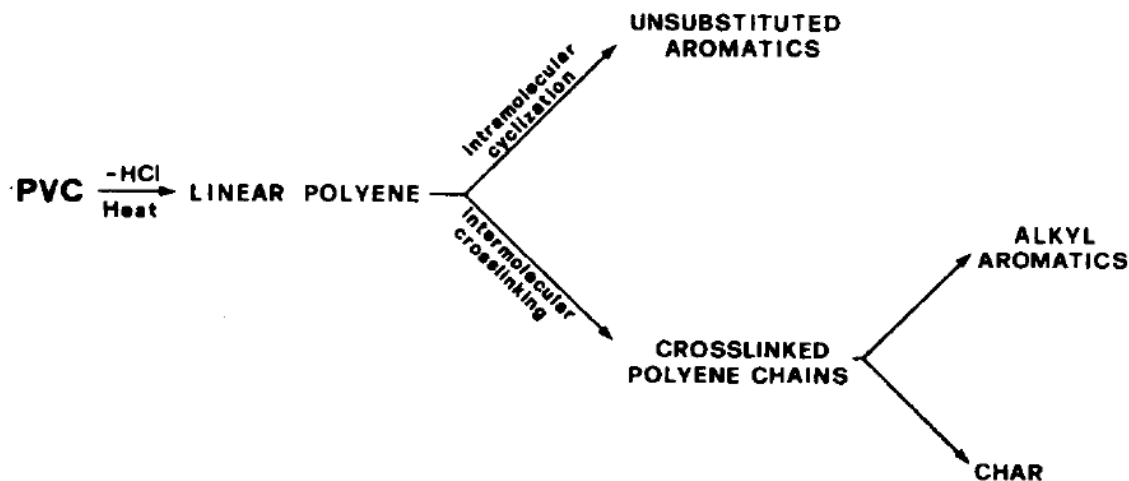


Figure 24: Total thermal degradation of PVC [27].

### 3.4.3.3 Kinetics of PVC degradation

Much research has been devoted to calculating the kinetics parameters of the first and second stage of PVC dissociation [9, 23, 28, 158]. Obtaining the activation energy and the frequency factor of the degradation stages, contributes to determining the rates of reactions that are necessary for performing mass and energy balances on reactors. The main technique used in studying the kinetics of PVC degradation stages is the non-isothermal technique, where the mass of the sample is recorded versus temperature at a fixed heating ramp. A number of methods were proposed by several authors for the non-isothermal kinetics TGA analysis such as: Ozawa-Flynn-Wall (OFW), Kissinger-Akahira-Sunose (KAS), and Friedman methods [167-171]. Other models such as the Coats and Redfern method [172] were also used. However, data obtained from single temperature programme methods such as the Coats and Redfern should be used with extreme caution as they can generate large errors for complicated multi-stage processes. Depending on the model used, a plot of a special function for each method versus the reciprocal of temperature should produce a straight line. The slope and the intercept of that line should provide values of the activation energy and the frequency factor respectively. Table 5 shows values of the activation energy and frequency factor of PVC degradation from different sources.

Table 5: Kinetics parameters of PVC degradation from different references.

Reference	Kinetics parameter			
	Activation energy, kJ/mol		Pre-Exponential factor, s <sup>-1</sup>	
	1 <sup>st</sup> stage (de-HCl)	2 <sup>nd</sup> stage (polyene thermal cracking)	1 <sup>st</sup> stage (de-HCl)	2 <sup>nd</sup> stage (polyene thermal cracking)
Ahmad and Manzoor [173] <sup>a</sup>	160.5	-	2.94 x 10 <sup>15</sup>	-
Zhang et al. [30]	173.0	-	-	-
Sivalingam et al. [31] <sup>b</sup>	147.7	177.4	5.25 x 10 <sup>14</sup>	6.44 x 10 <sup>12</sup>
Miranda et al. [157]	200.0	243	2.18 x 10 <sup>18</sup>	6.47 x 10 <sup>16</sup>
Kim [23] <sup>c</sup>	129.9	282.05	1.82 x 10 <sup>13</sup>	1.58 x 10 <sup>22</sup>
Marcilla and Beltrán [158] <sup>b</sup>	135.8	234	1.18 x 10 <sup>12</sup>	4.43 x 10 <sup>16</sup>

a: Coats and Redfern method.

b: Friedman method.

c: Waste PVC was used in this work.

The variation in the values of the kinetic parameters in Table 5 may be attributed to the fact that the authors above used different kinetic methods and probably due to variations in the PVC type (polymerisation degree, stabilised/un-stabilised PVC, plasticised/non-plasticised, etc.). The difference in the kinetics data might also be attributed to different analytical instrumentation used during the analysis from one study to another. In any case, the data presented above show that the activation energy for the first stage is always smaller than that of the second stage which is in line with the fact that the first stage starts at an appreciably lower temperature.

#### 3.4.3.4 Interaction of PVC with metal oxides

During the incineration of PVC, pure PVC exhibited different degradation behaviour compared to PVC with additives. The main PVC additives are stabilisers, plasticisers, fillers, and pigments [174]. Metal oxides are used as stabilisers and pigments in plastic manufacturing. The presence of metal oxides as stabilisers helps in preventing the degradation of PVC when exposed to heat and UV light in addition to the mitigation of hydrogen chloride emission [174]. In addition to the chlorine fixing ability, some metal oxides were reported to have excellent

ability in suppressing aromatic emissions produced from the cracking of the PVC backbone [27]. A summary on the effect of the main metal oxides present in EAFD on PVC degradation is presented in the following sections.

#### *3.4.3.4.1 PVC and ZnO*

A number of studies were conducted on the effect of zinc oxide addition to the behaviour of PVC degradation [27, 30, 32]. Ballistreri et al. [27], studied the effect of metal oxides addition on the suppression of the unsubstituted and alkyl aromatics emission. It was observed that the addition of ZnO drastically decreased the evolution of aromatics such as benzene, toluene, and naphthalene [27]. Moreover, this addition also significantly reduced the onset temperature of the de-hydrochlorination stage. The reaction between PVC and ZnO was proved by the detection of ZnCl<sub>2</sub> by a mass spectrometer, suggesting that ZnO can be considered an HCl fixator [27]. Masuda et al. [32] studied the effect of many metal oxides on the degradation products of PVC. The results of that study were close to those reported by Ballistreri et al. [27] such that the addition of ZnO significantly suppressed the emission of benzene and toluene [32]. In addition, it was shown that ZnO can also significantly prevent the emission of chlorinated hydrocarbons such as chlorobenzene which is considered one of the main precursors of the toxic polychlorinated dibenzo-p-dioxins (PCDDs) [32]. In the same study, around 51% of the initial amount of Cl in PVC was reported to be captured by ZnO [32]. Finally, the chlorine fixing ability of ZnO was also reported by Zhang et al. [30]. In the same study, the effect of ZnO on the onset decomposition temperature was also reported [30].

#### *3.4.3.4.2 PVC and PbO*

A number of studies investigated the ability of PbO to suppress the emission of HCl and low molecular weight organics from PVC dissociation [32, 175, 176]. Iida et al. [175], confirmed the ability of PbO to suppress the emission of unsubstituted aromatics. However, aliphatic, alkyl aromatics, and chlorobenzene emissions were promoted in the presence of PbO [175].

More importantly, PbO was reported to have superior chlorine fixing ability [32, 176] forming PbCl<sub>2</sub> in the process [176]. According to the study done by Masuda et al. [32], it was reported that only 30% of the initial chlorine in PVC escaped as HCl in the presence of PbO and the rest was captured.

#### *3.4.3.4.3 PVC and Fe<sub>2</sub>O<sub>3</sub>*

Many studies were performed on the effect of the addition of Fe<sub>2</sub>O<sub>3</sub> on the thermal behaviour of PVC degradation [181, 31, 32, 35]. In literature, it is believed that the metal chlorides resulting from metal oxide chlorination are responsible for affecting the de-hydrochlorination of PVC [31]. According to Al-Harabsheh [15], however, the chlorination of Fe<sub>2</sub>O<sub>3</sub> to FeCl<sub>3</sub> by HCl is thermodynamically not possible, yet it was found that Fe<sub>2</sub>O<sub>3</sub> does significantly affect PVC degradation [27, 177]. For instance, it was observed that Fe<sub>2</sub>O<sub>3</sub> resulted in the promotion of chlorobenzene emission, yet significantly reduces the emission of unsubstituted aromatics and alkyl aromatics [27, 32, 175]. According to Uegaki and Nakagawa [177], the interaction between Fe<sub>2</sub>O<sub>3</sub> and PVC can be attributed to an ionic mechanism, whereby the iron atom is believed to be responsible for facilitating the detachment of the chloride anion from the PVC chain. However, no further evidence supporting this theory on the chlorination of Fe<sub>2</sub>O<sub>3</sub> can be seen in literature.

#### *3.4.3.4.4 PVC and ZnFe<sub>2</sub>O<sub>4</sub>*

Only the study performed by Zhang et al. [30] addressed the effect of ZnFe<sub>2</sub>O<sub>4</sub> on the thermal behaviour of PVC. In that work, the formation of iron oxides at different oxidation states (FeO and Fe<sub>3</sub>O<sub>4</sub>) was also detected as a result from the chlorination of Zn by the emitted HCl [30] and the subsequent reduction of formed Fe<sub>2</sub>O<sub>3</sub> to lower oxidation states by emitted H<sub>2</sub> and carbonaceous materials. It was also observed that ZnFe<sub>2</sub>O<sub>4</sub> resulted in lowering the onset de-hydrochlorination temperature of PVC [30].

#### 3.4.3.4.5 PVC and $Fe_3O_4$

The only study undertaken investigating the effect of  $Fe_3O_4$  on the thermal behaviour and pyrolysis products of PVC degradation was done by Ye et al. [178]. In that work, different  $Fe_3O_4$ -PVC ratios (10, 20, 50, and 75 wt% of  $Fe_3O_4$ ) were studied [178]. It was concluded that the amount of HCl escaping is strongly dependent on the  $Fe_3O_4$  content in the  $Fe_3O_4$ -PVC mixture [178]. For instance, the mixture containing 75 wt%  $Fe_3O_4$  captured 97.6% of the HCl content present in PVC [178], while the mixtures containing 50, 20, and 10 wt%  $Fe_3O_4$  captured 80.8, 56.2, and 50.2%, respectively [178]. The study also confirmed the formation of iron chloride in the tetrahydrate form [178].

### 3.5 Literature on the co-thermal treatment of EAFD with PVC

From the work reported in the previous section, it can be seen that many metal oxides have the ability to capture emitted HCl during de-hydrochlorination of PVC. Waste EAFD contains large quantities of metal oxides in the form of ZnO,  $ZnFe_2O_4$ ,  $Fe_3O_4$ , and  $Fe_2O_3$ . Hence, in this section, an overview of the literature on the interaction of EAFD-PVC is presented in terms of kinetics, thermodynamics, and metal extraction under both inert and oxidative conditions.

#### 3.5.1 The kinetics of PVC degradation in the presence of EAFD

The kinetics of PVC dissociation with EAFD was only studied by Al-Harshseh et al. [9]. Some other studies, however, addressed the kinetics of PVC degradation with pure metal oxides [28, 30, 31]. It was reported that the addition of some metal oxides catalysed the de-hydrochlorination of PVC and resulted in lower values of the activation energy, while some other metal oxides such as CuO,  $Co_3O_4$ ,  $Cr_2O_3$ ,  $MoO_3$ , and  $PbO_2$  did not have a catalytic effect [28, 31]. There is a fair degree of consensus in literature that the catalysis of the de-hydrochlorination is in fact a result from the interaction of the formed metal chlorides with the chlorine atoms in the PVC chain which facilitates the degradation [31, 173]. It was reported

that PVC chlorinates the metal oxides to form metal chlorides, and the formation of metal chlorides, in turn, results in further catalysis of the dissociation of the polymer [31].

In the work performed by Al-Harashsheh et al. [9], the effect of EAFD on the thermal degradation kinetics of PVC was studied. Coats and Redfern [172], Van Krevelen [179], integral [180], and KAS [167, 171] methods were used and compared for the extraction of the kinetic parameters for the degradation of PVC and its mixtures with EAFD with ratios of 1:1, 1:2, and 1:3 (E-PVC1, E-PVC2, and E-PVC3). A summary of the activation energy associated with the thermal degradation of PVC in the presence of different ratios of EAFD can be seen in Figure 25.

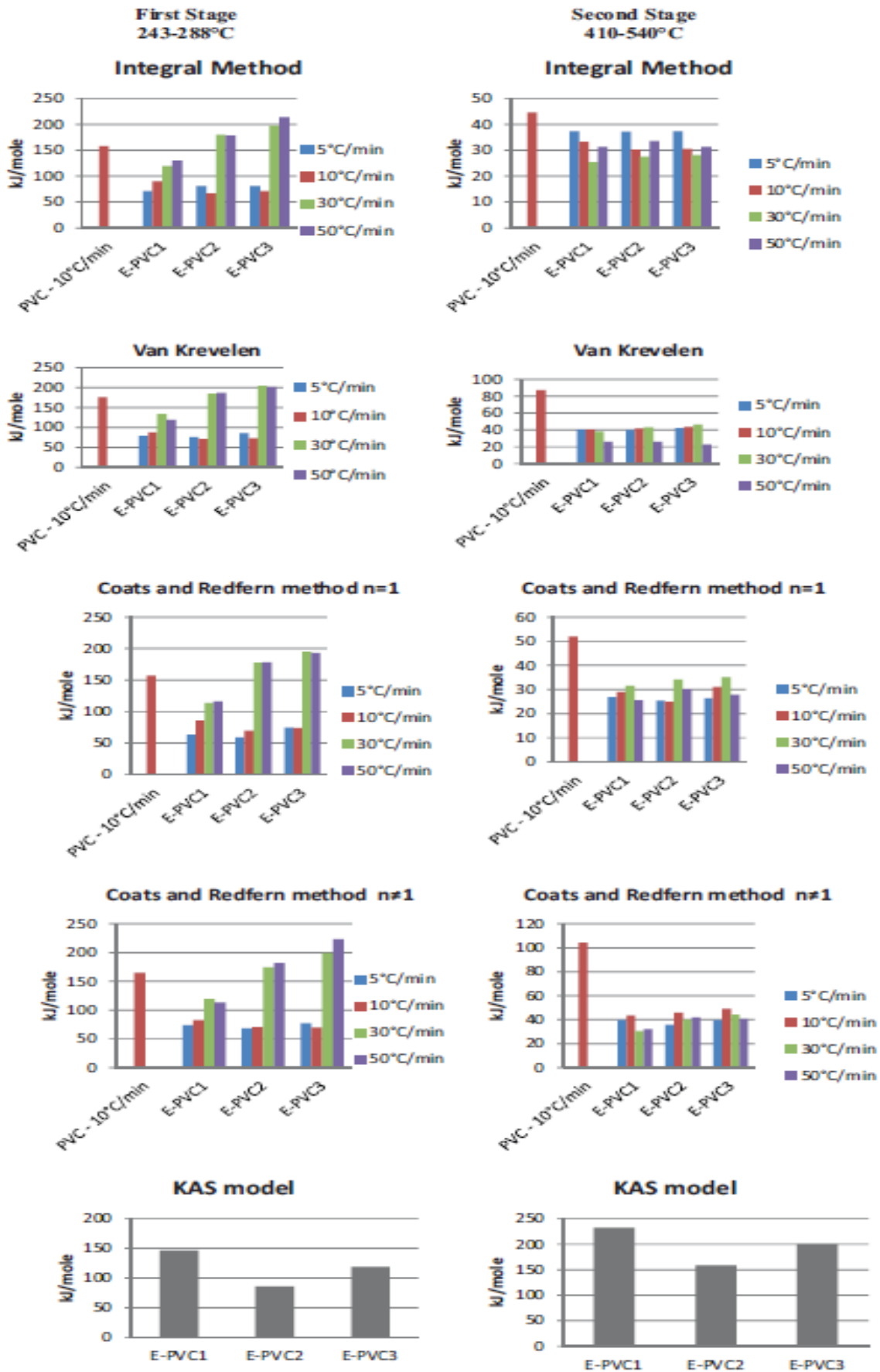


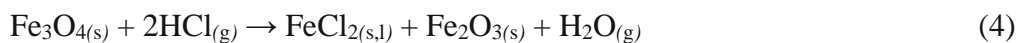
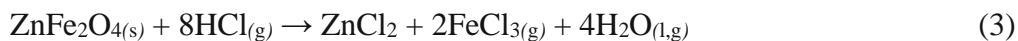
Figure 25: Activation energy of PVC dehydrochlorination (first stage) and backbone cracking (second stage) in the presence of EAFD at different ratios and heating rates [9].

Figure 25 shows that EAFD affected the kinetics of both the first and the second PVC degradation stages. It is also important to note that the heating rate showed a large effect on the value of the activation energy of the first stage, but not the second one. Such a result suggests that the de-hydrochlorination of PVC in the presence of EAFD involves more than one stage/reaction (i.e., a multi-step process); each process controlling the degradation to a varying extent depending on the heating rate. The polyene thermal cracking, in contrast, showed an almost constant activation energy when the heating rate was changed, suggesting the possibility that a single process is controlling the mass loss in that stage.

Considering the 10 °C/min graphs, it can be seen that the activation energy of PVC dehydrochlorination (1<sup>st</sup> stage) was lowered from ~ 160 kJ/mol when pure to 75-90 kJ/mol for a 1:1 EAFD to PVC ratio. The same “metal chloride” catalysis mechanism, might be applicable in the case of EAFD-PVC, since it was shown in Al-Harahsheh 2017 [15], that most metal oxides in EAFD are prone to chlorination by the emitted HCl as will be shown in the next section.

### 3.5.2 The thermodynamics of the chlorination of EAFD constituents

Al-Harahsheh [15] reported the thermodynamic data of the co-thermal treatment of EAFD with PVC. The following are the expected reactions occurring during the thermal treatment of EAFD with PVC and the Gibbs free energy plot associated with each reaction (Figure 26) [15].



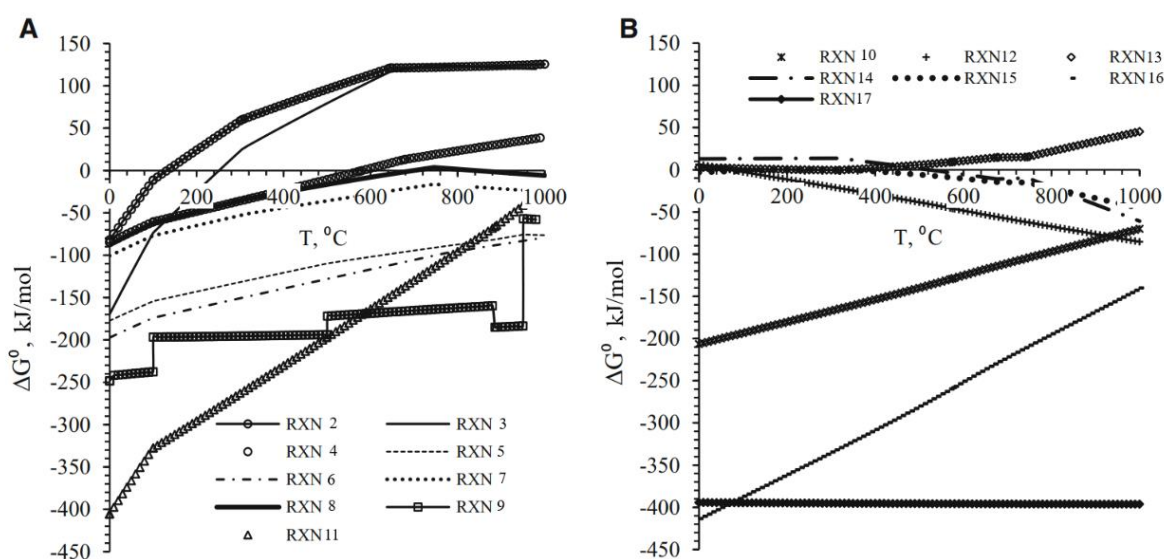
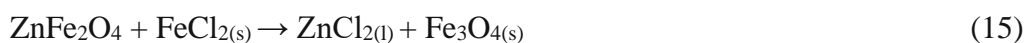
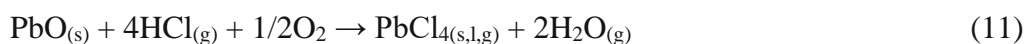


Figure 26: Gibbs free energy of the chlorination (A) and non-chlorination (B) reactions (FactSage 7.0) [15].

The chlorination of the zinc containing species  $\text{ZnO}$  and  $\text{ZnFe}_2\text{O}_4$  according to Reactions 7 and 8 is thermodynamically favourable in the temperature window 0 – 1000  $^\circ\text{C}$ . Nevertheless,  $\text{ZnFe}_2\text{O}_4$  shows equilibrium behaviour in the temperature range from ~ 650 to 950  $^\circ\text{C}$ . Likewise,  $\text{PbO}$  shows amenability towards chlorination forming  $\text{PbCl}_2$  or  $\text{PbCl}_4$  according to Reactions 5 and 11 respectively over the entire temperature range. This thermodynamic data, suggests that the chlorination of zinc and lead species is possible upon the thermal treatment with PVC [15]. In contrast, iron species show different behaviour. Iron is present in EAFD in three main species: hematite ( $\text{Fe}_2\text{O}_3$ ), magnetite ( $\text{Fe}_3\text{O}_4$ ) and franklinite ( $\text{ZnFe}_2\text{O}_4$ ). While the chlorination of iron from  $\text{Fe}_3\text{O}_4$  is possible in the temperature range 0 – ~570  $^\circ\text{C}$ , the chlorination of iron in  $\text{Fe}_2\text{O}_3$  and  $\text{ZnFe}_2\text{O}_4$  becomes thermodynamically unfavourable above

125 °C and 250 °C, respectively (Reactions 2 and 3). It is important to note that HCl gas was reported to be released from the pyrolysis of PVC at temperatures from 230 – 370 [9], which makes the formation of ferric chloride ( $\text{FeCl}_3$ ) from  $\text{Fe}_2\text{O}_3$  and  $\text{ZnFe}_2\text{O}_4$  unlikely. Hence, it is believed that if iron was present in the form of  $\text{Fe}_3\text{O}_4$ , the selectivity of zinc and lead extraction will be negatively affected due to the formation of  $\text{FeCl}_2$  according to Reaction 4 which is water soluble. It is important to note that in the presence of reducing agents such as CO and  $\text{H}_2$  the formation of  $\text{FeCl}_2$  from  $\text{Fe}_2\text{O}_3$  and  $\text{ZnFe}_2\text{O}_4$  can also become thermodynamically possible. From this point, the introduction of oxygen to the system is believed to have a positive effect on suppressing the formation of  $\text{FeCl}_2$  by oxidising  $\text{Fe}_3\text{O}_4$  to  $\text{Fe}_2\text{O}_3$  and by converting any formed  $\text{FeCl}_2$  back to  $\text{Fe}_2\text{O}_3$ .

### 3.5.3 Metal extraction from EAFD in the presence of PVC

In literature, many studies reported the extraction of metals (mainly zinc and lead) from EAFD by its co-thermal treatment with PVC [20, 24, 25, 33, 35]. The thermal treatment in these studies were either conducted under oxidative [24, 35] or pyrolytic [20, 25, 33] conditions both of which affected the percentage of metal extraction. The thermal treatments were also conducted using either conventional heating [24, 25, 33, 35] or microwave energy [20]. A summary of these studies is presented below, after which a commentary on limitations and future potential is provided.

#### 3.5.3.1 Metal extraction under pyrolytic conditions

##### 3.5.3.1.1 Conventional energy as the heating source

In the study done by Lee and Song [33] EAFD-PVC (EPVC) mixture was pyrolysed under argon at different heating rates, EPVC ratio, and holding temperatures. It was reported that increasing the heating rate significantly increased the amount of formed and volatilised  $\text{FeCl}_3$  due to an increase in the in-situ pressure/concentration of released HCl [33]. Changing the percentage of PVC in the mixture from 10 to 45% with a 5% step also had an impact on the recovery of the metals [33]. The recoveries of both zinc and lead increased from less than 40%

at a PVC percentage of 10% to recoveries higher than 95% at a PVC percentage of 45% [33]. The recovery of cadmium, however, remained almost unchanged ranging between 95 and 100% at all PVC percentages [33]. Finally, heat treatment at 1000 °C was not recommended since a portion of iron chloride volatilises (which is not desirable since it affects the selectivity) and since the particles at that temperature become sintered which can hinder the extraction by leaching [33].

EAFD in Lee and Song work [33] was studied without any pre-treatment. A new study conducted by Al-Harabsheh et al. [25] studied the effect of EAFD pre-washing on the recovery of metals when treated with PVC under pyrolytic conditions (nitrogen). The EPVC mass ratios of 1:1, 1:2 and 1:3 were also studied along with heating rates of 1, 5, 10 and 30 °C/min [25]. In these experiments, however, low temperature of 300 °C was used along with a holding time of only 20 min. In the EAFD collected from a Jordanian smelter, it was reported that soluble chlorine was present at 8.32% mainly from halite (NaCl) and sylvite (KCl) [25]. The recovery of zinc was reported to be 100% for both washed and unwashed EAFD when mixed with PVC at a ratio of 1:2 [25]. However, at a higher ratio (1:3) the recovery of zinc was reported to be higher for the washed at 100% compared to 48% for the unwashed (these values were obtained using a heating rate of 10 °C/min and a holding temperature of 300 °C) [25]. The washing of EAFD had a positive impact on lead recovery for the ratios 1:2 and 1:3 as well; recovery was 61 and 76% for 1:2 and 40.5 and 61.5% for 1:3 for unwashed and washed EAFD, respectively [25]. For the 1:1 EPVC ratio, however, washing had a negative impact on the recovery of both zinc and lead [25]. Since the thermal treatment was performed under pyrolytic conditions, no good control was possible to achieve on iron recovery; the recovery of iron was as high as 63.5% for washed 1:3 ratio [25]. However, it was reported that oxidising Fe<sup>2+</sup> in the leaching liquor can result in a reduction in the iron recovery [25].

### 3.5.3.1.2 Microwave energy as the heating source

Al-Harashseh et al. [20] utilised microwave energy to perform the thermal treatment of EPVC mixtures. Two EPVC ratios of 1:1 and 1:2 were studied [20]. In that work, the complex relative permittivity for both EAFD and PVC was measured to determine the suitability of microwave treatment; figures are shown below [20]:

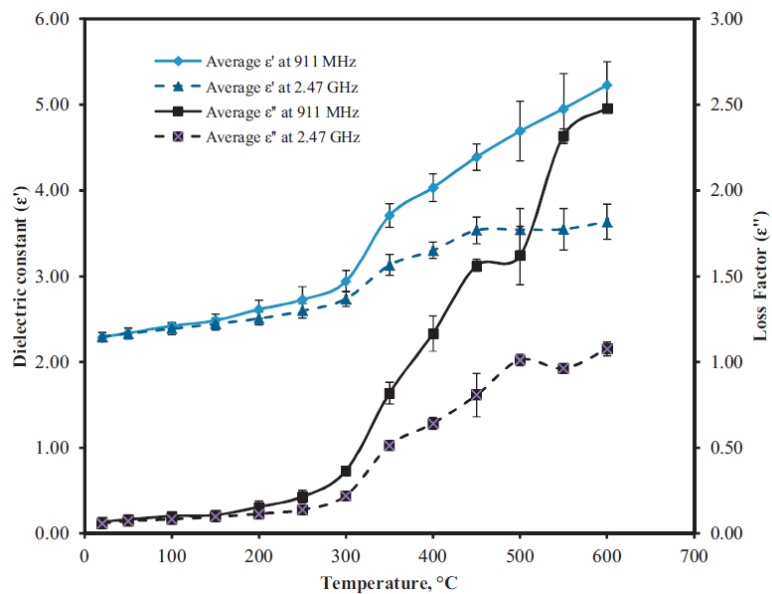


Figure 27: The complex relative permittivities (real and imaginary) of EAFD against temperature at the two frequencies 911 MHz and 2.47 GHz reported in Al-Harashseh et al. [20].

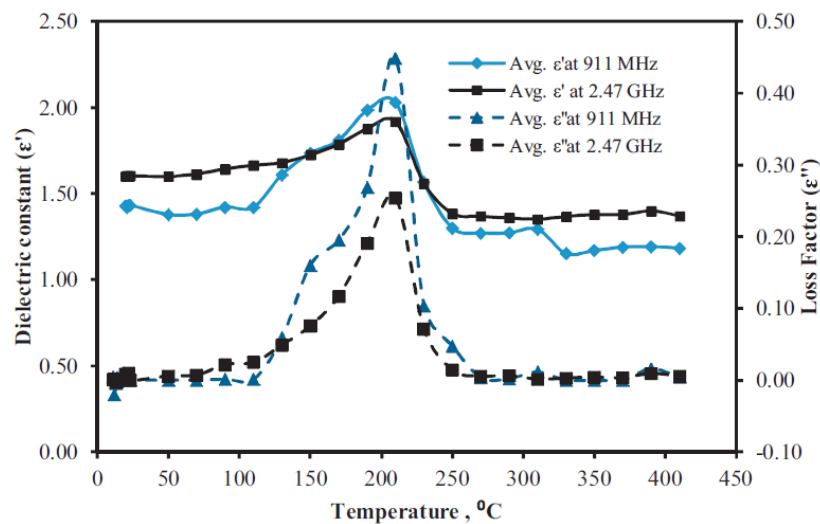


Figure 28: The complex relative permittivities (real and imaginary) of PVC against temperature at the two frequencies 911 MHz and 2.47 GHz reported in Al-Harashseh et al. [20].

It can be seen in Figure 27 and Figure 28 that EAFD causes the heating initially (at low temperatures) due to its higher value of loss factor. However, from a temperature of 100 to 250

°C, the loss factor of PVC increases appreciably making it the major microwave absorbing species in that range.

Results from the pyrolysis using microwave energy suggested that zinc can be extracted at a percentage as high as 97.14% [20] when the EPVC ratio 1:2 was used. However, at the same conditions, iron was extracted at 57.37% [20] which can complicate the extraction of zinc at high purity. The major advantage of this work (microwave) over the one reported earlier (conventional) is that the thermal treatment using microwaves was completed in 2 – 3 min compared with 20 min in conventional heating.

#### *3.5.3.2 Oxidative thermal treatment of EAFD-PVC blends*

The thermodynamics data presented earlier (section 3.5.2) reported by Al-Harashseh [15] asserted the huge advantage of oxygen introduction in the co-thermal treatment of EAFD with PVC. The results confirmed that the presence of oxygen can minimise iron extraction while the extraction of both zinc and lead can be enhanced [15]. The effect of oxygen is either attributed to the oxidation of  $\text{Fe}_3\text{O}_4$  to stable  $\text{Fe}_2\text{O}_3$  or the oxidation of any formed  $\text{FeCl}_2$  back to  $\text{Fe}_2\text{O}_3$ .

This theoretical data was confirmed experimentally by two separate studies performed by Al-Harashseh et al. [24, 35]. In the first work [24], the effect of the oxygen partial pressure on metal extraction was studied as the main parameter. Other factors such as holding temperature, holding time, and pH of the leaching solution were also addressed [24].

In that study [24] a systematic drop in iron recovery was seen with an increase in oxygen partial pressure; recovery dropped from 33% at 0 kPa to 21.6% at an oxygen pressure of 21 kPa. It was also reported that increasing the thermal treatment holding time from 30 to 60 min and the holding temperature from 250, to 300, 350 and 400 °C resulted in a drop in iron recovery [24]. The pH of the leaching solution was also reported to have a profound effect on the recoveries of both iron and lead; such that at a pH above 4, a significant reduction in recovery was

observed [24]. However, the lowest iron extraction with normal leaching water was reported to be 12.5% [24]. In the study that followed [35], it was noticed that to minimise iron recovery further, it is essential to increase the contact surface area of reactants with the surrounding gas (i.e., oxygen). Hence, EPVC mixtures were exposed to the thermal treatment in the form of thin discs or as powder, which increased the oxygen-solids contact surface area greatly [35]. Results from that work suggested that zinc could be extracted at 100% while iron recovery was minimised to ~ 0% [35]. The recovery of iron was 21.6, 8.6, and 0.26% for long cylinder, thin discs, and loose powder forms (see paper for shapes) [35]. These results confirmed the validity of the thermodynamics data reported by Al-Harashseh [15] on the importance of the presence of oxygen during the thermal treatment of EAFD and PVC.

### **3.6 Summary**

Both EAFD and PVC pose a significant threat to the environment due to their alarming rate of generation along with the absence of an environmentally sound or economically justified treatment procedure. Both the hydrometallurgical and pyrometallurgical approaches suffer from various limitations. In the former, the complete extraction of zinc cannot be achieved under ambient conditions, while the extreme hydrothermal leaching can result in a limited extraction selectivity towards zinc. Expensive resistive material of construction for reactors is also needed for the hydrometallurgical approach. Pyrometallurgical methods presented earlier, on the other hand, while being applied at a larger scale, they still suffer from many several drawbacks such as large amounts of greenhouse emissions, large energy consumption, and process justification in case of low zinc concentration in raw EAFD.

PVC is principally disposed of to landfills. The incineration of this material in the absence of emission fixators is hazardous practice due to the release of corrosive hydrogen chloride in large amounts along with toxic chlorinated hydrocarbons. In the sections above, the potential

of the recycling of PVC with emission fixators (e.g., metal oxides) has been explained. This entails the extraction of valuable metals in EAFD along with the mitigation of hazardous emissions during the thermal treatment of PVC.

# CHAPTER FOUR

## **Microwave selective heating of electric arc furnace dust constituents toward sustainable recycling: Contribution of electric and magnetic fields (paper 1)**

### **4.1 Overview**

The potential thermal recycling of waste EAFD and PVC has been reported for the purpose of metal extraction [20, 24, 25, 33, 35]. This, in turn, contribute towards mitigating the wider environmental footprint of these wastes while simultaneously utilising them for producing useful products. Among these studies, Al-Harahsheh et al. [20] reported the high potential of using microwave energy for the thermal treatment of these two wastes mixed together in a short time of 2 – 3 min. In that work, the complex permittivity of these materials was reported along with the recovery percentages of major metallic elements in EAFD from the post water leaching of the pyrolysis residues (zinc, lead, iron, cadmium, etc.) [20]. In another study conducted by Ye et al. [139] the complex permittivity was also reported for EAFD. The reduction of EAFD with biochar using microwave energy was also reported in that work [139]. The EAFDs used in these studies were collected from different sources and hence, a significant variation in the chemistry of EAFD can be seen (see sections 3.3.4.3 and 3.3.4.4). For instance, the average zinc and iron concentrations were 26.28 and 5.65 wt% (zinc) and 17.31 and 52.54 wt% (iron) from Al-Harahsheh et al. [20] and Ye et al. [139], respectively.

EAFDs with different mineralogy can thus exhibit different response to microwaves in terms of impedance matching (which affects the heating rate) due to the difference in the complex permittivity of each individual constituent in it. For example, the complex permittivity (real and imaginary) for  $\text{Fe}_3\text{O}_4$  is higher than  $\text{ZnFe}_2\text{O}_4$ . Thus, it would be expected for an EAFD sample containing higher concentrations of  $\text{Fe}_3\text{O}_4$  to exhibit an overall higher values of the real and imaginary relative permittivity than a sample containing more Fe in the form of  $\text{ZnFe}_2\text{O}_4$ .

Herein, the major components of EAFD were exposed to microwave testing whereby the complex relative permittivity for each component were extracted at frequencies 2.47 GHz and 912 MHz. The response of these components was also studied under the influence of separated microwave electric and magnetic fields. This data helps in predicting the behaviour of any EAFD sample to microwaves depending on its mineralogy.

Appendix 1. contains the manuscript titled “Microwave selective heating of electric arc furnace dust constituents toward sustainable recycling: Contribution of electric and magnetic fields” detailing the dielectric characterisation of the major EAFD constituents over a wide temperature range for the extraction of the real and imaginary parts of permittivity. The manuscript also provides details about the heating of these constituents in separated electromagnetic microwave fields (electric and magnetic), a feature which can be utilised for selective microwave heating of certain materials.

## **4.2 Dielectric characterisation**

To visualise how the constituents of EAFD exhibit significantly different permittivity values, the loss tangent ( $\tan\delta$ ) of the major EAFD components is shown in Figure 29; The loss tangent is defined as the ratio between the imaginary to the real permittivity:

$$\tan\delta = \frac{\epsilon''}{\epsilon'} \quad (29)$$

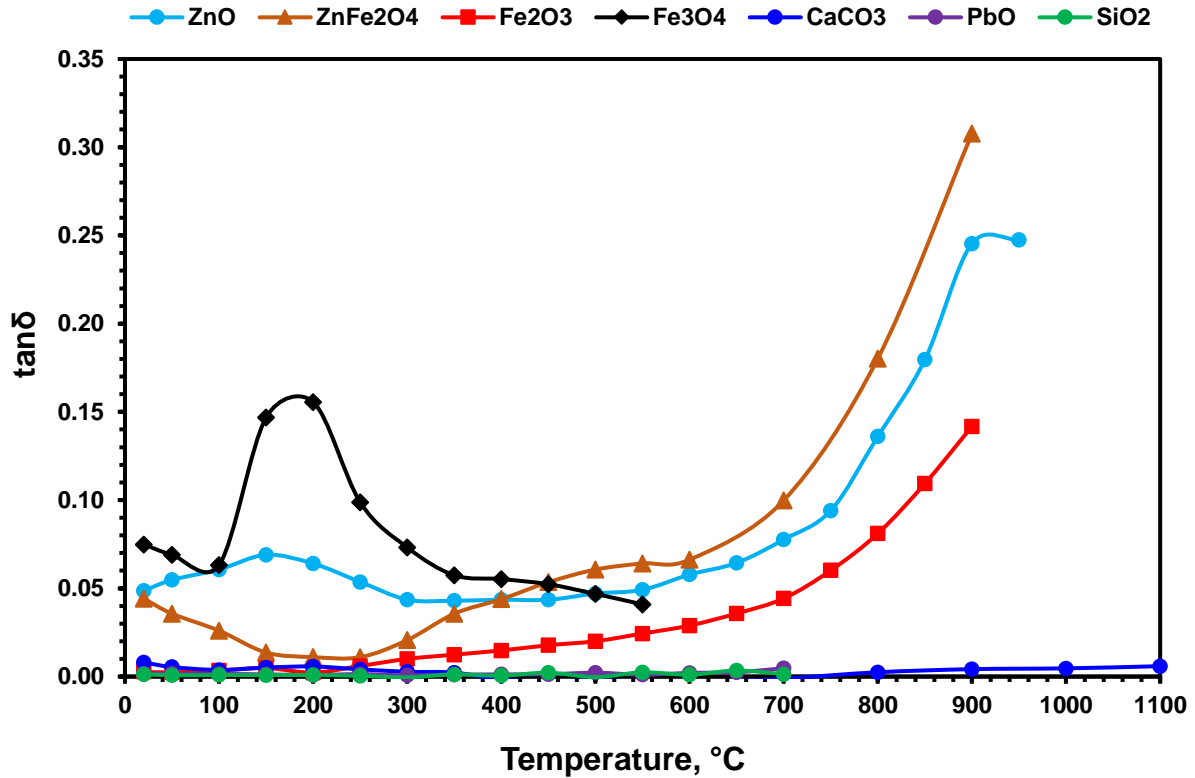
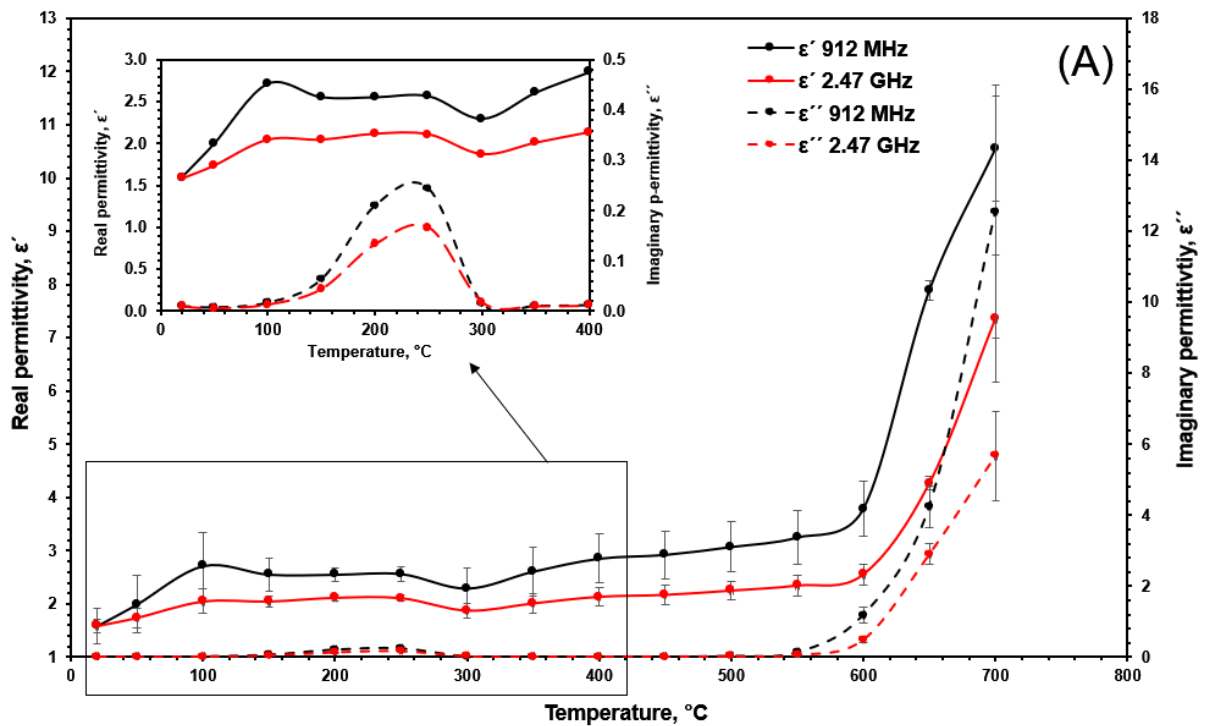


Figure 29: The loss tangent of the major EAFD components against temperature at a frequency of 2.47 GHz.

Data in Figure 29 shows that ZnO and Fe<sub>2</sub>O<sub>3</sub>, for example, show a large difference in the value of the loss tangent over the entire temperature range. Thus, making judgments on the dielectric susceptibility of EAFD cannot be generalised based on a measurement of a single EAFD sample. Instead, characterising the complex permittivity of the major components of EAFD can help in making sound predictions of the complex permittivity of EAFD samples based on relative composition. The complex permittivity of all these components is presented in detail in the published manuscript in Appendix 1.

Since the main goal (section 1.2) is to assess the microwave recycling possibility of EAFD mixed with PVC, the relative permittivity of two PVC samples are also presented in Figure 30 (A) and (B). The real and imaginary parts for both pure (Figure 30 (A)) and waste PVC (Figure 30 (B)) follow a very similar trend. Below 400 °C, the imaginary part for both pure and waste PVC show a peak between 200 – 250 °C. The increase, however, starts at a temperature of around 100 °C which is close to the glass transition temperature of PVC. Such a behaviour

suggests that molecules of PVC can now polarise in the direction of external electric field, thus promoting the value of the imaginary part. After the de-hydrochlorination of PVC ( $350\text{ }^{\circ}\text{C} < T$ ), polyene is formed (see Appendices 2, 3 and 4). Figure 30 (A) and (B) suggest that formed polyene is microwave transparent with loss factor values close to zero up to a temperature of  $550\text{ }^{\circ}\text{C}$ . Above  $550\text{ }^{\circ}\text{C}$ , char is formed, and both the real and imaginary parts increase for pure and waste PVC (Figure 30 (A) and (B)).



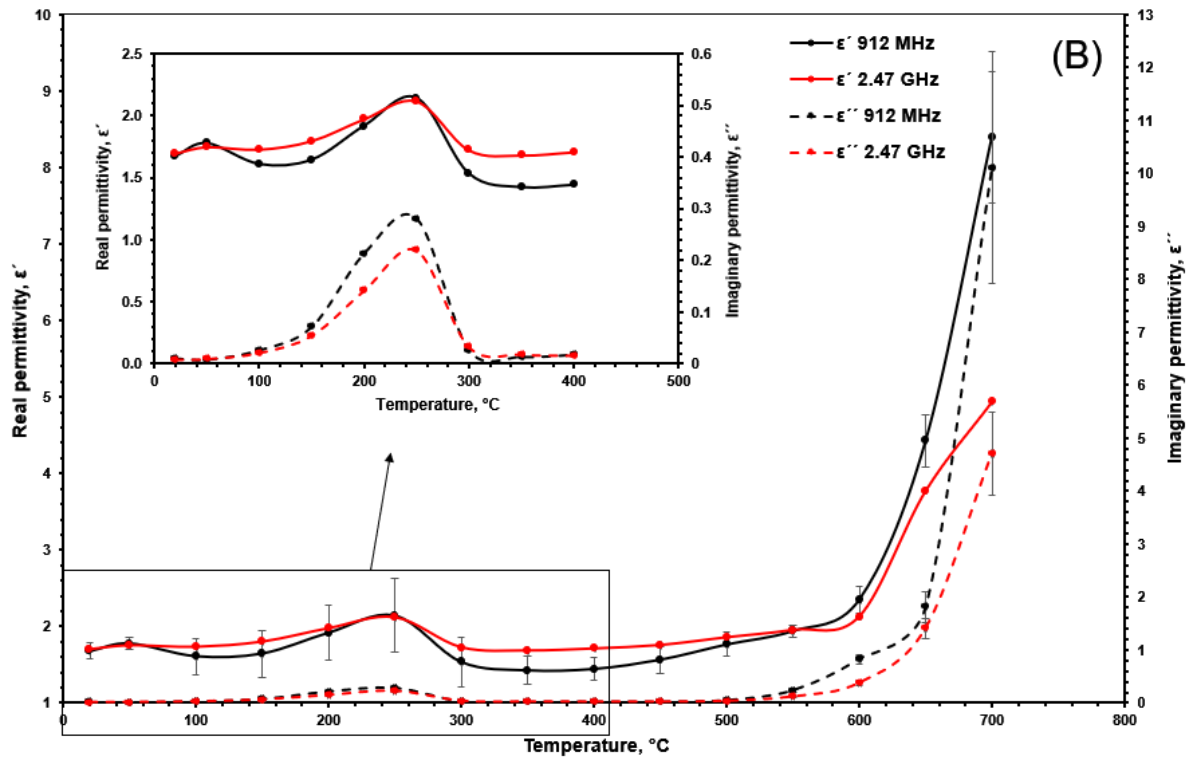


Figure 30: The dielectric properties of pure PVC (A) and waste unplasticized PVC (B) in the temperature window 25 – 700 °C.

### 4.3 Heating in separated electric (E) and magnetic (H) microwave fields

#### 4.3.1 Electromagnetic simulation and the experimental setup

A single mode  $TE_{10}$  microwave applicator was used to perform the heating. This applicator is connected from one end to a solid-state microwave generator and tuning stubs and from the other end to a metallic short circuit plunger. A 4 mm internal diameter quartz tube was used to introduce the sample to the cavity and this tube was purged with nitrogen at 99.9992% purity.

An image of the experimental setup is shown in Figure 31.

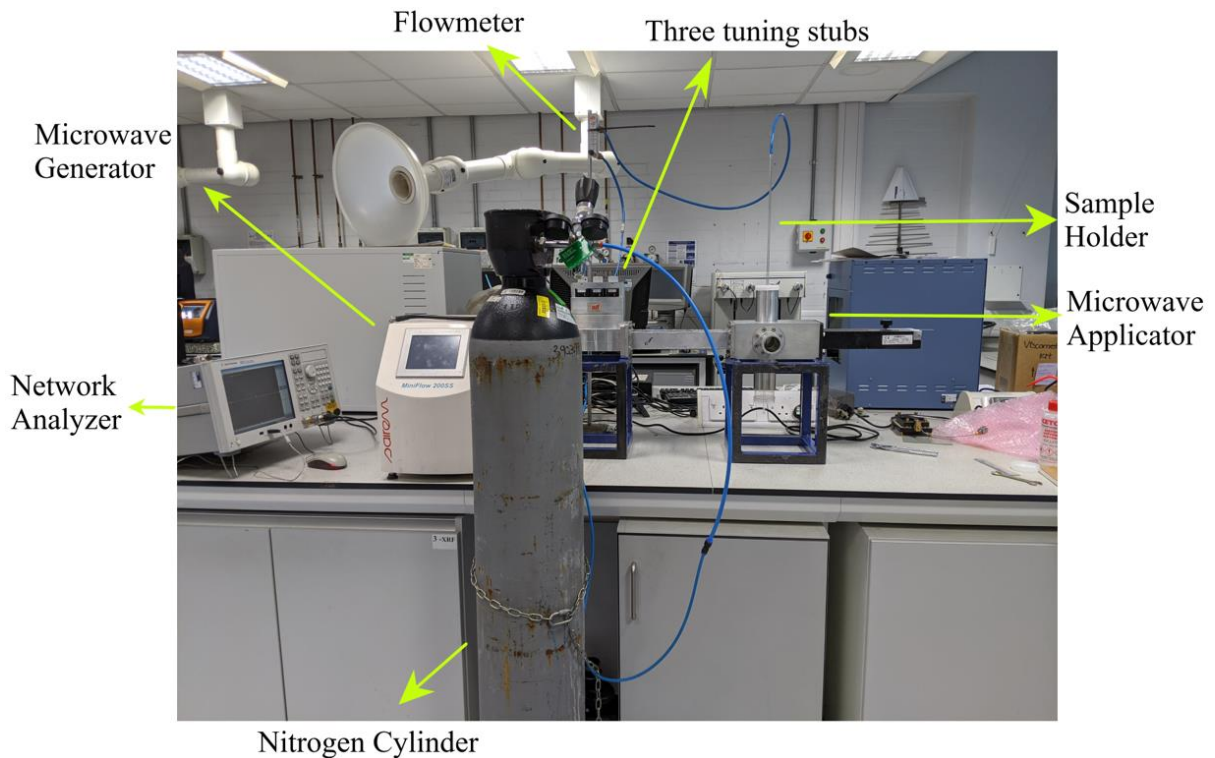


Figure 31: A photo of the experimental setup used to perform the electric/magnetic microwave heating.

The extracted relative complex permittivity of EAFD components were then inserted into an electromagnetic model using COMSOL Multiphysics which allowed specifying the relative positions of the microwave electric and magnetic fields inside the waveguide to be determined. The presence of a metallic short circuit at the end of the waveguide results in the formation of a standing wave such that at certain positions there is a maximum electric field and at a quarter wavelength away from that position there is a maximum magnetic field. A sample from the electromagnetic model is shown in Figure 32 in which the standing wave pattern of a microwave at a frequency of 2.47 GHz inside a  $WR340$  waveguide was utilised to expose the samples once to the electric field (Figure 32 (A)) and once to the magnetic field (Figure 32 (B)). More details on the setup (methodology) of the heating rig is presented in detail in the manuscript attached to Appendix 1.

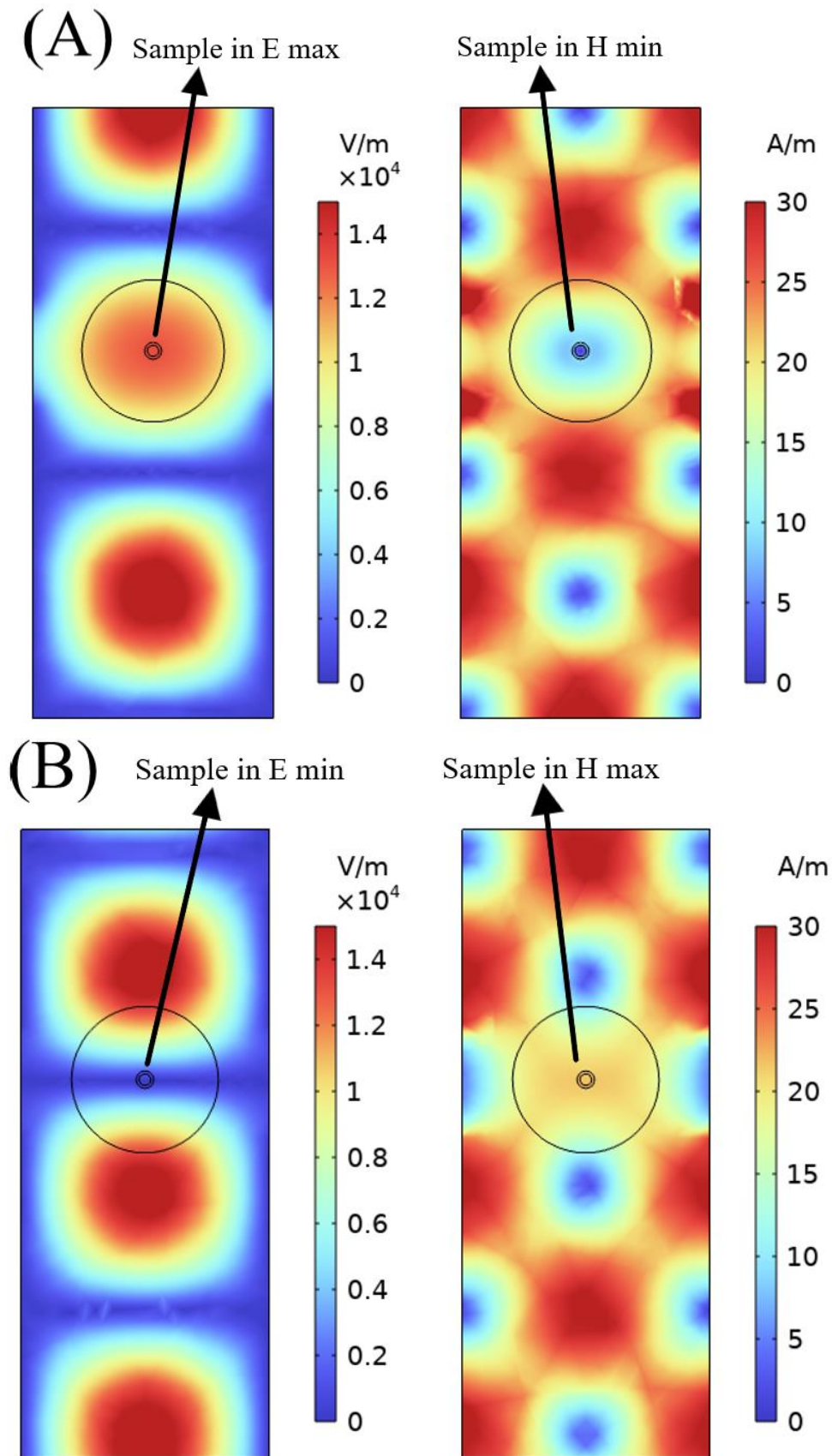


Figure 32: A top view of the waveguide showing the position of a ZnO sample in the maximum electric (A) and maximum magnetic (B) fields with a power input of 118 W.

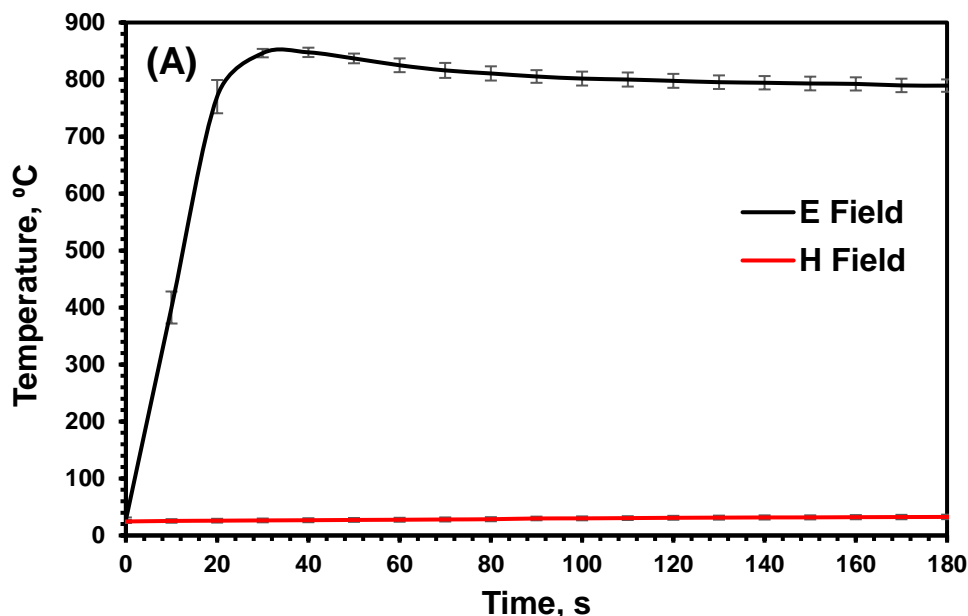
#### 4.3.2 Microwave heating profiles of metal oxides exposed to separated electric and magnetic fields

As a representative example from the heating runs, the heating curves for a pure dielectric material (ZnO) and for a dielectric magnetic material ( $\text{Fe}_3\text{O}_4$ ) are presented in Figure 33 (A) and (B). When ZnO was placed in the electric field maxima, a very rapid heating ( $\sim 37^\circ\text{C/s}$ ) was obtained, while placing it in the magnetic field did not cause any heating. In contrast,  $\text{Fe}_3\text{O}_4$  heated in both the electric and magnetic fields yielding even higher temperatures in the magnetic field (Figure 33 (B)). The results appearing in Figure 33 can be assigned to the difference in the values of permittivity and permeability of these two materials as shown in Table 6. Data associated with the heating of other EAFD components are presented in more detail in the manuscript (Appendix 1).

Table 6: Permittivity and permeability data for ZnO and  $\text{Fe}_3\text{O}_4$  at room temperature and a frequency of 2.47 GHz.

Material	Permittivity		Permeability	
	Real, $\epsilon'$	Imaginary, $\epsilon''$	Real, $\mu'$	Imaginary, $\mu''$
ZnO	2.7	0.14	Non-magnetic	Non-magnetic
$\text{Fe}_3\text{O}_4$	12.6	0.9	1.2 <sup>a</sup>	0.5 <sup>a</sup>

a: data was collected from Hotta et al. [181].



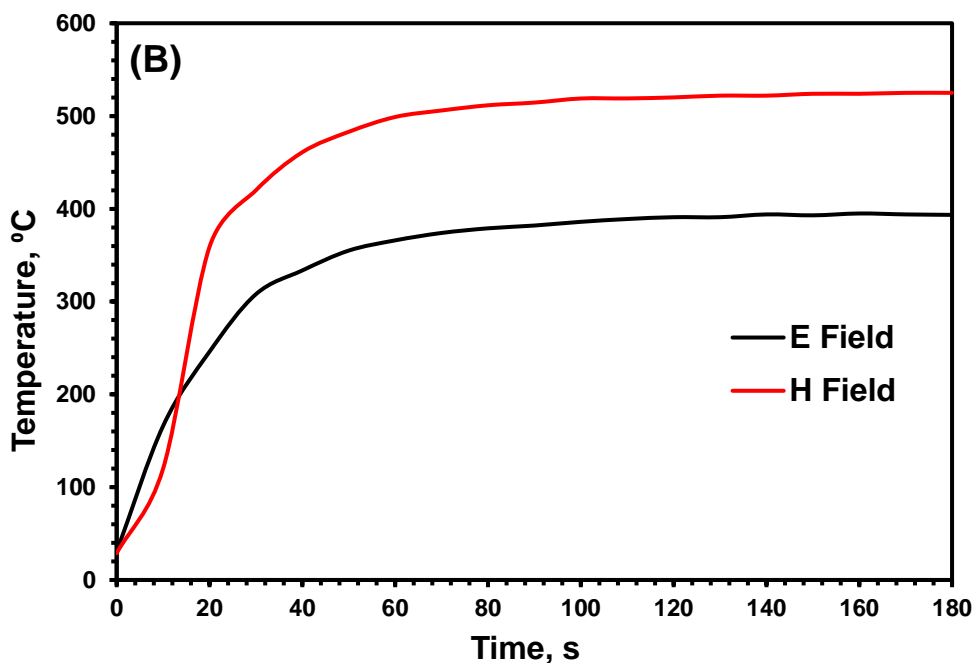


Figure 33: Response of ZnO (A) and  $\text{Fe}_3\text{O}_4$  (B) to pure electric and pure magnetic microwave fields in a single mode  $TE_{10}$  cavity under a microwave power of  $118 \pm 12$  W (E is electric field and H is magnetic field).

The results above show a very powerful property of microwaves which is its ability in selectively heating magnetic components while other dielectrics being inert to heating. With a sufficient supply of oxygen, heated  $\text{Fe}_3\text{O}_4$  can be converted to  $\text{Fe}_2\text{O}_3$  which could be useful in promoting the chlorination selectivity when EAFD is thermally treated with PVC. Further details on the thermodynamics of these reactions are presented in the manuscript in Appendix 1.

#### 4.4 Summary

A detailed investigation on the response of each EAFD component to the electric and magnetic microwave fields have been presented here. It was shown that materials with magnetic susceptibility or higher electrical conductivity (see manuscript appendix 1) are the only ones that heat when exposed purely to the magnetic field. Other dielectrics, in contrast, respond only to the electric field making them “inert” to heating at the magnetic maxima. Such a property can be utilised to achieving selective heating of certain components in a bulk sample.

The work presented here also reported the dielectric data for each EAFD component at the industrially used frequencies of ~ 2.47 GHz and 912 MHz and in a large temperature span. Such data can be used to make predictions of the response of different EAFD samples from different sources with different chemistry/mineralogy instead of generalising the relative permittivity data of a bulk EAFD sample to other samples world-wide.

# CHAPTER FIVE

## **The effect of zincite (ZnO) and franklinite (ZnFe<sub>2</sub>O<sub>4</sub>) as major zinc bearing oxides in EAFD on the thermal decomposition kinetics of polyvinyl chloride (papers 2 and 3)**

### **5.1 Overview**

Both ZnO and ZnFe<sub>2</sub>O<sub>4</sub> are considered major sources of zinc in EAFD [15]. Hence, several researches have focused on the possibility of extracting zinc from EAFD by the co-thermal treatment with PVC [20, 24, 25, 33, 35]. While these studies made a major contribution reporting the percentage of metal extraction upon the thermal treatment with PVC, none reported the mechanistic reaction pathway of PVC with zinc bearing oxides. Hence, some studies addressed the effect of these compounds (ZnO and ZnFe<sub>2</sub>O<sub>4</sub>) in their pure form on the degradation of PVC in terms of organic emissions and chlorine fixation [27, 30, 32, 182]. The only study which reported the kinetics of PVC-ZnO nanocomposite degradation was that done by Alfannakh [183]. In that work, however, only the KAS and FWO models [167, 169, 171] were used which both utilise an oversimplified approximation of the temperature integration. Moreover, no mentioning on how the frequency factor was calculated which could possibly be based on a presumed reaction model which could lead to significant errors when calculating the reaction rate [183]. Finally, the reaction model associated with the degradation was also not reported [183] and the reaction sequence and products were also not identified [183].

No systematic investigation was provided on the effect of ZnO and ZnFe<sub>2</sub>O<sub>4</sub> on the degradation kinetics of PVC whereby all the kinetic parameters (activation energy, frequency factor and reaction model) and reaction sequence and products were identified.

Herein, a non-isothermal thermogravimetric study was carried out which allowed the extraction of the temperature independent kinetic parameters. These parameters can then be used to

calculate reaction rates at different temperatures thus allowing the determination of processing times and temperatures required to achieve certain conversion levels.

Appendices 2 and 3 contain the manuscripts titled “Thermal degradation kinetics of polyvinyl chloride in presence of zinc oxide” [184] and “Thermodynamic, pyrolytic, and kinetic investigation on the thermal decomposition of polyvinyl chloride in the presence of franklinite” [185] detailing the thermal behaviour and the kinetics of the decomposition of polyvinyl chloride in the presence of stoichiometric quantities of ZnO and ZnFe<sub>2</sub>O<sub>4</sub> (as major zinc sources in EAFD).

## **5.2 Pyrolysis and thermal stability**

The thermal behaviour of pure PVC and its stoichiometric mixtures with ZnO and ZnFe<sub>2</sub>O<sub>4</sub> is presented in Figure 34. A clear effect of these oxides can be seen on the thermal stability of PVC. Using the tangent method, the onset de-hydrochlorination temperature dropped from 272 °C in case of pure PVC to 214 and 235 °C for ZnO-PVC and ZnFe<sub>2</sub>O<sub>4</sub>-PVC, respectively. Such a result is apparent from the derivative signals appearing in Figure 34 where the ZnO mixture shows a derivative peak before all the other systems, followed by ZnFe<sub>2</sub>O<sub>4</sub> mixture. This behaviour suggests a significant change in the de-hydrochlorination initiation pathway towards lower stability which can be assigned to the direct abstraction of Cl from the PVC monomer by these oxides at temperatures well below the normal de-hydrochlorination temperature (272 °C). This direct reaction appeared in the de-hydrochlorination stage in the form of DTG triplet/doublet as can be seen for both ZnO and ZnFe<sub>2</sub>O<sub>4</sub>-PVC mixtures (absent for the DTG of pure PVC). The Cl abstraction was accompanied by the formation of zinc chloride species (anhydrous, hydrate and oxy/hydroxide chloride) which was confirmed by several analytical techniques including XRD and are shown in detail in the published manuscript in Appendix 2.

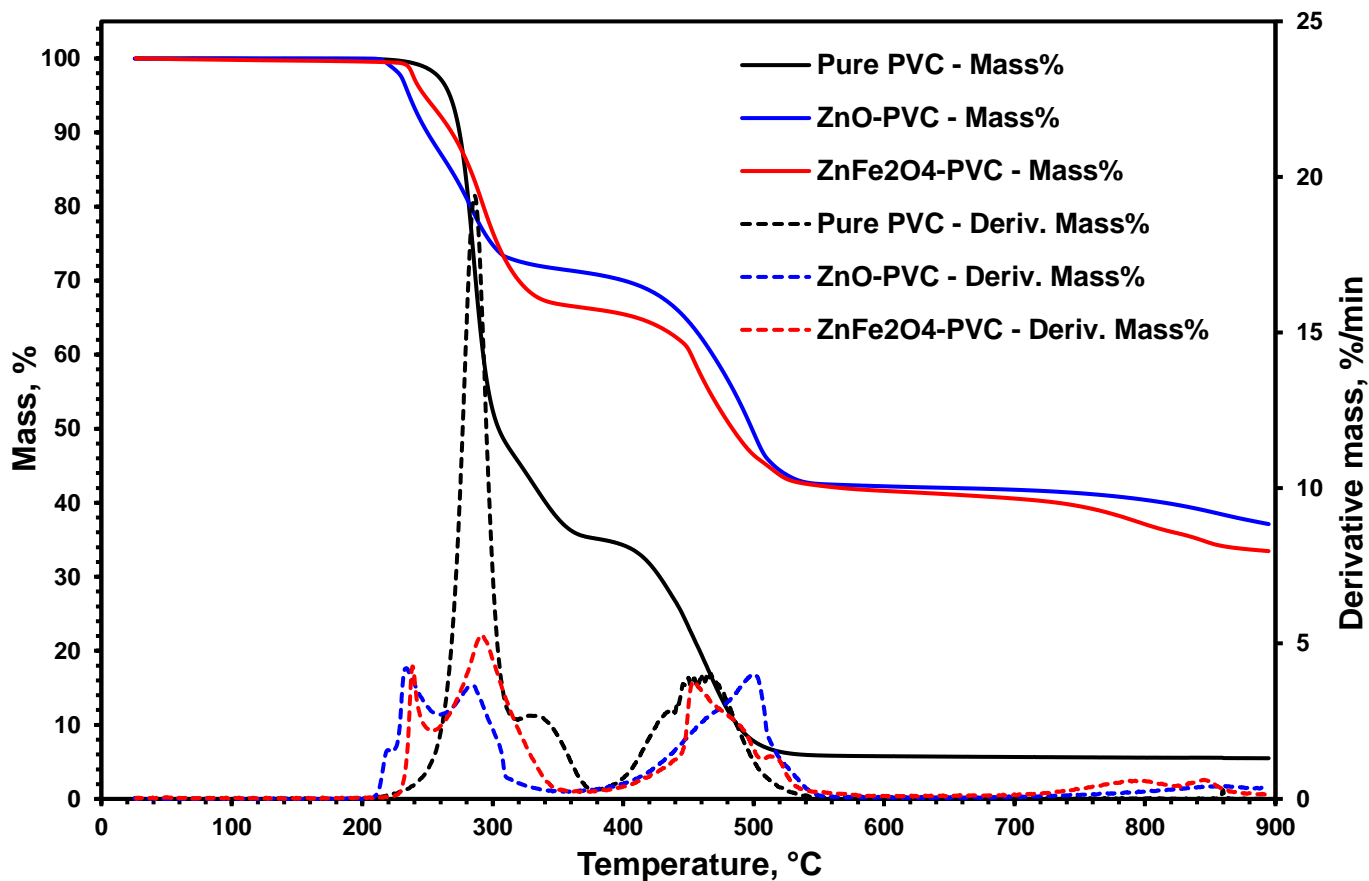
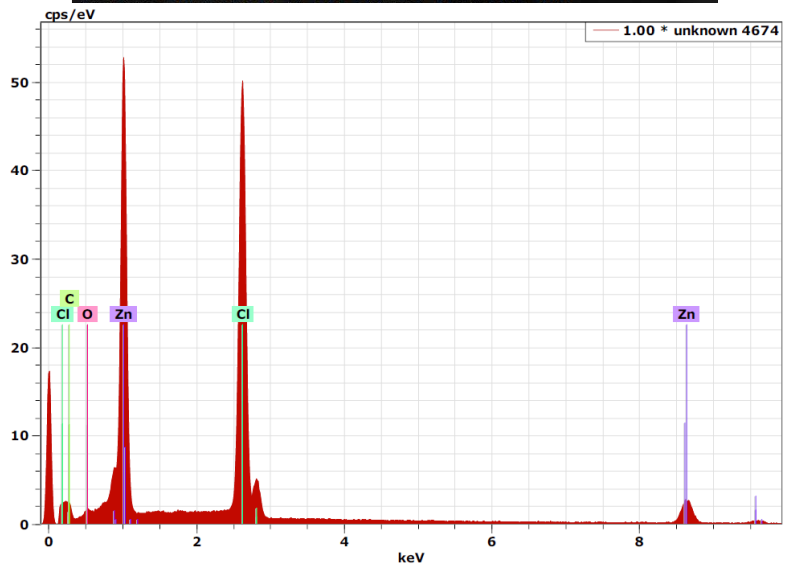
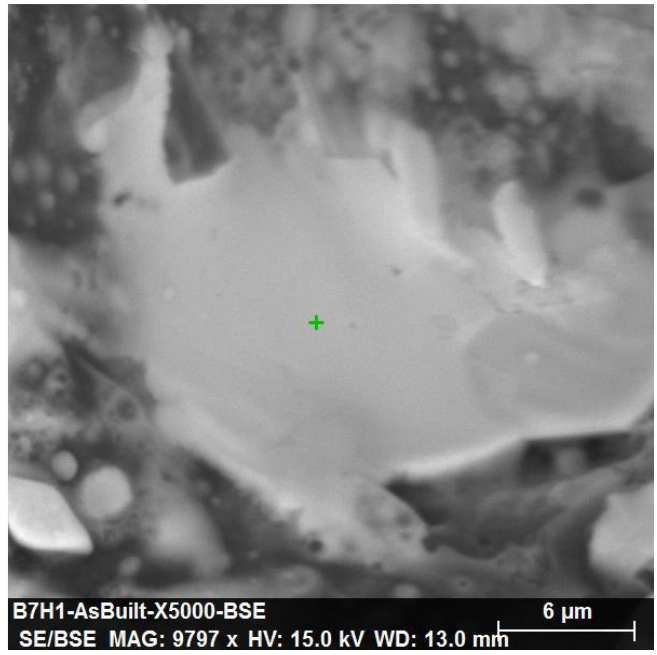


Figure 34: The thermal behaviour of pure PVC, ZnO-PVC (39.4 wt% ZnO), and ZnFe<sub>2</sub>O<sub>4</sub>-PVC (32.5 wt% ZnFe<sub>2</sub>O<sub>4</sub>) under a nitrogen flow of 100 mL/min and a heating rate of 10 °C/min.

SEM analysis was also utilised to analyse the chemistry and morphology of the reaction products. SEM scans of the post pyrolysis residue of ZnO-PVC at a temperature of 370 °C is shown in Figure 35.



Spectrum: unknown 4674

Element	Series	unn. [wt.%]	C norm. [wt.%]	Atom. [at.%]	C Error (3 Sigma) [wt.%]
Chlorine	K-series	37	46	56	04
Zinc	K-series	39	49	32	04
Oxygen	K-series	04	05	12	02
Total:		80	100	100	

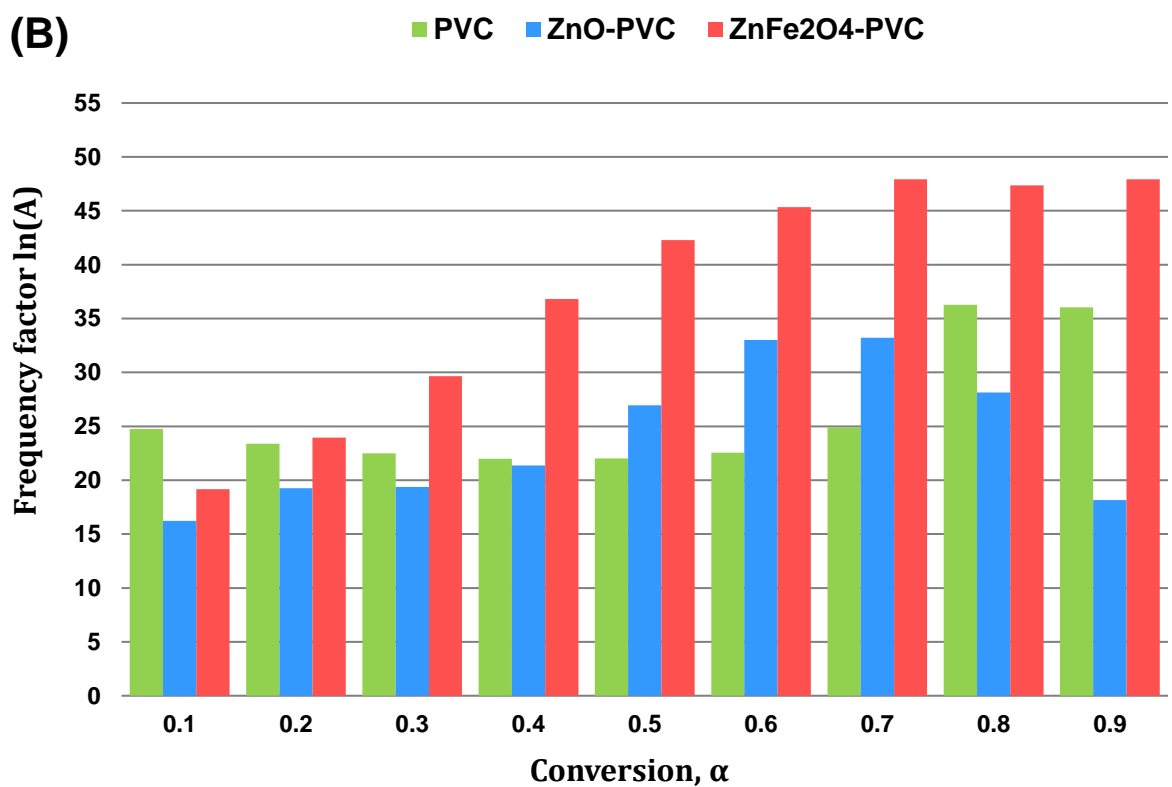
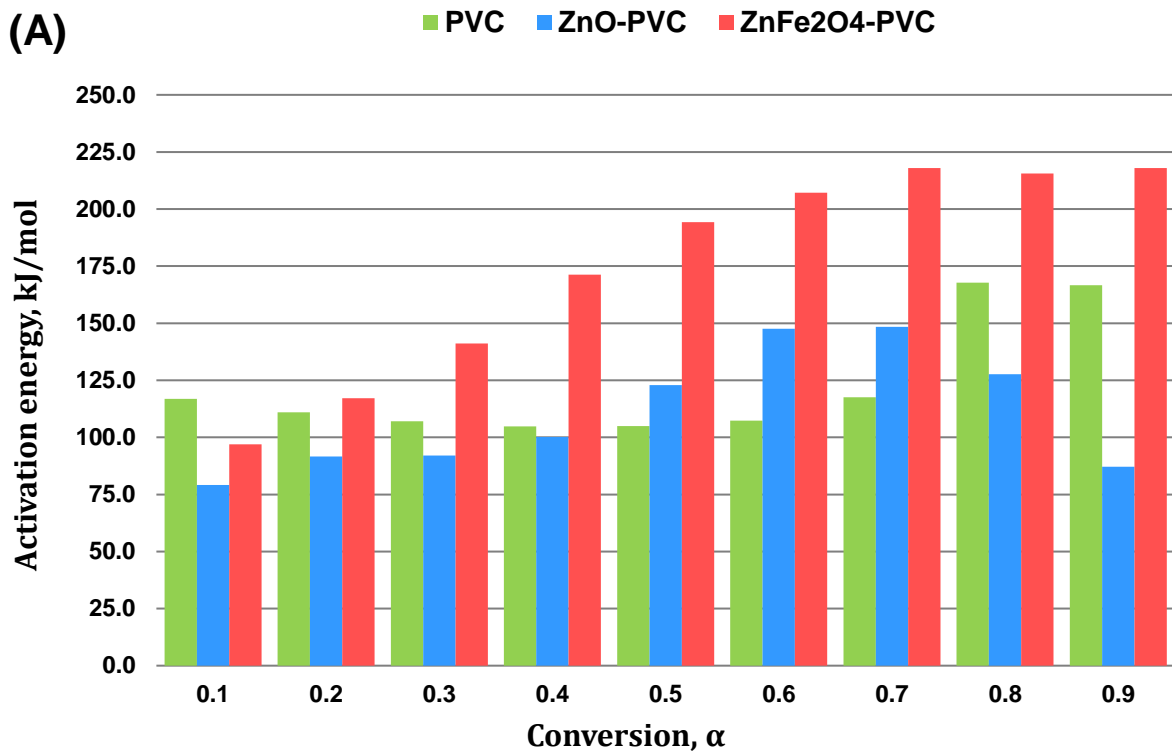
Figure 35: Chemistry and morphology of a particle in the pyrolysis residue of ZnO-PVC mixture at a temperature of 370 °C.

The crystal appearing in Figure 35 consists mainly of Zn and Cl suggesting that it can potentially be related to  $ZnCl_2$  (atomic ratio close to 1 : 2). The deviation of the atomic

percentage in the table in Figure 35 from the theoretical one of  $\text{ZnCl}_2$  could be assigned to the three dimensional nature of the sample which can potentially affect the electron count. The presence of contaminants affects the value of the atomic ratio making it deviate from theoretical value. Oxygen appearing in the table in Figure 35 can be attributed to the presence of other crystals in the vicinity of the crystal of interested and possibly due to adsorbed water on the surface. However, the maps presented in the supplementary material of the manuscript attached in Appendix 2 show that some star-shaped crystals are associated only with Zn and Cl. The data presented in Appendices 2 and 3 are in agreement with the thermodynamics results reported by Al-Harabsheh [15], such that the Cl in PVC is believed to be destroying these minerals and transforming them into their chloride counterparts; a result which can be utilised for the extraction of zinc from EAFD by means of post pyrolysis water leaching.

### **5.3 The kinetics of PVC de-hydrochlorination in the presence of ZnO and $\text{ZnFe}_2\text{O}_4$**

Knowledge of the temperature independent kinetic parameters (activation energy  $E_a$ , frequency factor  $A$ , and reaction model) makes it possible to make predictions of reaction rates at any arbitrary temperature. Moreover, it becomes possible to choose the optimal temperature at which zinc can be extracted selectively. In Figure 36, the activation energy and the natural logarithm of the frequency factor associated with the de-hydrochlorination of PVC alone and with stoichiometric quantities of ZnO and  $\text{ZnFe}_2\text{O}_4$  are presented. Different activation energies can be seen when ZnO and  $\text{ZnFe}_2\text{O}_4$  are mixed with PVC. The former yielded lower values (compared to pure PVC) up to a conversion of 0.4 after which it increases above pure PVC between 0.5 – 0.7 then becomes smaller again at conversions 0.8 and 0.9. A detailed description of the mechanisms involved in generating such behaviour is presented in the manuscript attached to Appendix 2.



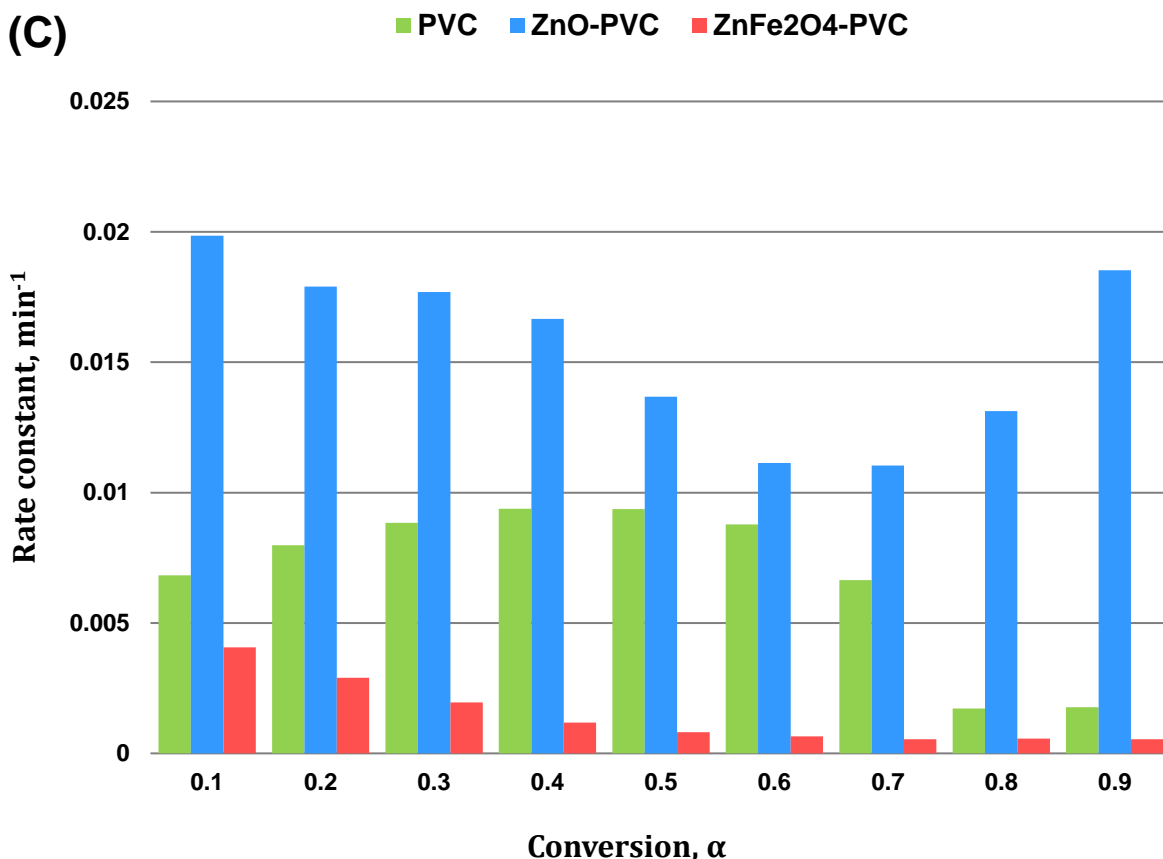
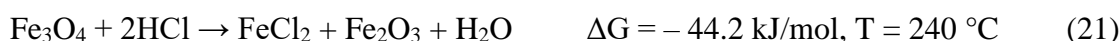
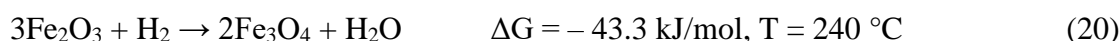
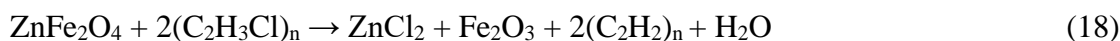


Figure 36: The activation energy (A), the natural logarithm of the frequency factor (unit of A is min<sup>-1</sup>) (B), and the rate constant at a temperature of 200 °C (C) associated with the de-hydrochlorination of PVC, ZnO-PVC, and ZnFe<sub>2</sub>O<sub>4</sub>-PVC under a nitrogen flow of 100 mL/min (kinetic parameters reported using Friedman method) [168].

In contrast, a drastic increase in the activation energy is seen when stoichiometric amount of ZnFe<sub>2</sub>O<sub>4</sub> is added to PVC. The main reason behind such an increase (which was not seen for ZnO) is the reduction of Fe<sub>2</sub>O<sub>3</sub> generated as a side product from the chlorination of ZnFe<sub>2</sub>O<sub>4</sub> by H<sub>2</sub> into Fe<sub>3</sub>O<sub>4</sub>. Fe<sub>3</sub>O<sub>4</sub> then captures any emitted HCl forming FeCl<sub>2</sub> thus preventing HCl from catalysing the de-hydrochlorination according to the mechanism reported by Starnes and Ge [186]. The reaction sequence can be written as follows:



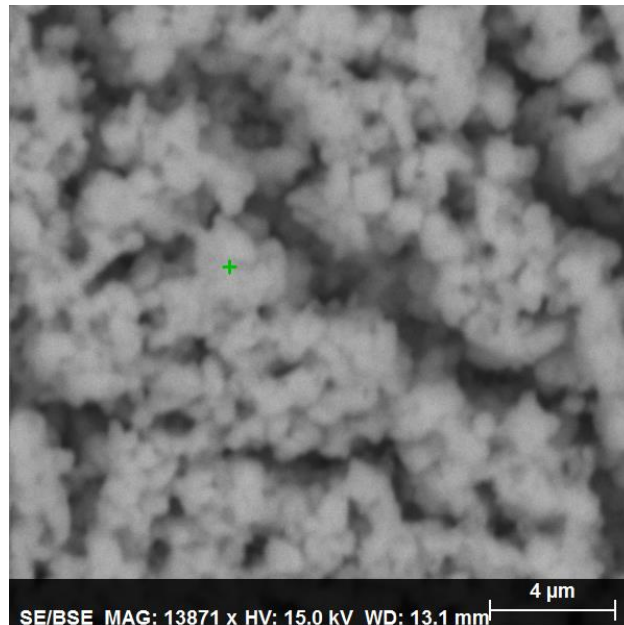
The evidence of this reaction sequence and the chlorination is shown in detail in the manuscript attached to Appendix 3. The morphology of formed  $\text{FeCl}_2$  is shown in Figure 37 along with the chemistry using EDS analysis. For a complete representation of kinetics, the effect of the frequency factor should also be taken into account. By combining the frequency factor and the activation energy, one can generate the values of the rate constant  $k(T)$  which is the most important parameter in determining reaction rates. The rate constant equation can be given according to the Arrhenius function:

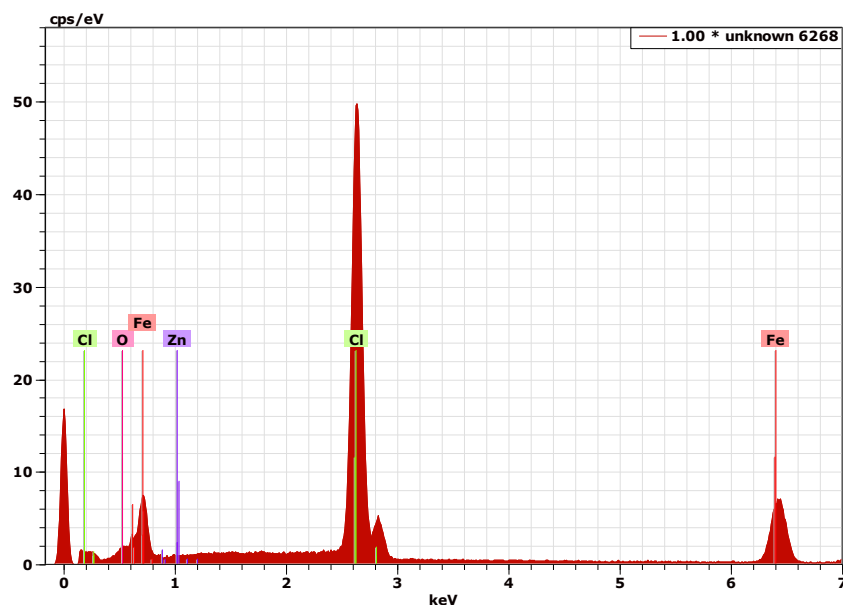
$$k(T) = A. \exp\left(\frac{-E}{RT}\right) \quad (30)$$

And enters in the overall rate equation as follows:

$$\frac{d\alpha}{dt} = k(T). f(\alpha) \quad (31)$$

Such that,  $\frac{d\alpha}{dt}$  is the reaction rate,  $k(T)$  is the rate constant,  $R$  is the universal gas constant and  $f(\alpha)$  is the reaction model.





Spectrum: unknown 6268

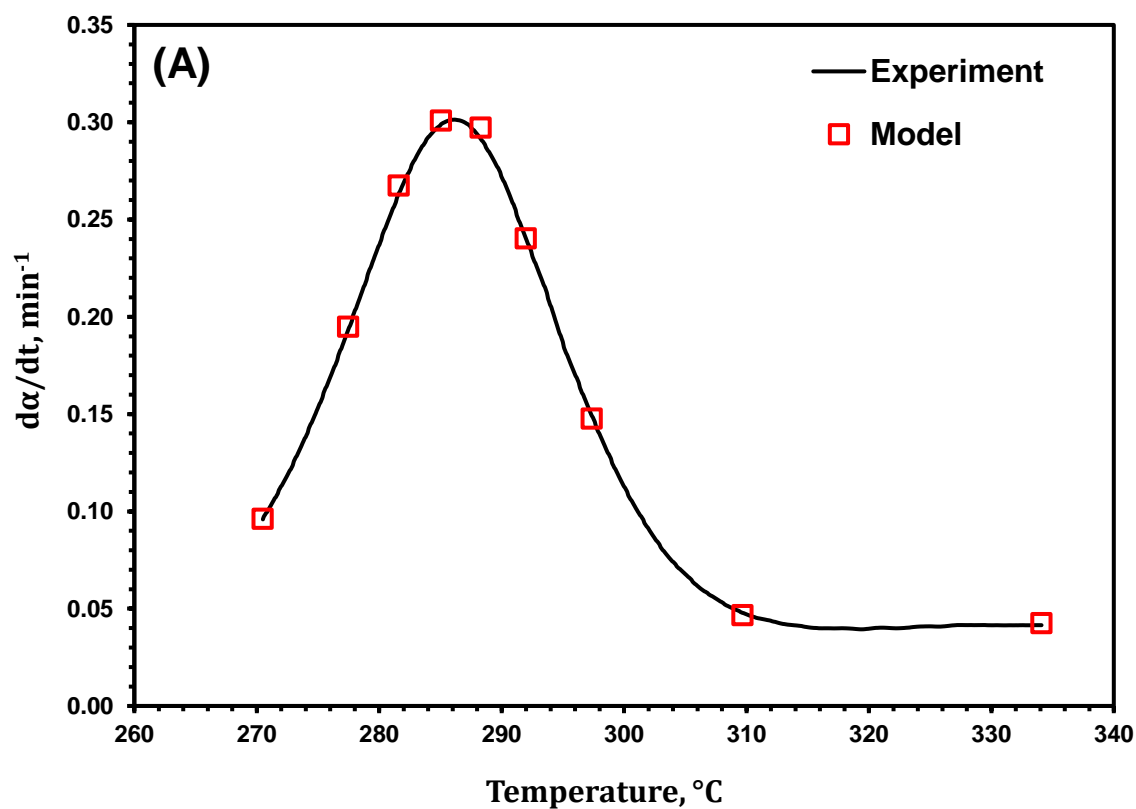
Element	Series	unn. C [wt.%]	norm. C [wt.%]	Atom. C [at.%]	Error (3 Sigma) [wt.%]
Zinc	K-series	0.1	0.2	0.1	0.2
Oxygen	K-series	4.5	5.8	14.3	2.5
Chlorine	K-series	38.0	49.3	54.3	3.9
Iron	K-series	34.5	44.7	31.3	3.2
Total:		77.1	100.1	100.00	

Figure 37: The morphology and chemistry of formed  $\text{FeCl}_2$  during the pyrolysis of  $\text{ZnFe}_2\text{O}_4$ -PVC (32.5 wt%  $\text{ZnFe}_2\text{O}_4$ ) at a temperature of 650 °C and under a nitrogen flow of ~ 5 mL/min.

According to Figure 36 (C), the addition of ZnO produced the highest rate constant over the conversion 0.1 – 0.9 followed by pure PVC and then  $\text{ZnFe}_2\text{O}_4$ -PVC at a temperature of 200 °C. Again, while  $\text{ZnFe}_2\text{O}_4$  initially catalysed the de-hydrochlorination causing the onset temperature to drop, it eventually can cause the degradation to slow down which can be seen from the lower values of the rate constant which keeps dropping with conversion, contrary to pure PVC. This can be explained by the mechanism suggested above where  $\text{Fe}_3\text{O}_4$  can capture released HCl preventing it from catalysing the de-hydrochlorination.

More details on the reaction models and the mechanisms involved in the mass loss of these mixtures are presented in the manuscripts attached to Appendices 2 and 3.

The reliability of the extracted kinetic data presented in Figure 36 was confirmed by comparing the reaction rates calculated using the kinetic data presented here with the reaction rate obtained experimentally (see Figure 38). Clearly from Figure 38 (A), (B) and (C) there is an excellent agreement between experimental rate and the rate calculated using the kinetic data presented here.



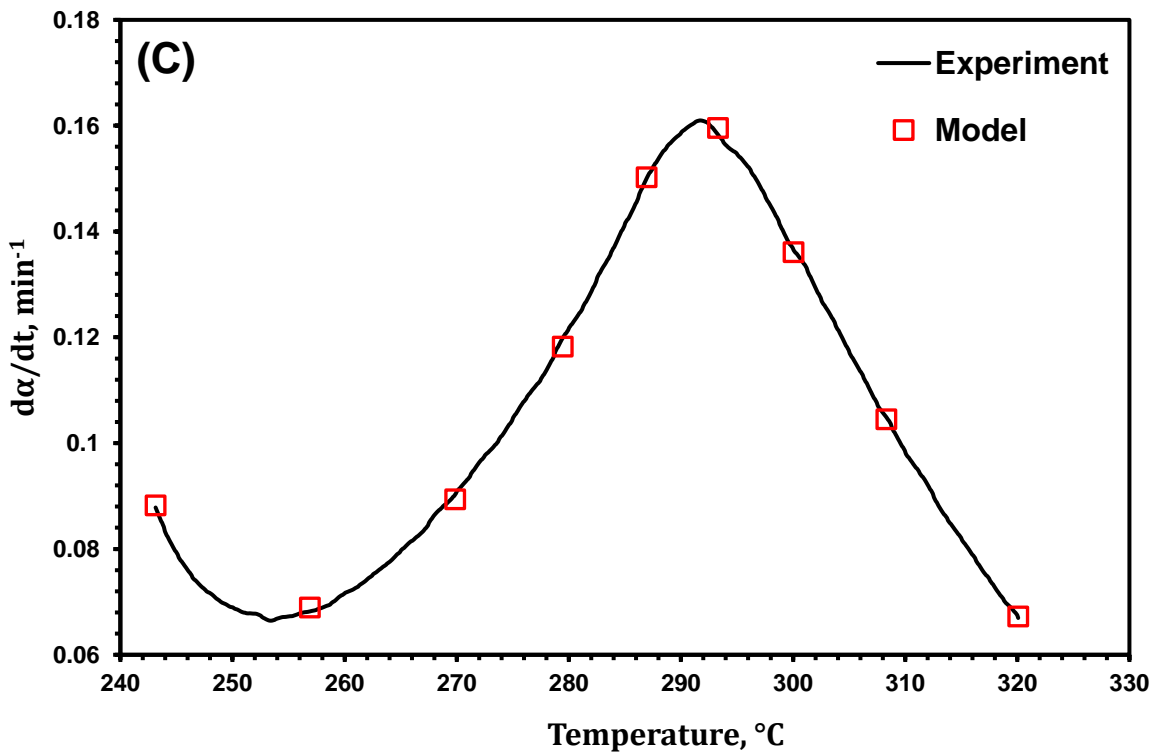
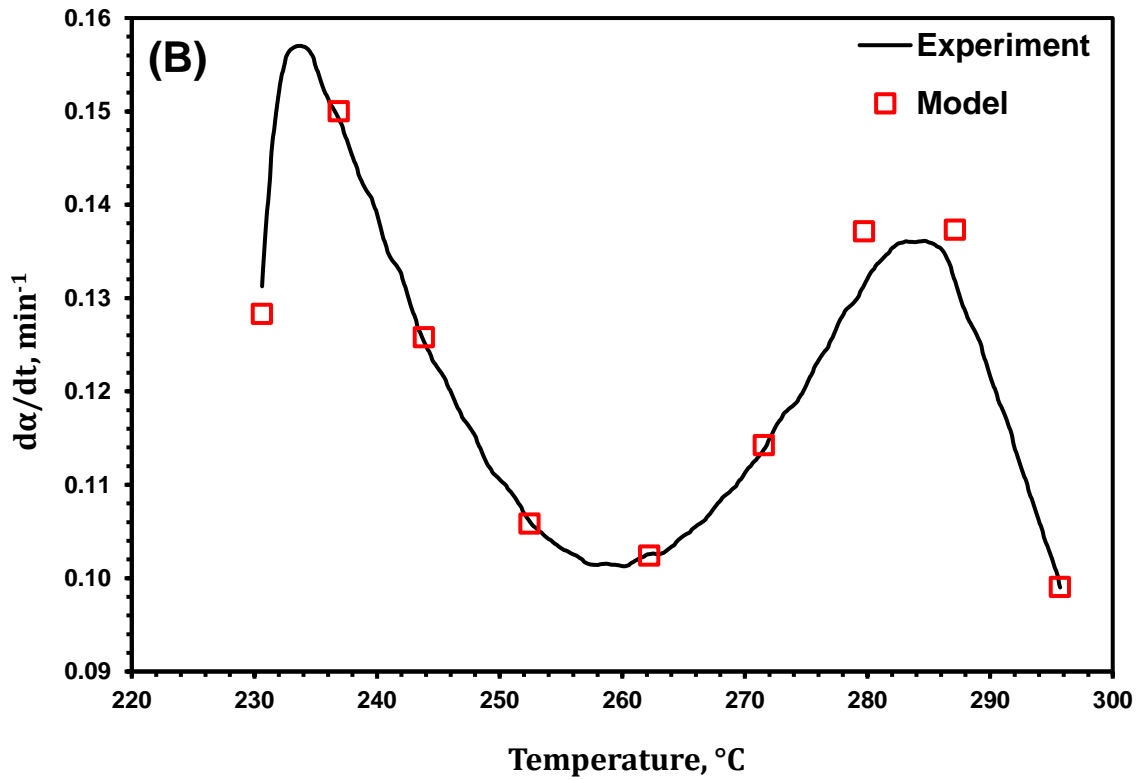


Figure 38: A comparison between experimental and model based de-hydrochlorination rate of (A) PVC, (B) ZnO-PVC mixture (39.4 wt% ZnO) and (C) ZnFe<sub>2</sub>O<sub>4</sub>-PVC mixture (32.5 wt% ZnFe<sub>2</sub>O<sub>4</sub>) using data extracted from Friedman model.

## 5.4 Summary

An investigation on the co-pyrolysis of ZnO and ZnFe<sub>2</sub>O<sub>4</sub> with PVC was reported in this chapter. This included performing non-isothermal thermogravimetric scans, pyrolysis of the solid mixture at different temperatures, and characterisation of the solid products from the pyrolysis. These experiments/measurements allowed for identifying the underpinning reaction mechanisms involved in the thermal degradation of PVC in the presence of these oxides. The kinetic data associated with the degradation were also extracted for pure PVC and for PVC in the presence of stoichiometric quantities of ZnO and ZnFe<sub>2</sub>O<sub>4</sub>.

The presence of ZnO resulted in a catalysis of the de-hydrochlorination while ZnFe<sub>2</sub>O<sub>4</sub> resulted in an initial catalysis only which both caused the onset de-hydrochlorination temperature to drop from 272 °C (pure PVC) to 214 and 235 °C for ZnO-PVC and ZnFe<sub>2</sub>O<sub>4</sub>-PVC, respectively. According to the kinetic calculations, the rate constant associated with ZnO-PVC at a low temperature of 200 °C exhibited higher values throughout the degradation (conversion range 0.1 – 0.9) compared to pure PVC. In contrast, the presence of iron bearing compounds in the ZnFe<sub>2</sub>O<sub>4</sub> resulted in an overall reduction in the rate of de-hydrochlorination which can be assigned to the ability of Fe<sub>3</sub>O<sub>4</sub> to capture gaseous emitted HCl thus preventing it from catalysing the de-hydrochlorination further. This caused the activation energy to increase, which in turn, resulted in an overall lower value of the rate constant at the low pyrolysis temperature of 200 °C. Finally, it was shown that both ZnO and ZnFe<sub>2</sub>O<sub>4</sub> can be completely removed by the chlorine present in PVC and transformed into their chloride counterparts. Such a behaviour suggests that zinc extraction via the co-thermal treatment of EAFD with PVC can be a viable option; a process which can be optimised using the kinetic data extracted in this work.

# CHAPTER SIX

## A thermo-kinetic investigation on the thermal degradation of polyvinyl chloride in the presence of magnetite and hematite (paper 4)

### 6.1 Overview

Among many potential iron phases, magnetite ( $\text{Fe}_3\text{O}_4$ ) and hematite ( $\text{Fe}_2\text{O}_3$ ) (aside to franklinite mentioned in the previous chapter) are considered the major mineralogical forms in which iron is present in EAFD. These oxides can have a huge impact on the choice of processing temperatures and holding times needed to achieve certain PVC degradation conversion levels since they affect its the thermal degradation kinetics. Several attempts were made in literature to extract zinc and lead selectively from EAFD by the co-thermal treatment with PVC [20, 25]. However, in these studies, iron was also extracted with these metals which can complicate the downstream processing for obtaining them at high purity. Hence, the mechanistic understanding of how PVC interacts with the iron bearing oxides individually can greatly facilitate any attempt concerned with the extraction of zinc and lead selectively. For that, several studies addressed the impact of the addition of both  $\text{Fe}_3\text{O}_4$  and  $\text{Fe}_2\text{O}_3$  on the thermal decomposition of PVC [30, 32, 178, 182]. Zhang et al. [30] studied the effect of  $\text{Fe}_2\text{O}_3$  on the de-hydrochlorination onset temperature of PVC and the gaseous emissions during the degradation. Masuda et al. [32] studied the emissions from PVC degradation (liquid and gaseous) in the presence of several metal oxides. It was shown that the addition of  $\text{Fe}_2\text{O}_3$  appreciably suppressed liquid products from PVC degradation [32]. This was attributed to the potential formation of a small catalytic amount of  $\text{FeCl}_3$  despite the fact that no iron chloride phases were detected using XRD [32]. Meng et al. [182] reported the chlorine capturing capability of several metal oxides including  $\text{Fe}_2\text{O}_3$ . The study also reported the effect of these oxides on Cl distribution, thermodynamics, kinetics of PVC de-hydrochlorination, and the percentages of formed volatiles [182]. Finally, Ye et al. [178] studied the effect of  $\text{Fe}_3\text{O}_4$  on

the gaseous emissions of PVC during its degradation. Their study also reported the solid products from these reactions (organic and inorganic) [178]. None of the aforementioned studies addressed systematically the effect of both  $\text{Fe}_3\text{O}_4$  and  $\text{Fe}_2\text{O}_3$  on the kinetics of PVC dehydrochlorination. Herein, the effect of both  $\text{Fe}_3\text{O}_4$  and  $\text{Fe}_2\text{O}_3$  on the decomposition kinetics is studied systematically using non-isothermal thermogravimetric scans coupled with iso-conversional techniques for the extraction of the temperature independent kinetic parameters (activation energy, frequency factor and reaction model).

The manuscript titled “A thermo-kinetic investigation on the thermal degradation of polyvinyl chloride in the presence of magnetite and hematite” in Appendix 4 shows a detailed investigation on the thermal stability, pyrolysis behaviour, reaction products and kinetic parameters of PVC dehydrochlorination in the presence of stoichiometric quantities of  $\text{Fe}_3\text{O}_4$  and  $\text{Fe}_2\text{O}_3$  powders (mixed with PVC). In that study, mixtures of  $\text{Fe}_3\text{O}_4$ -PVC and  $\text{Fe}_2\text{O}_3$ -PVC were pyrolysed at different temperatures and analysed using appropriate analytical techniques. Thermal analysis was used to extract the kinetic parameters associated with the mass loss of these mixtures.

## **6.2 Pyrolysis and thermal stability**

The thermal behaviour of pure PVC,  $\text{Fe}_3\text{O}_4$ -PVC and  $\text{Fe}_2\text{O}_3$ -PVC mixtures is shown in Figure 39. Contrary to zinc bearing oxides (Chapter 5), the onset dehydrochlorination temperature of PVC was not affected appreciably by the presence of iron oxides and remained at around 272 °C. Despite this similarity, the initiation mechanism involved in the dehydrochlorination was clearly affected by the presence of these oxides. Such a result is confirmed from the significant difference in the values of the activation energy of pure PVC and its mixtures with  $\text{Fe}_3\text{O}_4$  and  $\text{Fe}_2\text{O}_3$  at a conversion of 0.004 with values of 109.9, 204.2, and 215.1 kJ/mol for pure PVC,  $\text{Fe}_3\text{O}_4$ -PVC, and  $\text{Fe}_2\text{O}_3$ -PVC, respectively. Unlike zinc compounds,  $\text{Fe}_3\text{O}_4$  is believed to react

with gaseous HCl which can be confirmed from the absence of DTG doublet/triplet (seen earlier for zinc compounds); further confirmation on this is present from the kinetic data. Fe<sub>2</sub>O<sub>3</sub>, in contrast, is thermodynamically stable and does not chlorinate [15] before being reduced into Fe<sub>3</sub>O<sub>4</sub> by the H<sub>2</sub> emitted during the de-hydrochlorination step.

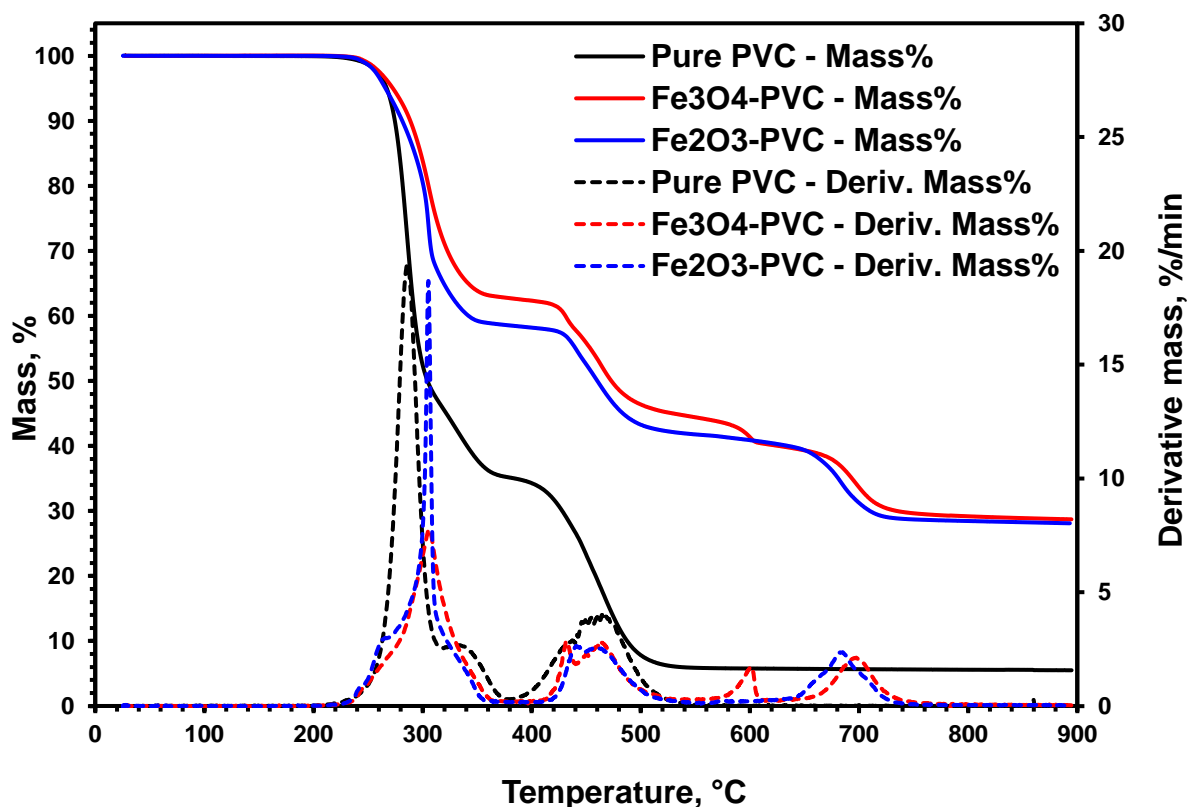


Figure 39: The thermal behaviour of pure PVC, Fe<sub>3</sub>O<sub>4</sub>-PVC (31.6 wt% Fe<sub>3</sub>O<sub>4</sub>), and Fe<sub>2</sub>O<sub>3</sub>-PVC (29.9 wt% Fe<sub>2</sub>O<sub>3</sub>) under a nitrogen flow of 100 mL/min and a heating rate of 10 °C/min.

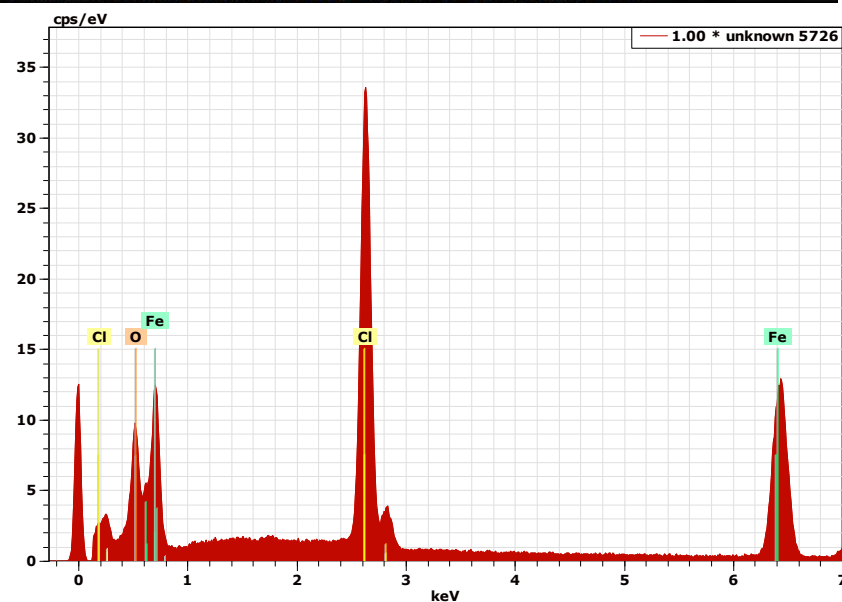
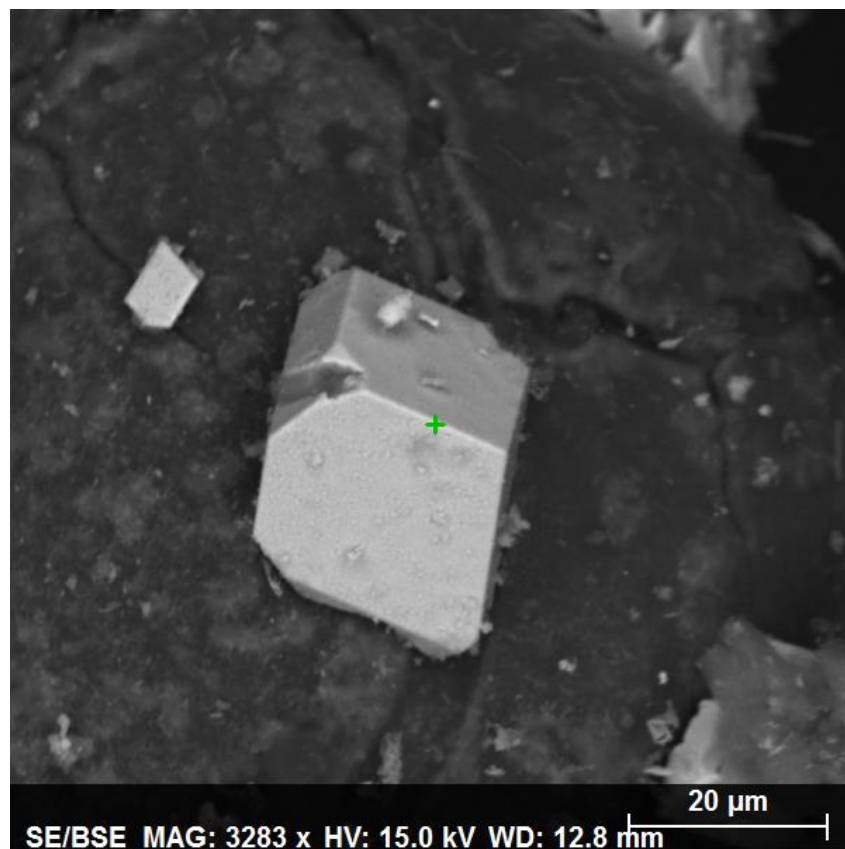
After the de-hydrochlorination stage of Fe<sub>3</sub>O<sub>4</sub>-PVC and Fe<sub>2</sub>O<sub>3</sub>-PVC, chlorides of FeCl<sub>2</sub> and FeCl<sub>2</sub>·2H<sub>2</sub>O were detected by XRD and are shown in the manuscript attached to Appendix 4.

The morphology and the chemistry of these compounds were also revealed using SEM analysis. An example of this is shown in

Spectrum: unknown 5726

Element	unn. C [wt.%]	norm. C [wt.%]	Atom. C [at.%]	Compound norm. Comp. C [wt.%]	Rel. error (1 Sigma), %
Oxygen	14	16	36	16	14
Chlorine	21	25	25	25	03
Iron	50	59	39	59	03
Total:	85	100	100		

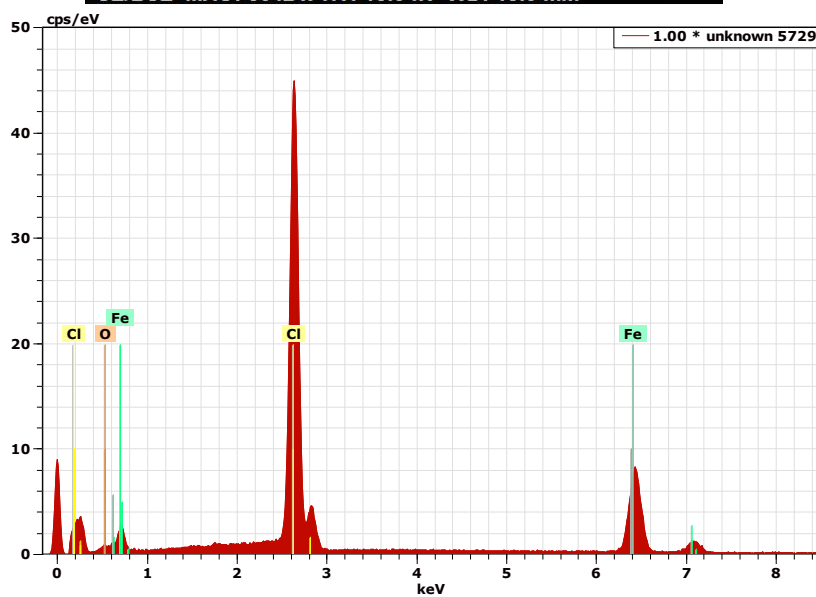
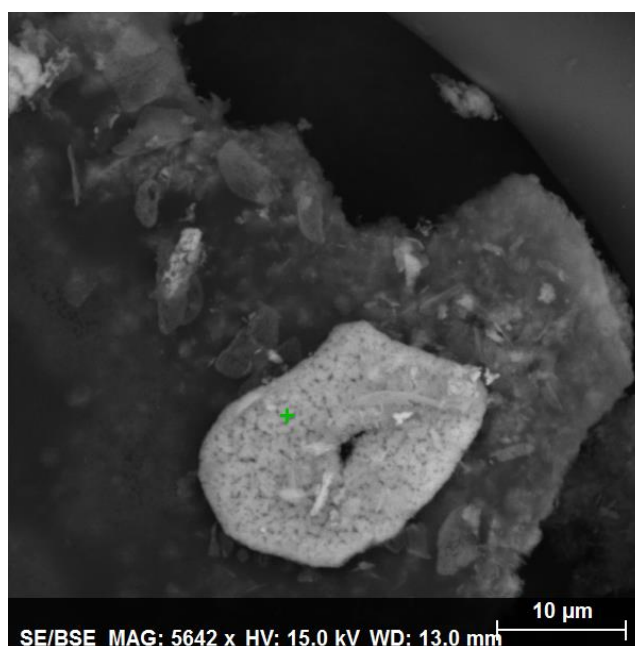
Figure 40 and Figure 41 showing the chemistry and morphology of formed chlorides at a temperature of 600 °C for a mixture of Fe<sub>2</sub>O<sub>3</sub>-PVC.



Spectrum: unknown 5726

Element	unn. C [wt.%]	norm. C [wt.%]	Atom. C [at.%]	Compound norm. Comp. C [wt.%]	Rel. error (1 Sigma), %
Oxygen	14	16	36	16	14
Chlorine	21	25	25	25	03
Iron	50	59	39	59	03
-----					
Total:	85	100	100		

Figure 40: The morphology and chemistry of a crystal obtained from the pyrolysis of Fe<sub>2</sub>O<sub>3</sub>-PVC mixture at a temperature of 600 °C which is potentially related to FeCl<sub>2</sub>·2H<sub>2</sub>O.



Spectrum: unknown 5729

Element	unn. C [wt.%]	norm. C [wt.%]	Atom. C [at.%]	Compound norm. Comp. C [wt.%]	Rel. error (1 Sigma), %
Oxygen	02	02	06	02	23
Chlorine	41	50	58	49	03
Iron	40	48	36	48	03
Total:	83	100	100		

Figure 41: The morphology and chemistry of FeCl<sub>2</sub> obtained from the pyrolysis of Fe<sub>2</sub>O<sub>3</sub>-PVC mixture at a temperature of 600 °C.

The deviation of the atomic percentages in the tables in

Spectrum: unknown 5726

Element	unn. C [wt.%]	norm. C [wt.%]	Atom. C [at.%]	Compound norm. Comp. C [wt.%]	Rel. error (1 Sigma), %
Oxygen	14	16	36	16	14
Chlorine	21	25	25	25	03
Iron	50	59	39	59	03
Total:	85	100	100		

Figure 40 and Figure 41 from the theoretical atomic percentage of these minerals can be assigned to the three dimensional nature of the sample and the contamination by other crystals which affects the electron count. All the details regarding the reaction mechanisms are presented in detail in the manuscript attached to Appendix 4 which also includes a thermodynamics assessment of all the reduction reactions associated with the de-hydrochlorination stage.

A further increase in temperature of these mixtures results in a sequence of reduction reactions by the H<sub>2</sub> and the char generated from the thermal cracking of the polymer. At the end, iron is present in its elemental form as α-Fe along with iron carbide Fe<sub>3</sub>C (see Appendix 4).

### 6.3 The kinetics of PVC de-hydrochlorination in the presence of Fe<sub>3</sub>O<sub>4</sub> and Fe<sub>2</sub>O<sub>3</sub>

On a fundamental level, knowledge of the kinetic parameters allows making predictions of reaction rates at any processing temperature, hence assessing the thermal stability of reactive

systems. The temperature independent kinetic parameters represented by the activation energy and the frequency factor are presented in Figure 42 (A) and (B). Both  $\text{Fe}_3\text{O}_4$  and  $\text{Fe}_2\text{O}_3$  result in a significant increase in the values of the activation energy. In the case of  $\text{Fe}_2\text{O}_3$ , however, the increase is drastic especially in the conversion range 0.4 – 0.6. The reason for the increase in the activation energy can be assigned to the ability of these oxides ( $\text{Fe}_3\text{O}_4$ ) and ( $\text{Fe}_2\text{O}_3$  after reduction) to capture HCl; a material identified before as an accelerating agent for the dehydrochlorination [186]. The evidence for this can be seen in Appendix 4 where peaks of  $\text{FeCl}_2$  and  $\text{FeCl}_2 \cdot 2\text{H}_2\text{O}$  can be seen for both the reaction systems of  $\text{Fe}_3\text{O}_4$ -PVC and  $\text{Fe}_2\text{O}_3$ -PVC suggesting the capturing of HCl.

To properly assess reaction rates and thermal stability, the effect of the frequency factor should also be taken into account. According to the compensation effect explained in the manuscripts in Appendices 2, 3, and 4, the frequency factor should follow a similar trend to that of the activation energy. Thus, the same spike for  $\text{Fe}_2\text{O}_3$ -PVC mixture is seen for the frequency factor in the conversion range 0.4 – 0.6. The huge increase in the activation energy and frequency factor for  $\text{Fe}_3\text{O}_4$ -PVC and  $\text{Fe}_2\text{O}_3$ -PVC in that conversion range can be assigned to the capturing of HCl thus causing a shift in the overall controlling mechanism.

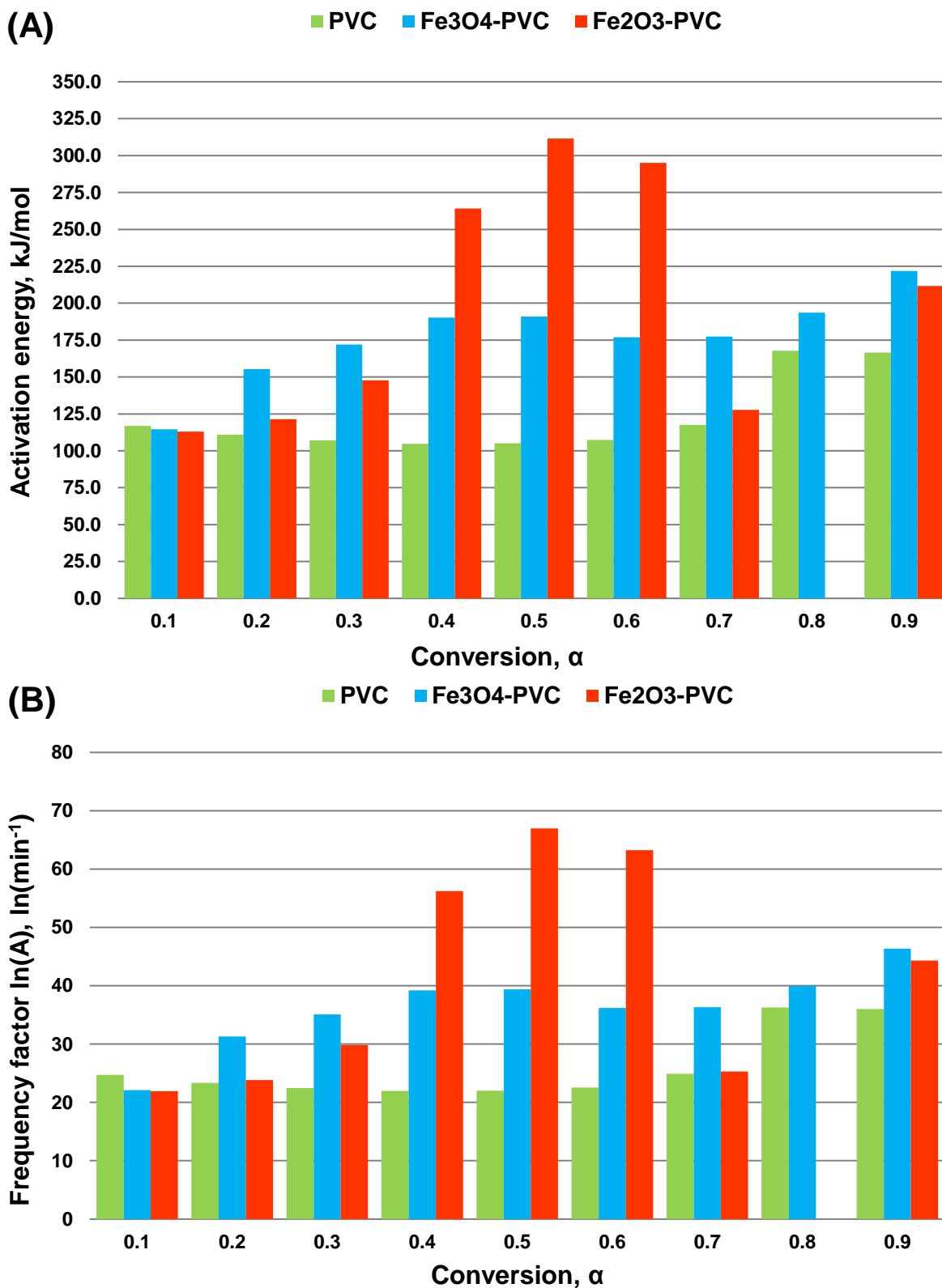
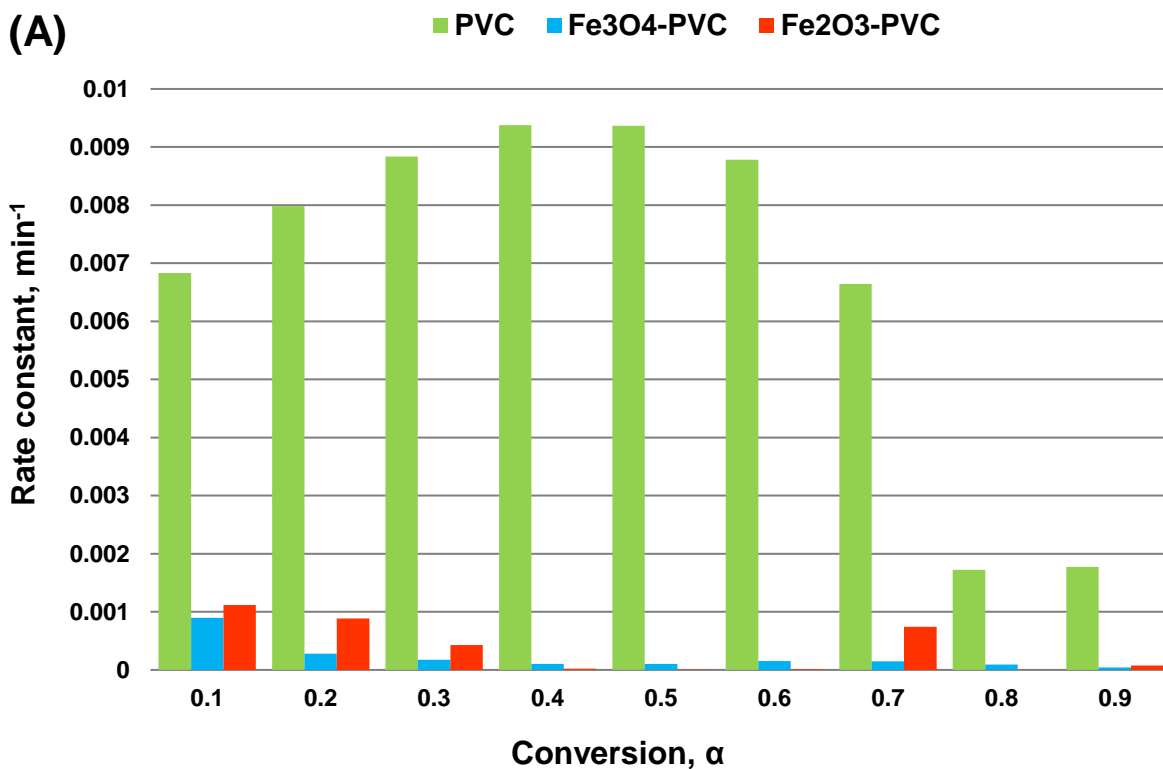


Figure 42: The kinetic parameters (A) activation energy and (B) frequency factor (units  $\text{min}^{-1}$ ) associated with PVC de-hydrochlorination alone and in the presence of stoichiometric quantities of  $\text{Fe}_3\text{O}_4$  (31.6 wt%  $\text{Fe}_3\text{O}_4$ ) and  $\text{Fe}_2\text{O}_3$  (29.9 wt%  $\text{Fe}_2\text{O}_3$ ).

Due to the high activation energy associated with Fe<sub>3</sub>O<sub>4</sub>-PVC and Fe<sub>2</sub>O<sub>3</sub>-PVC degradation, they can be considered as “temperature demanding” processes. This can be confirmed by taking a look at the value of the rate constant at different temperatures of 200 and 300 °C (Figure 43 (A) and (B)). At 200 °C, the rate constant for PVC is significantly higher at all conversion values. However, a temperature increase up to 300 °C yields a rate constant of Fe<sub>2</sub>O<sub>3</sub>-PVC higher than that of PVC in the conversion range 0.4 – 0.6. This is because, the energy barrier is overcome by the high vibrational activity at high temperature along with a large increase in the frequency factor (from the compensation effect) yielding a rate constant with a larger value than that of pure PVC. This, however, does not necessarily mean that the rate associated with Fe<sub>2</sub>O<sub>3</sub>-PVC degradation is higher at that temperature since the reaction model  $f(\alpha)$  can also have an impact on the overall rate. A detailed comparison on the rate constant and reaction rates is presented in the paper attached to Appendix 4.



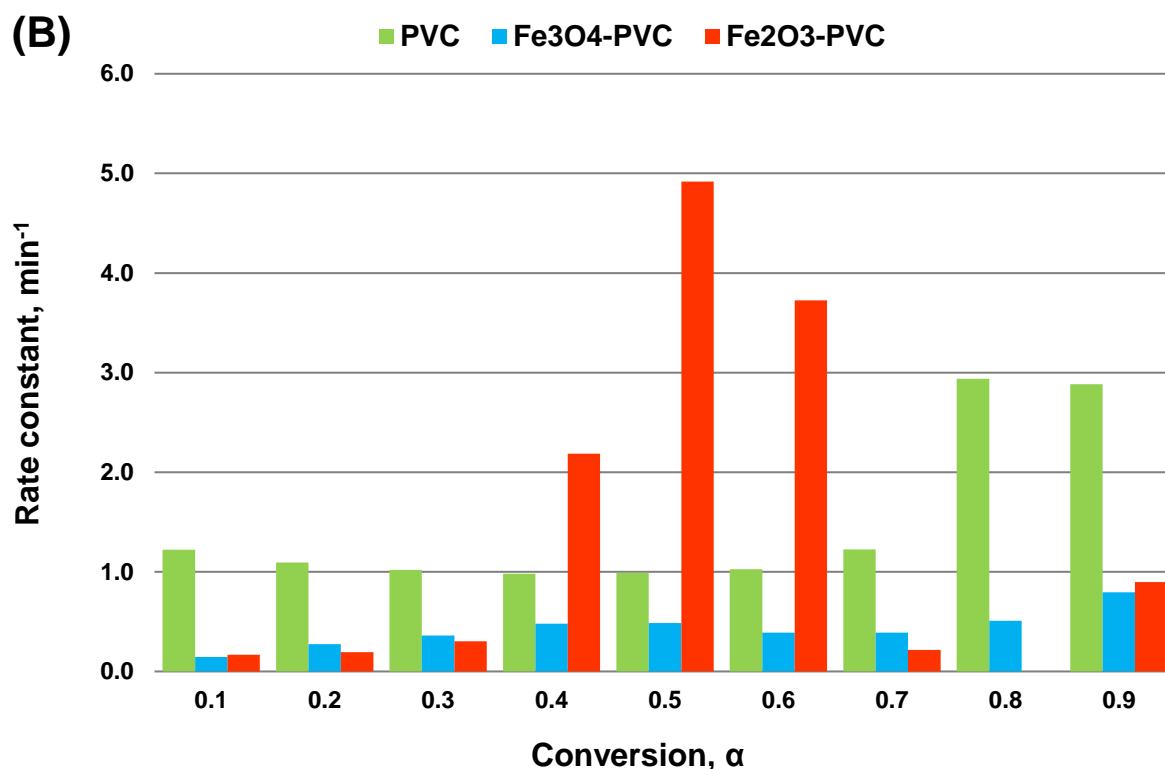


Figure 43: The rate constant at temperatures of 200 (A) and 300 °C (B) for the de-hydrochlorination of PVC alone and in the presence of stoichiometric quantities of Fe<sub>3</sub>O<sub>4</sub> (31.6 wt% Fe<sub>3</sub>O<sub>4</sub>) and Fe<sub>2</sub>O<sub>3</sub> (29.9 wt% Fe<sub>2</sub>O<sub>3</sub>).

To confirm the reliability of the kinetic data shown in Figure 42 (A) and (B), the experimental rate and the rate generated from these kinetic data were compared and are presented in Figure 44.

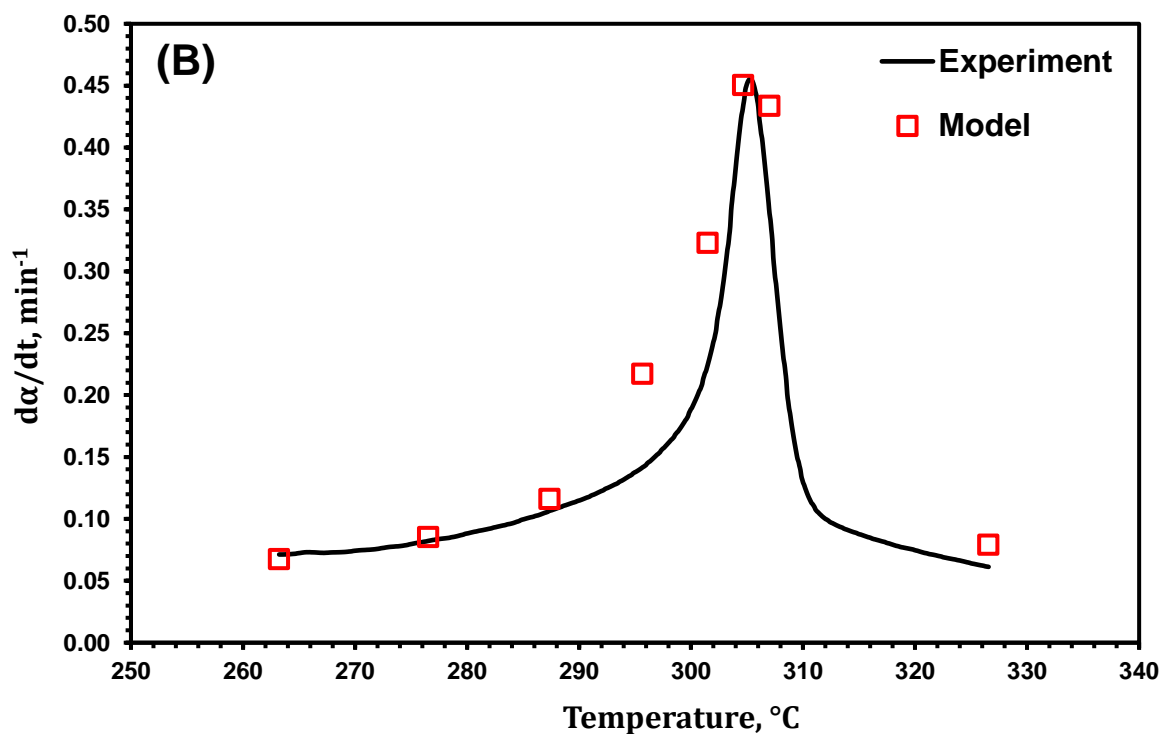
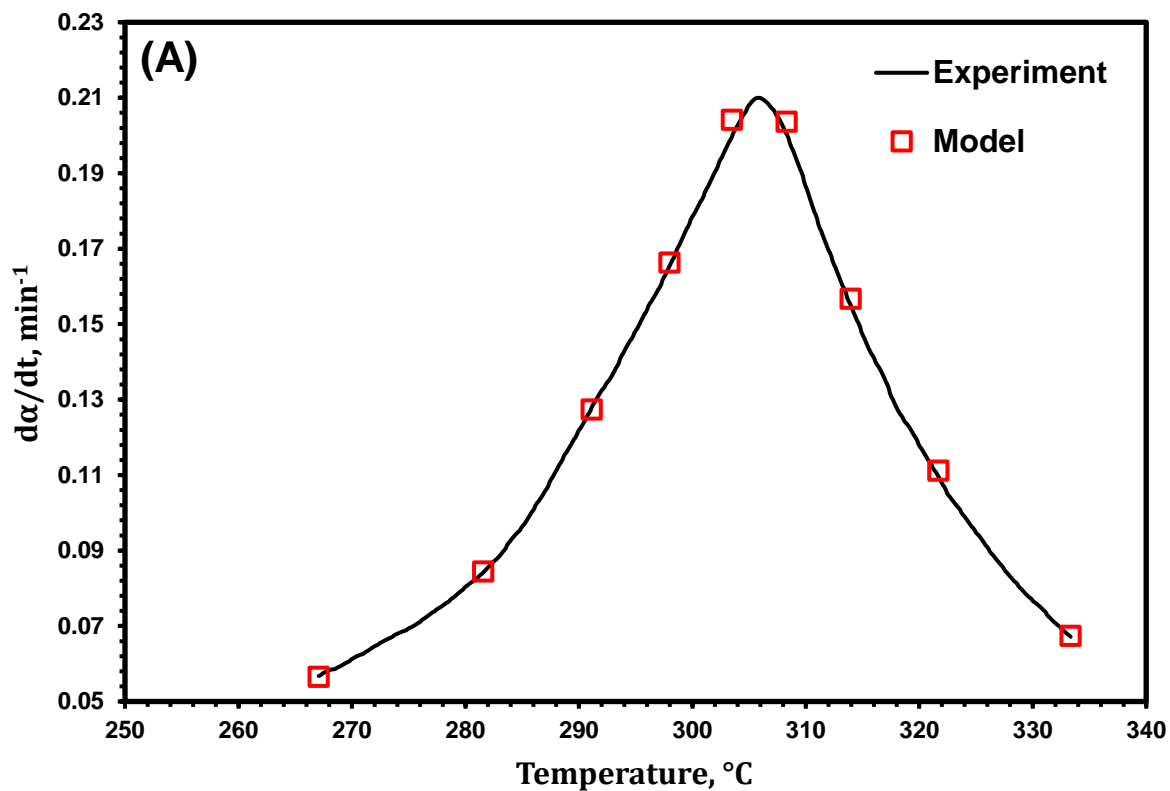


Figure 44: A comparison between experimental and model based de-hydrochlorination rate of (A)  $\text{Fe}_3\text{O}_4$ -PVC (31.6 wt%  $\text{Fe}_3\text{O}_4$ ) and (B)  $\text{Fe}_2\text{O}_3$ -PVC (29.9 wt%  $\text{Fe}_2\text{O}_3$ ) mixtures using data extracted from Friedman model.

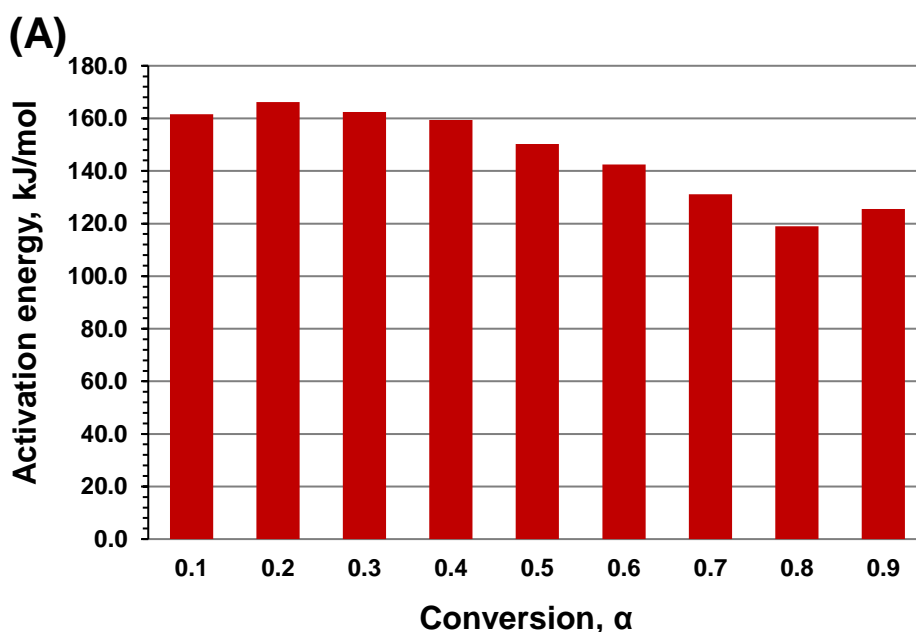
A good agreement can be seen between the rate obtained from the kinetic data and the rate obtained experimentally suggesting the reliability of the extracted kinetic parameters.

## 6.4 Kinetics of the carbothermic reduction of Fe<sub>3</sub>O<sub>4</sub> and FeO by the char generated from PVC degradation

For the Fe<sub>3</sub>O<sub>4</sub>-PVC mixture, in the temperature window 575 – 615 °C, a mass loss of about 4.0% can be seen (Figure 39). The char formed from the thermal cracking of the polymer backbone reacts with excess Fe<sub>3</sub>O<sub>4</sub> (major reduction stage) forming FeO as follows:



The formation of FeO in large amounts is confirmed from the large XRD peaks shown in the manuscript attached to Appendix 4. The kinetic data for this reduction stage is presented in Figure 45 (A) and (B). The activation energy does not show large variation throughout the conversion 0.1 – 0.9 averaging at 146.4 kJ/mol. Following the compensation effect, the frequency factor also did not change appreciably with conversion suggesting a single controlling mechanism with a reaction model of  $f(\alpha) = \alpha^{0.44}$  in the conversion range 0.8 – 0.9.



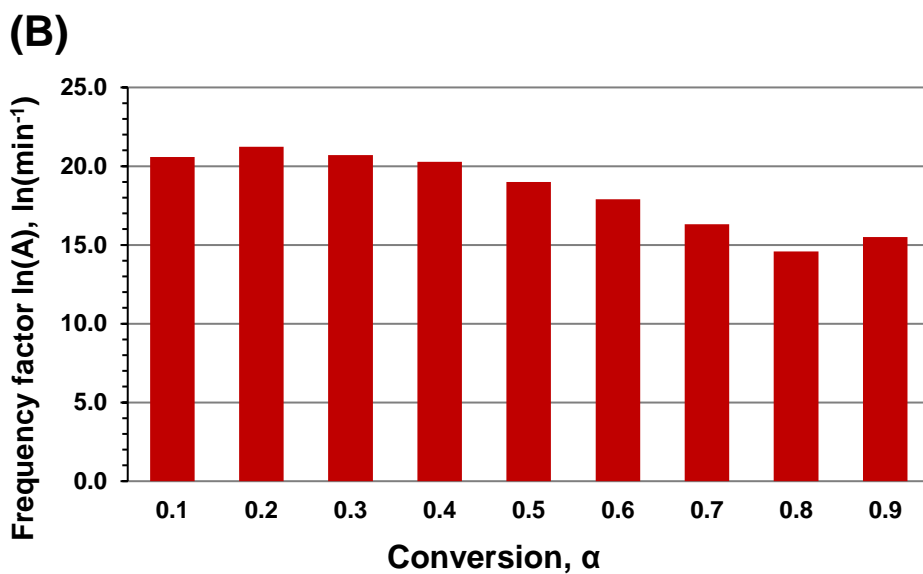
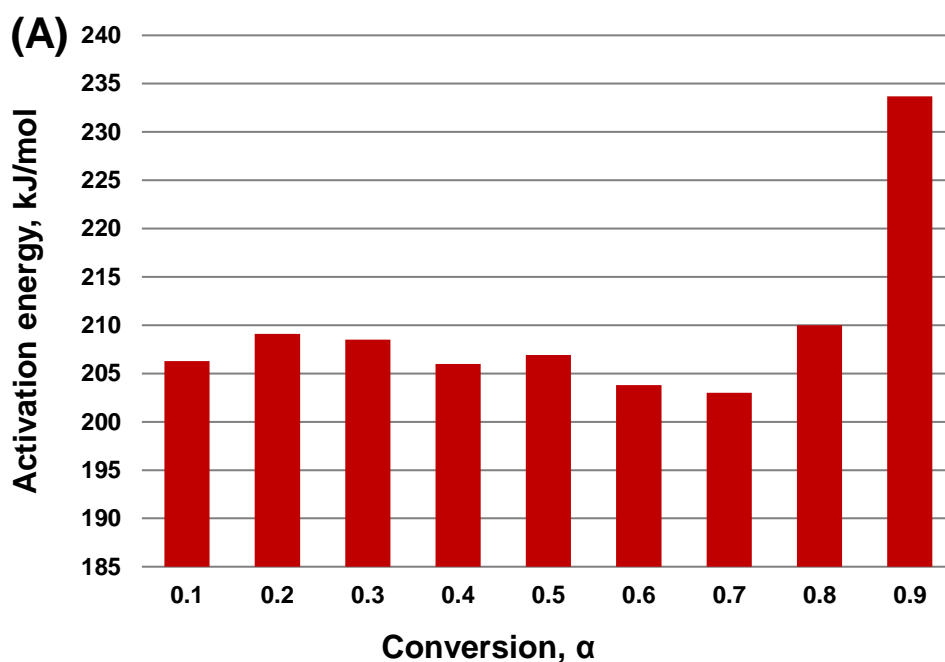


Figure 45: The kinetic parameters (A) activation energy and (B) frequency factor (unit is  $\text{min}^{-1}$ ) associated with the carbothermic reduction of  $\text{Fe}_3\text{O}_4$  to  $\text{FeO}$  by the char generated from PVC degradation.

With a further increase in temperature ( $655 - 750\text{ }^\circ\text{C}$ ), a second major reduction stage appears which is related to the transformation of  $\text{FeO}$  to elemental iron ( $\alpha\text{-Fe}$ ). The kinetic data associated with this stage is shown in Figure 46 (A) and (B).



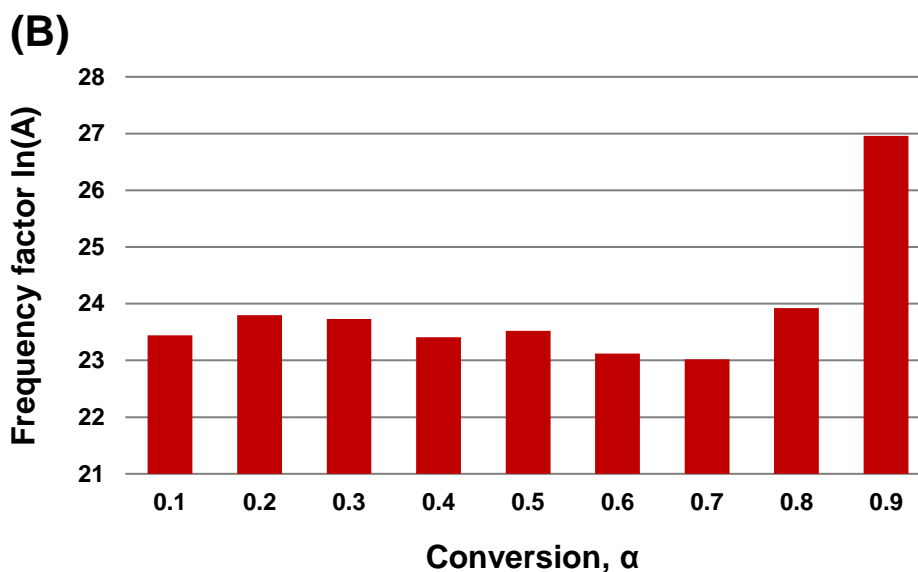


Figure 46: The kinetic parameters ((A) activation energy and (B) frequency factor) associated with the carbothermic reduction of FeO to  $\alpha$ -Fe by the char generated from PVC degradation.

Clearly, the activation energies associated with these reduction stages especially the second one are significantly higher than those associated with PVC de-hydrochlorination. This explains why these processes occur at significantly higher temperatures. Moreover, the data in Figure 45 and Figure 46 show comparable frequency factor values, however, with much higher values of activation energy for the transformation of FeO into  $\alpha$ -Fe which is also in line with the fact that this reduction stage occurs at a significantly higher temperature. The reliability of the data presented in Figure 45 and Figure 46 was confirmed by comparing the experimental rate with the rate generated using extracted kinetic data (Figure 47 (A) and (B)).

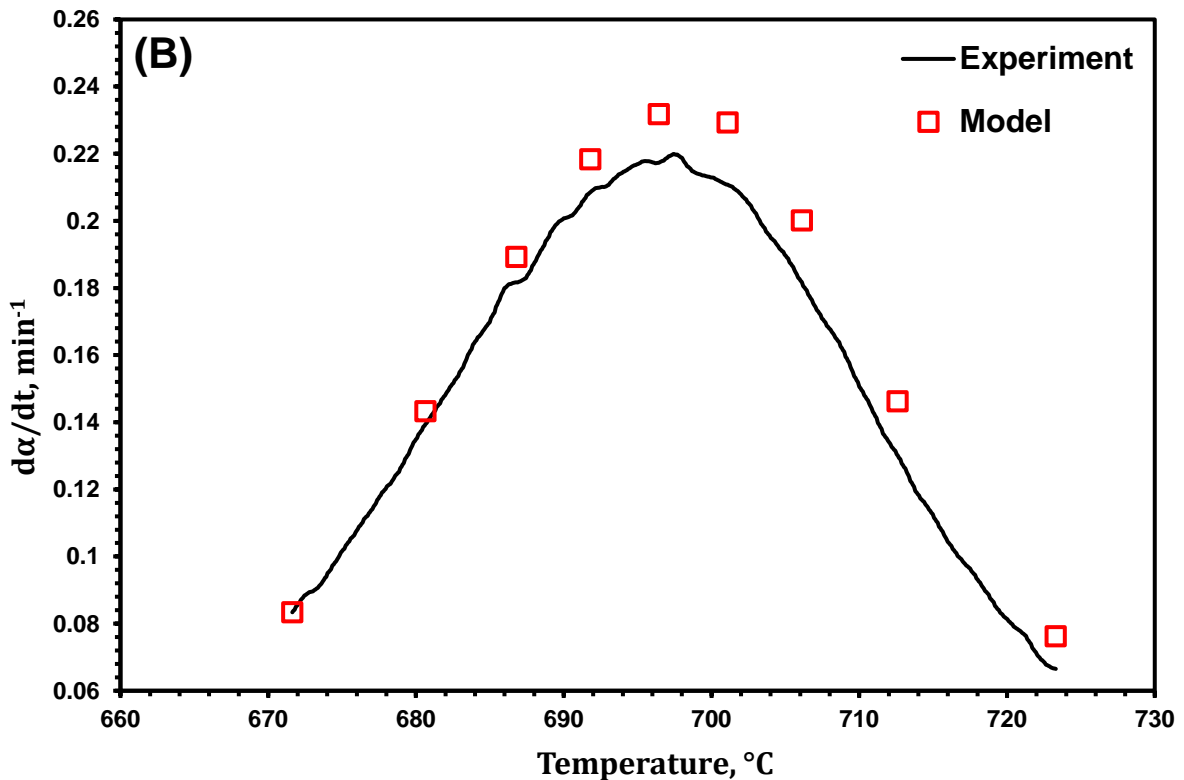
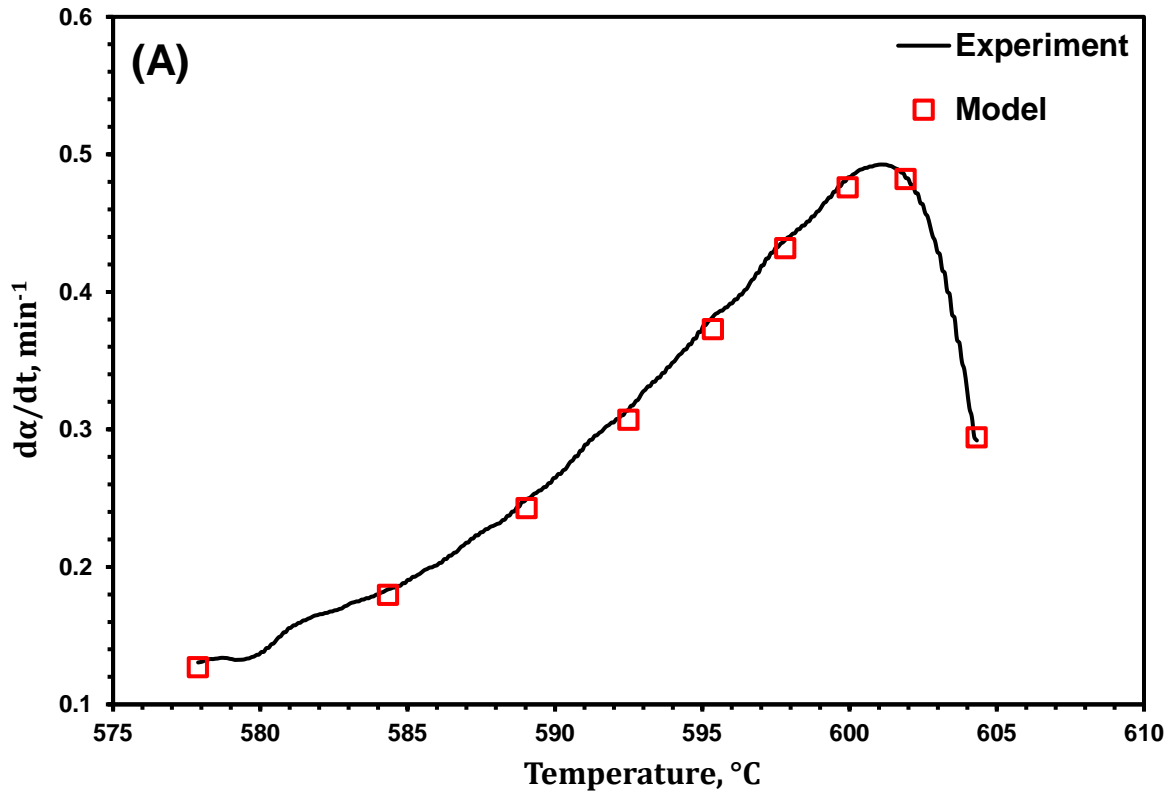


Figure 47: A comparison between experimental and model based carbothermic reduction rate of (A)  $\text{Fe}_3\text{O}_4$  to  $\text{FeO}$  and (B)  $\text{FeO}$  to  $\alpha\text{-Fe}$  using data extracted from Friedman model.

Experimental and model based data in Figure 47 (A) and (B) are in good agreement suggesting that the extracted kinetic data are reasonably accurate.

## 6.5 Summary

The effect of the major iron containing compounds in EAFD on the thermal degradation kinetics of PVC was reported. Both  $\text{Fe}_3\text{O}_4$  and  $\text{Fe}_2\text{O}_3$  showed a good ability in capturing HCl such that the former reacted directly with HCl while the latter was first reduced by  $\text{H}_2$  evolved from the de-hydrochlorination into  $\text{Fe}_3\text{O}_4$  after which it was transformed into iron chloride. The HCl scavenging ability of these oxides resulted in a drastic increase in the activation energy associated with the de-hydrochlorination which upon combining with the frequency factor yielded an overall lower value of the rate constant, especially at low pyrolysis temperatures such as 200 °C. Such a result suggests that these oxides have an inhibiting effect on the degradation of PVC.

# CHAPTER SEVEN

## Conclusions and future work

### 7.1 Conclusions

The manuscripts attached in the appendices provide a foundation on which the potential recycling of EAFD with halogenated plastics (namely PVC) can be based. Initially, the major components of EAFD were analysed for their relative permittivity over wide temperature range thus facilitating making predictions on the microwave interaction with any EAFD sample carrying different chemistries/mineralogy. Afterwards, a fundamental phenomenon which is the interaction of different electromagnetic microwave fields with these components was addressed. This was achieved by inserting the dielectric properties of these components into an electromagnetic simulation using COMSOL Multiphysics, thus allowing exposing these materials to pure electric and pure magnetic microwave fields. This phenomenon can be exploited to use microwave heating for the selective heating of certain components over the others (depending on dielectric, magnetic and electrical conductivity nature of the material).

In the manuscripts that follow, the thermal behaviour of PVC mixed with the major components of EAFD was studied. The effect of the following oxides: ZnO, ZnFe<sub>2</sub>O<sub>4</sub>, Fe<sub>2</sub>O<sub>3</sub>, and Fe<sub>3</sub>O<sub>4</sub> was studied. These studies involved reporting the fundamental parameters related to the thermal stability of thermally stimulated materials: the activation energy, the frequency factor, and the reaction model. Knowledge of these temperature independent kinetic parameters allows making predictions of reaction rates of PVC mixed with EAFD with different chemistries at different pyrolysis temperatures. Additionally, the optimisation of processes from a yield and an economic point of view can only be done when accurate kinetic data are available.

The key findings derived from the work presented in each manuscript is summarised as follows:

➤ **Electromagnetism manuscript (appendix 1):**

1. The separation of microwave electromagnetic fields was achieved in a  $TE_{10}$  cavity followed by the selective heating of the major components of EAFD using pure electric and magnetic fields. When isolating the microwave electromagnetic fields, the following points were also concluded as well:
  - a. An electromagnetic simulation is needed and the mere calculation of a quarter wavelength from the short circuit position is not enough to precisely determine fields distribution. This is because the chokes and the observation ports result in a change in the positions of the electromagnetic fields due to scattering of the waves through them.
  - b. In order to utilise each microwave field separately, a sample with a small dimension needs to be introduced; in this study, the diameter of the sample was 2.3% of the wavelength of the guided wave inside the waveguide (microwave at a frequency of 2.47 GHz was used in a WR340 waveguide).
  - c. The permittivity and permeability parameters of the material of interest need to be introduced in the model to take into account its effect on the resonant frequency inside the waveguide.
2. ZnO, ZnFe<sub>2</sub>O<sub>4</sub>, Fe<sub>3</sub>O<sub>4</sub>, and graphite were found to be the major components of EAFD contributing to the overall microwave heating. Other components such as Fe<sub>2</sub>O<sub>3</sub>, SiO<sub>2</sub>, CaCO<sub>3</sub>, and PbO were found to be poor microwave absorbents, especially PbO and SiO<sub>2</sub>.
3. A very good agreement was seen between the heating behaviour and the extracted permittivity data of materials; materials with low imaginary permittivity showed very slow heating rates while those with high one exhibited fast heating rates when exposed

to the electric component of the microwave (see the manuscript attached to Appendix 1).

4. The selective heating of magnetic ( $\text{Fe}_3\text{O}_4$ ) and electrically conductive (graphite) materials present in EAFD was achieved using the magnetic component of microwaves; a property can be used for the selective heating of magnetic and electrically conductive components in EAFD. Other dielectrics in EAFD did not heat in the magnetic field maxima of the microwaves.

➤ **Kinetics manuscripts (Appendices 2, 3, and 4):**

1. The addition of both ZnO and  $\text{ZnFe}_2\text{O}_4$  reduced the thermal stability of PVC which appeared as a drop in the onset de-hydrochlorination temperature from 272 °C to values of 214 and 235 °C for the addition of ZnO and  $\text{ZnFe}_2\text{O}_4$ , respectively.
2. Chlorine present in PVC resulted in a complete destruction of the stable structure of  $\text{ZnFe}_2\text{O}_4$  transforming it into its chloride counterparts which can be utilised for zinc extraction.
3. Both ZnO and  $\text{ZnFe}_2\text{O}_4$  were found to react directly with the PVC monomer abstracting Cl via a direct reaction and thus changing the de-hydrochlorination initiation pathway. This, in turn, reflected on the value of the initiation activation energy which changed from 109.9 kJ/mol for pure PVC to 121.9 and 148.2 kJ/mol for ZnO-PVC and  $\text{ZnFe}_2\text{O}_4$ -PVC mixtures, respectively.
4. Since the overall activation energy decreased when ZnO was added to PVC, a higher rate constant was calculated at all conversion levels at the low pyrolysis temperature 200 °C for the ZnO-PVC mixture.
5. For  $\text{ZnFe}_2\text{O}_4$ , the presence of  $\text{Fe}^{2+}$  bearing oxides post chlorination and reduction resulted in capturing of emitted gaseous HCl. This, in turn, yielded high values of activation energy associated with the de-hydrochlorination when compared to pure

PVC due to the capturing of gaseous HCl by  $\text{Fe}_3\text{O}_4$  formed after the chlorination of  $\text{ZnFe}_2\text{O}_4$  and the reduction of  $\text{Fe}_2\text{O}_3$  side product.

6.  $\text{Fe}_3\text{O}_4$  and  $\text{Fe}_2\text{O}_3$  were found to increase the activation energy of de-hydrochlorination to values much higher than those related to pure PVC due to the capturing of emitted gaseous HCl which is a known catalyst for the de-hydrochlorination. Operating at low pyrolysis temperature of 200 °C yielded lower rate constants for both  $\text{Fe}_3\text{O}_4$ -PVC and  $\text{Fe}_2\text{O}_3$ -PVC compared to pure PVC. This means that both  $\text{Fe}_3\text{O}_4$  and  $\text{Fe}_2\text{O}_3$  can be deemed as PVC de-hydrochlorination inhibitors.
7. The capturing of HCl by the iron bearing oxides resulted in the drastic increase in the activation energy thus slowing the de-hydrochlorination stage.

## 7.2 Future work

In the previous section, the main conclusions arising from the attached manuscripts have been reported. While a significant effort has been directed towards generating comprehensive data related to the co-thermal treatment of EAFD-PVC, many gaps still need to be filled.

### 7.2.1 Microwave electromagnetic interaction with EAFD and PVC – selective heating using separated microwave fields

On a fundamental level, the manuscript attached to Appendix 1 provided answers to the phenomenon whereby different materials with different permittivities/permeabilities responded in a different manner to different electromagnetic waves. Here, the microwaves were introduced to the system at the high frequency 2.47 GHz. At an industrial level, however, this frequency is not usually used as it provides low penetration depths, thus preventing the operation at a larger scale. Moreover, the isolation of the electromagnetic field requires a sample having a dimension smaller than a quarter of the wavelength of the guided wave. Hence, trials using microwaves at a frequency of 912 MHz should be conducted which would allow separating the electric and magnetic fields for a reasonably sized sample. At that level, studying

the concept discussed in the manuscript in Appendix 1 reflects more realistically to the industrial applicability of the separated electric and magnetic fields concept. The major challenge that will be faced when trying to operate at that scale, however, is that it will potentially require using high power input to achieve a certain power/mass ratio. Powers at that level are mainly generated using magnetrons which are not considered solid state generators. Hence, a broad band of frequencies can also be generated with the frequency of interest, thus complicating the procedure of separating the electric and magnetic microwave fields.

7.2.2 The effect of different EAFD components on the degradation kinetics of PVC  
Several points still need addressing and has not been covered in this thesis:

1. Here, the studied PVC was of high purity and the effect of different additives was not taken into account. Studying the kinetics of PVC degradation from different sources with different properties (stabilised, plasticized, coloured etc.) still needs to be undertaken.
2. The produced models need to be combined and compared with the obtained kinetic data from the degradation of PVC mixed with different EAFDs with different chemistry/mineralogy.
3. The effect of synthetic mixtures of different EAFD constituents on the degradation kinetics of PVC need to be studied and the results need to be reflected on real EAFD samples.
4. Systematic iso-thermal kinetic studies need also to be carried out to further confirm the data extracted from the iso-conversional methods reported here. This is because, in the iso-conversional (non-isothermal) approach, different controlling mechanisms occur at different temperatures leading to variation of activation energy and frequency factor with conversion. Such a result sometimes is avoided when iso-thermal analysis is

carried out, whereby a single controlling mechanism is obtained since the other mechanisms were not thermally activated by increasing the temperature.

## References

1. Wang, J., et al., Pyrometallurgical recovery of zinc and valuable metals from electric arc furnace dust—a review. *Journal of Cleaner Production*, 2021. 298: p. 126788.
2. Stefanova, A., J. Aromaa, and O. Forsen, Alkaline leaching of zinc from stainless steel electric arc furnace dusts. *Physicochemical problems of mineral processing*, 2015. 51.
3. KiranKumar, T. and G.G. Roy, A Review on Processing of Electric Arc Furnace Dust (EAFD) by Pyro-Metallurgical Processes. *Transactions of the Indian Institute of Metals*, 2022: p. 1-12.
4. Mantovani, M., C. Takano, and P. Büchler, EAF and secondary dust characterisation. *Ironmaking & steelmaking*, 2004. 31(4): p. 325-332.
5. NAGAI, K., Y. MATSUMOTO, and H. WATANABE, EAF dust treatment practice at the Shisaka Works. *Journal of MMIJ*, 2007. 123(12): p. 726-729.
6. SUGIMOTO, H., H. TAKIZAWA, and H. UEDA, Treatment of EAF Dust at Sotetsu Metal Co., Ltd. *Journal of MMIJ*, 2007. 123(12): p. 723-725.
7. Suetens, T., et al., Comparison of electric arc furnace dust treatment technologies using exergy efficiency. *Journal of cleaner production*, 2014. 65: p. 152-167.
8. Leclerc, N., E. Meux, and J.-M. Lecuire, Hydrometallurgical extraction of zinc from zinc ferrites. *Hydrometallurgy*, 2003. 70(1-3): p. 175-183.
9. Al-Harabsheh, M., et al., Pyrolysis of poly(vinyl chloride) and—electric arc furnacedust mixtures. *Journal of Hazardous Materials*, 2015. 299: p. 425-436.
10. Havlik, T., et al., Atmospheric leaching of EAF dust with diluted sulphuric acid. *Hydrometallurgy*, 2005. 77(1): p. 41-50.
11. Langová, Š., J. Leško, and D. Matýsek, Selective leaching of zinc from zinc ferrite with hydrochloric acid. *Hydrometallurgy*, 2009. 95(3): p. 179-182.
12. Oustadakis, P., et al., Hydrometallurgical process for zinc recovery from electric arc furnace dust (EAFD): Part I: Characterization and leaching by diluted sulphuric acid. *Journal of Hazardous Materials*, 2010. 179(1): p. 1-7.
13. Tsakiridis, P.E., et al., Hydrometallurgical process for zinc recovery from electric arc furnace dust (EAFD). Part II: Downstream processing and zinc recovery by electrowinning. *Journal of Hazardous Materials*, 2010. 179(1): p. 8-14.
14. Al-Makhadmeh, L.A., et al., The Effectiveness of Zn Leaching from EAFD Using Caustic Soda. *Water, Air, & Soil Pollution*, 2018. 229(2): p. 33.
15. Al-Harabsheh, M., Thermodynamic Analysis on the Thermal Treatment of Electric Arc Furnace Dust-PVC Blends. *Arabian Journal for Science and Engineering*, 2017: p. 1-13.
16. Xia, D. and C. Picklesi, Microwave caustic leaching of electric arc furnace dust. *Minerals Engineering*, 2000. 13(1): p. 79-94.
17. Yu, J., et al., Thermal degradation of PVC: A review. *Waste Management*, 2016. 48: p. 300-314.
18. Plastics-Europe, *Plastics – the Facts 2021*. 2021.
19. Zhou, Y., N. Yang, and S. Hu, Industrial metabolism of PVC in China: A dynamic material flow analysis. *Resources, Conservation and Recycling*, 2013. 73: p. 33-40.
20. Al-harabsheh, M., et al., Microwave treatment of electric arc furnace dust with PVC: Dielectric characterization and pyrolysis-leaching. *Journal of Hazardous Materials*, 2014. 274: p. 87-97.
21. Al-Harabsheh, M., et al., Treatments of electric arc furnace dust and halogenated plastic wastes: A review. *Journal of Environmental Chemical Engineering*, 2018: p. 102856.

22. Miranda, R., et al., Vacuum pyrolysis of PVCII: Product analysis. *Polymer Degradation and Stability*, 1999. 66(1): p. 107-125.
23. Kim, S., Pyrolysis kinetics of waste PVC pipe. *Waste management*, 2001. 21(7): p. 609-616.
24. Al-Harabsheh, M., et al., Leaching behavior of zinc and lead from electric arc furnace dust–Poly (vinyl) chloride residues after oxidative thermal treatment. *Journal of Cleaner Production*, 2021. 328: p. 129622.
25. Al-Harabsheh, M., Y. Orabi, and S. Al-Asheh, Comparative study on the pyrolysis and leachability of washed/unwashed electric arc furnace dust-PVC mixtures and their residues. *Journal of Environmental Chemical Engineering*, 2021: p. 105410.
26. Iida, T. and K. Gotō, Investigations on poly (vinyl chloride). III. Effects of metal oxides upon thermal decomposition of poly (vinyl chloride). *Journal of Polymer Science: Polymer Chemistry Edition*, 1977. 15(10): p. 2427-2433.
27. Ballistreri, A., et al., Effect of metal oxides on the evolution of aromatic hydrocarbons in the thermal decomposition of PVC. *Journal of Polymer Science: Polymer Chemistry Edition*, 1980. 18(10): p. 3101-3110.
28. Gupta, M. and S. Viswanath, Role of metal oxides in the thermal degradation of poly (vinyl chloride). *Industrial & engineering chemistry research*, 1998. 37(7): p. 2707-2712.
29. Blazso, M. and E. Jakab, Effect of metals, metal oxides, and carboxylates on the thermal decomposition processes of poly (vinyl chloride). *Journal of Analytical and Applied Pyrolysis*, 1999. 49(1-2): p. 125-143.
30. Zhang, B., et al., Thermogravimetric-mass spectrometric analysis of the reactions between oxide (ZnO, Fe<sub>2</sub>O<sub>3</sub> or ZnFe<sub>2</sub>O<sub>4</sub>) and polyvinyl chloride under inert atmosphere. *Materials Transactions, JIM*, 2000. 41(10): p. 1342-1350.
31. Sivalingam, G., R. Karthik, and G. Madras, Effect of metal oxides on thermal degradation of poly (vinyl acetate) and poly (vinyl chloride) and their blends. *Industrial & engineering chemistry research*, 2003. 42(16): p. 3647-3653.
32. Masuda, Y., et al., Pyrolysis study of poly (vinyl chloride)–metal oxide mixtures: quantitative product analysis and the chlorine fixing ability of metal oxides. *Journal of Analytical and Applied Pyrolysis*, 2006. 77(2): p. 159-168.
33. Lee, G.-S. and Y.J. Song, Recycling EAF dust by heat treatment with PVC. *Minerals engineering*, 2007. 20(8): p. 739-746.
34. Al-Harabsheh, M., et al., Leaching of valuable metals from electric arc furnace dust—Tetrabromobisphenol A pyrolysis residues. *Journal of Analytical and Applied Pyrolysis*, 2017. 125: p. 50-60.
35. Al-Harabsheh, M., S. Altarawneh, and M. Al-Omari, Selective dissolution of zinc and lead from electric arc furnace dust via oxidative thermolysis with polyvinyl chloride and water-leaching process. *Hydrometallurgy*, 2022: p. 105898.
36. Al-Harabsheh, M., S. Kingman, and I. Hamilton, Microwave treatment of electric arc furnace dust with tetrabromobisphenol A: dielectric characterization and pyrolysis-leaching. *Journal of Analytical and Applied Pyrolysis*, 2017. 128: p. 168-175.
37. Sun, J., W. Wang, and Q. Yue, Review on microwave-matter interaction fundamentals and efficient microwave-associated heating strategies. *Materials*, 2016. 9(4): p. 231.
38. El Khaled, D., et al., Microwave dielectric heating: Applications on metals processing. *Renewable and Sustainable Energy Reviews*, 2018. 82: p. 2880-2892.
39. Menéndez, J., et al., Microwave heating processes involving carbon materials. *Fuel Processing Technology*, 2010. 91(1): p. 1-8.

40. Jones, D.A., et al., Microwave heating applications in environmental engineering—a review. *Resources, conservation and recycling*, 2002. 34(2): p. 75-90.
41. Metaxas, A., Microwave Heating. *Power Engineering Journal*, 1991. 5: p. 237-247.
42. Haque, K.E., Microwave energy for mineral treatment processes—a brief review. *International journal of mineral processing*, 1999. 57(1): p. 1-24.
43. Al-Harabsheh, M., et al., The influence of microwaves on the leaching kinetics of chalcopyrite. *Minerals engineering*, 2005. 18(13-14): p. 1259-1268.
44. Metaxas, A.a. and R.J. Meredith, *Industrial microwave heating*. 1983: IET.
45. Schaefer, M.D., *Microwave tempering of shrimp with susceptors*. 1999, Virginia Tech.
46. Debye, P.J.W., *Polar molecules*. 1929: Chemical Catalog Company, Incorporated.
47. Altarawneh, S., et al., Microwave selective heating of electric arc furnace dust constituents toward sustainable recycling: Contribution of electric and magnetic fields. *Journal of Industrial and Engineering Chemistry*, 2021. 104: p. 521-528.
48. Galema, S.A., Microwave chemistry. *Chemical Society Reviews*, 1997. 26(3): p. 233-238.
49. Thostenson, E. and T.-W. Chou, *Microwave processing: fundamentals and applications*. *Composites Part A: Applied Science and Manufacturing*, 1999. 30(9): p. 1055-1071.
50. Bobicki, E., et al., High temperature permittivity measurements of selected industrially relevant ores: Review and analysis. *Minerals Engineering*, 2020. 145: p. 106055.
51. Fröhlich, H., Dielectric properties of dipolar solids. *Proceedings of the Royal Society of London. Series A. Mathematical and Physical Sciences*, 1946. 185(1003): p. 399-414.
52. Michael P áMingos, D., Tilden Lecture. Applications of microwave dielectric heating effects to synthetic problems in chemistry. *Chemical Society Reviews*, 1991. 20(1): p. 1-47.
53. Jonscher, A.K., Dielectric relaxation in solids. *Journal of Physics D: Applied Physics*, 1999. 32(14): p. R57.
54. Dobbs, E., *Electricity and magnetism*. 2013: Springer Science & Business Media.
55. Saini, S., et al., *Magnetism: a primer and review*. *American Journal of Roentgenology*, 1988. 150(4): p. 735-743.
56. Van der Zaag, P., P. Van der Valk, and M.T. Rekveldt, A domain size effect in the magnetic hysteresis of NiZn-ferrites. *Applied physics letters*, 1996. 69(19): p. 2927-2929.
57. Johnk, C.T.A., *Engineering electromagnetic fields and waves*. New York, 1975.
58. Cuenca, J.A., et al., Study of the magnetite to maghemite transition using microwave permittivity and permeability measurements. *Journal of Physics: Condensed Matter*, 2016. 28(10): p. 106002.
59. Al-Harabsheh, M., et al., Dielectric properties of Jordanian oil shales. *Fuel Processing Technology*, 2009. 90(10): p. 1259-1264.
60. Parkash, A., J. Vaid, and A. Mansingh, Measurement of dielectric parameters at microwave frequencies by cavity-perturbation technique. *IEEE Transactions on microwave theory and techniques*, 1979. 27(9): p. 791-795.
61. Vollmer, M., *Physics of the microwave oven*. *Physics Education*, 2004. 39(1): p. 74.
62. Meredith, R.J., *Engineers' handbook of industrial microwave heating*. 1998: Iet.
63. Adam, M.A., *Understanding microwave pyrolysis of biomass materials*. 2017, University of Nottingham.

64. Andrews, C.L., Standing electromagnetic waves. Selective experiments in physics, 1961.
65. Peng, Z., et al., Microwave penetration depth in materials with non-zero magnetic susceptibility. *ISIJ international*, 2010. 50(11): p. 1590-1596.
66. Birat, J.-P., et al., CO<sub>2</sub> emissions and the steel industry's available responses to the greenhouse effect. *REVUE DE METALLURGIE CAHIERS D INFORMATION TECHNIQUES*, 1999. 96: p. 1203-1216.
67. Aula, M., et al., Some environmental aspects of BF, EAF and BOF. 2012.
68. Madias, J., Electric Furnace Steelmaking, in *Treatise on Process Metallurgy*. 2014. p. 271-300.
69. Bowman, B., Performance comparison between AC and DC furnaces. *Steel Times International*, 1993. 17(3): p. 12.
70. Elizarov, K., et al., New trends in the development of dc arc furnaces. *Russian Metallurgy*, 2014. 2014(6): p. 443.
71. Andrei, H., C. Cepisca, and S. Grigorescu. Power quality and electrical arc furnaces. in *Power Quality*. 2011. IntechOpen.
72. Lauria, A.T. and L.J. Voisinet, Electric arc furnace component. 1984, Google Patents.
73. Dragna, E., A. Ioana, and N. Constantin. Methods of steel manufacturing-The electric arc furnace. in *IOP Conference Series: Materials Science and Engineering*. 2018. IOP Publishing.
74. Jones, J.A., B. Bowman, and P. Lefrank, Electric arc furnace steelmaking. *Steelmaking and Refining Volume*, The AIST Steel Foundation, Pittsburgh, PA, 1998.
75. Jack, N., F.W. Edward, and W. E.F, Steel. 2019, Encyclopædia Britannica, inc.
76. Gyllenram, R., W. WEI, and P. Jönsson. Raw material assessment for electric arc furnace steelmaking. in *6th International Congress on the Science and Technology of Steelmaking, ICS 2015, 12 May 2015 through 14 May 2015*. 2015. Chinese Society for Metals.
77. Li, C.-L. and M.-S. Tsai, Mechanism of spinel ferrite dust formation in electric arc furnace steelmaking. *ISIJ international*, 1993. 33(2): p. 284-290.
78. Birat, J., et al., Dust generation and recycling in the EAF, co-recycling of zinc and steel. *Journées Sidérurgiques Internationales ATS*, Paris, 1998.
79. Müller, K.T., L. Holappa, and D. Neuschütz, Control of ejections caused by bubble bursting in steelmaking processes. *steel research international*, 2003. 74(2): p. 61-69.
80. Guézennec, A., et al., Dust formation in electric arc furnace: Birth of the particles. *Powder Technology*, 2005. 157: p. 2-11.
81. Pickles, C., Thermodynamic modelling of the formation of zinc–manganese ferrite spinel in electric arc furnace dust. *Journal of hazardous materials*, 2010. 179(1-3): p. 309-317.
82. Wang, J.C., M.T. Hepworth, and K.J. Reid, Recovering Zn, Pb, Cd and Fe from electric furnace dust. *JOM*, 1990. 42(4): p. 42-45.
83. Huber, J., et al. The formation of EAF dust. in *58 th Electric Furnace Conference and 17 th Process Technology Conference*. 2000.
84. Ma, G. and A. Garbers-Craig, A review on the characteristics, formation mechanisms and treatment processes of Cr (VI)-containing pyrometallurgical wastes. *Journal of the Southern African Institute of Mining and Metallurgy*, 2006. 106(11): p. 753-763.
85. Morcali, M., et al., Carbothermic reduction of electric arc furnace dust and calcination of waelz oxide by semi-pilot scale rotary furnace. *Journal of Mining and Metallurgy B: Metallurgy*, 2012. 48(2): p. 173-184.

86. de Buzin, P.J.W.K., N.C. Heck, and A.C.F. Vilela, EAF dust: An overview on the influences of physical, chemical and mineral features in its recycling and waste incorporation routes. *Journal of materials research and technology*, 2017. 6(2): p. 194-202.
87. Yang, Q. and B. Gustafsson, Studies on dust recycling in the electric arc furnace at Uddeholm Tooling AB. *Scandinavian journal of metallurgy*, 2003. 32(3): p. 147-156.
88. López, F.A. and A. López-Delgado, Enhancement of electric arc furnace dust by recycling to electric arc furnace. *Journal of environmental engineering*, 2002. 128(12): p. 1169-1174.
89. A, L.F.L.-D., Enhancement of electric arc furnace dust by recycling to electric arc furnace. *Journal of Environmental Engineering. Journal of Environmental Engineering*, 2002: p. 1169–1174.
90. Sofilić, T., et al., Characterization of steel mill electric-arc furnace dust. *Journal of Hazardous Materials*, 2004. 109(1): p. 59-70.
91. Machado, J.G., et al., Chemical, physical, structural and morphological characterization of the electric arc furnace dust. *Journal of hazardous materials*, 2006. 136(3): p. 953-960.
92. Da Silva, M., et al., Characterisation of electric arc furnace dust generated during plain carbon steel production. *Ironmaking & Steelmaking*, 2008. 35(4): p. 315-320.
93. Sekula, R., et al., Electric arc furnace dust treatment: investigation on mechanical and magnetic separation methods. *Waste management & research*, 2001. 19(4): p. 271-275.
94. Menad, N., et al., Study of the presence of fluorine in the recycled fractions during carbothermal treatment of EAF dust. *Waste Management*, 2003. 23(6): p. 483-491.
95. Rizescu, C., et al., Characterisation of steel mill electric-arc furnace dust. *Advances in waste management*, 2010.
96. de Vargas, A.S., Â.B. Masuero, and A.C. Vilela, Investigations on the use of electric-arc furnace dust (EAFD) in Pozzolan-modified Portland cement I (MP) pastes. *Cement and Concrete research*, 2006. 36(10): p. 1833-1841.
97. Barreneche, C., et al., Development and characterization of new shape-stabilized phase change material (PCM)—Polymer including electrical arc furnace dust (EAFD), for acoustic and thermal comfort in buildings. *Energy and Buildings*, 2013. 61: p. 210-214.
98. Lanzerstorfer, C., Electric arc furnace (EAF) dust: Application of air classification for improved zinc enrichment in in-plant recycling. *Journal of Cleaner Production*, 2018. 174: p. 1-6.
99. Nyirenda, R.L., The processing of steelmaking flue-dust: A review. *Minerals Engineering*, 1991. 4(7): p. 1003-1025.
100. Jha, M.K., V. Kumar, and R.J. Singh, Review of hydrometallurgical recovery of zinc from industrial wastes. *Resources, Conservation and Recycling*, 2001. 33(1): p. 1-22.
101. C. Sikalidis, M. Mitraka, and R. Tsitouridou, Immobilization of electric arc furnacedust toxic elements within the matrix of concrete based products. *Global NEST*, 2010. 12(4): p. 368–373.
102. Dutra, A.J.B., P.R.P. Paiva, and L.M. Tavares, Alkaline leaching of zinc from electric arc furnace steel dust. *Minerals Engineering*, 2006. 19(5): p. 478-485.
103. Montenegro, V., et al., Hydrometallurgical treatment of steelmaking electric arc furnace dusts (EAFD). *Metallurgical and Materials Transactions B*, 2013. 44(5): p. 1058-1069.

104. Salihoglu, G. and V. Pinarli, Steel foundry electric arc furnace dust management: Stabilization by using lime and Portland cement. *Journal of hazardous materials*, 2008. 153(3): p. 1110-1116.
105. Keyser, N., et al. Characterization, recovery and recycling of Electric Arc Furnace dust. in *Symposium on Iron and Steel Pollution Abatement Technology*, Chicago. 1981.
106. Tsubouchi, N., et al., Chemical characterization of dust particles recovered from bag filters of electric arc furnaces for steelmaking: Some factors influencing the formation of hexachlorobenzene. *Journal of hazardous materials*, 2010. 183(1-3): p. 116-124.
107. Havlik, T., B. Friedrich, and S. Stopic, Pressure leaching of EAF dust with sulphuric acid. *Erzmetall*, 2004. 57(2): p. 83-90.
108. Zhang, D., et al., Selective leaching of zinc from electric arc furnace dust by a hydrothermal reduction method in a sodium hydroxide system. *Journal of cleaner production*, 2019. 224: p. 536-544.
109. Havlík, T., et al., Hydrometallurgical processing of carbon steel EAF dust. *Journal of Hazardous Materials*, 2006. 135(1): p. 311-318.
110. Miki, T., et al., Hydrometallurgical extraction of zinc from CaO treated EAF dust in ammonium chloride solution. *Journal of Hazardous Materials*, 2016. 302: p. 90-96.
111. Havlik, T., G. Maruskinova, and A. Miskufova, Determination of ZnO amount in electric arc furnace dust and temperature dependence of leaching in ammonium carbonate by using of X-ray diffraction. *Archives of Metallurgy and Materials*, 2018. 63.
112. Antrekowitsch, J., G. Rösler, and S. Steinacker, State of the art in steel mill dust recycling. *Chemie Ingenieur Technik*, 2015. 87(11): p. 1498-1503.
113. Antrekowitsch, J.r. 2004, *Montanuniversitaet Leoben*.
114. Ru`tten, J., *Proc. of the 3rd Seminar Networking between Zinc and Steel* (Ed: J. Harre). 2011: *Gesellschaft der Metallurgen und Bergleute e.V., Leoben*.
115. Lin, X., et al., Pyrometallurgical recycling of electric arc furnace dust. *Journal of Cleaner Production*, 2017. 149: p. 1079-1100.
116. Coronado, M., A. Andrés, and C. Cheeseman, Acid gas emissions from structural clay products containing secondary resources: foundry sand dust and Waelz slag. *Journal of Cleaner Production*, 2016. 115: p. 191-202.
117. Mager, K., U. Meurer, and J. Wirling, Minimizing dioxin and furan emissions during zinc dust recycle by the Waelz process. *JOM*, 2003. 55(8): p. 20-25.
118. Hansmann, T., et al., Primus- a new process for the recycling of by-products and the prereduktion of iron ore. *Stahl Eisen*, 2000. 120(11): p. 49-54.
119. Kurunov, I., Environmental aspects of industrial technologies for recycling sludge and dust that contain iron and zinc. *Metallurgist*, 2012. 55(9): p. 634-639.
120. Lu, W.-K. and D. Huang, Mechanisms of reduction of iron ore/coal agglomerates and scientific issues in RHF operations. *Mineral Processing Extractive Metall. Rev.*, 2003. 24(3-4): p. 293-324.
121. Wu, Y.-l., et al., Numerical simulation of the direct reduction of pellets in a rotary hearth furnace for zinc-containing metallurgical dust treatment. *International Journal of Minerals, Metallurgy, and Materials*, 2013. 20(7): p. 636-644.
122. Kuwauchi, Y. and M. Barati, A mathematical model for carbothermic reduction of dust-carbon composite agglomerates. *ISIJ international*, 2013. 53(6): p. 1097-1105.
123. Tsutsumi, H., S. Yoshida, and M. Tetsumoto, Features of fastmet process. *Kobelco technology review*, 2010. 12: p. 85-92.

124. Leclerc, N., E. Meux, and J.-M. Lecuire, Hydrometallurgical recovery of zinc and lead from electric arc furnace dust using mononitritotriacetate anion and hexahydrated ferric chloride. *Journal of Hazardous Materials*, 2002. 91(1): p. 257-270.
125. Palencia, I., et al., Recycling EAF dust leaching residue to the furnace: A simulation study. *JOM*, 1999. 51(8): p. 28-32.
126. Kukurugya, F., T. Vindt, and T. Havlík, Behavior of zinc, iron and calcium from electric arc furnace (EAF) dust in hydrometallurgical processing in sulfuric acid solutions: Thermodynamic and kinetic aspects. *Hydrometallurgy*, 2015. 154: p. 20-32.
127. Cruells, M., A. Roca, and C. Núnñez, Electric arc furnace flue dusts: characterization and leaching with sulphuric acid. *Hydrometallurgy*, 1992. 31(3): p. 213-231.
128. Teo, Y.Y., et al., Hydrometallurgical extraction of zinc and iron from electric arc furnace dust (EAFD) using hydrochloric acid. *Journal of Physical Science*, 2018. 29: p. 49-54.
129. Shawabkeh, R.A., Hydrometallurgical extraction of zinc from Jordanian electric arc furnace dust. *Hydrometallurgy*, 2010. 104(1): p. 61-65.
130. Yücel, T., et al., Hydrometallurgical Extraction of Zinc from EAF Dust in Nitric Acid Solution. 2018.
131. Youcai, Z. and R. Stanforth, Integrated hydrometallurgical process for production of zinc from electric arc furnace dust in alkaline medium. *Journal of Hazardous Materials*, 2000. 80(1-3): p. 223-240.
132. Orhan, G., Leaching and cementation of heavy metals from electric arc furnace dust in alkaline medium. *Hydrometallurgy*, 2005. 78(3): p. 236-245.
133. Palımağa, P., et al., Zinc recovery from steelmaking dust by hydrometallurgical methods. *Metals*, 2018. 8(7): p. 547.
134. Wang, H.-g., et al., A novel hydrothermal method for zinc extraction and separation from zinc ferrite and electric arc furnace dust. *International Journal of Minerals, Metallurgy, and Materials*, 2016. 23(2): p. 146-155.
135. Chairaksa-Fujimoto, R., et al., The selective alkaline leaching of zinc oxide from Electric Arc Furnace dust pre-treated with calcium oxide. *Hydrometallurgy*, 2016. 159: p. 120-125.
136. Nyirenda, R. and A. Lugtmeijer, Ammonium carbonate leaching of carbon steelmaking dust. Detoxification potential and economic feasibility of a conceptual process. *Minerals engineering*, 1993. 6(7): p. 785-797.
137. Zhou, Y., et al., Separation of ZnO from the stainless steelmaking dust and graphite mixture by microwave irradiation. *High Temperature Materials and Processes*, 2015. 34(2): p. 177-184.
138. Omran, M., T. Fabritius, and E.-P. Heikkinen, Selective Zinc Removal from Electric Arc Furnace (EAF) Dust by Using Microwave Heating. *Journal of Sustainable Metallurgy*, 2019. 5(3): p. 331-340.
139. Ye, Q., et al., Microwave-assisted reduction of electric arc furnace dust with biochar: an examination of transition of heating mechanism. *ACS Sustainable Chemistry & Engineering*, 2019.
140. Ye, Q., et al., Microwave-assisted self-reduction of EAF dust-biochar composite briquettes for production of direct reduced iron. *Powder Technology*, 2020. 362: p. 781-789.
141. Shah, A.C. and D.J. Poledna, Review of specialty PVC resins. *Journal of Vinyl and Additive Technology*, 2002. 8(3): p. 214-221.
142. Zhu, H., et al., TG-FTIR analysis of PVC thermal degradation and HCl removal. *Journal of analytical and applied pyrolysis*, 2008. 82(1): p. 1-9.

143. Zhao, P., et al., Fate of sodium and chlorine during the co-hydrothermal carbonization of high-alkali coal and polyvinyl chloride. *Fuel Processing Technology*, 2020. 199: p. 106277.
144. Huggett, C. and B.C. Levin, Toxicity of the pyrolysis and combustion products of poly (vinyl chlorides): A literature assessment. *Fire and materials*, 1987. 11(3): p. 131-142.
145. Fatima, S., Chemical recycle of plastic. *American Journal Engineering Research*, 2014. 3(11): p. 93-108.
146. Sherwood, J., Closed-loop recycling of polymers using solvents. *Johnson Matthey Technology Review*, 2020: p. 4-15.
147. Vandenhende, B. and J.-P. Dumont, Method for recycling a plastic material. 2001, Google Patents.
148. Kreißig, J., et al., PVC recovery options concept for environmental and economic system analysis. PE Europe GmbH, Leinfelden-Echterdingen, DE, 2003.
149. Matsuzawa, Y., et al., Evaluation of char fuel ratio in municipal pyrolysis waste. *Fuel*, 2004. 83(11): p. 1675-1687.
150. Martín-Gullón, I., M. Esperanza, and R. Font, Kinetic model for the pyrolysis and combustion of poly-(ethylene terephthalate) (PET). *Journal of Analytical and Applied Pyrolysis*, 2001. 58-59: p. 635-650.
151. Starnes, W.H., Structural and mechanistic aspects of the thermal degradation of poly(vinyl chloride). *Progress in Polymer Science*, 2002. 27(10): p. 2133-2170.
152. Sánchez-Jiménez, P.E., et al., Kinetic model for thermal dehydrochlorination of poly(vinyl chloride). *Polymer*, 2010. 51(17): p. 3998-4007.
153. Iván, B., Thermal stability, degradation, and stabilization mechanisms of poly (vinyl chloride). 1996, ACS Publications.
154. Minsker, K., Characteristic effects in degradation and stabilization of halogen-containing polymers. *International Journal of Polymeric Materials*, 1994. 24(1-4): p. 235-251.
155. Crawley, S. and I. McNeill, Preparation and degradation of head-to-head PVC. *Journal of Polymer Science: Polymer Chemistry Edition*, 1978. 16(10): p. 2593-2606.
156. Bacaloglu, R. and M. Fisch, Degradation and stabilization of poly (vinyl chloride). I. Kinetics of the thermal degradation of poly (vinyl chloride). *Polymer degradation and stability*, 1994. 45(3): p. 301-313.
157. Miranda, R., et al., Vacuum pyrolysis of PVC I. Kinetic study. *Polymer degradation and stability*, 1999. 64(1): p. 127-144.
158. Marcilla, A. and M. Beltrán, Thermogravimetric kinetic study of poly(vinyl chloride) pyrolysis. *Polymer Degradation and Stability*, 1995. 48(2): p. 219-229.
159. Basan, S. and O. Güven, A comparison of various isothermal thermogravimetric methods applied to the degradation of PVC. *Thermochimica acta*, 1986. 106: p. 169-178.
160. Oh, S.C., W.-T. Kwon, and S.-R. Kim, Dehydrochlorination characteristics of waste PVC wires by thermal decomposition. *Journal of Industrial and Engineering Chemistry*, 2009. 15(3): p. 438-441.
161. Levchik, S.V. and E.D. Weil, Overview of the recent literature on flame retardancy and smoke suppression in PVC. *Polymers for Advanced Technologies*, 2005. 16(10): p. 707-716.
162. Michell, E., True stabilization: A mechanism for the behavior of lead compounds and other primary stabilizers against PVC thermal dehydrochlorination. *Journal of Vinyl Technology*, 1986. 8(2): p. 55-65.
163. Braun, D. and R. Bender, *Eur. Polym. J., Suppl.* 1969.

164. Winkler, D., Mechanism of polyvinyl chloride degradation and stabilization. *Journal of Polymer Science*, 1959. 35(128): p. 3-16.
165. Rieche, A., A. Grimm, and H. Mücke, Untersuchungen über Stabilität von Suspensions-PVC. *Kunststoffe*, 1962. 52: p. 265-8.
166. Stromberg, I., R. Straus, S. and Achhammer, BG: *J. Polym. Sci*, 1959. 35: p. 355.
167. Kissinger, H.E., Reaction kinetics in differential thermal analysis. *Analytical chemistry*, 1957. 29(11): p. 1702-1706.
168. Friedman, H.L. Kinetics of thermal degradation of char-forming plastics from thermogravimetry. Application to a phenolic plastic. in *Journal of polymer science part C: polymer symposia*. 1964. Wiley Online Library.
169. Ozawa, T., A new method of analyzing thermogravimetric data. *Bulletin of the chemical society of Japan*, 1965. 38(11): p. 1881-1886.
170. Flynn, J.H. and L.A. Wall, General treatment of the thermogravimetry of polymers. *Journal of Research of the National Bureau of Standards. Section A, Physics and Chemistry*, 1966. 70(6): p. 487.
171. Akahira, T. and T. Sunose, Res. Report Chiba Inst. Technol. Sci. Technol, 1971. 16: p. 22.
172. Coats, A.W. and J. Redfern, Kinetic parameters from thermogravimetric data. *Nature*, 1964. 201(4914): p. 68-69.
173. Ahmad, Z. and W. Manzoor, Thermogravimetric analysis of ZnCl<sub>2</sub> catalyzed degradation of PVC. *Journal of thermal analysis*, 1992. 38(10): p. 2349-2357.
174. Baitz, M., et al., Life Cycle Assessment of PVC and of principal competing materials. PE Europe GmbH (Germany), Institut für Kunststoffkunde und Kunststoffprüfung (IKP)(Germany, Instituttet for Produktudvikling (IPU), DTU (Denmark), RANDA GROUP (Spain). Commissioned by the European Commission, 2004.
175. Iida, T. and K. Gotō, Investigations on poly(vinyl chloride). III. Effects of metal oxides upon thermal decomposition of poly(vinyl chloride). *Journal of Polymer Science: Polymer Chemistry Edition*, 1977. 15(10): p. 2427-2433.
176. Wang, S.-J., et al., Thermochemical reaction mechanism of lead oxide with poly(vinyl chloride) in waste thermal treatment. *Chemosphere*, 2014. 117: p. 353-359.
177. Uegaki, Y. and T. Nakagawa, Thermal dehydrochlorination of poly(vinyl chloride). I. Effect of iron oxide on the rate of dehydrochlorination. *Journal of Applied Polymer Science*, 1977. 21(4): p. 965-973.
178. Ye, L., T. Li, and L. Hong, Co-pyrolysis of Fe<sub>3</sub>O<sub>4</sub>-poly(vinyl chloride)(PVC) mixtures: Mitigation of chlorine emissions during PVC recycling. *Waste Management*, 2021. 126: p. 832-842.
179. Van Krevelen, D., C. Van Herden, and F. Hutjens, Kinetic study by thermogravimetry. *Fuel*, 1951. 30: p. 253-258.
180. Slapak, M.J.P., J.M.N. van Kasteren, and A.A.H. Drinkenburg, Determination of the pyrolytic degradation kinetics of virgin-PVC and PVC-waste by analytical and computational methods. *Computational and Theoretical Polymer Science*, 2000. 10(6): p. 481-489.
181. Hotta, M., M. Hayashi, and K. Nagata, High temperature measurement of complex permittivity and permeability of Fe<sub>3</sub>O<sub>4</sub> powders in the frequency range of 0.2 to 13.5 GHz. *ISIJ international*, 2011. 51(3): p. 491-497.
182. Meng, T.-T., et al., Comparing the effects of different metal oxides on low temperature decomposition of PVC. *Journal of Analytical and Applied Pyrolysis*, 2021. 159: p. 105312.

183. AlFannakh, H., Nonisothermal Kinetic Analysis and AC Conductivity for Polyvinyl Chloride (PVC)/Zinc Oxide (ZnO) Nanocomposite. *Advances in Polymer Technology*, 2020. 2020.
184. Altarawneh, S., et al., Thermal degradation kinetics of polyvinyl chloride in presence of zinc oxide. *Thermochimica Acta*, 2021: p. 179105.
185. Altarawneh, S., et al., Thermodynamic, pyrolytic, and kinetic investigation on the thermal decomposition of polyvinyl chloride in the presence of franklinite. *Process Safety and Environmental Protection*, 2022.
186. Starnes, W.H. and X. Ge, Mechanism of autocatalysis in the thermal dehydrochlorination of poly (vinyl chloride). *Macromolecules*, 2004. 37(2): p. 352-359.

## **Appendix 1: Microwave selective heating of electric arc furnace dust constituents toward sustainable recycling: contribution of electric and magnetic fields**

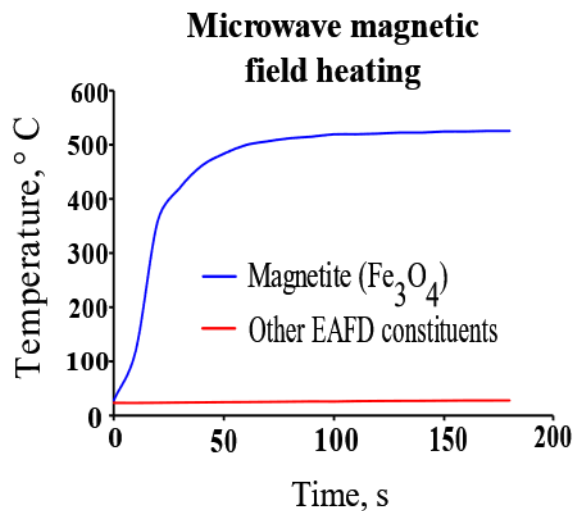
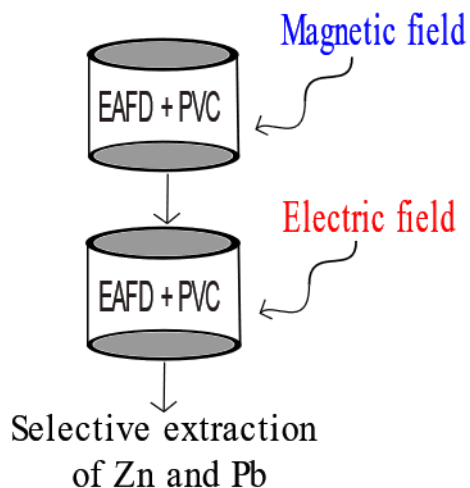
Sanad Altarawneh,<sup>1,\*</sup> Mohammad Al-Harabsheh,<sup>2</sup> Adam Buttress,<sup>1</sup> Chris Dodds,<sup>1</sup> Jose Rodriguez,<sup>1</sup> Sam Kingman,<sup>1</sup>

<sup>1</sup> Faculty of Engineering, University of Nottingham, Nottingham, NG7 2RD, UK

<sup>2</sup> Chemical Engineering Department, Jordan University of Science and Technology, Irbid, 22110, Jordan

### **Abstract**

Microwave heating of waste electric arc furnace dust (EAFD) for the purpose of its remediation has been studied extensively. However, these studies considered EAFD as a bulk material without addressing either the relative response of its individual constituents or the specific interactions with either the electric or magnetic fields of an electromagnetic wave. In this work, we present a study of the relative contribution of the electromagnetic wave components to the heating of EAFD constituents using separated electric and magnetic microwave fields. ZnO, ZnFe<sub>2</sub>O<sub>4</sub>, Fe<sub>3</sub>O<sub>4</sub>, and graphite were found to be the main contributors to the heating of EAFD based on their dielectric properties and heating profiles. ZnO and ZnFe<sub>2</sub>O<sub>4</sub> heated only in the electric field yielding temperatures of 846 and 720 °C after heating for 30 and 40 s, respectively at a power input of  $118 \pm 12$  W. Fe<sub>3</sub>O<sub>4</sub> and graphite, in contrast, heated in both electric and magnetic fields owing to their respective magnetic and conductive nature. It is suggested that the selective magnetic heating of Fe<sub>3</sub>O<sub>4</sub> has significant implications for the selective extraction of zinc and lead through thermal treatment of EAFD with halogenated plastics such as polyvinyl chloride (PVC).



Keywords: EAFD, Metal extraction, Dielectric properties, Magnetic hysteresis, Magnetite

\*corresponding author

Tel.: +447979038915

E-mail address: [sanad.altarawneh@nottingham.ac.uk](mailto:sanad.altarawneh@nottingham.ac.uk)

E-mail addresses of authors:

Mohammad Al-Harshseh: [msalharahsheh@just.edu.jo](mailto:msalharahsheh@just.edu.jo)

Adam Buttress: [ezzajb@exmail.nottingham.ac.uk](mailto:ezzajb@exmail.nottingham.ac.uk)

Chris Dodds: [enzcjd@exmail.nottingham.ac.uk](mailto:enzcjd@exmail.nottingham.ac.uk)

Jose Rodriguez: [ezzjr1@exmail.nottingham.ac.uk](mailto:ezzjr1@exmail.nottingham.ac.uk)

Sam Kingman: [enzsk@exmail.nottingham.ac.uk](mailto:enzsk@exmail.nottingham.ac.uk)

## 1. Introduction

Steel manufacturing is strongly linked to the economic development and growth [1]. The amount of crude steel produced globally per year in 1950 was 189 Mt, which increased to 850 Mt in 2000 and up to 1809 Mt in 2018; the share of electric arc furnaces (EAFs) amounts to 28% of the total production in 2018 [1]. During steel manufacturing, hazardous EAFD is generated in large amounts [2]. According to estimations, 15-20 kg of EAFD is emitted for every ton of recycled steel [3]. Most of the charge supplied to EAFs is steel scrap [4], and since most of the recycled steel is galvanised, high zinc concentrations are generally found in EAFD [5-8]. The high zinc content and the large accumulation rate render EAFD an attractive secondary source for zinc. Methods used for the utilisation of EAFD as a zinc source can be categorised into hydrometallurgical and pyrometallurgical [2]. While the hydrometallurgical methods are less energy intensive and more environmentally sound, this approach suffers from incomplete metallic extraction, harshness of the leaching medium, and the contamination of the leaching solutions with undesired metallic species [3, 9-12]. The pyrometallurgical approach, on the other hand, has found wider commercial application. The Waelz process, for instance, is the most commonly applied pyrometallurgical method for the treatment of EAFD [13]. According to estimates, 80% of the recycled dust is treated in the Waelz kiln [14]. In this kiln, EAFD is exposed to a high temperature carbothermic reduction where zinc is selectively volatilised, oxidised, and finally collected as ZnO. More recently, however, attention has been directed towards the thermal treatment of EAFD with halogenated plastics such as polyvinyl chloride (PVC) and tetrabromobisphenol A (TBBPA) [2, 8, 15-20]. In these studies, EAFD is reacted with the halogen acids generated from these plastics when heated up to temperatures of 200 – 300 °C, followed by water leaching of the resulting metal halides [8, 16]. A problem encountered in this approach, is the reaction of Fe<sub>3</sub>O<sub>4</sub> in EAFD with the halogen acids, leading to the formation of iron chloride/bromide, which is carried over to the final leaching solution

as  $\text{Fe}^{2+}$  and impairs the extraction of zinc at a high purity [16, 17, 21]. Since these techniques require significant heat addition, much work has been directed towards studying the use of microwave energy as a heating source for the treatment of EAFD [16, 17, 22-27]. Ye et al. [27, 28] reported the possibility of using microwaves for the carbothermic reduction of EAFD with biochar and identified the main heating mechanisms for the system. Zhou et al. [23] and Omran et al. [25] studied the microwave-assisted reduction of EAFD using graphite as a reducing agent, while Sun et al. [22] reported the effect of different carbon types for the reduction of EAFD. Al-Harashseh et al. [16, 17], measured the dielectric properties of EAFD and pyrolysed it with halogenated plastics for metal extraction using microwave energy as the heating source. In these studies, only the bulk temperature rise was considered when EAFD was microwave treated as a whole. The contribution of the individual component phases to the bulk temperature rise was not identified. The detailed knowledge of the relative response of each mineral phase to microwave energy can significantly improve the understanding of the underpinning mechanism of microwave-assisted recycling of EAFD. The presence of magnetic and electrically conductive species in EAFD has been reported in the literature [21, 29, 30]. Magnetite ( $\text{Fe}_3\text{O}_4$ ), a well-known iron bearing magnetic mineral, was reported in many studies to be present in appreciable amounts in EAFD [6, 21, 31, 32]. Al-Harashseh [21], reported that  $\text{Fe}_3\text{O}_4$  is present at a mass percentage of 10.4%, which in turn suggests that a different response of EAFD should be observed when placed in either magnetic or electric field components of a microwave cavity. In this work we seek to understand this fundamental concept, whereby microwaves are applied to high purity EAFD constituents in separated electric and magnetic microwave fields with a power input of  $118 \pm 12$  W. Dielectric characterisation of the individual mineral phases was undertaken. These properties were input into an electromagnetic model (COMSOL Multiphysics) of the microwave heating system, to enable the system to be

adjusted so the interaction of the minerals with either the magnetic or electric field component could be controlled.

The implication of the current work for the selective extraction of zinc and lead from EAFD through the thermal treatment with halogenated plastics was also assessed based on a previously conducted thermodynamics analysis by Al-Harabsheh [19, 21].

## 2. Microwave-matter interaction

### 2.1 Heating mechanisms

An electromagnetic wave can best be visualised in the form of a dual sinusoidal function carrying both electric and magnetic fields as seen in Figure 1.

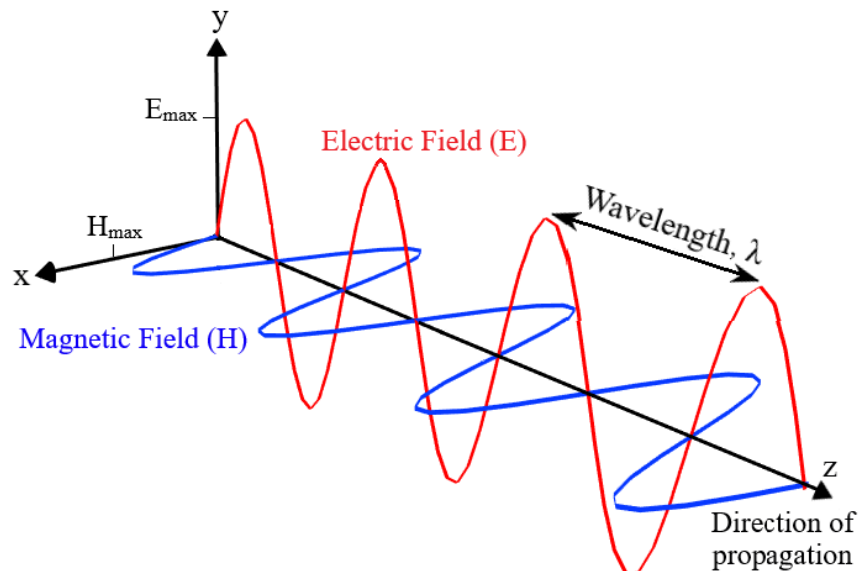


Figure 1. A schematic representation of a travelling electromagnetic wave.

The interaction of a material with microwaves causes either the electric or magnetic fields to be disturbed which ultimately depends on the nature of the material. Thus, the heating action of microwaves can be attributed to dielectric, magnetic, and conductive losses [33].

#### 2.1.1 Dipolar polarisation loss

Materials with permanent molecular dipoles heat by the dipolar polarisation mechanism due to their interaction with the electric field component of microwaves [34]. Quantitatively, the material's response to the electric field is usually represented by the dielectric constant ( $\epsilon'$ ) and the loss factor ( $\epsilon''$ ) of the material. The former represents the ability of the material to store energy as charge polarisation, while the latter represents the ability of the material to dissipate this energy as heat [34-36]. Both are expressed in terms of the complex dielectric constant ( $\epsilon$ ) as follows [37]:

$$\epsilon = \epsilon' - j \epsilon'' \quad (1)$$

Where  $j = \sqrt{-1}$ . The power dissipated in the material as heat shows a direct dependency on the imaginary part of the complex dielectric constant of the material [38]:

$$\text{Power} = \omega \cdot \epsilon'' \cdot \epsilon_0 E_{\text{rms}}^2 \quad (2)$$

Where  $\omega$  is the angular frequency of microwaves,  $\epsilon_0$  is the permittivity of free space,  $E_{\text{rms}}$  is the root mean square of the intensity of the microwave electric field.

### 2.1.2 Magnetic hysteresis loss

Similar to dielectrics, an external alternating magnetic field interacts with the magnetic dipoles present in magnetic materials which makes them oscillate as well [39]. Since the domains in magnetic materials become permanently magnetised in a certain direction [40], a magnetic field in the opposite direction is needed in order to demagnetise and eventually magnetise in the opposite direction, forming a magnetisation hysteresis loop. The amount of energy dissipated in the material is directly related to the area enclosed in the hysteresis loop [41]. Likewise, a complex magnetic permeability can be defined for magnetic materials [42]:

$$\mu = \mu' - j \mu'' \quad (3)$$

Where  $\mu'$  is a measure of the ability of the material to store magnetic energy in the form of magnetisation (magnetic polarisation) and  $\mu''$  is its ability to dissipate this energy as heat. The power dissipated in the magnetic field is primarily related to the imaginary part of permeability as follows [38]:

$$\text{Power} = \omega \cdot \mu'' \cdot \mu_0 H_{\text{rms}}^2 \quad (4)$$

Where  $\mu_0$  is the permeability of free space and  $H_{\text{rms}}$  is the root mean square of the intensity of the microwave magnetic field.

### 2.1.3 Electric field conductive loss

Translational motion of charge in the form of electrons or ions also contribute significantly to microwave heating. When a conductive material is exposed to microwaves, the electric field drives the free charge through the material resulting in resistive heating [42-45]. The conduction loss factor and the power dissipated per unit volume of the material are given by:

$$\epsilon''_{\text{conduction}} = \frac{\sigma}{\omega\epsilon_0} \quad (5)$$

$$\text{Power} = \sigma \cdot E_{\text{rms}}^2 \quad (6)$$

Where  $\sigma$  is the electrical conductivity of the material.

#### 2.1.4 Magnetic field conductive loss

The alternating nature of the magnetic field in microwaves produces an electromotive force (emf) in conductive materials (Faraday's law). This emf pushes an electric current through the material resulting in resistive heating. If the material is solid and not hollow, densely packed currents form which are referred to as eddy currents. The power dissipated in a conductive solid disc due to eddy currents is given as [46]:

$$\text{Power} = \frac{\pi}{256} D^4 \cdot h \cdot \frac{B_0^2 \omega^2}{\rho} \quad (7)$$

Where  $D$  is the diameter of the disc,  $h$  is the disc thickness,  $B_0$  is the intensity of the magnetic flux, and  $\rho$  is the electrical resistivity of the material.

### 3. Experimental work

#### 3.1 Materials

All materials used in this work were of high purity. ZnO, Fe<sub>2</sub>O<sub>3</sub>, PbO, C, and CaCO<sub>3</sub> were purchased from Fisher Scientific with purities > 99.99% except for CaCO<sub>3</sub> which was at 99.95%. Fe<sub>3</sub>O<sub>4</sub> and SiO<sub>2</sub>, were purchased from Sigma-Aldrich with purities of 99.99 and 99.995%, respectively. Finally, ZnFe<sub>2</sub>O<sub>4</sub> was purchased from Alpha Aesar with a purity  $\geq$  99%.

#### 3.2 Cavity perturbation measurements

The cavity perturbation technique was used for measuring the dielectric properties [42, 47]. A schematic diagram of the apparatus is presented in Figure 2.

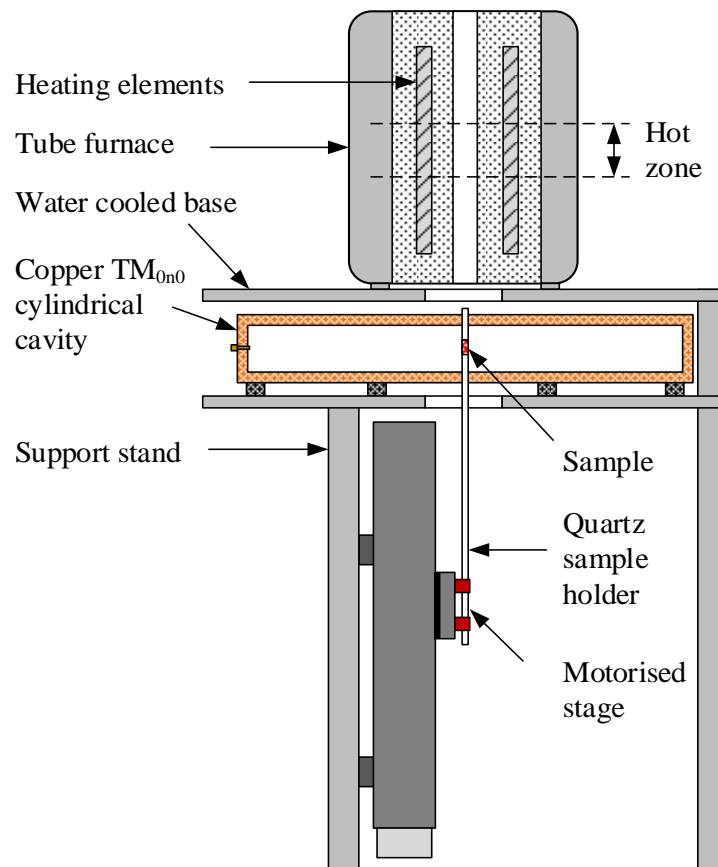


Figure 2. Schematic diagram of the cavity perturbation apparatus.

A quartz sample holder with an internal diameter of 4 mm was used. Before measuring the properties of the powders, the effect of the empty tube was first measured and subtracted later. A specified mass of powder sample was loaded inside the tube and was packed to a specific height, so that samples with similar bulk density can be reproduced. The sample holder was then mounted on a motorised stage which elevates the sample to an electrically controlled furnace to adjust the temperature of the sample (Figure 2). Once the desired temperature was reached, the sample was held at that temperature for 8 – 10 min, to ensure homogeneity of the temperature inside the sample. The motorised stage then immediately lowers the sample into the cylindrical copper cavity, where the dielectric properties of the sample are derived from the change in the resonance frequency and the quality factor (with and without the sample).

Measurements were performed in the temperature range of 25 – 1100 °C at frequencies of 2.47 GHz and 912/910 MHz. Dielectric properties extracted at 2.47 GHz were important for understanding the heating behaviour and for the building of the electromagnetic simulation of the heating setup. Moreover, these frequencies were used since they fall within the range of the allocated frequency bands for Industrial, Scientific, and Medical purposes (ISM). Materials that were prone to oxidation such as Fe<sub>3</sub>O<sub>4</sub> were purged through the lower portion of the quartz sample holder with 99.9992 % pure N<sub>2</sub> at ~ 10 mL/min. Since N<sub>2</sub> gas contains trace amounts of O<sub>2</sub>, it was initially passed through a sacrificial Fe<sub>3</sub>O<sub>4</sub> sample which scrubbed the purging gas completely from O<sub>2</sub> traces. Powders were analysed using X-Ray Diffraction (XRD) technique before and after the measurements.

### 3.3 Microwave electric and magnetic field heating

#### 3.3.1 Rectangular waveguide and TE<sub>10</sub> cavity

A straight aluminium rectangular waveguide connected to a TE<sub>10</sub> cavity with a height and width of 43 and 86 mm was used for the heating trials. A schematic diagram of the setup is shown in Figure 3.

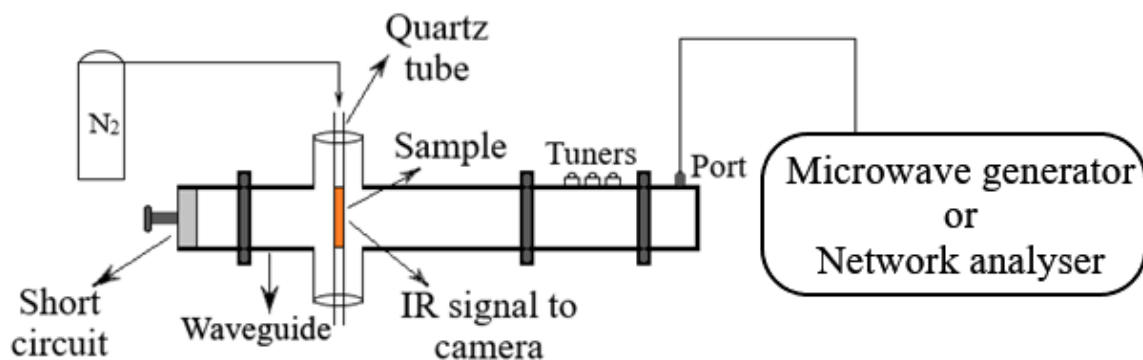


Figure 3. Schematic diagram of the experimental setup for the electric and magnetic heating.

In a TE<sub>10</sub> cavity, the microwave electric field is polarised parallel to the height of the sample (Figure 4), while the magnetic field rotates in circles around the electric field. The distribution of the microwave fields inside the cavity is presented in Figure 4 in the form of green lines.

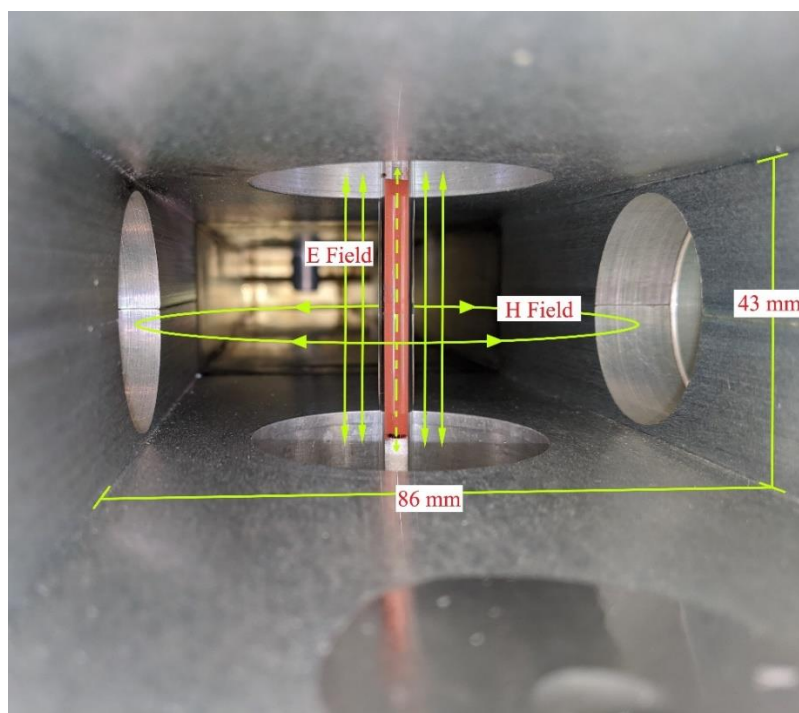


Figure 4. Vertical positioning of hematite ( $\text{Fe}_2\text{O}_3$ ) sample inside a  $\text{TE}_{10}$  cavity; green lines show the distribution of the electric (E) and magnetic (H) fields.

In the case shown in Figure 4, the electric field passes through the sample, while the magnetic field does not, and hence, electric field interaction with the sample is at a maximum. As the short circuit is moved away from the sample (Figure 3), the circular magnetic field lines will start passing through the sample, penetrating it from the side at an angle of  $90^\circ$ , with the electric field shifted away. At this point, heating via the magnetic component of the microwaves dominates.

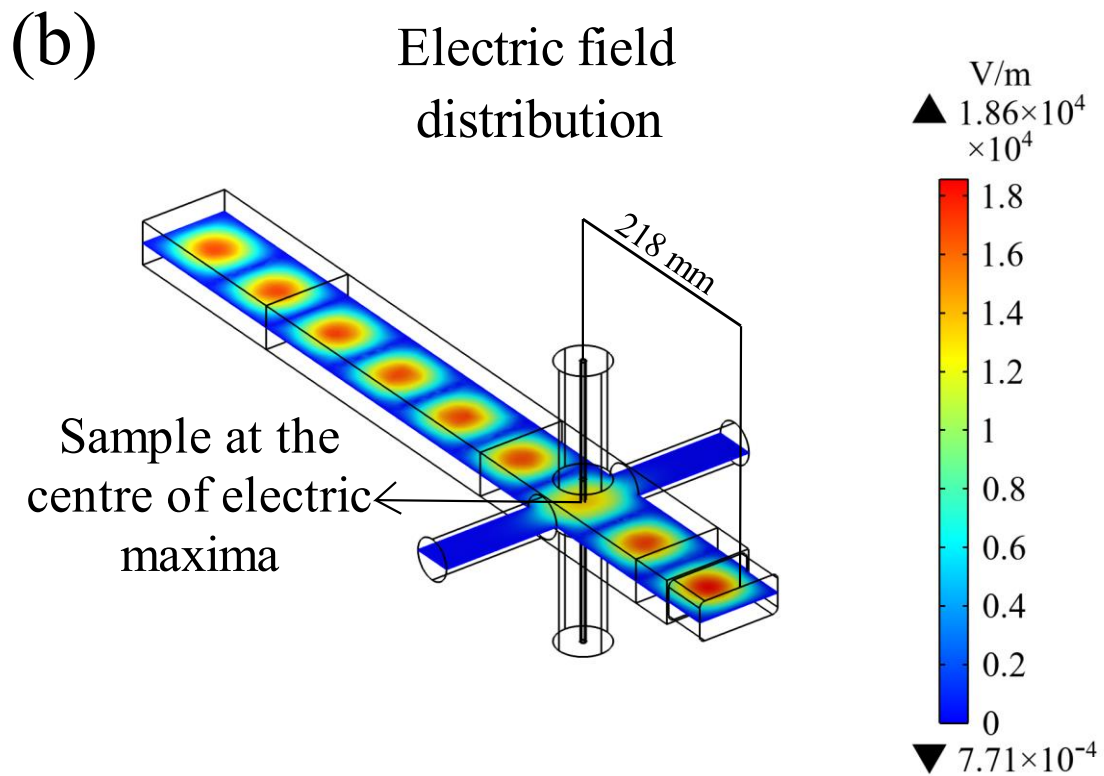
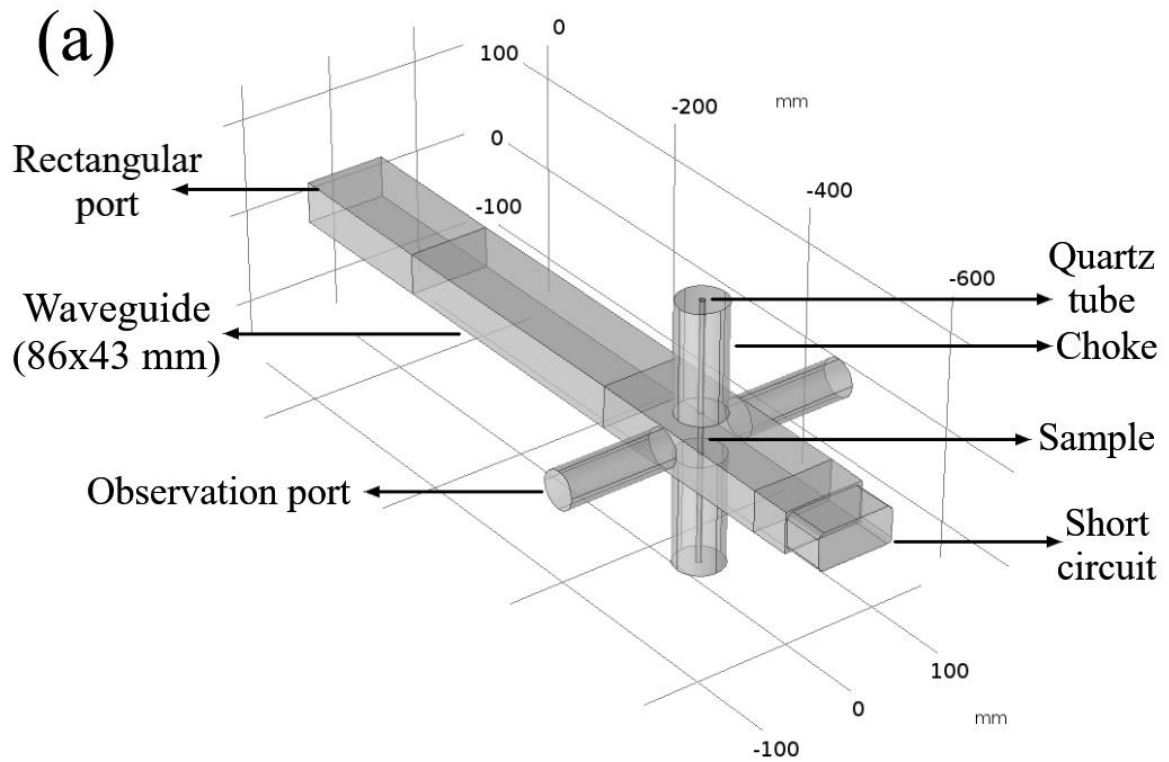
### 3.3.2 Sample size consideration and heating procedure

Samples were loaded in powder form in a quartz tube with an internal diameter of 4 mm as shown in Figure 4. Since the maximum intensities of the electric and magnetic fields for a 2.47 GHz standing guided wave are theoretically separated by a distance of  $\sim 43$  mm, using a small sample size was crucial to reduce the interference between the electric and the magnetic fields (i.e., to expose the sample to one field at a time). The quartz tube was vertically fixed through the chokes by means of guide bungs which allowed accurate positioning of the sample through the centre of the cavity at an angle of  $90^\circ$  with respect to horizontal.

An electromagnetic model of the heating setup was constructed on COMSOL Multiphysics, based on the measured dimensions of the cavity to confirm the positions of the electric and magnetic fields within the waveguide. The position of the short circuit in the model was adjusted until it gave either maximum electric or magnetic field within the sample. To confirm the reliability of the model, a vector network analyser (Agilent E5071C) was connected from the port side (Figure 3) to measure the degree of power absorption in each case. For the heating tests, a microwave generator (SAIREM Miniflow 200SS) was connected through a N-Type port using a coaxial transmission line. The power deposited into the waveguide during the heating tests was  $118 \pm 12$  W at a frequency of 2.47 GHz. Through the observation port (left hole in Figure 4), a thermal Infra-Red camera (NEC Avio H2640) was used to measure the surface temperature of the sample with the emissivity set at 0.75. Samples that are prone to oxidation (graphite and  $\text{Fe}_3\text{O}_4$ ) were purged with 99.9992% pure  $\text{N}_2$  for at least 10 min., after which the flow was shut off and heating was started.

### 3.3.3 Electromagnetic simulation

Figure 5 shows the components of the heating setup on COMSOL Multiphysics software and the distribution of the electric and magnetic fields inside the waveguide.



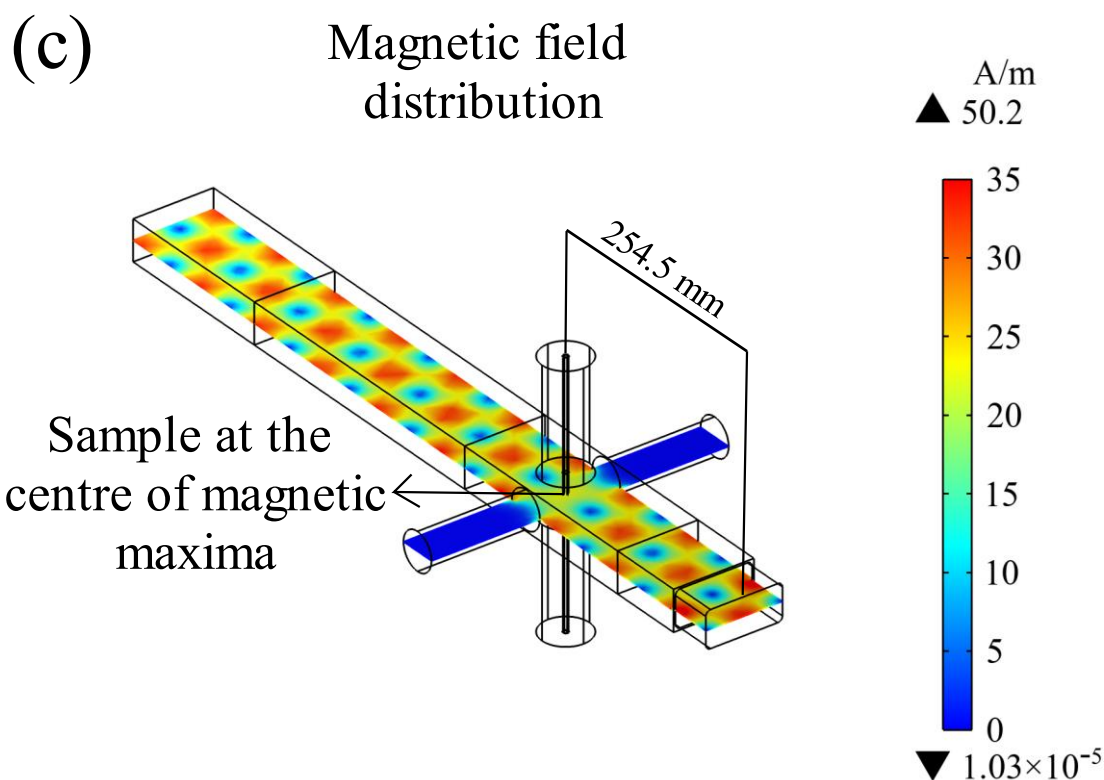


Figure 5. COMSOL Multiphysics simulation of the components of the heating setup (a) and the distribution of the electric (b) and magnetic (c) microwave fields at different short circuit positions at a power level of 130 W.

The maximum field intensity (either electric or magnetic) passing through the sample relies principally on the distance between the sample and the short circuit. The shifts in the short circuit position in Figure 5 (b) and (c) were adapted in the experiment and based on this simulation the experimental heating behaviour was studied. In highly lossy materials (e.g., graphite) slight variation to short circuit shift was introduced (refer to supplementary material Table S1 for more details).

### 3.4 X-Ray Diffraction analysis

XRD analysis was carried out for solid samples after cavity perturbation measurements and also after electric and magnetic heating experiments. A Bruker D8 Advance with a LYNXEYE 2D detector and a Cu  $k\alpha$  radiation source was used for this analysis. The instrument was operated at a current and voltage of 40 mA and 40 kV, respectively. Data interpretation was performed using QualX 2.0 software [48].

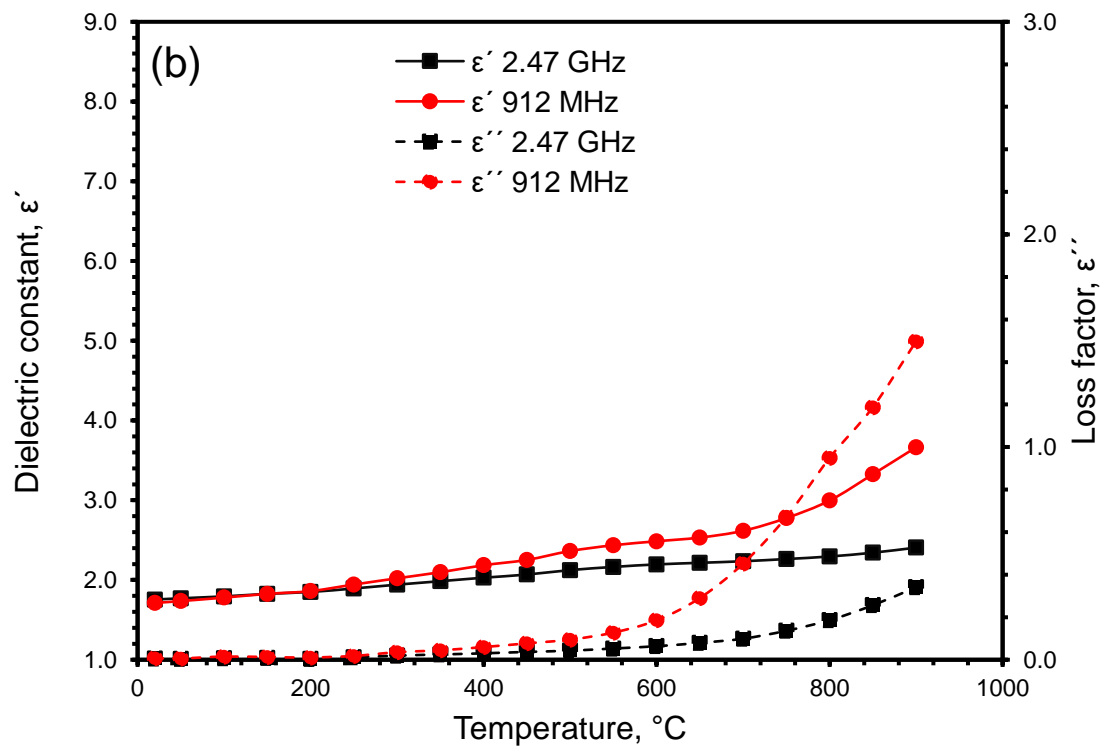
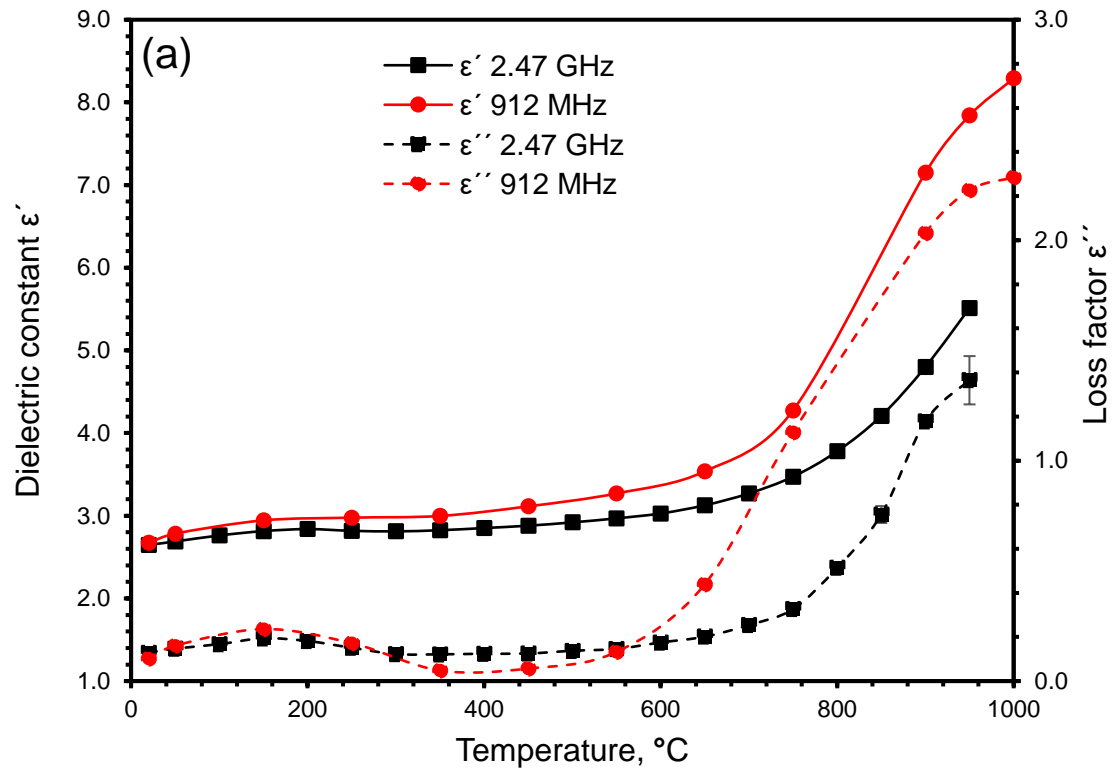
### **3.5 Laser diffraction analysis**

The performance of microwave heating is known to be affected by the particle size of the material [49]. Hence, the particle sizes of the powders used in this work were measured and are presented in Table 1. Beckman Coulter LS13320MW laser diffraction analyser with Aqueous Liquid Module (ALM) was used for the measurements of the particle size.

## **4. Results and Discussion**

### **4.1 Dielectric characterisation**

The dielectric properties of ZnO, Fe<sub>2</sub>O<sub>3</sub>, and ZnFe<sub>2</sub>O<sub>4</sub> are presented in Figure 6. The behaviour of the dielectric properties of ZnO, Fe<sub>2</sub>O<sub>3</sub>, and ZnFe<sub>2</sub>O<sub>4</sub> is very similar. Both the dielectric constant and the loss factor remain at values close to those seen at room temperature until temperatures of 600 – 700 °C. Above these temperatures, a sharp increase is observed. The variations in the dielectric properties may be attributed to the effect of temperature on the crystal lattice and the polarisability of molecules. The increase in the dielectric constant may be assigned to the increase in the crystal lattice spacing at high temperatures [42]. Consequently, more electron cloud deformation can be achieved [42]. The increase in lattice spacing also grants the ions forming the crystal broader potentials and more movement becomes attainable [42].



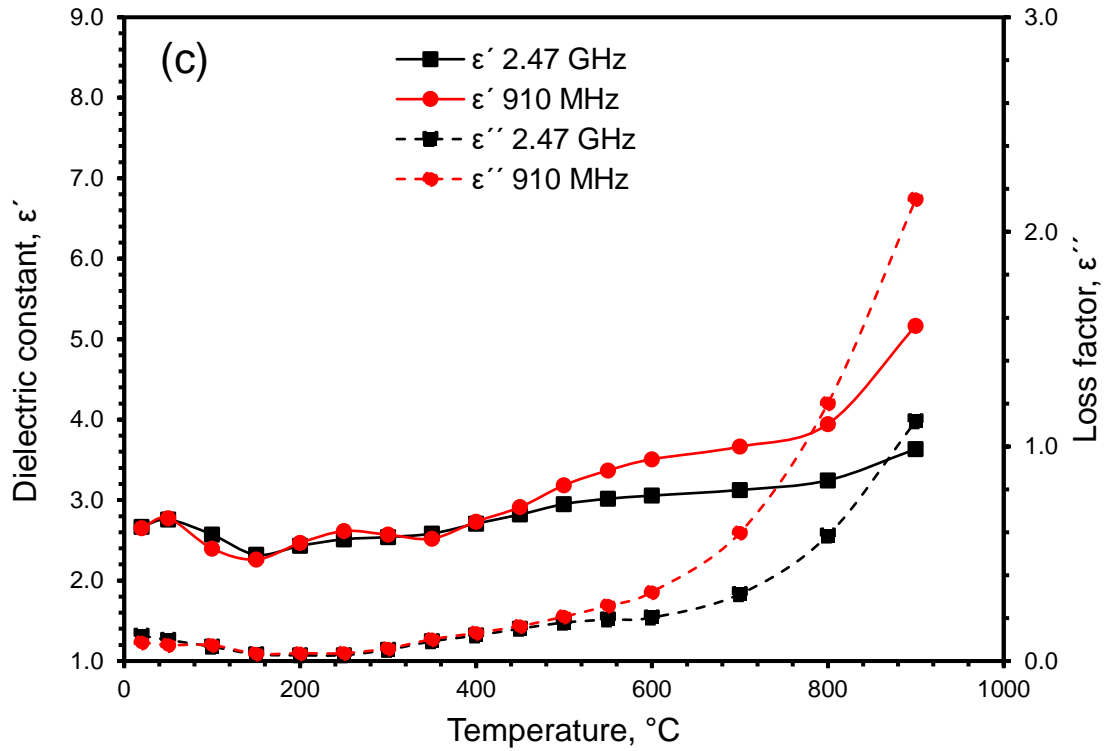


Figure 6. Dielectric properties profiles as a function of temperature at frequencies of 2.47 GHz and 912/910 MHz for (a) ZnO with a density of 1.89 g/cm<sup>3</sup>, (b) Fe<sub>2</sub>O<sub>3</sub> with a density of 0.58 g/cm<sup>3</sup> and (c) ZnFe<sub>2</sub>O<sub>4</sub> with density of 1.09 g/cm<sup>3</sup>.

The behaviour seen in Figure 6, can be understood by considering the effect of temperature on the relaxation time of dipoles in the sample. A relaxation time is defined as the time needed for a dipole to change orientation from one equilibrium position to another. For that, the potential double well theorem [34] was used in which the relaxation time  $\tau_o$  is related to an activation energy  $U_a$  [34]. This activation energy resembles the energy barrier that must be overcome in order to polarise a dipole from one equiprobable position to another in materials where the intermolecular interactions are significant (e.g., solids). The relation is written as follows [34]:

$$\tau_o = \frac{U_a}{e^{k_b T}} \left[ \frac{\epsilon_s + 2}{\epsilon_\infty + 2} \right] \quad (8)$$

Where,  $k_b$  is Boltzmann constant, T is absolute temperature,  $1/v$  is the time for a single oscillation in the potential well, and  $\epsilon_s$  and  $\epsilon_\infty$  are dielectric constant at static and very high frequency, respectively. In Equation 8, increasing the temperature, lowers the value of the term

“ $\frac{U_a}{k_b T}$ ” which decreases the relaxation time. As the relaxation time drops, more molecules are able to follow the rapid electric field oscillations, thus enhancing the extent of polarisation, which in turn, increases the value of the dielectric constant.

Table 1: Particle size of the powders used in this work.

Material	Mean particle size <sup>a</sup> , $\mu\text{m}$
ZnO	$466.2 \pm 25.4$
ZnFe <sub>2</sub> O <sub>4</sub>	$13.2 \pm 4.2$
Fe <sub>2</sub> O <sub>3</sub>	$36.6 \pm 4.8$
Fe <sub>3</sub> O <sub>4</sub>	$31.7 \pm 5.0$
SiO <sub>2</sub>	$224.5 \pm 7.6$
PbO	$101.1 \pm 6.7$
CaCO <sub>3</sub>	$3.3 \pm 0.05$
Graphite	$60.8 \pm 1.1$

a: Mean  $\pm$  SD.

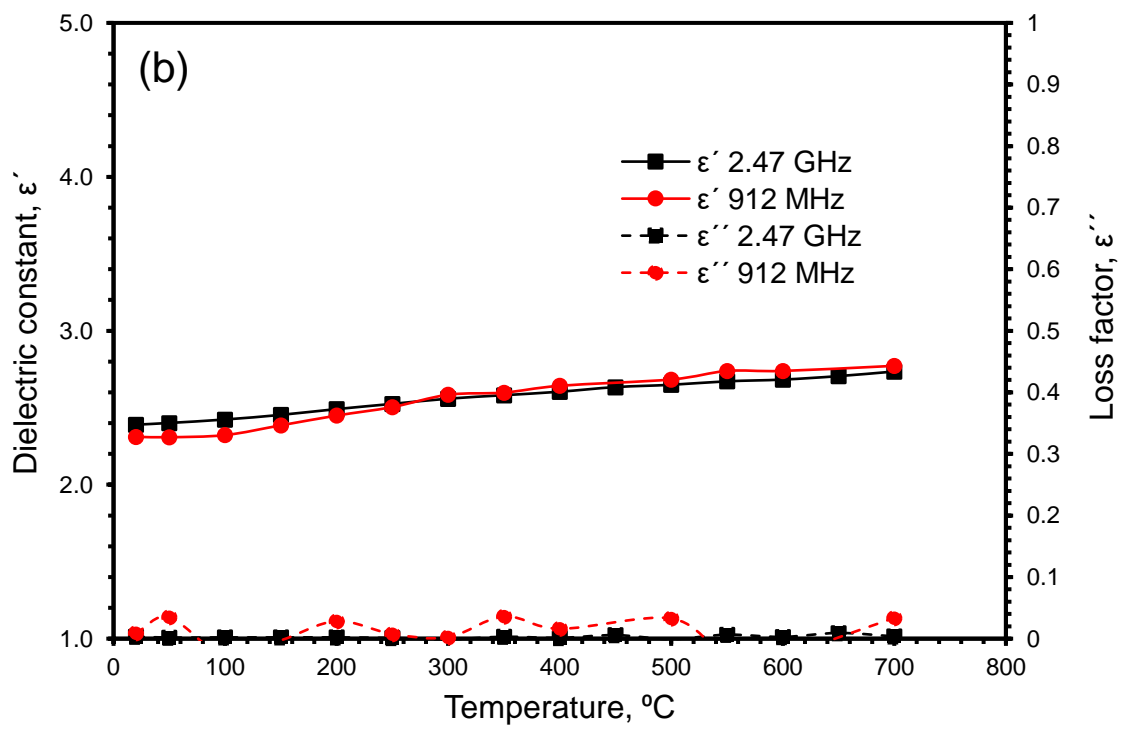
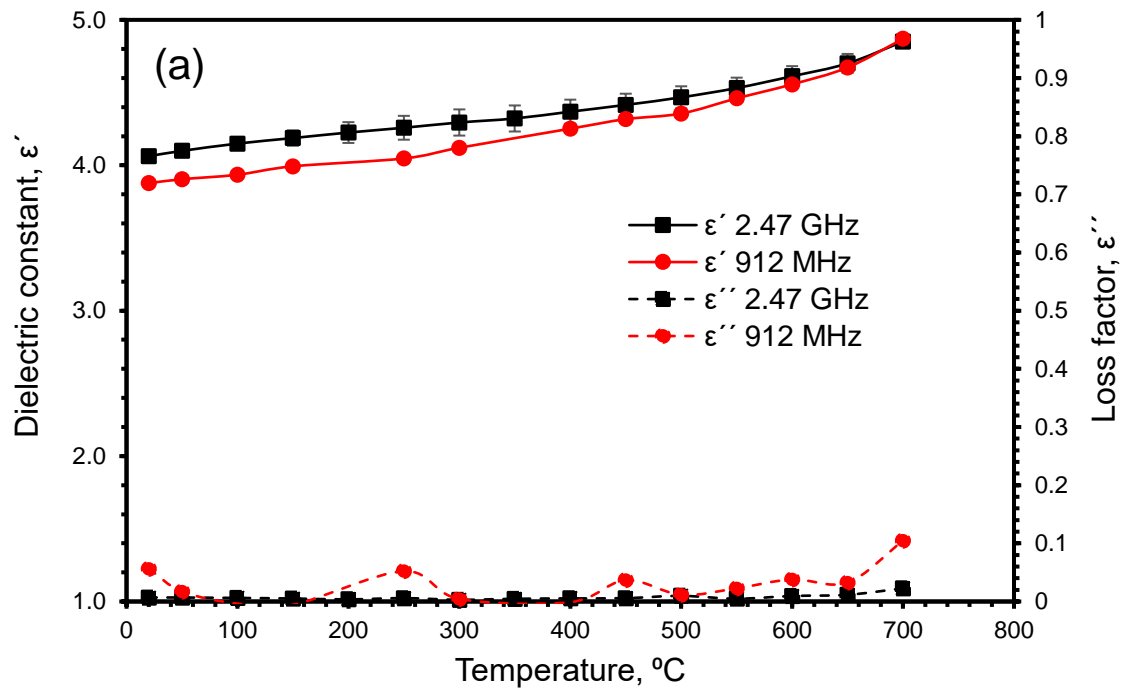
The loss factor, in contrast, increases with a sharper slope. Such behaviour is attributed to the increase in the electrical conductivity at high temperatures [42]. The loss factor presented in Figure 6 is the “effective loss factor” which lumps the contribution from different microwave-matter interaction phenomena which in our case may be given as:

$$\varepsilon''_{\text{effective}} = \overbrace{\varepsilon''_{\text{conduction}}^1} + \overbrace{\varepsilon''_{\text{polarisation}}^2} \quad (9)$$

Where term 1 represents the contribution of electrical conductivity to the loss factor, while term 2 represents the contribution of dipolar polarisation. When crystalline solids are heated to high temperatures, lattice defects are formed under the action of thermal excitation which results in the formation of vacancies through which ionic conduction occurs under the influence of an external electric field [50]. Thus, the increase in the effective loss factor is mainly attributed to the increase in the conduction loss factor due to the increase in electrical conductivity at high temperatures (Equation 5). This point can further be emphasised by understanding the behaviour of the loss factor at different frequencies. At temperatures above 700 °C, the loss factor at 912/910 MHz is always greater than that at 2.47 GHz as seen in Figure

6. This is attributed to the inverse dependency of the conduction loss factor on the frequency of the radiation (Equation 5). The large difference in loss factor between 2.47 GHz and 912/910 MHz is only clearly seen at high temperatures where the electrical conduction contribution to the loss factor becomes significant. Since ZnO and ZnFe<sub>2</sub>O<sub>4</sub> have relatively high loss factor at room temperature, dipolar polarisation might be assigned as the heating mechanism initially, followed by conduction loss at high temperatures.

Figure 7 represents the dielectric properties for PbO, SiO<sub>2</sub>, and CaCO<sub>3</sub>. The dielectric constant increases steadily from room temperature for all of them. The transformation of CaCO<sub>3</sub> into CaO in the temperature range 600 – 700 °C did not affect either the dielectric constant or the loss factor. PbO, on the other hand, shows a slight increase in the slope of the dielectric constant and loss factor at 650 °C which maybe regarded to the softening of the material (melting point is 888 °C). In general, however, the loss factor for all these materials does not show any significant increase and remains very close to zero at all temperatures. Comparing the data in Figures 7 and 6, it can be concluded that PbO, SiO<sub>2</sub>, and CaCO<sub>3</sub> are expected to make the lowest contribution to the overall microwave heating of EAFD, while both ZnO and ZnFe<sub>2</sub>O<sub>4</sub> can be classified as part of the major contributors to bulk heating. Fe<sub>2</sub>O<sub>3</sub> might start contributing significantly to heating at temperatures above 600 °C.



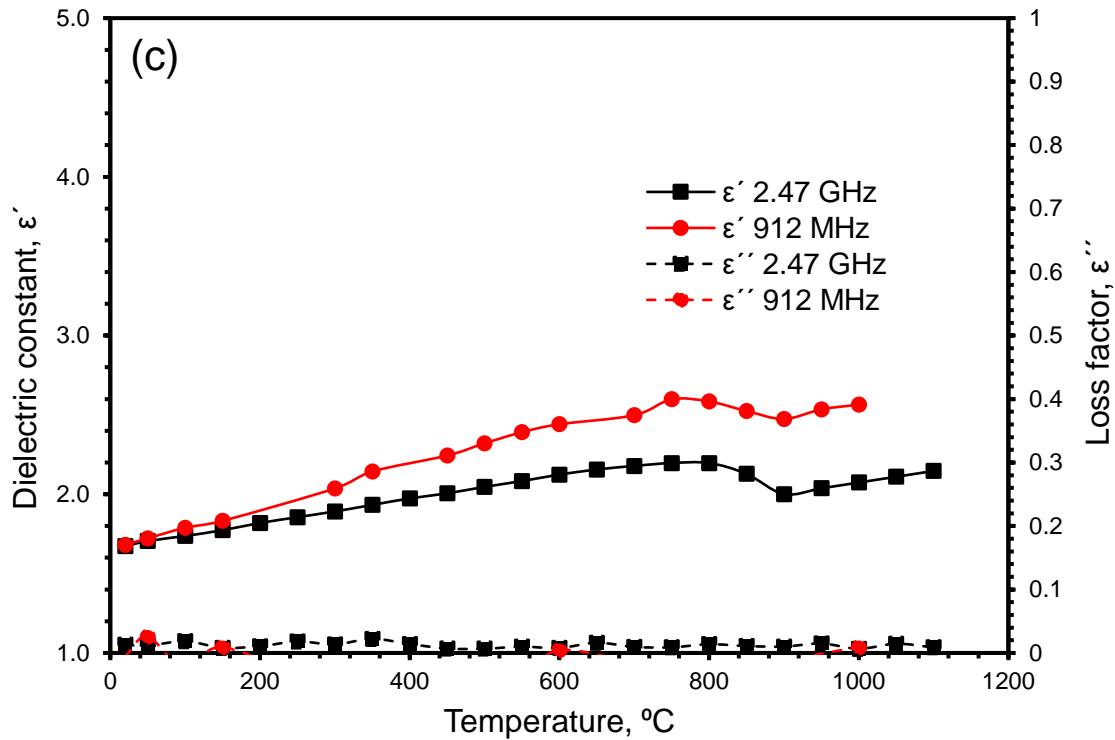


Figure 7. Dielectric properties profiles as a function of temperature at frequencies of 2.47 GHz and 912 MHz for (a) PbO with a density of 3.55 g/cm<sup>3</sup>, (b) SiO<sub>2</sub> with a density of 1.50 g/cm<sup>3</sup> and (c) CaCO<sub>3</sub> with density of 0.50 g/cm<sup>3</sup>.

Figure 8 shows the dielectric properties of Fe<sub>3</sub>O<sub>4</sub> as a function of temperature at frequencies of 2.47 GHz and 910 MHz. The dielectric constant and the loss factor profiles show a unique behaviour for a solid since they follow the Debye theory of relaxation. The only difference is that Figure 8 shows the dielectric properties against temperature rather than frequency. The theory suggested by Debye, however, should still hold based on the qualitative shape of the curve and quantitative data obtained from it. At low temperatures, the material has a high relaxation time, which prohibits any form of polarisation thus yielding relatively low dielectric constant and loss factor. As the temperature increases (~ 100 °C), polarisation commences, leading to an increase in both the dielectric constant and the loss factor. With further temperature increase (~300 °C), the relaxation time becomes very short, and the polarisation vector stops lagging the electric field. At that point, the loss factor drops and the dielectric constant plateaus. Quantitatively, substituting the values of  $\epsilon_s$  and  $\epsilon_\infty$  (Figure 8) in the

following equation:  $\epsilon''_{max} = \frac{\epsilon_s - \epsilon_\infty}{2}$  which is extracted from Debye model, produces theoretical maximum loss factor values very close to those reported from the experiment; theoretical values are 2.53 and 2.24, while experimental values (Figure 8) are 2.56 and 2.15 at 2.47 GHz and 910 MHz, respectively. The relatively high loss factor seen for Fe<sub>3</sub>O<sub>4</sub> compared with other EAFD constituents might be explained by the relatively high dc electrical conductivity reported in Miles et al. [51] for the material. This suggests that heating of Fe<sub>3</sub>O<sub>4</sub> in the electric field can be attributed to dipolar polarisation and conduction loss mechanisms simultaneously and a maximum heating rate should be expected to be around 150 and 200 °C at frequencies of 910 MHz and 2.47 GHz, respectively.

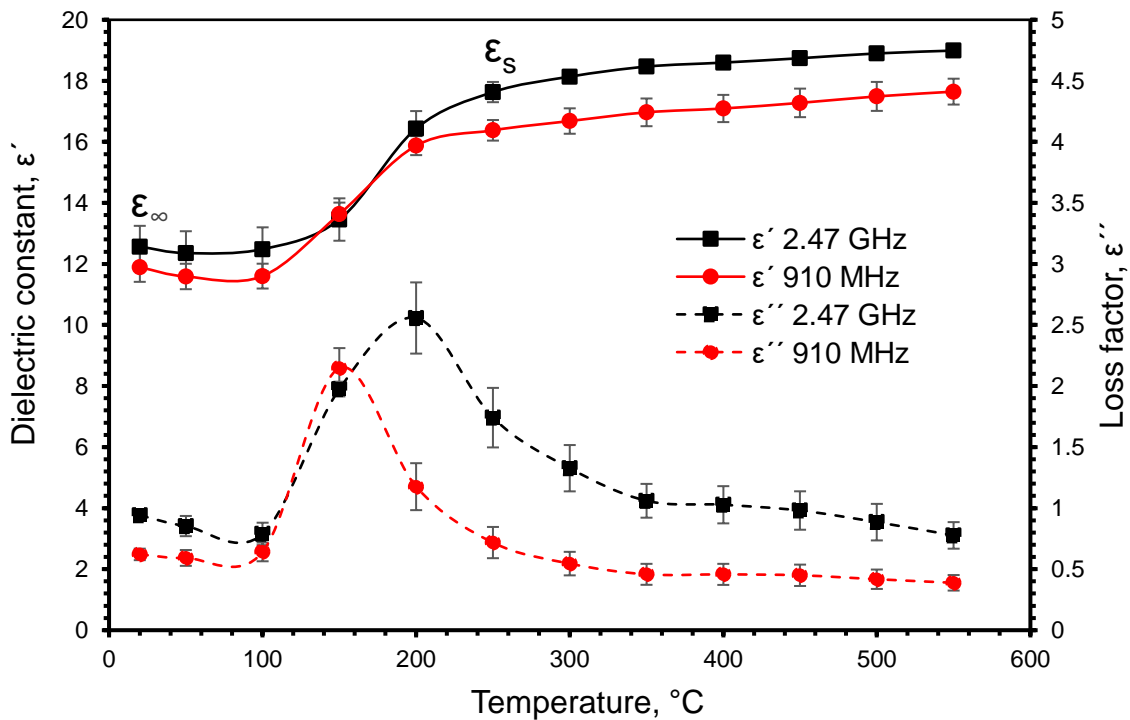


Figure 8. Dielectric properties profiles as a function of temperature for Fe<sub>3</sub>O<sub>4</sub> at frequencies of 2.47 GHz and 910 MHz and a bulk density of  $1.01 \pm 0.012$  g/cm<sup>3</sup>.

#### 4.2 Microwave electric and magnetic heating

Table 2 shows the heating rates and temperatures of EAFD constituents when exposed to pure electric and magnetic microwave fields at a frequency of 2.47 GHz and a power input of  $118 \pm 12$  W. Heating profiles are in Figure S3 in the supplementary material.

Table 2: Microwave heating under the influence of pure electric and magnetic microwave fields at a frequency of 2.47 GHz and a power input of  $118 \pm 12$  W.

Material	Electric Field			Magnetic Field		
	Heating rate °C/s <sup>a</sup>	Heating time, s	Temperature, °C	Heating rate °C/s <sup>a</sup>	Heating time, s	Temperature, °C
ZnO	37.1	30	846	No heating	No heating	No heating
ZnFe <sub>2</sub> O <sub>4</sub>	16.8	40	720	No heating	No heating	No heating
Fe <sub>2</sub> O <sub>3</sub>	1.65	210	180	No heating	No heating	No heating
Fe <sub>3</sub> O <sub>4</sub>	10.8	70	374	16.5	70	506
PbO	0.20	360	50	No heating	No heating	No heating
SiO <sub>2</sub>	0.43	360	51	No heating	No heating	No heating
CaCO <sub>3</sub>	2.31	150	168	No heating	No heating	No heating
C (graphite)	46.2	30	1026	18.2	70	560

a: Heating rate at first 20 seconds of heating.

The major contributors to the heating of EAFD are ZnO, ZnFe<sub>2</sub>O<sub>4</sub>, Fe<sub>3</sub>O<sub>4</sub>, and graphite having heating rates of 37.1, 16.8, 10.8, and 46.2 °C/s when heated in the electric field. Such result is directly related to their high loss factors reported earlier (Figures 6 and 8). This result also agrees with the high dielectric properties ( $\epsilon' = 26$  and  $\epsilon'' = 11$ ) reported for graphite in Hotta et al. [52]. PbO, SiO<sub>2</sub>, CaCO<sub>3</sub>, and Fe<sub>2</sub>O<sub>3</sub> all exhibited very low heating rates and final temperatures (especially PbO and SiO<sub>2</sub>) which is in agreement with the low loss factor values determined for these materials (Figures 6 and 7), rendering them the poorest contributors to EAFD microwave heating.

The most important feature in Table 2, however, is the distinctive response of Fe<sub>3</sub>O<sub>4</sub> and graphite to the microwave magnetic field. Both Fe<sub>3</sub>O<sub>4</sub> and graphite showed high heating rates of 16.5 and 18.2 °C/s, respectively, in the magnetic field, while the other constituents did not heat at all. This behaviour is attributed to the magnetic and electrically conductive nature of Fe<sub>3</sub>O<sub>4</sub> and graphite, respectively. Heating of Fe<sub>3</sub>O<sub>4</sub> can be attributed to magnetic hysteresis loss

mechanism up to the curie temperature, while heating of graphite can be assigned to eddy currents formed in alternating magnetic fields. An attempt was made to heat  $\text{Fe}_3\text{O}_4$  above its curie temperature ( $580\text{ }^\circ\text{C}$ ) by setting the microwave generator to its highest power output of  $155 \pm 12\text{ W}$ . A temperature of  $594\text{ }^\circ\text{C}$  was achieved in 60 s and up to  $606\text{ }^\circ\text{C}$  in 180 s; both are above the curie point. Despite the loss of magnetism of  $\text{Fe}_3\text{O}_4$  at  $580\text{ }^\circ\text{C}$ , the sample was able to be heated  $26\text{ }^\circ\text{C}$  above its curie temperature. This behaviour might be explained by the relatively high electrical conductivity of  $\text{Fe}_3\text{O}_4$  since the material has a band gap of  $0.1\text{ eV}$  [53]. With such a small energy barrier between valence and conduction bands, significant electrical currents might form in the sample when exposed to external alternating magnetic fields. Exceeding the curie temperature might thus be assigned to the formation of eddy currents in the sample which causes Joule heating.

#### **4.3 Magnetic heating and the selective extraction of Zn and Pb**

In previous works, Al-Harashsheh et al. [19, 21] reported the significance of  $\text{Fe}_3\text{O}_4$  elimination from EAFD on the selective extraction of zinc and lead upon the thermal treatment with halogenated plastics such as PVC and TBBPA. The elimination of  $\text{Fe}_3\text{O}_4$  is meant to be through oxidising it to its higher oxidation state and more stable phase  $\text{Fe}_2\text{O}_3$  [21]. The thermodynamics reported in these works provide a good insight to the spontaneity of chlorination/bromination of iron bearing compounds [19, 21]. Figure 9 shows the change in the Gibbs free energy of  $\text{ZnO}$ ,  $\text{PbO}$ ,  $\text{Fe}_3\text{O}_4$ , and  $\text{Fe}_2\text{O}_3$  chlorination and the oxidation of  $\text{Fe}_3\text{O}_4$  into  $\text{Fe}_2\text{O}_3$  [21].

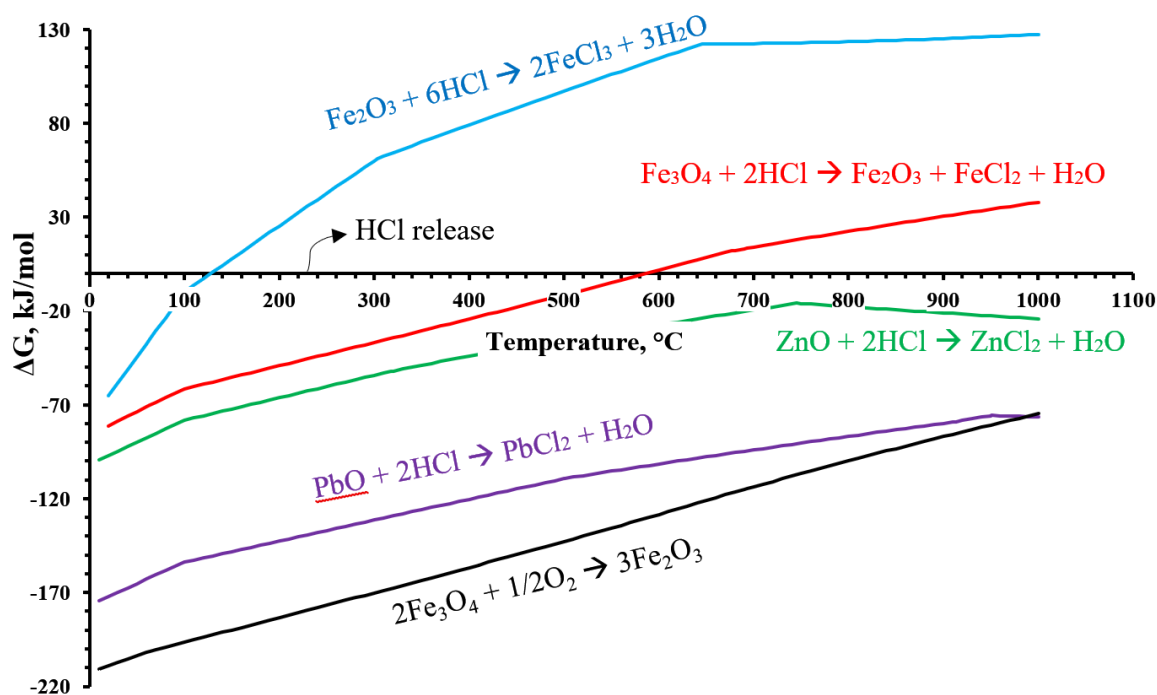


Figure 9. Change in Gibbs free energy of the main reactions of EAFD constituents with PVC decomposition product (HCl) using FACT SAGE software package [21].

The decomposition of PVC occurs at  $\sim 230$  °C as reported in Al-Harashseh et al. [2] after which approximately 58.3% of the polymer mass is transformed into gaseous HCl. The chlorination of both ZnO and PbO by HCl are thermodynamically favourable, resulting in the formation of water leachable chlorides ( $\text{ZnCl}_2$  and  $\text{PbCl}_2$ ). However, the chlorination of  $\text{Fe}_3\text{O}_4$  is also thermodynamically possible in the temperature window 0 – 580 °C, yielding soluble  $\text{FeCl}_2$  during water leaching step. To prevent the chlorination of  $\text{Fe}_3\text{O}_4$ , it must be oxidised to  $\text{Fe}_2\text{O}_3$ .  $\text{Fe}_2\text{O}_3$  is impervious to chlorination and its reaction with HCl has  $\Delta G$  values higher than zero above 120 °C. The kinetics of  $\text{Fe}_3\text{O}_4$  oxidation, however, are known to be strongly temperature dependent [54, 55], such that increasing the temperature increases the reaction rate. Hence, efficient elimination of  $\text{Fe}_3\text{O}_4$  can only be achieved at elevated temperatures. The utilisation of the microwave magnetic field allows targeting  $\text{Fe}_3\text{O}_4$  alone without heating the other constituents.  $\text{Fe}_3\text{O}_4$  can be heated selectively and oxidised efficiently (fast kinetics) to  $\text{Fe}_2\text{O}_3$  prior to any polymer decomposition into gaseous HCl. In contrast, using microwave electric field will heat up the entire EAFD-PVC mixture which causes the polymer to degrade

before appreciable oxidation of  $\text{Fe}_3\text{O}_4$  has taken place. This can negatively impact the extraction selectivity of other valuable metals such as zinc and lead.

The selective magnetic heating of  $\text{Fe}_3\text{O}_4$  present in appreciable quantities in EAFD, in presence of  $\text{O}_2$ , will potentially contribute to more effective and sustainable recycling for this hazardous waste. Further investigation, however, is required to examine the implication of the reported results toward selective separation of zinc and lead from EAFD.

## 5. Conclusions

Dielectric characterisation and microwave heating of the main EAFD constituents in isolated electric and magnetic fields was carried out in this work. The main findings are the following:

- In the electric field maxima, ZnO, ZnFe<sub>2</sub>O<sub>4</sub>, Fe<sub>3</sub>O<sub>4</sub>, and graphite were found to be the main contributors to the microwave heating of EAFD, while Fe<sub>2</sub>O<sub>3</sub>, CaCO<sub>3</sub>, SiO<sub>2</sub>, and PbO were found to be the minor contributors to the overall heating (especially SiO<sub>2</sub> and PbO).
- The selective heating of Fe<sub>3</sub>O<sub>4</sub> can be achieved by exposing it to a microwave magnetic field. Magnetic hysteresis loss mechanism is believed to be the source of heating up to the curie temperature (580 °C) above which eddy currents due to relatively high electrical conductivity are believed to be the source of heating.
- At temperatures above 600 °C, conduction loss becomes the dominant heating mechanism for the heating of ZnO, ZnFe<sub>2</sub>O<sub>4</sub>, and Fe<sub>2</sub>O<sub>3</sub> as evident from their measured dielectric properties.

## Acknowledgement

This work was supported by the Advanced Materials Research Group (AMRG)/Faculty of Engineering/University of Nottingham.

The authors would like to thank Teresa Needham from the Geography department at the University of Nottingham for conducting the particle size measurements.

## References

1. Association, W.S., Steel Facts. A collection of amazing facts about steel. Worldsteel. 2018.
2. Al-Harashseh, M., et al., Pyrolysis of poly(vinyl chloride) and—electric arc furnacedust mixtures. *Journal of Hazardous Materials*, 2015. 299: p. 425-436.
3. Oustadakis, P., et al., Hydrometallurgical process for zinc recovery from electric arc furnace dust (EAFD): Part I: Characterization and leaching by diluted sulphuric acid. *Journal of Hazardous Materials*, 2010. 179(1–3): p. 1-7.
4. Madias, J., Electric Furnace Steelmaking, in *Treatise on Process Metallurgy*. 2014. p. 271-300.
5. Xia, D. and C. Picklesi, Microwave caustic leaching of electric arc furnace dust. *Minerals Engineering*, 2000. 13(1): p. 79-94.
6. Tsubouchi, N., et al., Chemical characterization of dust particles recovered from bag filters of electric arc furnaces for steelmaking: Some factors influencing the formation of hexachlorobenzene. *Journal of hazardous materials*, 2010. 183(1-3): p. 116-124.
7. Montenegro, V., et al., Hydrometallurgical treatment of steelmaking electric arc furnace dusts (EAFD). *Metallurgical and Materials Transactions B*, 2013. 44(5): p. 1058-1069.
8. Al-Harashseh, M., et al., Leaching of valuable metals from electric arc furnace dust—Tetrabromobisphenol A pyrolysis residues. *Journal of Analytical and Applied Pyrolysis*, 2017. 125: p. 50-60.
9. Havlik, T., et al., Atmospheric leaching of EAF dust with diluted sulphuric acid. *Hydrometallurgy*, 2005. 77(1–2): p. 41-50.
10. Dutra, A.J.B., P.R.P. Paiva, and L.M. Tavares, Alkaline leaching of zinc from electric arc furnace steel dust. *Minerals Engineering*, 2006. 19(5): p. 478-485.
11. Al-Makhadmeh, L.A., et al., The Effectiveness of Zn Leaching from EAFD Using Caustic Soda. *Water, Air, & Soil Pollution*, 2018. 229(2): p. 33.
12. Teo, Y.Y., et al., Hydrometallurgical extraction of zinc and iron from electric arc furnace dust (EAFD) using hydrochloric acid. *Journal of Physical Science*, 2018. 29: p. 49-54.
13. Morcali, M., et al., Carbothermic reduction of electric arc furnace dust and calcination of waelz oxide by semi-pilot scale rotary furnace. *Journal of Mining and Metallurgy B: Metallurgy*, 2012. 48(2): p. 173-184.
14. Suetens, T., et al., Comparison of electric arc furnace dust treatment technologies using exergy efficiency. *Journal of cleaner production*, 2014. 65: p. 152-167.
15. Lee, G.-S. and Y.J. Song, Recycling EAF dust by heat treatment with PVC. *Minerals engineering*, 2007. 20(8): p. 739-746.
16. Al-harashseh, M., et al., Microwave treatment of electric arc furnace dust with PVC: Dielectric characterization and pyrolysis-leaching. *Journal of Hazardous Materials*, 2014. 274: p. 87-97.
17. Al-harashseh, M., S. Kingman, and I. Hamilton, Microwave treatment of electric arc furnace dust with Tetrabromobisphenol A: Dielectric characterization and pyrolysis-leaching. *Journal of Analytical and Applied Pyrolysis*, 2017. 128: p. 168-175.
18. Al-Harashseh, M., et al., Treatments of electric arc furnace dust and halogenated plastic wastes: A review. *Journal of Environmental Chemical Engineering*, 2018: p. 102856.
19. Al-Harashseh, M. and M. Altarawneh, Thermodynamic analysis on the oxidative pyrolytic treatment of electric arc furnace Dust–TBBA blends. *Oxidation of Metals*, 2018: p. 1-28.

20. Al-Harashseh, M., et al., Bromine fixing ability of electric arc furnace dust during thermal degradation of tetrabromobisphenol: Experimental and thermodynamic analysis study. *Journal of analytical and applied pyrolysis*, 2018. 134: p. 503-509.
21. Al-Harashseh, M., Thermodynamic Analysis on the Thermal Treatment of Electric Arc Furnace Dust-PVC Blends. *Arabian Journal for Science and Engineering*, 2017: p. 1-13.
22. Sun, X., J.-Y. Hwang, and X. Huang, The microwave processing of electric arc furnace dust. *Jom*, 2008. 60(10): p. 35-39.
23. Zhou, Y., et al., Separation of ZnO from the stainless steelmaking dust and graphite mixture by microwave irradiation. *High Temperature Materials and Processes*, 2015. 34(2): p. 177-184.
24. Omran, M., et al., Dielectric properties and carbothermic reduction of zinc oxide and zinc ferrite by microwave heating. *Royal Society Open Science*, 2017. 4(9): p. 170710.
25. Omran, M., T. Fabritius, and E.-P. Heikkinen, Selective Zinc Removal from Electric Arc Furnace (EAF) Dust by Using Microwave Heating. *Journal of Sustainable Metallurgy*, 2019. 5(3): p. 331-340.
26. Ye, Q., et al., Microwave-assisted reduction of electric arc furnace dust with biochar: an examination of transition of heating mechanism. *ACS Sustainable Chemistry & Engineering*, 2019. 7(10): p. 9515-9524.
27. Ye, Q., et al., Microwave-assisted self-reduction of EAF dust-biochar composite briquettes for production of direct reduced iron. *Powder Technology*, 2020. 362: p. 781-789.
28. Ye, Q., et al., Microwave-assisted reduction of electric arc furnace dust with biochar: an examination of transition of heating mechanism. *ACS Sustainable Chemistry & Engineering*, 2019.
29. Cruells, M., A. Roca, and C. Núnñez, Electric arc furnace flue dusts: characterization and leaching with sulphuric acid. *Hydrometallurgy*, 1992. 31(3): p. 213-231.
30. Sekula, R., et al., Electric arc furnace dust treatment: investigation on mechanical and magnetic separation methods. *Waste management & research*, 2001. 19(4): p. 271-275.
31. Sofilić, T., et al., Characterization of steel mill electric-arc furnace dust. *Journal of Hazardous Materials*, 2004. 109(1-3): p. 59-70.
32. de Vargas, A.S., Â.B. Masuero, and A.C. Vilela, Investigations on the use of electric-arc furnace dust (EAFD) in Pozzolan-modified Portland cement I (MP) pastes. *Cement and Concrete research*, 2006. 36(10): p. 1833-1841.
33. Sun, J., W. Wang, and Q. Yue, Review on microwave-matter interaction fundamentals and efficient microwave-associated heating strategies. *Materials*, 2016. 9(4): p. 231.
34. Metaxas, A.a. and R.J. Meredith, *Industrial microwave heating*. 1983: IET.
35. Galema, S.A., Microwave chemistry. *Chemical Society Reviews*, 1997. 26(3): p. 233-238.
36. Thostenson, E. and T.-W. Chou, Microwave processing: fundamentals and applications. *Composites Part A: Applied Science and Manufacturing*, 1999. 30(9): p. 1055-1071.
37. Kingman, S., Recent developments in microwave processing of minerals. *International materials reviews*, 2006. 51(1): p. 1-12.
38. Rosa, R., P. Veronesi, and C. Leonelli, A review on combustion synthesis intensification by means of microwave energy. *Chemical Engineering and Processing: Process Intensification*, 2013. 71: p. 2-18.

39. Haimbaugh, R., Theory of heating by induction. Practical Induction Heat Treating, 2001: p. 5-11.
40. Saini, S., et al., Magnetism: a primer and review. American Journal of Roentgenology, 1988. 150(4): p. 735-743.
41. Van der Zaag, P., P. Van der Valk, and M.T. Rekveldt, A domain size effect in the magnetic hysteresis of NiZn-ferrites. Applied physics letters, 1996. 69(19): p. 2927-2929.
42. Bobicki, E., et al., High temperature permittivity measurements of selected industrially relevant ores: Review and analysis. Minerals Engineering, 2020. 145: p. 106055.
43. Gabriel, C., et al., Dielectric parameters relevant to microwave dielectric heating. Chemical Society Reviews, 1998. 27(3): p. 213-224.
44. Al-Harashseh, M. and S. Kingman, Microwave-assisted leaching—a review. Hydrometallurgy, 2004. 73(3-4): p. 189-203.
45. Horikoshi, S., T. Sumi, and N. Serpone, Unusual effect of the magnetic field component of the microwave radiation on aqueous electrolyte solutions. Journal of Microwave Power and Electromagnetic Energy, 2012. 46(4): p. 215-228.
46. Aguiar, P.M., J.-F. Jacquinet, and D. Sakellariou, Experimental and numerical examination of eddy (Foucault) currents in rotating micro-coils: Generation of heat and its impact on sample temperature. Journal of Magnetic Resonance, 2009. 200(1): p. 6-14.
47. Al-Harashseh, M., et al., Dielectric properties of Jordanian oil shales. Fuel Processing Technology, 2009. 90(10): p. 1259-1264.
48. Altomare, A., et al., QUALX2. 0: a qualitative phase analysis software using the freely available database POW\_COD. Journal of Applied Crystallography, 2015. 48(2): p. 598-603.
49. Yoshikawa, N., E. Ishizuka, and S. Taniguchi, Heating of metal particles in a single-mode microwave applicator. Materials transactions, 2006. 47(3): p. 898-902.
50. Jonscher, A.K., Dielectric relaxation in solids. Journal of Physics D: Applied Physics, 1999. 32(14): p. R57.
51. Miles, P., W. Westphal, and A. Von Hippel, Dielectric spectroscopy of ferromagnetic semiconductors. Reviews of Modern Physics, 1957. 29(3): p. 279.
52. Hotta, M., et al., Complex permittivity of graphite, carbon black and coal powders in the ranges of X-band frequencies (8.2 to 12.4 GHz) and between 1 and 10 GHz. ISIJ international, 2011. 51(11): p. 1766-1772.
53. Cornell, R.M. and U. Schwertmann, The iron oxides: structure, properties, reactions, occurrences and uses. 2003: John Wiley & Sons.
54. Papanastassiou, D. and G. Bitsianes, Mechanisms and kinetics underlying the oxidation of magnetite in the induration of iron ore pellets. Metallurgical Transactions, 1973. 4(2): p. 487-496.
55. Monazam, E.R., R.W. Breault, and R. Siriwardane, Kinetics of Magnetite (Fe<sub>3</sub>O<sub>4</sub>) Oxidation to Hematite (Fe<sub>2</sub>O<sub>3</sub>) in Air for Chemical Looping Combustion. Industrial & Engineering Chemistry Research, 2014. 53(34): p. 13320-13328.

## Appendix 2: Thermal degradation kinetics of polyvinyl chloride in presence of zinc oxide

Sanad Altarawneh<sup>1,\*</sup>, Mohammad Al-Harabsheh<sup>2</sup>, Chris Dodds<sup>1</sup>, Adam Buttress<sup>1</sup>, Sam Kingman<sup>1</sup>

<sup>1</sup> Faculty of Engineering, University of Nottingham, Nottingham, NG7 2RD, UK

<sup>2</sup> Chemical Engineering Department, Jordan University of Science and Technology, Irbid, 22110, Jordan

\*corresponding author

[Sanad.altarawneh@nottingham.ac.uk](mailto:Sanad.altarawneh@nottingham.ac.uk)

### Abstract

This work investigates the degradation kinetics and the pyrolysis behaviour of Poly (vinyl chloride) (PVC) and its mixture with ZnO using thermogravimetric analysis under an inert atmosphere. The investigation was carried out due to the increased interest in the co-thermal treatment of the hazardous waste electric arc furnace dust (EAFD) which contains significant quantities of ZnO with PVC. The degradation of pure PVC was characterised by three main decomposition stages: PVC de-hydrochlorination (two overlapped stages) and subsequent polyene thermal cracking, while ZnO-PVC mixture (ZPVC) demonstrated four decomposition/volatilisation stages. The Flynn-Wall-Ozawa (FWO), Kissinger-Akahira-Sunose (KAS), and Friedman models were utilised for the extraction of the kinetic parameters. The average activation energy for pure PVC de-hydrochlorination was calculated to be  $119.8 \pm 12.4$  kJ/mol, which changed to  $110.6 \pm 11.2$  kJ/mol when a stoichiometric quantity of ZnO was added to it. The suggested mechanism for the ZPVC de-hydrochlorination starts by chlorine abstraction on ZnO at temperatures well-below 272 °C with an activation energy comparable to that of pure PVC de-hydrochlorination (115.8 kJ/mol). The chlorination of ZnO then yields zinc oxy/hydroxide chloride phases ( $Zn_2OCl_2 \cdot 2H_2O/\beta-Zn(OH)Cl$ ) by the reaction between  $ZnCl_2$ , ZnO and emitted  $H_2O$ . These phases then decompose at approximately 222 °C into  $ZnCl_2$ , ZnO, and  $H_2O$  with a relatively low energy barrier of 102.2 kJ/mol. Formed  $ZnCl_2$  then lowers the activation energy for the polyene thermal cracking of PVC from  $218.4 \pm 17.7$

(PVC) to  $87.3 \pm 9.7$  kJ/mol (ZPVC) due to the physical contribution of volatilisation to the overall mass loss.

Keywords: PVC, ZnO, polymer degradation, pyrolysis, TGA, non-isothermal kinetics

## 1. Introduction

Electric arc furnace dust (EAFD) is globally considered a major hazardous waste material which is generated from steel manufacturing in electric arc furnaces (EAFs) [1]. Between 15 and 20 kg of EAFD is generated for every ton of recycled steel [2]. Each year approximately 8 million tons of EAFD are generated and this is predicted to increase to a minimum of 18 million tons/year by 2050 [3]. This alarming production rate with the absence of a sustainable recycling route poses a great challenge to environmental engineers. The major part of the feed supplied to EAFs is steel scrap [4] and since a significant portion of this scrap is galvanised, high zinc concentrations are usually seen in EAFD [2, 5-7]. This, in turn, rendered EAFD as a potential secondary source for zinc. The conventional methods suggested in literature for the extraction of zinc from EAFD can be categorised into hydrometallurgical [2, 8-11] and pyrometallurgical [12-14]. The former approach, whilst typically lower in energy consumption and more environmentally benign, suffers from incomplete extraction [15-17], harshness of the leaching medium [16], and poor selectivity [16, 18]. Pyrometallurgical treatments, have found industrial scale applications such as the Waelz kiln. However, this approach is highly energy intensive (furnace operates above 1000 °C) and environmentally harmful and therefore requires complicated gas/dust filtration systems downstream [1].

Parallel to accumulations of EAFD, polyvinyl chloride (PVC) is another waste stream generated in huge quantities. This material is one of the most widely used plastics and it finds use in a diverse range of applications including construction, packaging, piping, cable insulation, and medical applications [19]. The global production and consumption capacity of PVC in 2013 was 61 and 38.5 million tons [20] with an estimated annual rise in demand of 3.2% until 2021 [21]. Using this percentage (3.2%/year), today, a consumption rate of about 49.5 million tons is expected. Consequently, it has become increasingly important to address the associated PVC waste streams which arise at the end of the life cycle of these various

products. A Landfill strategy was the most prevalent disposal route, but over time, it has become an obsolete option due to the decreased number of landfilling sites [22] and the associated environmental burden. In addition, the high stability of PVC in landfills [23] requires vast dumping areas which significantly increase the costs of landfilling. An alternative to landfilling is the pyrolysis of PVC. This treatment, however, yields harmful emissions such as hydrogen chloride (HCl) gas and chlorinated hydrocarbons such as polychlorinated dibenzo-p-dioxins (PCDDs) and polychlorinated dibenzofurans (PCDFs) [24, 25].

Recently, there has been a growing interest among researchers towards the co-thermal treatment of waste EAFD with halogenated plastics such as PVC [1, 5, 7, 26, 27]. The metal oxides present in EAFD proved to have remarkable fixing ability of the emissions generated from the pyrolysis of PVC, especially HCl [7, 22, 27]. Masuda et al. [28] studied the HCl fixing ability of eight metal oxides including ZnO. It was concluded that ZnO is capable of capturing 51% of the initial chlorine content of PVC when pyrolysed at a temperature of 400 °C. Likewise, ZnO resulted in a significant reduction in the yield of chlorobenzene; one of the main precursors of PCDD/Fs [28]. Ballistreri et al. [29] studied the effect of eight metal oxides on the decomposition of PVC among which ZnO showed a very powerful suppressing effect on the emission of aromatic species. In the same study, the formation of volatilised ZnCl<sub>2</sub> was detected by a mass spectrometer [29]. Zhang et al. [30], studied the decomposition of PVC in the presence of ZnO, ZnFe<sub>2</sub>O<sub>4</sub>, and Fe<sub>2</sub>O<sub>3</sub> and concluded that the degradation of PVC proceeded at a lower temperature in the presence of ZnO. The chlorine fixation on ZnO was also confirmed by the detection of H<sub>2</sub>O fragments evolved from chlorination using a mass spectrometer [30].

Since the interest in the co-thermal treatment of waste EAFD and waste PVC grew for the purpose of zinc extraction, and since a major portion of zinc in EAFD is present in the form of ZnO, a comprehensive kinetics study on the effect of ZnO on the decomposition of PVC has

become necessary in order to predict reaction rates at different holding temperatures and conversions. This also helps in understanding the underpinning reaction mechanisms by means of comparing the activation energy and the reaction mechanism  $f(\alpha)$  for ZnO-PVC (ZPVC) mixture and pure PVC. In this study, we present a complete non-isothermal kinetic study of pure PVC and ZPVC mixtures in the temperature window 25 – 900 °C and under inert environment. From this, the activation energy, the frequency factor, and the reaction mechanism  $f(\alpha)$  can be extracted using different iso-conversional kinetics models -namely the well-known FWO, KAS, and Friedman [31-35] along with a linear fitting method. Pyrolysis products of ZPVC mixture were also identified using X-Ray diffraction (XRD) and Scanning electron microscopy (SEM) techniques to support the validity of the derived mechanisms.

## **2. Materials and method**

### **2.1 Thermogravimetric analysis and differential scanning calorimetry**

The ZnO used in this work was purchased from Fisher Scientific with a purity of 99.999%, and powdered PVC was obtained from Sigma-Aldrich. A stoichiometric mixture of ZnO and PVC (ZPVC) was prepared based on the stoichiometric amount of HCl in the PVC monomer; this produced a mixture containing 39.4 wt% ZnO. Before mixing, ZnO powder was finely ground using pestle and mortar to increase the homogeneity of the mixture and to increase the contact surface area for the chemical reaction (see Figures S1 and S2 in the supplementary material). The ZPVC mixture was then tumbled for 15 minutes in a glass vial containing stainless steel balls in order to prevent particles agglomeration and make sure the particle size is uniform throughout. An empty ceramic sample holder was first exposed to the thermal analysis to produce a baseline for the heat flow signal. A sample of about 10 mg of pure PVC and ZPVC mixture were then exposed to thermal analysis using a simultaneous differential scanning calorimetry (DSC) and Thermogravimetric Analysis (TGA) instrument (SDT Q600). The

thermal analysis was performed at three different heating rates (10, 30, and 50 K/min) in the temperature window of 25 – 900 °C and under a nitrogen flow of 100 mL/min.

## **2.2 Pyrolysis of ZPVC mixture**

A sample with a mass of 0.3 g (for 200 and 230 °C) and 0.5 g (for 370 °C) of ZPVC mixture was loaded into a 4 mm quartz tube. The usage of two different masses for different pyrolysis temperatures was because of the different mass loss at different temperatures. This, in turn, ensures that a comparable amount of powder residue was obtained after the pyrolysis. The tube was connected from one end to high purity nitrogen (99.9992%) to purge the ZPVC mixture at a rate of ~ 5 mL/min, and the other end was vented into an extraction system. The powder was surrounded from the top and bottom with ceramic fibre to prevent it from fluidising. The bottom ceramic fibre also acted as a gas distributor (to distribute the gas evenly through the powder). Prior to heating, the system was purged with nitrogen for at least 15 minutes to confirm that the reactants are completely surrounded with a nitrogen blanket. The quartz tube was then inserted vertically into a tube furnace. Three pyrolysis runs were performed at three different temperatures of 200, 230 and 370 °C and the mixture was held at these temperatures for 30 minutes. Products from each run were collected in a vial, purged with nitrogen, and stored in a desiccator for characterisation.

## **2.3 Scanning electron microscopy analysis**

A FEI Quanta600 MLA scanning electron microscope (SEM) coupled with Energy Dispersive Spectroscopy (EDS) was used for the morphological and elemental analysis of the powder before and after pyrolysis. A spot size of 4.5 and an accelerating voltage of 15000 kV were used during the analysis. To enhance the electrical conductivity of the powder and avoid charging during the analysis, powders were carbon coated.

## **2.4 X-ray diffraction analysis**

Residues generated from the pyrolysis were subjected to X-ray diffraction (XRD) for mineralogical identification of products. To minimise the effect of moisture on the materials, powders on the sample holder were covered from the top with a piece of tape to prevent fresh air from being in contact with it. A Bruker D8 Advance with a LYNXEYE 2D detector and a Cu  $\alpha$  source was used for the mineralogical analysis. The instrument was operated at a current and voltage of 40 mA and 40 kV, respectively. Pyrolysis residues were scanned in the  $2\theta$  range  $5 - 90^\circ$  with a step size of  $0.02^\circ$  and a scan rate of 1.7 sec/step while pure ZnO was scanned at 0.1 sec/step due to its high purity and non-noisy signal. Data was interpreted using QualX 2.0 [36] and DIFFRAC.EVA V5.2 softwares which use COD and PDF-2 databases, respectively.

### 3. Non-isothermal kinetics model

#### 3.1 General rate equation

The rate of solid decomposition ( $r_A$ ) can be given by the product of the temperature dependent rate constant  $k(T)$  and the temperature independent conversion function  $f(\alpha)$  (reaction model):

$$r_A = \frac{d\alpha}{dt} = k(T) \cdot f(\alpha) \quad (1)$$

In which  $\alpha$  is the degree of conversion and  $\frac{d\alpha}{dt}$  is its derivative with respect to time.

The mathematical expression used for the  $f(\alpha)$  function depends on the controlling mechanism of the reaction. An empirical model introduced by Šesták and Berggren [37] for the form of  $f(\alpha)$  can be written as:

$$f(\alpha) = \alpha^m (1 - \alpha)^n [-\ln(1 - \alpha)]^p \quad (2)$$

Where different combinations of  $m$ ,  $n$ , and  $p$  result in different reaction models [38]. The conversion  $\alpha$  is calculated from the wt% data produced from the TGA profile as follows:

$$\alpha = \frac{W_o - W}{W_o - W_f} \quad (3)$$

Where  $W$  is the wt% at time  $t$ ,  $W_o$  is the initial wt% and  $W_f$  is the final wt%. The rate constant in Equation 1 depends on temperature according to the Arrhenius function:

$$k(T) = A. e^{\frac{-E}{RT}} \quad (4)$$

Where  $A$  is the temperature independent frequency factor given in  $\text{min}^{-1}$ ,  $E$  is the activation energy in J/mol,  $R$  is the universal gas constant (8.314 J/mol.K) and  $T$  is the absolute temperature in K. Combining Equations 1 and 4 and multiplying both sides with the reciprocal of the heating rate  $\left(\frac{1}{\beta} = \frac{dt}{dT}\right)$  yields the following equation:

$$\frac{r_A}{\beta} = \frac{d\alpha}{dT} = \frac{A}{\beta} e^{\frac{-E}{RT}}. f(\alpha) \quad (5)$$

Equation 5 is the derivative form of the rate equation. Rearranging and integrating both sides yields the integral form of the rate equation:

$$g(\alpha) = \int_0^\alpha \frac{d\alpha}{f(\alpha)} = \frac{A}{\beta} \int_{T_o}^T e^{\frac{-E}{RT}} dT \quad (6)$$

In which  $T_o$  corresponds to a conversion of zero. The right-hand side of Equation 6 has no analytical solution [39]. Thus, different methods were developed to either utilise the differential form (Equation 5) or use estimations for the temperature integral in Equation 6 to calculate the activation energy and the frequency factor. Among many kinetics methods, the iso-conversional technique allows for a reliable prediction of the kinetic parameters [40, 41].

## 3.2 Model-Free methods

### 3.2.1 Calculation of the activation energy

The Flynn-Wall-Ozawa (FWO) method [33, 34] uses the Doyle [42] approximation of the integration in Equation 6 for the calculation of the kinetic parameters. Their model can be written as follows:

$$\ln\beta_i = \ln\left(\frac{A_\alpha E_\alpha}{g(\alpha)R}\right) - 5.331 - 1.052 \frac{E_\alpha}{RT_{\alpha i}} \quad (7)$$

For a specific value of conversion ( $\alpha$ ), three different temperatures are obtained for three thermograms at three different heating rates. A plot of  $\ln\beta_i$  versus  $\frac{1}{T_{\alpha i}}$  should produce a straight line with a slope of  $-1.052 \frac{E_\alpha}{R}$  from which the apparent activation energy is obtained.

Kissinger-Akahira-Sunose (KAS) [31, 35] is another method that uses the integral form of the rate equation for the calculation of the kinetic parameters. Their model can be written according to the following equation:

$$\ln\left(\frac{\beta_i}{T_{\alpha i}^2}\right) = \ln\left(\frac{A_\alpha R}{E_\alpha g(\alpha)}\right) - \frac{E_\alpha}{RT_{\alpha i}} \quad (8)$$

Likewise, a plot of  $\ln\left(\frac{\beta_i}{T_{\alpha i}^2}\right)$  against  $\frac{1}{T_{\alpha i}}$  at a constant conversion for three different thermograms at three different heating rates must yield a straight line with a slope of  $-\frac{E_\alpha}{R}$ .

Friedman method [32] uses the differential form of the rate equation. The model can be written as follows:

$$\ln\left(\frac{d\alpha}{dt}\right)_i = \ln A + \ln f(\alpha) - \frac{E_\alpha}{RT_{\alpha i}} \quad (9)$$

A plot of  $\ln\left(\frac{d\alpha}{dt}\right)_i$  against  $\frac{1}{T_{\alpha i}}$  at a constant conversion for three heating rates produces a straight line with a slope of  $-\frac{E_\alpha}{R}$ .

### 3.2.2 Calculation of the frequency factor

The extraction of the frequency factor can be achieved using the compensation effect described in Vyazovkin [43]. Fitting the experimental data (Equation 11) using a set of different reaction models generates a set of values of activation energy and frequency factor. The activation

energies and frequency factors can then be linearly correlated (see Figure S3 in supplementary material) according to the following Equation [43]:

$$\ln(A_i) = aE_i + b \quad (10)$$

Such that a and b are constants obtained from linear regression. Activation energies obtained from the model-free methods can then be inserted into Equation 10 to extract iso-conversional values of  $\ln(A)_\alpha$ .

### 3.3 Prediction of the reaction model

These methods, usually referred to as “iso-conversional” or “model free”, are useful when calculating the activation energy, since the exact knowledge of the reaction model “ $f(\alpha)$ ” is not required. Hence, these methods cannot be used to predict the reaction model. The rearrangement of Equation 5 into Equation 11 allows the prediction of the reaction model  $f(\alpha)$

by means of linear fitting of  $\ln\left(\frac{d\alpha}{dt} \cdot \frac{1}{f(\alpha)}\right)$  against  $\frac{1}{T}$ :

$$\ln\left(\frac{d\alpha}{dt} \cdot \frac{1}{f(\alpha)}\right) = \ln(A) - \frac{E}{RT} \quad (11)$$

The criteria followed for this method was that the accepted reaction model is the one that gives the best linearity, and its slope should generate a value of activation energy that is as close as possible to the average value obtained from the Friedman model on the studied conversion range. When possible, the chosen reaction orders were those that generate a meaningful reaction model, rather than random polynomials.

## 4. Results and Discussion

### 4.1. TGA/DSC analysis

#### 4.1.1. TGA/DSC analysis of pure PVC

Figure 1 shows the TGA and Differential thermogravimetric (DTG) (derivative mass) profiles for the decomposition of pure PVC at heating rates of 10, 30 and 50 K/min. PVC degradation

follows three decomposition stages. The first two stages are overlapped while the third one is well separated.

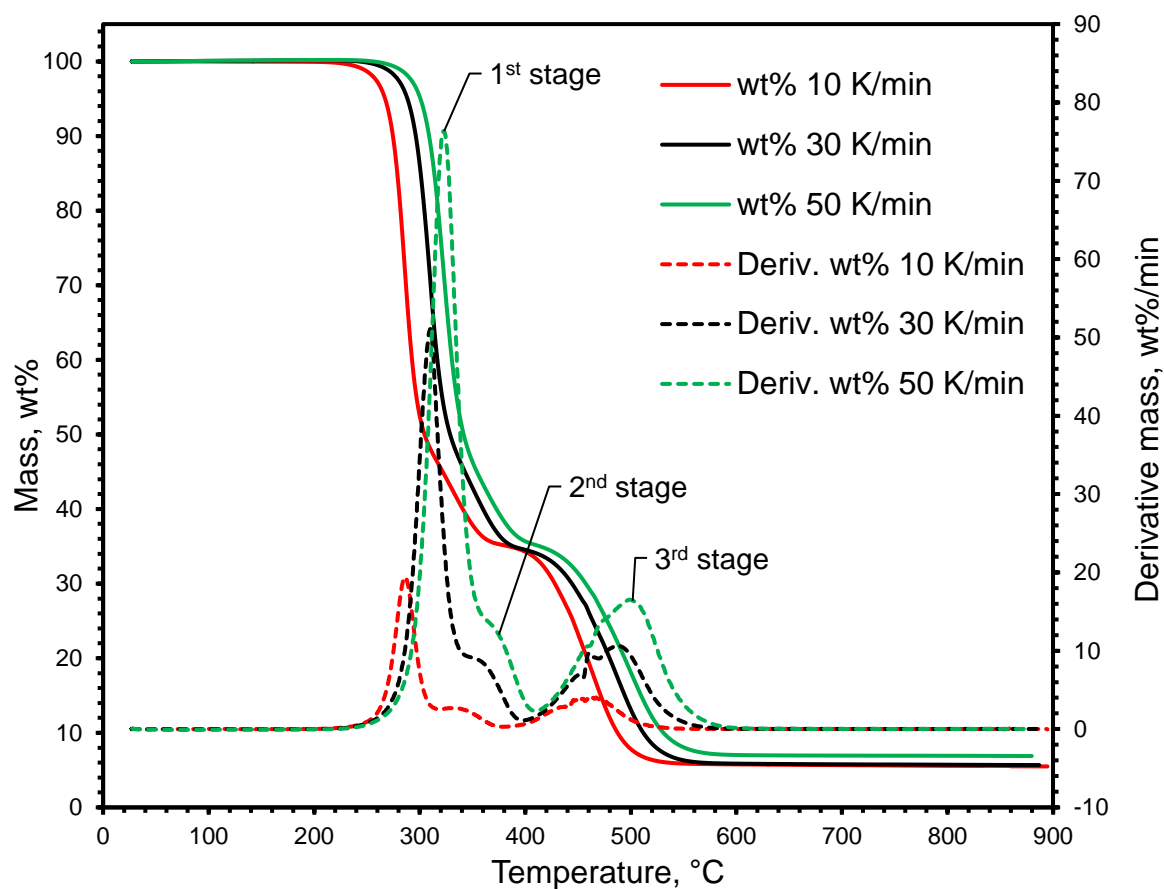


Figure 1: TGA/DTG profiles for PVC decomposition at heating rates of 10, 30, and 50 K/min and under a nitrogen flow of 100 mL/min.

The first two overlapped stages with an onset temperature of 272 °C have an overall mass loss of 65%. This mass loss is assigned to the de-hydrochlorination of the polymer chain and the evolution of hydrogen chloride gas (HCl) [44]. The theoretical HCl content in the PVC monomer is 58.3%. The disparity between 65% and 58.3% was assigned to the emission of volatile aromatic compounds, such as benzene, naphthalene, and anthracene [29]. At the end of the first two stages, the PVC chain is stripped from its chlorine content and the remaining solid is a conjugated polyene structure [20, 44]. The chemical reaction in the first two stages can be written as follows [45]:



The third stage with an onset temperature of 423 °C and represented by a mass loss of 29%, is attributed to the thermal cracking of the polymer backbone (polyene structure) into other hydrocarbons such as polyenyl aromatics, alkyl aromatics, and polyaromatics [46]. At the end of the third stage, about 6% of the initial weight remains in the crucible. The pyrolysis residue was reported to be char [1, 29]. Hence, the chemical reaction occurring during the third stage can be written as:



Both the de-hydrochlorination (first two stages) and the polyene thermal cracking (third stage) are accompanied by endothermic events as evident from the heat flow signals (peaks 2 and 3 in Figure 2).

#### 4.1.2. TGA/DSC analysis of ZPVC mixture

Figure 3 (a) shows the decomposition of the ZPVC mixture at heating rates of 10, 30, and 50 K/min. The decomposition follows four degradations stages; the first three are overlapped showing a DTG triplet, while the fourth is well separated. The de-hydrochlorination onset temperature for the ZPVC mixture is 214 °C, well-below that of pure PVC (Figure 2).

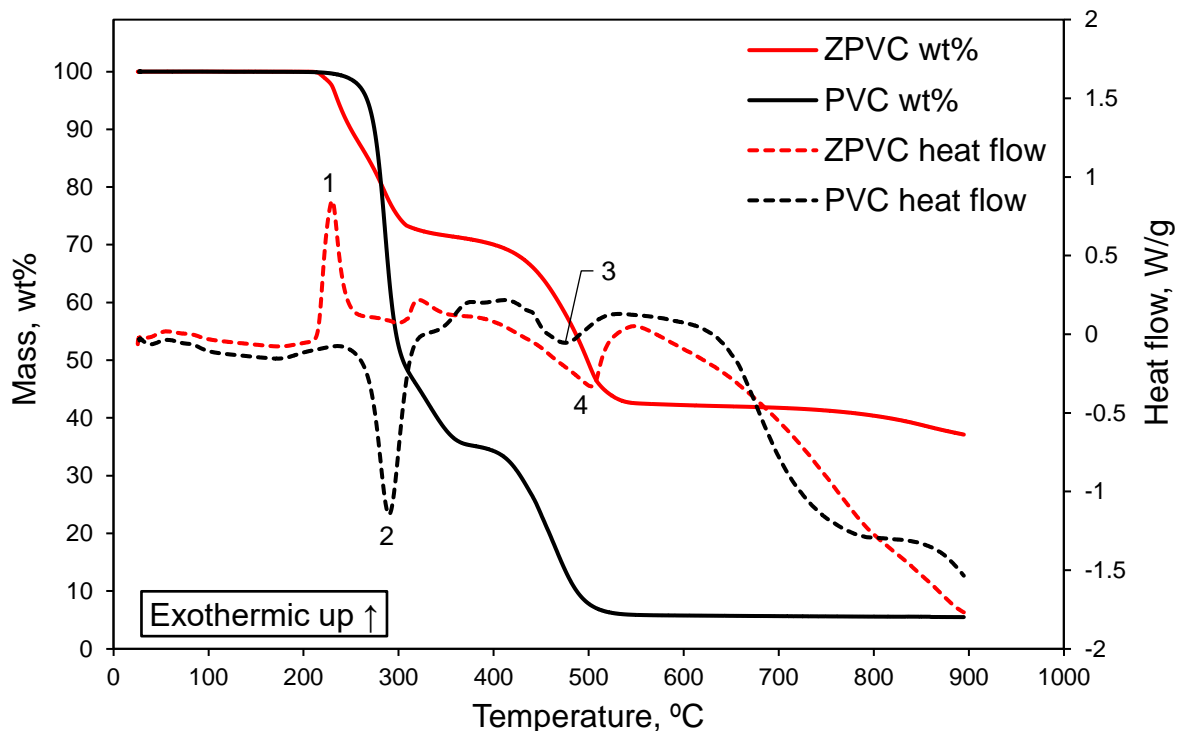


Figure 2: Simultaneous TGA/DSC profiles for PVC and ZPVC mixture at a heating rate of 10 K/min and a nitrogen flow of 100 mL/min (DSC signals can be assigned as follows: 1. ZnO chlorination, 2. PVC dehydrochlorination, 3. polyene thermal cracking and 4. simultaneous  $\text{ZnCl}_2$  volatilisation and polyene thermal cracking).

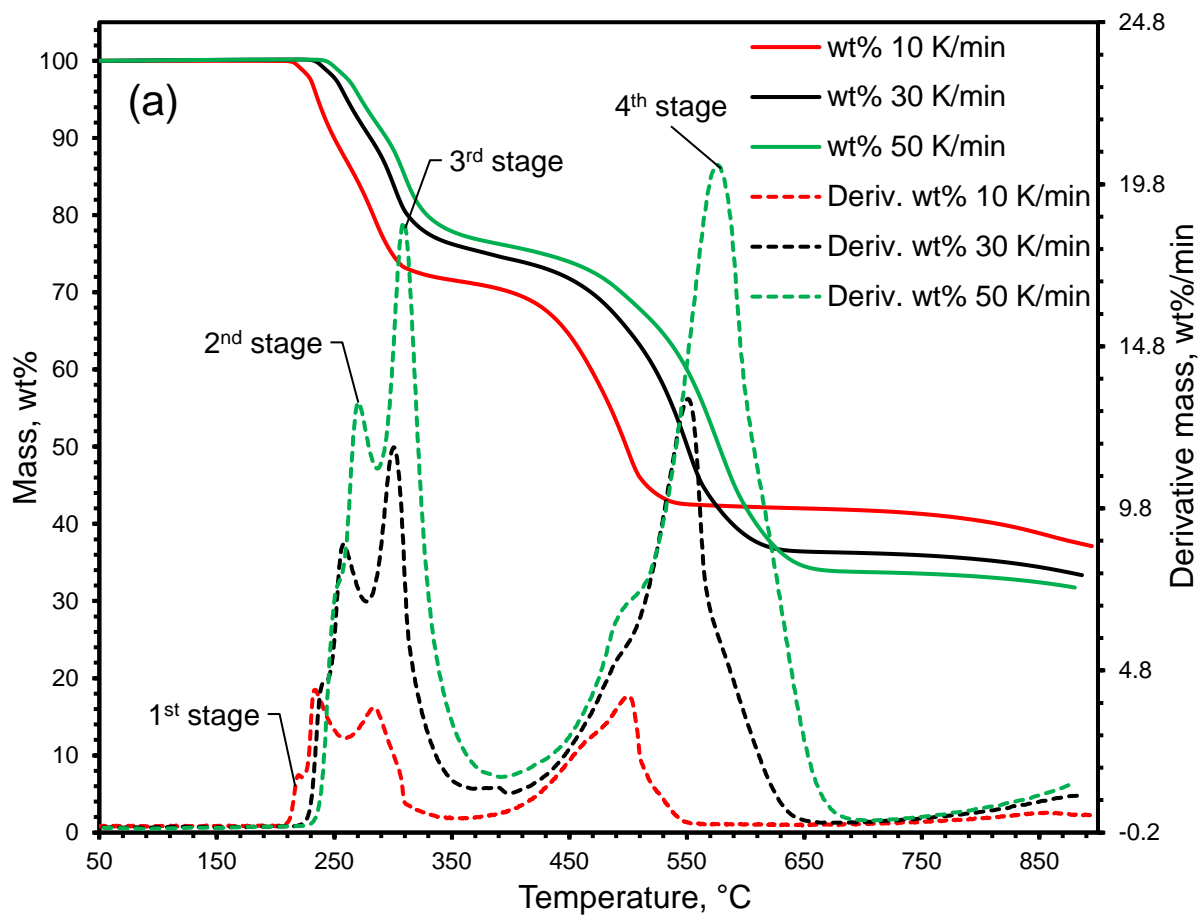
Such behaviour suggests that ZnO can be categorised as an active catalyst for the dehydrochlorination of PVC changing its initiation pathway. The start of PVC degradation at a lower temperature when mixed with ZnO was also seen in the work from Zhang et al. [30] and Kosuda et al. [47]. The pyrolysis of EAFD-PVC mixture by Al-Harabsheh et al. [1] also showed similar results where the onset temperature significantly decreased when PVC was pyrolysed in presence of EAFD; the latter contained more than 29 wt% zinc with a large portion in the form of ZnO [1, 7].

Figure 3 (a) shows that increasing the heating rate increases the percentage of captured HCl as evident from the lower mass loss at higher heating rates. An estimation of how much HCl was captured by ZnO can be obtained from the mass loss in the first three stages and the knowledge of the initial composition of the mixture. This procedure gives only an estimation since it assumes that the first three stages are only related to HCl evolution (i.e., neglecting organic emissions) and that the chlorination occurs according to Equation 15.

The percentage fixed can be given as follows:

$$\text{Fixed HCl (wt\%)} = \frac{W - W^*}{W' - W^*} \times 100\% \quad (14)$$

Where  $W^*$  is the wt% left in crucible if no HCl was captured (64.7%),  $W'$  is the wt% left if all HCl was captured (91.3%) and  $W$ , as defined earlier, is the actual wt% remaining from the experiment. Using Equation 14, the percentage of HCl captured by ZnO was calculated to be 28.9, 42.6 and 46.3% at 10, 30 and 50 K/min, respectively. These percentages, at high heating rates, are comparable to the HCl fixation values reported by Masuda et al. [28].



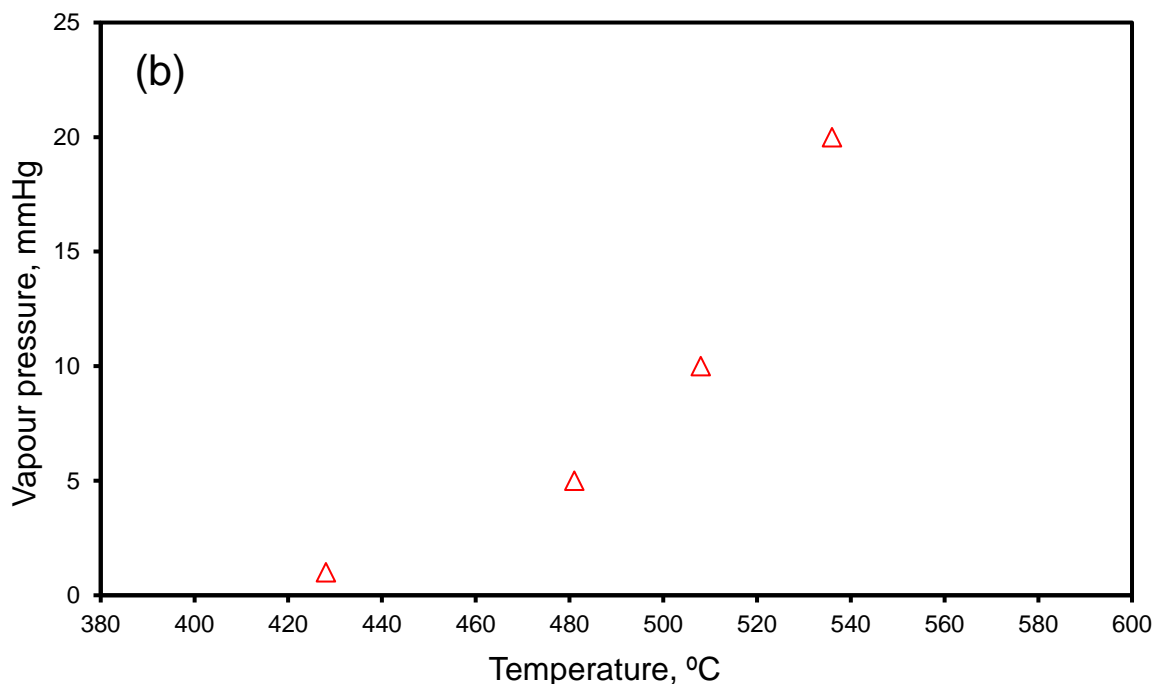


Figure 3: (a) TGA/DTG profiles for the ZPVC mixture (39.4 wt% ZnO) at heating rates of 10, 30 and 50 K/min and under a nitrogen flow of 100 mL/min (b) vapour pressure of  $\text{ZnCl}_2$  against temperature [48].

In Figure 3 (a), the first two stages may be attributed to the release of  $\text{H}_2\text{O}$  resulting from the chlorination of ZnO [27, 30].  $\text{H}_2\text{O}$  also evolves from the decomposition of intermediate zinc oxy/hydroxide chloride species as will be shown later. The chlorination of ZnO can be confirmed from the high exothermic peak appearing in the temperature range 210 – 260 °C in Figure 2, which is absent in the case of pure PVC. XRD characterisation of the products generated from the pyrolysis experiments performed at 200, 230 and 370 °C, shows peaks related to  $\beta\text{-Zn(OH)Cl}$ ,  $\text{Zn}_2\text{OCl}_2 \cdot 2\text{H}_2\text{O}$ ,  $\alpha\text{-ZnCl}_2$ , and  $\text{ZnCl}_2 \cdot 1.33\text{H}_2\text{O}$  (Figure 4). One more phase (Simonkolleite:  $\text{Zn}_5(\text{OH})_8\text{Cl}_2 \cdot \text{H}_2\text{O}$ ) was reported to form at temperatures 180 – 200 °C by Kosuda et al. [47] which acts as a precursor for the  $\beta\text{-Zn(OH)Cl}$  and  $\text{Zn}_2\text{OCl}_2 \cdot 2\text{H}_2\text{O}$  phases reported here [49, 50]. Distinguishing whether  $\beta\text{-Zn(OH)Cl}$  or  $\text{Zn}_2\text{OCl}_2 \cdot 2\text{H}_2\text{O}$  was the formed phase is difficult since both phases have the same  $2\theta$  angles. The thermal behaviour of both  $\beta\text{-Zn(OH)Cl}$  and  $\text{Zn}_2\text{OCl}_2 \cdot 2\text{H}_2\text{O}$  reported in literature [51-53] is very comparable to one another and both agree well with the TGA data reported in Figure 3 (a) as will be discussed later. It is noted that the abundance of the formed chloride species is affected by the temperature at which

the pyrolysis takes place. When the pyrolysis temperature was increased from 200 to 230 and 370 °C, the intensity of  $\text{Zn}_2\text{OCl}_2 \cdot 2\text{H}_2\text{O}/\beta\text{-Zn(OH)Cl}$  peaks waned. This drop in intensity was accompanied by the appearance of  $\alpha\text{-ZnCl}_2$  and  $\text{ZnCl}_2 \cdot 1.33\text{H}_2\text{O}$  peaks at 230 °C and  $\alpha\text{-ZnCl}_2$  peaks at 370 °C. This suggests that  $\text{Zn}_2\text{OCl}_2 \cdot 2\text{H}_2\text{O}/\beta\text{-Zn(OH)Cl}$  can be considered as intermediate chloride species which decompose into  $\alpha\text{-ZnCl}_2$ ,  $\text{ZnCl}_2 \cdot 1.33\text{H}_2\text{O}$ ,  $\text{ZnO}$  and  $\text{H}_2\text{O}$  when the temperature increases further. This result is in agreement with the work performed by Ahmed et al. [54]. In their study, a thermo-kinetic model on the dissociative adsorption and reaction of gaseous molecular  $\text{HCl}$  with  $\text{ZnO}$  ( $10\bar{1}0$ ) surface was constructed and the mechanistic pathway of the reactions including all intermediates was reported [54]. The formation of surface zinc chloride on the  $\text{ZnO}$  crystal and the attachment of hydrogen atom from the  $\text{HCl}$  molecule with the oxygen on  $\text{ZnO}$  crystal was also reported. This, in turn, led to the conclusion that a zinc oxychloride intermediate was formed prior to the formation of zinc chloride.

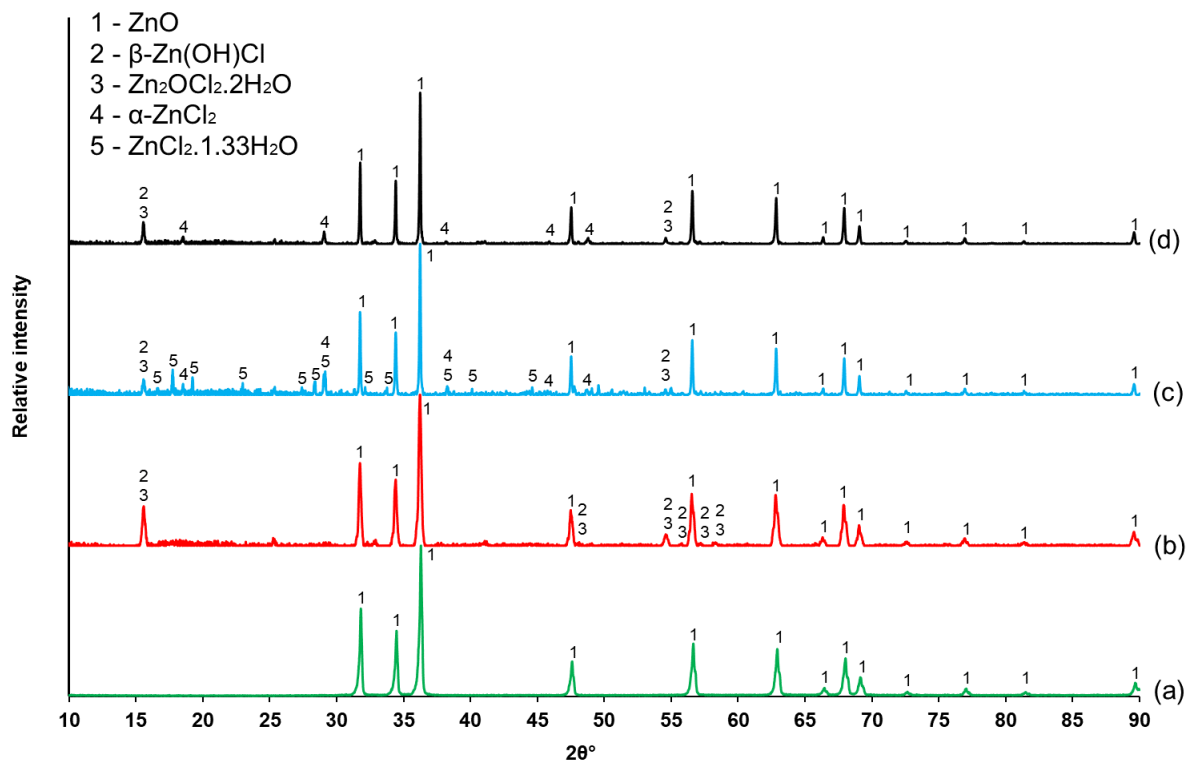


Figure 4: XRD pattern of ZnO (a), the post pyrolysis residue of ZPVC mixture at 200 (b), 230 (c), and 370 °C (d) all under nitrogen atmosphere.

SEM analysis was also utilised to confirm the association of both zinc and chlorine in the same crystal after the pyrolysis. Figure 5 shows hexagonal star crystals on a large ceramic fibre particle. These crystals are collected from the powder generated from the pyrolysis of the ZPVC mixture at 370 °C. EDS mapping confirms that these crystals contain both zinc and chlorine which suggests that they could be those of  $\alpha$ -ZnCl<sub>2</sub>.

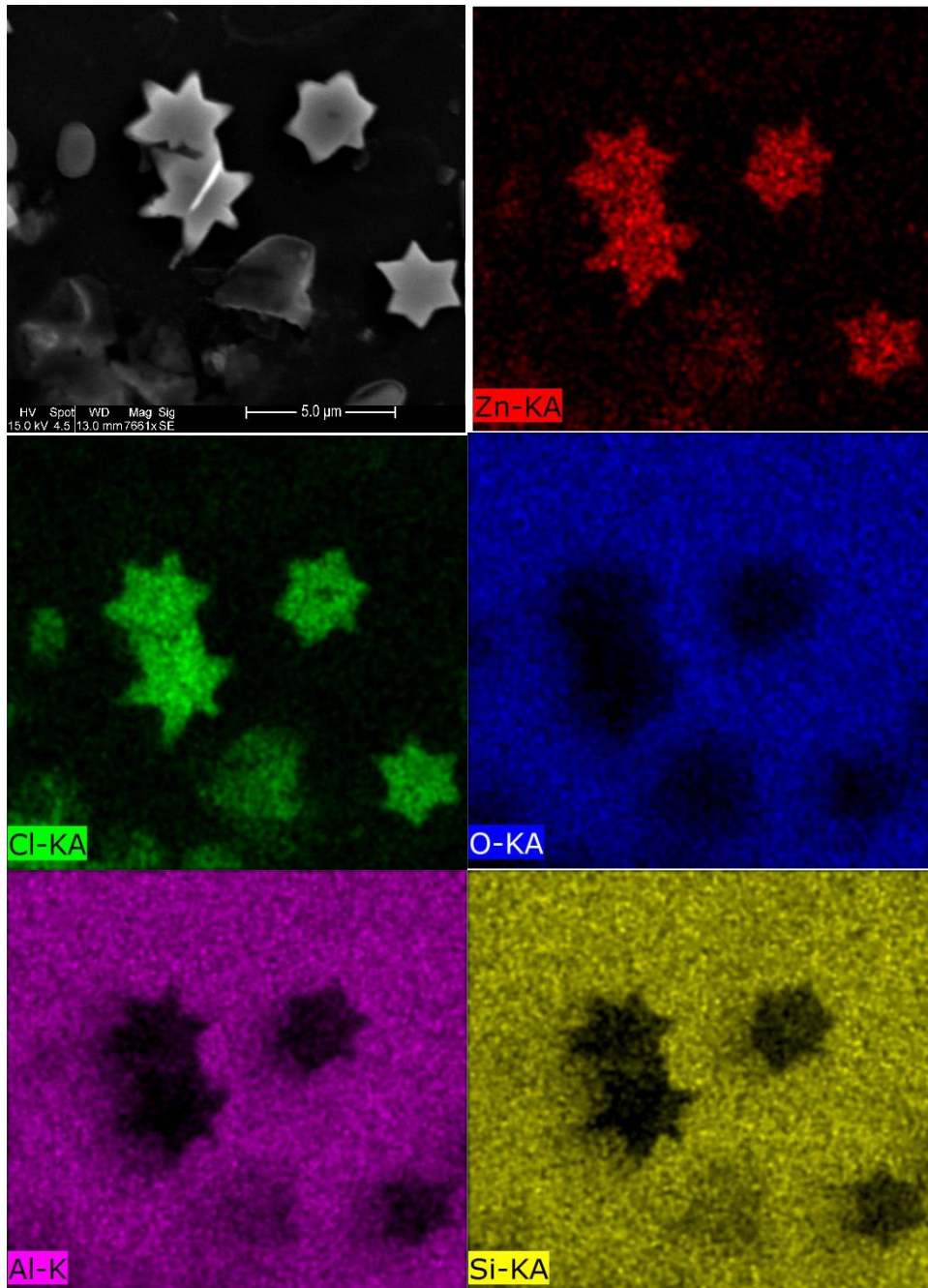


Figure 5: Secondary electron image of hexagonal star shaped crystals on a large ceramic fibre particle in a powder generated from the pyrolysis of ZPVC mixture under nitrogen at 370 °C.

Moreover, the formation of  $\text{ZnCl}_2$  is also confirmed from the endothermic peak appearing in the temperature range 411 – 545 °C in Figure 2 which is attributed to its volatilisation into the gas phase. The endothermic peak appearing for ZPVC mixture is larger and sharper than that seen for pure PVC. The maximum heat flow is also slightly shifted to the right in the case of ZPVC showing a maximum evaporation rate at a temperature of about 503 °C which is in line with the high vapour pressure shown for  $\text{ZnCl}_2$  in Figure 3 (b) with a value of 10 mmHg at 508 °C. This volatilisation behaviour is also in line with the thermodynamic analysis reported by Al-Harahsheh [7] and the TGA profile of pure  $\text{ZnCl}_2$  reported by Jones et al. [55].

Two potential mechanistic pathways can be associated with the chlorination of ZnO:

1. Direct reaction of ZnO with hydrogen and chlorine in the PVC monomer.
2. Reaction of ZnO with the emitted gaseous HCl from PVC decomposition.

In the former case, the overall reaction can be written as in Equation 16, while in the latter, it is written as follows:



Evidence within literature suggests that the chlorination of ZnO is caused by a direct reaction with the PVC monomer [30, 47]. Zhang et al. [30] reported that the mass drop for ZPVC mixture started at a temperature of ~ 200 °C and that up to a temperature of about 271 °C, only  $\text{H}_2\text{O}$  fragments (from ZnO chlorination) were detected by the mass spectrometer with no evidence of HCl in the outlet stream. At temperatures slightly above 271 °C, HCl fragments started to appear [30]. Comparing that result with the data shown in Figure 3 (a) (10 K/min curve), it is clear that the third stage onset temperature is approximately 274 °C which is almost identical to the temperature reported in Zhang et al. [30]. This suggests that this stage is mainly associated with the evolution of HCl gas from the de-hydrochlorination of excess unreacted PVC. It is also clear that the heat flow signal (Figure 2) associated with the chlorination of ZnO

rises significantly earlier than the endothermic one associated with pure PVC dehydrochlorination. The XRD data in Figure 4 also shows that  $Zn_2OCl_2 \cdot 2H_2O/\beta-Zn(OH)Cl$  phases form when the pyrolysis was done at 200 °C which is much lower than the onset temperature of pure PVC dehydrochlorination; suggesting a direct interaction of ZnO with PVC. Data in the kinetics section 4.2.1 is also in favour of this conclusion.

Based on mineralogical data presented in Figure 4, the TGA/DTG profiles in Figure 3 (a), and the thermal behaviour of zinc oxy/hydroxide chloride species reported in literature [51-53], the following reaction sequence can be suggested for our reaction system based on starting and ceasing points of the DTG peaks of the ZPVC mixture:

1. Initial chlorine abstraction from PVC by ZnO (First DTG peak):

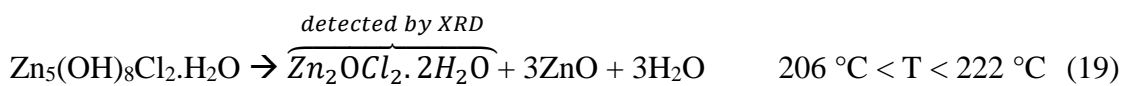
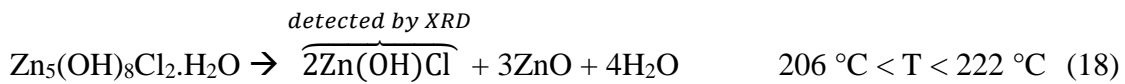


2. Immediate capturing of formed  $H_2O$  and the simultaneous formation and decomposition of simonkolleite ( $Zn_5(OH)_8Cl_2 \cdot H_2O$ ):

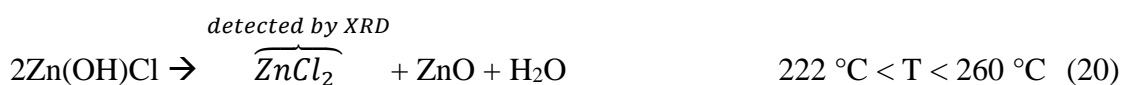
❖ Formation:

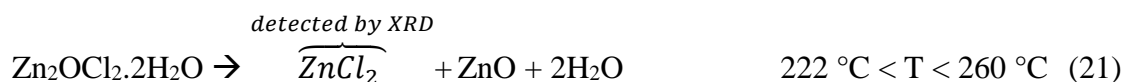


❖ Decomposition (First DTG peak):



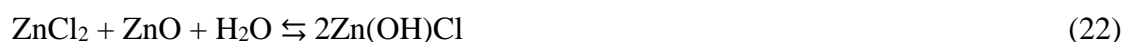
3. Thermal decomposition of  $Zn_2OCl_2 \cdot 2H_2O/\beta-Zn(OH)Cl$  (Second DTG peak):





#### 4. Excess unreacted PVC decomposition (Third DTG peak) (Reaction 12)

Following the sequence above, the DTG triplet in Figure 3 (a) can now be explained. The appearance of  $\beta\text{-Zn(OH)Cl/Zn}_2\text{OCl}_2 \cdot 2\text{H}_2\text{O}$  (Figure 4) at 370 °C, despite being reported to decompose completely at a lower temperature, might be explained by the reversible reaction of ZnO with ZnCl<sub>2</sub> in presence of H<sub>2</sub>O reported by Sorrell [52] and Garcia -Martinez et al. [53] at room temperature:



The formation of zinc oxychloride was further confirmed by exposing a ZPVC residue generated at 370 °C to an open atmosphere for at least 6 hours, then analysing it using XRD (Figure 6). All the peaks in pattern (a) except one peak of ZnO at 36.4° completely disappeared, generating a new phase Zn<sub>5</sub>(OH)<sub>8</sub>Cl<sub>2</sub>·H<sub>2</sub>O (simonkolleite). The zinc oxy/hydroxide chloride phases (Zn<sub>2</sub>OCl<sub>2</sub>·2H<sub>2</sub>O/ $\beta\text{-Zn(OH)Cl}$ ), however, are believed to form as intermediates prior to the formation of the Zn<sub>5</sub>(OH)<sub>8</sub>Cl<sub>2</sub>·H<sub>2</sub>O phase. ZnCl<sub>2</sub> is a deliquescent material, which means that it is highly hygroscopic and tends to form in-situ acidic aqueous solutions. This results in the dissolution of ZnO in contact with it. The resultant solution then starts precipitating as Zn<sub>2</sub>OCl<sub>2</sub>·2H<sub>2</sub>O/ $\beta\text{-Zn(OH)Cl}$  which finally transforms to Zn<sub>5</sub>(OH)<sub>8</sub>Cl<sub>2</sub>·H<sub>2</sub>O. Such result suggests that if the extraction of zinc is of interest, excess amount of PVC should be added to the mixture to chlorinate all ZnO, thus preventing the formation of the insoluble Zn<sub>5</sub>(OH)<sub>8</sub>Cl<sub>2</sub>·H<sub>2</sub>O phase. Moreover, products generated from the pyrolysis of ZPVC should be protected from moisture to preserve the soluble ZnCl<sub>2</sub> crystals.

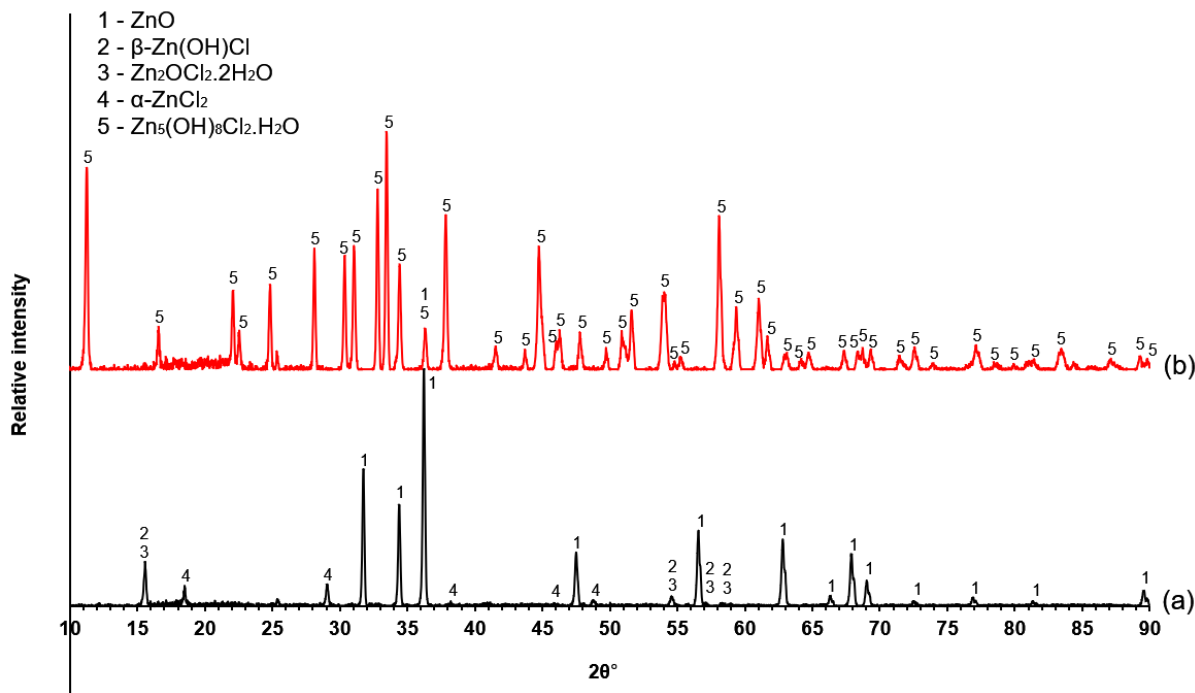


Figure 6: XRD pattern of the pyrolysis residue of ZPVC at 370 °C (a) and the same powder when exposed to the atmosphere for at least 6 hours (b).

The fourth mass loss in Figure 3 (a) is assigned to the simultaneous volatilisation of ZnCl<sub>2</sub> along with the thermal cracking of polyene structure; for 10 K/min curve, the loss is 28.5% where the thermal cracking accounts for 17.5% while the rest is related to ZnCl<sub>2</sub> volatilisation. The overall mass loss in that stage increases with increasing heating rate from 28.5% at 10 K/min to 37.9 and 41.7% at 30 and 50 K/min, respectively. This is attributed to the volatilisation of larger amounts of ZnCl<sub>2</sub> at higher heating rates which is in line with the percentages captured of HCl calculated earlier.

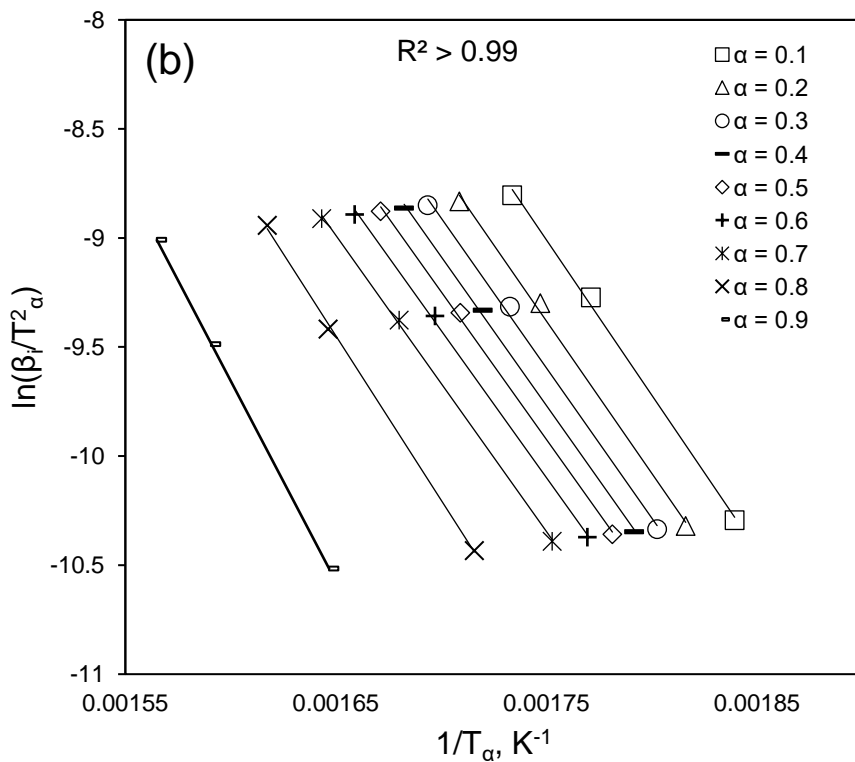
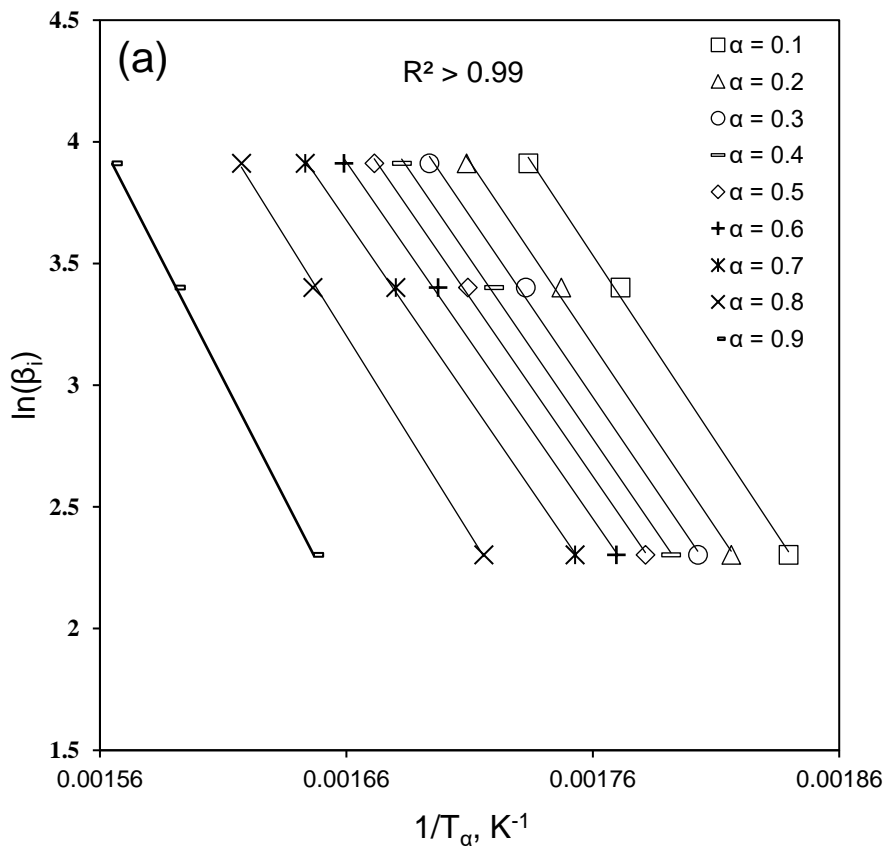
#### 4.2. Non-isothermal kinetics

In the kinetics section, the mass loss in the temperature range 210 – 365 °C for pure PVC and ZPVC will be referred to as the “de-hydrochlorination” stage while the mass loss in the temperature range 390 – 550 °C will be referred to as “polyene thermal cracking” stage. Both the activation energy and the frequency factor calculated here represent apparent values that reflect the contribution of different processes occurring either sequentially or simultaneously.

Thus, their values will change with temperature/conversion due to the beginning or ceasing of chemical/physical events.

#### 4.2.1. Kinetics of de-hydrochlorination stage for PVC and ZPVC

Figure 7 shows a sample of experimental data fitting for the de-hydrochlorination stage of pure PVC using FWO, KAS, and Friedman models. Slopes in Figure 7 were used to calculate the activation energy in the conversion range 0.1 – 0.9. Data fitting for obtaining the reaction model is also presented in Figure 7 (d). Compensation effect graphs for the estimation of the frequency factor are presented in the supplementary material (Figure S3).



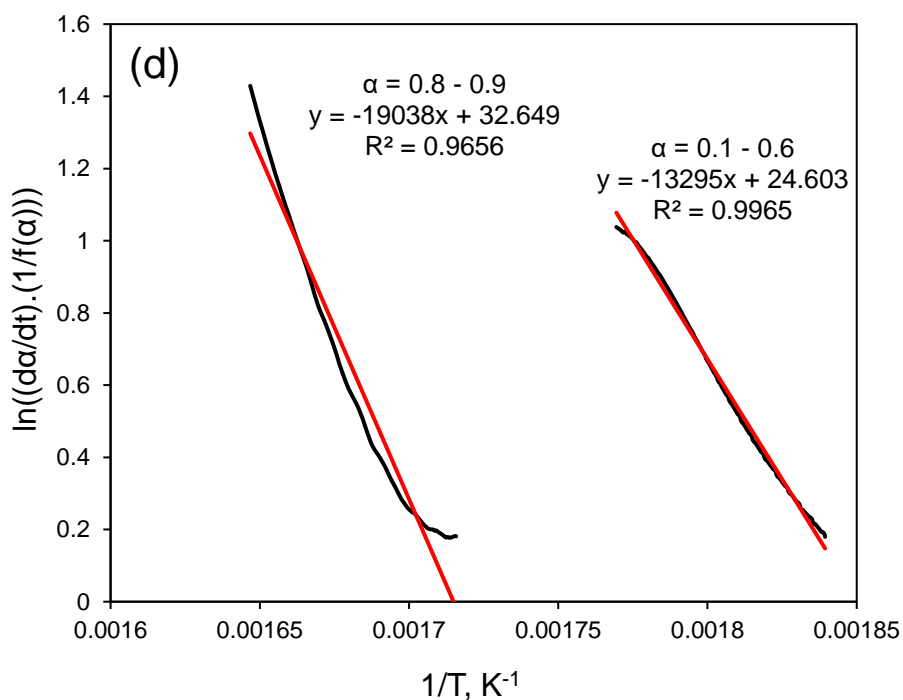
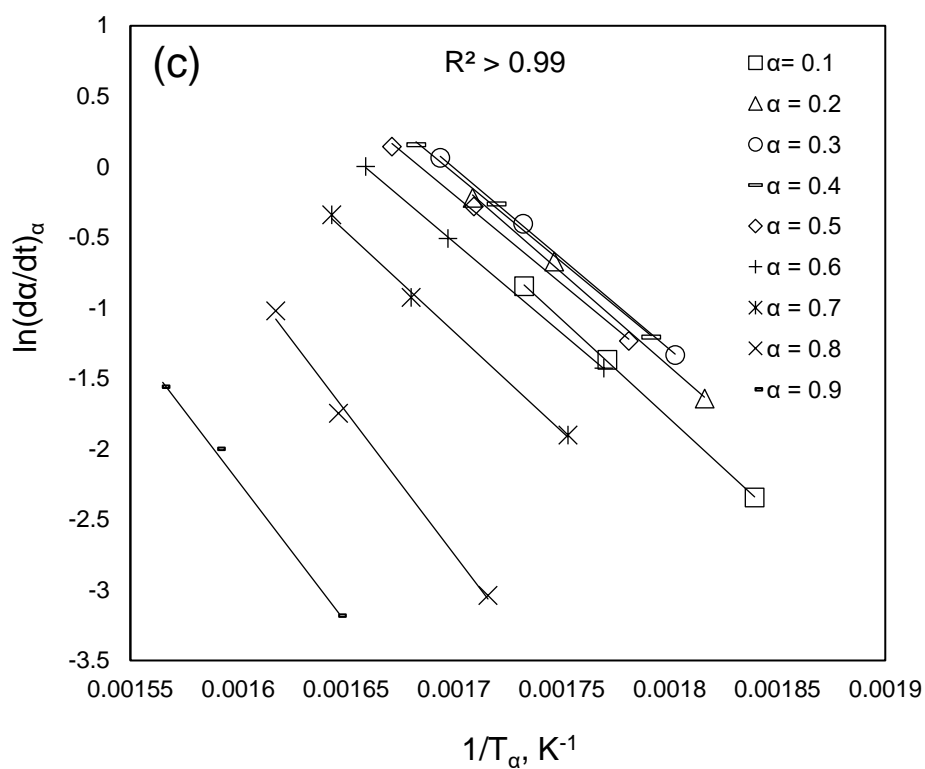


Figure 7: Experimental data fitting of the de-hydrochlorination stage of pure PVC using (a) FWO, (b) KAS and (c) Friedman models for activation energy and (d) Linear model fitting for the prediction of the reaction model  $f(\alpha)$  (see Figure S4 in the supplementary material for other decomposition stages).

Table 1 shows the kinetic parameters for the de-hydrochlorination of pure PVC. The average activation energy calculated using FWO, KAS and Friedman models are  $123.1 \pm 12.0$ ,  $119.8 \pm$

12.4 and  $122.6 \pm 24.2$  kJ/mol, respectively. Values presented here are in good agreement with those reported in literature [44, 56, 57]. The activation energy does not change significantly with conversion until a conversion level of 0.7 is reached. This suggests that a single reaction mechanism controls the degradation in the conversion range 0.1 – 0.7. Above 0.7, the activation energy rises appreciably to a maximum of 153.2 kJ/mol at a conversion of 0.9 (KAS). It is also noticed that above a conversion level of 0.7, the degradation changes from being controlled by the reaction model  $f(\alpha) = \alpha(1 - \alpha)^{2.13}$  to a second order reaction model  $f(\alpha) = (1 - \alpha)^2$ . Such behaviour might be attributed to the auto catalytic effect of PVC reported by Starnes and Ge [58]. In their work, they reported that the emitted HCl interacts with the formed polyene sequences to form polyenyl cation radicals leading to auto catalysis of de-hydrochlorination [58]. Thus, at high conversions (e.g., > 0.7), most of the emitted HCl will have already been swept by the purging gas resulting in lean amount of HCl in the vicinity of degrading PVC which makes further decomposition slow down, leading to high values of activation energy and an alteration in the reaction model. This also agrees with the fact that the used flow rate of nitrogen during the TGA runs was high (100 mL/min) which helps in sweeping emitted HCl at a faster rate.

Table 1: Kinetic parameters of de-hydrochlorination stage for pure PVC (first two stages in Figure 1).

Conversion, $\alpha$	FWO		KAS		Friedman		Linear model fitting		
	Activation energy, kJ/mol	Frequency factor, $\ln(A)^a$	Activation energy, kJ/mol	Frequency factor, $\ln(A)^a$	Activation energy, kJ/mol	Frequency factor, $\ln(A)^a$	Activation energy, kJ/mol	Frequency factor, $\ln(A)^a$	$f(\alpha)$
0.1	121.2	25.71	118.2	25.03	116.9	24.74	110.5	24.60	$\alpha(1 - \alpha)^{2.13}$
0.2	119.2	25.26	116.0	24.53	110.9	23.37			
0.3	117.7	24.92	114.3	24.14	107.0	22.48			
0.4	117.0	24.76	113.5	23.96	104.8	21.98			
0.5	116.2	24.58	112.6	23.76	105.0	22.03			
0.6	115.8	24.48	112.1	23.64	107.3	22.55			
0.7	116.6	24.67	112.9	23.83	117.6	24.89	<i>Transition region (no fitting)</i>		
0.8	128.5	27.37	125.2	26.62	167.7	36.28	158.3	32.65	$(1 - \alpha)^2$
0.9	155.4	33.49	153.2	32.99	166.6	36.03			
Average <sup>b</sup>	$123.1 \pm 12.0$	$26.14 \pm 2.73$	$119.8 \pm 12.4$	$25.39 \pm 2.83$	$122.6 \pm 24.2$	$26.04 \pm 5.50$	—		

a: Unit of A is  $\text{min}^{-1}$ .

b: Mean  $\pm$  SD

Table 2: Kinetic parameters of de-hydrochlorination stage for ZPVC mixture (stages two and three in Figure 3 (a)).

Conversion, $\alpha$	FWO		KAS		Friedman		Linear model fitting		
	Activation energy, kJ/mol	Frequency factor, $\ln(A)^a$	$f(\alpha)$						
0.1	117.2	25.56	114.7	24.94	79.2	16.22	87.7	20.09	$\frac{1}{2}(1-\alpha)^3$
0.2	104.3	22.39	101.0	21.58	91.6	19.27			
0.3	101.3	21.65	97.7	20.76	92.0	19.36			
0.4	100.0	21.33	96.2	20.40	100.1	21.36			
0.5	105.0	22.56	101.3	21.65	122.9	26.96			
0.5	105.0	22.56	101.3	21.65	122.9	26.96	125.9	26.60	$1-\alpha$
0.6	116.2	25.31	113.0	24.53	147.5	33.01			
0.7	125.8	27.67	123.0	26.98	148.4	33.23			
0.8	131.1	28.98	128.4	28.31	127.7	28.14			
0.9	123.2	27.03	119.8	26.20	87.1	18.16			
Average <sup>b</sup>	113.8 $\pm$ 10.9	24.72 $\pm$ 2.67	110.6 $\pm$ 11.2	23.93 $\pm$ 2.75	110.7 $\pm$ 24.9	23.97 $\pm$ 6.13	—		

a: Unit of A is  $\text{min}^{-1}$ .

b: Mean  $\pm$  SD

The addition of ZnO to PVC resulted in a change in the activation energy of the de-hydrochlorination stage (Table 2). The average activation energy over a conversion range of 0.1 – 0.9 changed from  $119.8 \pm 12.4$  to  $110.6 \pm 11.2$  kJ/mol when ZnO was added. To properly track the sequence of reactions, DTG and activation energy profiles were plotted against temperature for both PVC and ZPVC mixtures (Figure 8). Since the ZPVC mixture involves the decomposition of formed zinc oxy/hydroxide chlorides into solids (ZnO and  $\text{ZnCl}_2$ ) and gaseous  $\text{H}_2\text{O}$ , the studied kinetic parameters will therefore be for sequential reactions. This means, the reported parameters will represent those related to the slowest step in the sequence. As mentioned earlier, the first DTG peak for ZPVC in Figure 8 ( $206^\circ\text{C} < T < 222^\circ\text{C}$ ) is believed to be due to water evolution from the sequential ZnO chlorination (Reaction 16) followed by the formation/decomposition of  $\text{Zn}_5(\text{OH})_8\text{Cl}_2 \cdot \text{H}_2\text{O}$  (Reactions 17, 18 and 19). While these reactions are sequential, they could also proceed to a small extent in parallel due to possible incomplete reaction of emitted  $\text{H}_2\text{O}$  with  $\text{ZnCl}_2$  and ZnO. The activation energies in the same temperature range for that peak compare very well with those related to pure PVC

de-hydrochlorination (Figure 8) which involves the scission of the C-Cl bond. This means, at that stage, the controlling mechanism could therefore be related to the chlorine abstraction from PVC by ZnO, while the decomposition of the hydroxide chloride ( $Zn_5(OH)_8Cl_2 \cdot H_2O$ ) phase being the faster step. When the temperature increases to 230 °C (middle of second DTG peak of ZPVC), a drop in the activation energies can be seen to an average value of about 102.2 kJ/mol. This corresponds to a conversion range of 0.1 – 0.5, meaning that it is possible that a significant portion of the chlorine atoms in the PVC chain have been abstracted. This, in turn, would leave many chlorine atoms in the allylic position making their abstraction from PVC by ZnO more facile, and hence the drop in the activation energy (Figure 9). Rieche et al. [59] suggested that the charge separation in the C-Cl bond becomes accentuated when allylic sites are formed in the PVC chain. This would make the scission of this bond easier. Hence, for the second DTG peak of ZPVC, the controlling mechanism could be the decomposition of  $\beta$ - $Zn(OH)Cl/Zn_2OCl_2 \cdot 2H_2O$  into ZnO, ZnCl<sub>2</sub> and gaseous H<sub>2</sub>O. Such result is in agreement with the theoretical thermo-kinetic study performed by Ahmed et al. [54], where in their work the reported activation energy associated with the desorption of water from zinc oxychloride was 97.9 kJ/mol which compares well with the one reported here (102.2 kJ/mol). When the temperature reaches 262 °C, the activation energy starts rising to values comparable to those of pure PVC de-hydrochlorination (Figure 8). This is due to the fact that PVC in the ZPVC mixture starts to decompose normally into HCl and polyene. The similarity in the activation energy between ZPVC and PVC in the temperature range of 272 – 297 °C confirms what was suggested before by Zhang et al. [30] and Kosuda et al. [47] regarding the initial ZnO-PVC direct reaction and the subsequent normal PVC decomposition into HCl.

## PVC de-hydrochlorination alone and with ZnO

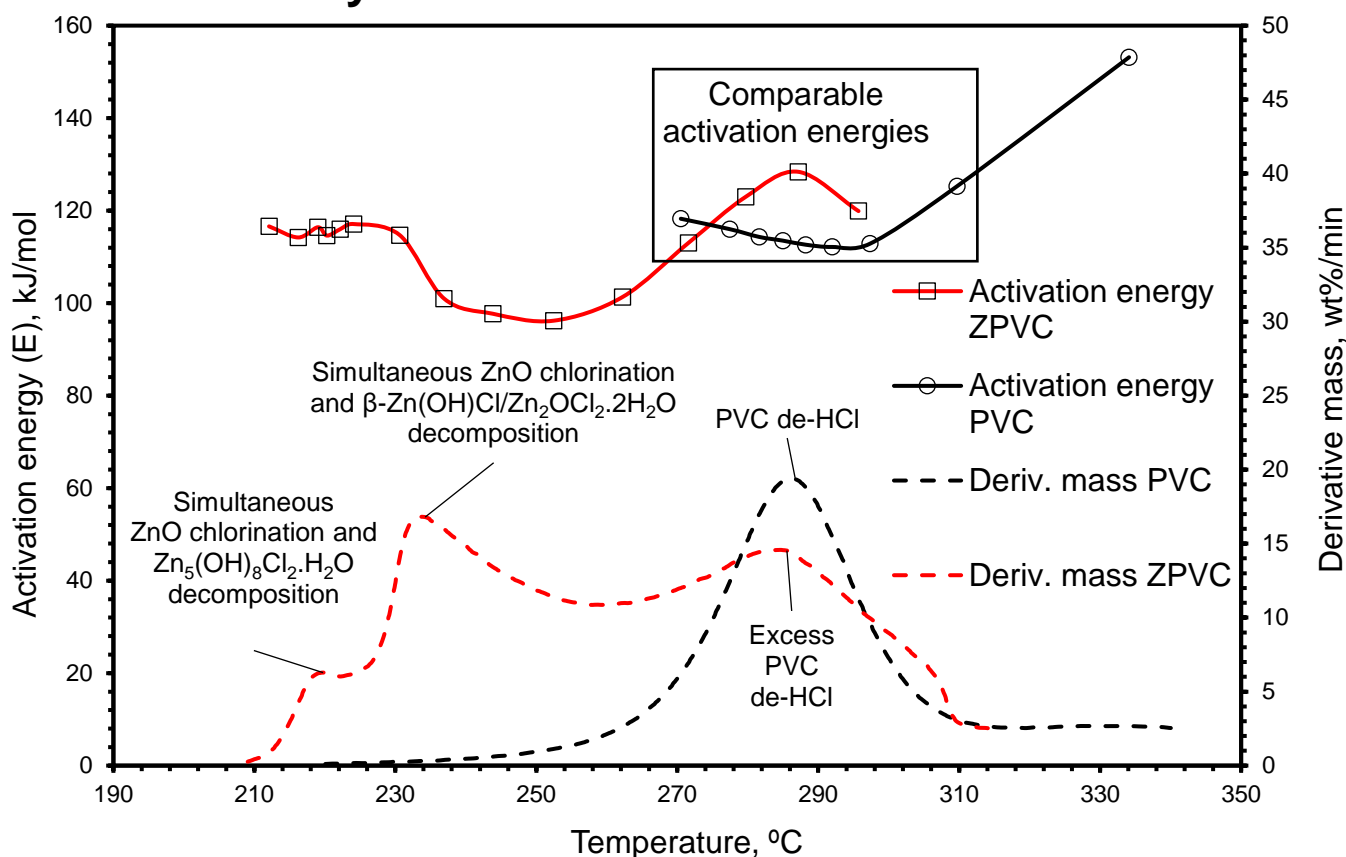


Figure 8: Activation energy and DTG profiles of the de-hydrochlorination stage in the case of ZPVC and PVC (activation energies were substituted from KAS model and all plots (including activation energy plots) were prepared based on 10 K/min profiles/data).

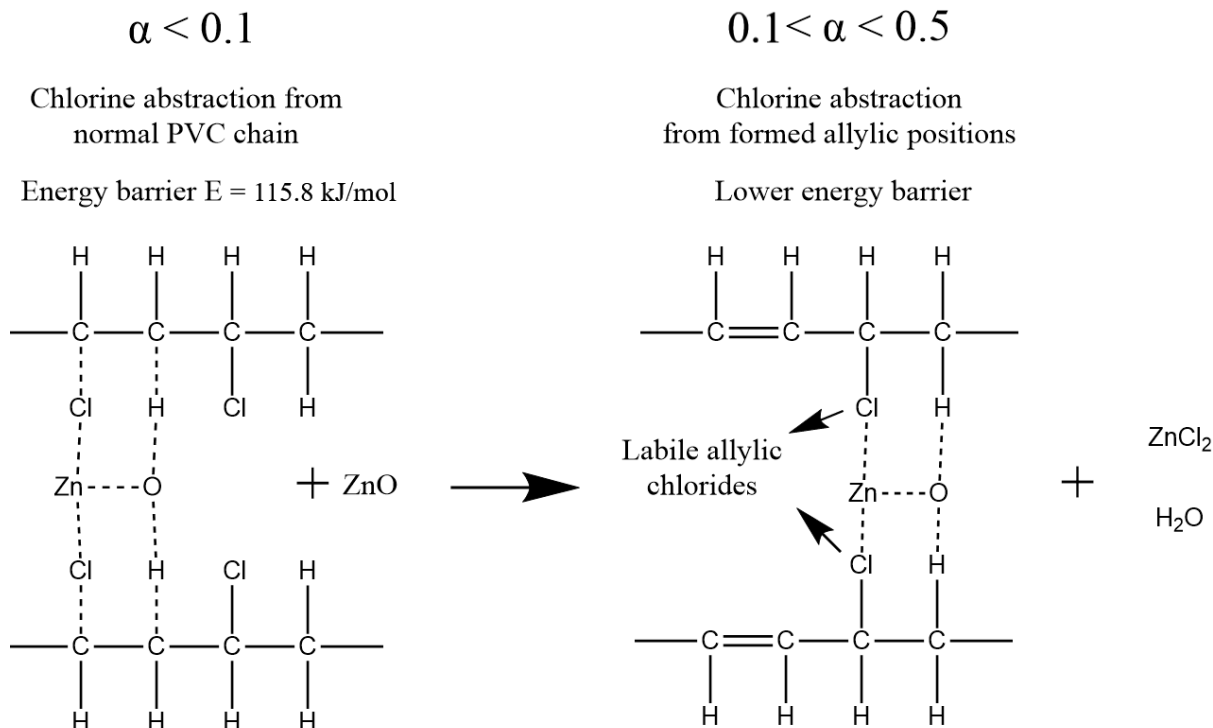


Figure 9: Possible formation of allylic chloride sites in the PVC chain by chlorine abstraction on ZnO.

#### 4.2.2. Kinetics of polyene thermal cracking stage for PVC and ZPVC

Table 3 shows the kinetic parameters of the polyene thermal cracking in the case of pure PVC.

Values of the activation energies for this stage are significantly higher than those related to dehydrochlorination; values averaged over a conversion range 0.1 – 0.9 are  $219.4 \pm 16.4$ ,  $218.4 \pm 17.7$  and  $205.8 \pm 13.9$  kJ/mol calculated using FWO, KAS and Friedman models, respectively.

Table 3: Kinetic parameters of polyene thermal cracking stage for pure PVC (third stage in Figure 1).

Conversion, $\alpha$	FWO		KAS		Friedman		Linear model fitting		
	Activation energy, kJ/mol	Frequency factor, $\ln(A)^a$	$f(\alpha)$						
0.1	254.6	41.28	256.2	41.56	226.7	36.37	201.8	31.67	$2(1 - \alpha)^{\frac{3}{2}}$
0.2	235.4	37.90	235.7	37.95	211.1	33.62			
0.3	228.2	36.63	227.9	36.58	230.5	37.04			
0.4	220.4	35.26	219.6	35.12	192.6	30.36			
0.5	213.8	34.10	212.5	33.87	208.2	33.11			
0.6	210.4	33.50	208.8	33.21	200.0	31.66			
0.7	207.7	33.02	205.8	32.69	198.4	31.38			
0.8	204.6	32.47	202.4	32.09	195.4	30.85			
0.9	199.9	31.65	197.2	31.17	189.0	29.73			
Average <sup>b</sup>	$219.4 \pm 16.4$	$35.09 \pm 2.89$	$218.4 \pm 17.7$	$34.92 \pm 3.11$	$205.8 \pm 13.9$	$32.68 \pm 2.45$	—————		

a: Unit of A is  $\text{min}^{-1}$ .

b: Mean  $\pm$  SD.

Table 4: Kinetic parameters of polyene thermal cracking stage for ZPVC mixture (fourth stage in Figure 3 (a)).

Conversion, $\alpha$	FWO		KAS		Friedman		Linear model fitting		
	Activation energy, kJ/mol	Frequency factor, $\ln(A)^a$	$f(\alpha)$						
0.1	115.3	16.38	109.3	15.36	97.5	13.34	101.2	13.82	$\frac{3}{2}(1 - \alpha)^{\frac{1}{3}}$
0.2	104.3	14.50	97.2	13.29	71.6	8.92			
0.3	95.5	13.00	87.7	11.67	70.1	8.66			
0.4	92.7	12.52	84.5	11.12	80.0	10.35			
0.5	92.7	12.52	84.4	11.10	87.2	11.58			
0.6	93.2	12.61	84.7	11.16	85.1	11.22			
0.7	92.5	12.49	83.9	11.02	73.2	9.19			
0.8	88.8	11.86	79.8	10.32	45.6	4.47			
0.9	83.5	10.95	74.0	9.33	66.4	8.03			
Average <sup>b</sup>	$95.4 \pm 8.7$	$12.98 \pm 1.49$	$87.3 \pm 9.7$	$11.60 \pm 1.66$	$75.2 \pm 14.0$	$9.53 \pm 2.39$	Did not fit in the model		

a: Unit of A is  $\text{min}^{-1}$ .

b: Mean  $\pm$  SD.

A drop in the values of the activation energy is observed as the reaction progresses further. This might be attributed to the fact that the polyene thermal cracking stage involves the evolution of different hydrocarbons [46]. This, in turn, may lead to the formation of separate transition states at different conversion levels based on the structure of the formed hydrocarbon, which then leads to a continuous change in the activation energy barrier with conversion. Despite the variation of the activation energy with conversion, a single reaction model was able to fit the experimental data in the conversion range of 0.1 – 0.9. The reaction model suggests that the decomposition is chemical reaction controlled throughout the stage with a reaction order of  $\frac{3}{2}$  (Table 3).

Table 4 reports the kinetic parameters of the polyene thermal cracking stage for the ZPVC mixture. Figure 3 (b) as well as the thermodynamics analysis reported in Al-Harashseh [7] and the TGA profile for  $\text{ZnCl}_2$  presented in Jones et al. [55] suggest that  $\text{ZnCl}_2$  volatilises in the temperature range of 400 – 520 °C. This means that the reported kinetic parameters in Table 4 represent apparent values from simultaneous polyene thermal cracking and volatilisation of  $\text{ZnCl}_2$ . The activation energy dropped considerably from  $218.4 \pm 17.7$  kJ/mol in the case of pure PVC (Table 3) to  $87.3 \pm 9.7$  kJ/mol in the case of ZPVC mixture. Such a drop can be attributed to the contribution of the volatilisation of  $\text{ZnCl}_2$  on the apparent activation energy. This is because physical processes, in general, are known to exhibit significantly lower activation energies compared to chemical ones. Thus, the overall calculated activation energy significantly decreased. The overall process was able to be described by one reaction model with a reaction order of  $\frac{1}{3}$ .

The importance of the data reported in this work lies in the fact that there is a significant variation in the chemistry of EAFD world-wide which depends on the followed smelting practices and the type of the feeding materials to EAFs. In fact, further studies on the effect of other important minerals in EAFD such  $\text{Fe}_2\text{O}_3$ ,  $\text{Fe}_3\text{O}_4$ ,  $\text{ZnFe}_2\text{O}_4$ , and  $\text{PbO}$  on the decomposition

kinetics of PVC should be done. Such studies on the interaction between PVC and other metal oxides allow the prediction of the process kinetics and the appropriate holding temperatures for best process economics for different EAFDs with different chemistries (i.e., EAFD from different sources/countries). Thus, for future work, we believe other deep kinetics investigations on the effect of other EAFD constituents (mentioned earlier) on PVC degradation should be considered.

## 5. Conclusions

This work studied the kinetics and the behaviour of PVC thermal decomposition in the presence of a stoichiometric quantity of ZnO. Apparent activation energy, frequency factor, and the reaction model were extracted based on non-isothermal study of thermogravimetric scans at 10, 30, and 50 K/min under inert environment. The following conclusions are made:

- The TGA data suggests an excellent chlorine fixing ability of ZnO such that when a stoichiometric amount of ZnO was added (39.4 wt%), the percentage of HCl captured was ~ 28.9, 42.6 and 46.3% at heating rates of 10, 30 and 50 K/min, respectively.
- The formation of water soluble zinc chloride is clearly seen in the SEM and XRD scans suggesting that PVC can be incorporated with metallurgical wastes such as EAFD for the extraction of metallic zinc through water leaching of the post pyrolysis residue.
- It is recommended that an excess PVC amount is used in the co-thermal treatment with ZnO containing wastes (such as EAFD) to completely chlorinate this constituent, thus preventing the formation of the insoluble  $Zn_5(OH)_8Cl_2 \cdot H_2O$  (Simonkolleite) phase.
- A noticeable change in the activation energy of PVC de-hydrochlorination was witnessed when ZnO was added. The variation of the activation energy with temperature suggested different controlling mechanisms at different conversion ranges between chlorine abstraction and thermal decomposition of zinc oxy/hydroxide chloride species.

- ZnO can be categorised as an active catalyst for PVC de-hydrochlorination decreasing its onset decomposition temperature from 272 to 214 °C.
- It is suggested that ZnO initially abstracts chlorine from PVC to form ZnCl<sub>2</sub> which then reacts with ZnO and emitted H<sub>2</sub>O to form the oxy/hydroxide chloride species Zn<sub>2</sub>OCl<sub>2</sub>.2H<sub>2</sub>O/β-Zn(OH)Cl. These phases then start to decompose at temperatures above 222 °C into ZnCl<sub>2</sub>, ZnO and H<sub>2</sub>O.
- A significant drop in the activation energy of polyene thermal cracking was seen when ZnO was added which might be assigned to the physical contribution of the volatilisation of formed ZnCl<sub>2</sub> in that temperature range.

## References

- [1] M. Al-Harashsheh, A. Al-Otoom, L. Al-Makhadmeh, I.E. Hamilton, S. Kingman, S. Al-Asheh, M. Hararah, Pyrolysis of poly(vinyl chloride) and—electric arc furnace dust mixtures, *Journal of Hazardous Materials*, 299 (2015) 425-436.
- [2] P. Oustadakis, P.E. Tsakiridis, A. Katsiapi, S. Agatzini-Leonardou, Hydrometallurgical process for zinc recovery from electric arc furnace dust (EAFD): Part I: Characterization and leaching by diluted sulphuric acid, *Journal of Hazardous Materials*, 179 (2010) 1-7.
- [3] U. Brandner, J. Antrekowitsch, M. Leuchtenmueller, A review on the fundamentals of hydrogen-based reduction and recycling concepts for electric arc furnace dust extended by a novel conceptualization, *International Journal of Hydrogen Energy*, (2021).
- [4] J. Madias, *Electric Furnace Steelmaking*, in: *Treatise on Process Metallurgy*, 2014, pp. 271-300.
- [5] G.-S. Lee, Y.J. Song, Recycling EAF dust by heat treatment with PVC, *Minerals engineering*, 20 (2007) 739-746.
- [6] N. Tsubouchi, H. Hashimoto, N. Ohtaka, Y. Ohtsuka, Chemical characterization of dust particles recovered from bag filters of electric arc furnaces for steelmaking: Some factors influencing the formation of hexachlorobenzene, *Journal of hazardous materials*, 183 (2010) 116-124.
- [7] M. Al-Harashsheh, Thermodynamic Analysis on the Thermal Treatment of Electric Arc Furnace Dust-PVC Blends, *Arabian Journal for Science and Engineering*, (2017) 1-13.
- [8] T. Havlik, B. Friedrich, S. Stopic, Pressure leaching of EAF dust with sulphuric acid, *Erzmetall*, 57 (2004) 83-90.
- [9] T. Havlik, M. Turzakova, S. Stopic, B. Friedrich, Atmospheric leaching of EAF dust with diluted sulphuric acid, *Hydrometallurgy*, 77 (2005) 41-50.
- [10] A.J.B. Dutra, P.R.P. Paiva, L.M. Tavares, Alkaline leaching of zinc from electric arc furnace steel dust, *Minerals Engineering*, 19 (2006) 478-485.
- [11] L.A. Al-Makhadmeh, M.A. Batiha, M.S. Al-Harashsheh, I.S. Altarawneh, S.E. Rawadieh, The Effectiveness of Zn Leaching from EAFD Using Caustic Soda, *Water, Air, & Soil Pollution*, 229 (2018) 33.
- [12] M. Morcali, O. Yucel, A. Aydin, B. Derin, Carbothermic reduction of electric arc furnace dust and calcination of waelz oxide by semi-pilot scale rotary furnace, *Journal of Mining and Metallurgy B: Metallurgy*, 48 (2012) 173-184.
- [13] T. Suetens, B. Klaasen, K. Van Acker, B. Blanpain, Comparison of electric arc furnace dust treatment technologies using exergy efficiency, *Journal of cleaner production*, 65 (2014) 152-167.
- [14] H.-n. Zhang, J.-l. Li, A.-j. Xu, Q.-x. Yang, D.-f. He, N.-y. Tian, Carbothermic reduction of zinc and iron oxides in electric arc furnace dust, *Journal of iron and steel research international*, 21 (2014) 427-432.
- [15] M. Cruells, A. Roca, C. Núnñez, Electric arc furnace flue dusts: characterization and leaching with sulphuric acid, *Hydrometallurgy*, 31 (1992) 213-231.
- [16] V. Montenegro, P. Oustadakis, P.E. Tsakiridis, S. Agatzini-Leonardou, Hydrometallurgical treatment of steelmaking electric arc furnace dusts (EAFD), *Metallurgical and Materials Transactions B*, 44 (2013) 1058-1069.
- [17] F. Kukurugya, T. Vindt, T. Havlík, Behavior of zinc, iron and calcium from electric arc furnace (EAF) dust in hydrometallurgical processing in sulfuric acid solutions: Thermodynamic and kinetic aspects, *Hydrometallurgy*, 154 (2015) 20-32.
- [18] Y.Y. Teo, H.S. Lee, Y.C. Low, S.W. Choong, K.O. Low, Hydrometallurgical extraction of zinc and iron from electric arc furnace dust (EAFD) using hydrochloric acid, *Journal of Physical Science*, 29 (2018) 49-54.

- [19] M.A. Keane, Catalytic conversion of waste plastics: focus on waste PVC, *Journal of Chemical Technology & Biotechnology: International Research in Process, Environmental & Clean Technology*, 82 (2007) 787-795.
- [20] J. Yu, L. Sun, C. Ma, Y. Qiao, H. Yao, Thermal degradation of PVC: A review, *Waste Management*, 48 (2016) 300-314.
- [21] Ceresana-Research, Additives for polymers, (2014) pp. 10–11.
- [22] M. Al-Harashseh, J. Al-Nu'airat, A. Al-Otoom, H. Al-jabali, M. Al-zoubi, Treatments of electric arc furnace dust and halogenated plastic wastes: A review, *Journal of Environmental Chemical Engineering*, (2018) 102856.
- [23] I. Mersiowsky, R. Stegmann, J. Ejlertsson, Long term behaviour of poly (vinyl chloride) products under soil buried and landfill conditions, *Plastics, rubber and composites*, 28 (1999) 321-326.
- [24] J.C. Wagner, A.E. Green, Correlation of chlorinated organic compound emissions from incineration with chlorinated organic input, *Chemosphere*, 26 (1993) 2039-2054.
- [25] T. Katami, A. Yasuhara, T. Okuda, T. Shibamoto, Formation of PCDDs, PCDFs, and coplanar PCBs from polyvinyl chloride during combustion in an incinerator, *Environmental science & technology*, 36 (2002) 1320-1324.
- [26] M. Al-harashseh, S. Kingman, L. Al-Makhadmah, I.E. Hamilton, Microwave treatment of electric arc furnace dust with PVC: Dielectric characterization and pyrolysis-leaching, *Journal of Hazardous Materials*, 274 (2014) 87-97.
- [27] M. Al-Harashseh, Y. Orabi, S. Al-Asheh, Comparative study on the pyrolysis and leachability of washed/unwashed electric arc furnace dust-PVC mixtures and their residues, *Journal of Environmental Chemical Engineering*, (2021) 105410.
- [28] Y. Masuda, T. Uda, O. Terakado, M. Hirasawa, Pyrolysis study of poly (vinyl chloride)–metal oxide mixtures: quantitative product analysis and the chlorine fixing ability of metal oxides, *Journal of Analytical and Applied Pyrolysis*, 77 (2006) 159-168.
- [29] A. Ballistreri, S. Foti, P. Maravigna, G. Montaudo, E. Scamporrino, Effect of metal oxides on the evolution of aromatic hydrocarbons in the thermal decomposition of PVC, *Journal of Polymer Science: Polymer Chemistry Edition*, 18 (1980) 3101-3110.
- [30] B. Zhang, X.-Y. Yan, K. Shibata, T. Uda, M. Tada, M. Hirasawa, Thermogravimetric-mass spectrometric analysis of the reactions between oxide (ZnO, Fe<sub>2</sub>O<sub>3</sub> or ZnFe<sub>2</sub>O<sub>4</sub>) and polyvinyl chloride under inert atmosphere, *Materials Transactions, JIM*, 41 (2000) 1342-1350.
- [31] H.E. Kissinger, Reaction kinetics in differential thermal analysis, *Analytical chemistry*, 29 (1957) 1702-1706.
- [32] H.L. Friedman, Kinetics of thermal degradation of char-forming plastics from thermogravimetry. Application to a phenolic plastic, in: *Journal of polymer science part C: polymer symposia*, Wiley Online Library, 1964, pp. 183-195.
- [33] T. Ozawa, A new method of analyzing thermogravimetric data, *Bulletin of the chemical society of Japan*, 38 (1965) 1881-1886.
- [34] J.H. Flynn, L.A. Wall, General treatment of the thermogravimetry of polymers, *Journal of Research of the National Bureau of Standards. Section A, Physics and Chemistry*, 70 (1966) 487.
- [35] T. Akahira, T. Sunose, Res. Report Chiba Inst. Technol, Sci. Technol, 16 (1971) 22.
- [36] A. Altomare, N. Corriero, C. Cuocci, A. Falcicchio, A. Moliterni, R. Rizzi, QUALX2. 0: a qualitative phase analysis software using the freely available database POW\_COD, *Journal of Applied Crystallography*, 48 (2015) 598-603.
- [37] J. Šesták, G. Berggren, Study of the kinetics of the mechanism of solid-state reactions at increasing temperatures, *Thermochimica Acta*, 3 (1971) 1-12.

- [38] S. Vyazovkin, A.K. Burnham, J.M. Criado, L.A. Pérez-Maqueda, C. Popescu, N. Sbirrazzuoli, ICTAC Kinetics Committee recommendations for performing kinetic computations on thermal analysis data, *Thermochimica acta*, 520 (2011) 1-19.
- [39] A.W. Coats, J. Redfern, Kinetic parameters from thermogravimetric data, *Nature*, 201 (1964) 68-69.
- [40] S. Vyazovkin, N. Sbirrazzuoli, Isoconversional kinetic analysis of thermally stimulated processes in polymers, *Macromolecular Rapid Communications*, 27 (2006) 1515-1532.
- [41] S. Vyazovkin, Isoconversional kinetics, in: *Handbook of thermal analysis and calorimetry*, Elsevier, 2008, pp. 503-538.
- [42] C. Doyle, Estimating isothermal life from thermogravimetric data, *Journal of Applied Polymer Science*, 6 (1962) 639-642.
- [43] S. Vyazovkin, Determining Preexponential Factor in Model-Free Kinetic Methods: How and Why?, *Molecules*, 26 (2021) 3077.
- [44] A. Marcilla, M. Beltrán, Thermogravimetric kinetic study of poly(vinyl chloride) pyrolysis, *Polymer Degradation and Stability*, 48 (1995) 219-229.
- [45] S.C. Oh, W.-T. Kwon, S.-R. Kim, Dehydrochlorination characteristics of waste PVC wires by thermal decomposition, *Journal of Industrial and Engineering Chemistry*, 15 (2009) 438-441.
- [46] M. Blazso, E. Jakab, Effect of metals, metal oxides, and carboxylates on the thermal decomposition processes of poly (vinyl chloride), *Journal of Analytical and Applied Pyrolysis*, 49 (1999) 125-143.
- [47] T. Kosuda, T. Okada, S. Nozaka, Y. Matsuzawa, T. Shimizu, S. Hamanaka, S. Mishima, Characteristics and mechanism of low temperature dehydrochlorination of poly (vinyl chloride) in the presence of zinc (II) oxide, *Polymer degradation and stability*, 97 (2012) 584-591.
- [48] D.W. Green, R.H. Perry, *Perry's Chemical Engineers' Handbook*, Eighth Edition, McGraw-Hill Education, 2007.
- [49] H. Tanaka, A. Fujioka, Influence of thermal treatment on the structure and adsorption properties of layered zinc hydroxychloride, *Materials Research Bulletin*, 45 (2010) 46-51.
- [50] A. Moezzi, M. Cortie, A. McDonagh, Transformation of zinc hydroxide chloride monohydrate to crystalline zinc oxide, *Dalton Transactions*, 45 (2016) 7385-7390.
- [51] O. Srivastava, E. Secco, Studies on metal hydroxy compounds. I. Thermal analyses of zinc derivatives  $\epsilon$ -Zn(OH)<sub>2</sub>, Zn<sub>5</sub>(OH)<sub>8</sub>Cl<sub>2</sub>·H<sub>2</sub>O,  $\beta$ -ZnOHCl, and ZnOHF, *Canadian Journal of Chemistry*, 45 (1967) 579-583.
- [52] C.A. Sorrell, Suggested chemistry of zinc oxychloride cements, *Journal of the American Ceramic Society*, 60 (1977) 217-220.
- [53] O. Garcia-Martinez, E. Vila, J.M. de Vidales, R. Rojas, K. Petrov, On the thermal decomposition of the zinc (II) hydroxide chlorides Zn<sub>5</sub>(OH)<sub>8</sub>Cl<sub>2</sub>·H<sub>2</sub>O and  $\beta$ -Zn(OH)Cl, *Journal of Materials Science*, 29 (1994) 5429-5434.
- [54] O.H. Ahmed, M. Altarawneh, M. Al-Harashseh, Z.-T. Jiang, B.Z. Dlugogorski, Recycling of zincite (ZnO) via uptake of hydrogen halides, *Physical Chemistry Chemical Physics*, 20 (2018) 1221-1230.
- [55] F. Jones, H. Tran, D. Lindberg, L. Zhao, M. Hupa, Thermal stability of zinc compounds, *Energy & fuels*, 27 (2013) 5663-5669.
- [56] S. Kim, Pyrolysis kinetics of waste PVC pipe, *Waste management*, 21 (2001) 609-616.
- [57] G. Sivalingam, R. Karthik, G. Madras, Effect of metal oxides on thermal degradation of poly (vinyl acetate) and poly (vinyl chloride) and their blends, *Industrial & engineering chemistry research*, 42 (2003) 3647-3653.
- [58] W.H. Starnes, X. Ge, Mechanism of autocatalysis in the thermal dehydrochlorination of poly (vinyl chloride), *Macromolecules*, 37 (2004) 352-359.

[59] A. Rieche, A. Grimm, H. Mücke, Untersuchungen über Stabilität von Suspensions-PVC, Kunststoffe, 52 (1962) 265-268.

### **Appendix 3: Thermodynamic, pyrolytic, and kinetic investigation on the thermal decomposition of polyvinyl chloride in the presence of franklinite**

Sanad Altarawneh<sup>1,\*</sup>, Mohammad Al-Harabsheh<sup>2</sup>, Chris Dodds<sup>1</sup>, Adam Buttress<sup>1</sup>, Sam Kingman<sup>1</sup>

<sup>1</sup> Faculty of Engineering, University of Nottingham, Nottingham, NG7 2RD, UK

<sup>2</sup> Chemical Engineering Department, Jordan University of Science and Technology, Irbid, 22110, Jordan

\*corresponding author: [sanad.altarawneh@nottingham.ac.uk](mailto:sanad.altarawneh@nottingham.ac.uk)

#### **Abstract**

Thermal co-treatment of Electric Arc Furnace Dust (EAFD) and polyvinyl chloride (PVC) may provide a viable route for reprocessing these hazardous materials within the circular economy. To develop and optimise a commercial treatment process, the complex mechanistic pathway resulting from the reaction of these two wastes must be understood. Franklinite ( $\text{ZnFe}_2\text{O}_4$ ) is a major zinc containing phase in EAFD and to date, little work has been undertaken on the decomposition of PVC in its presence. Herein, we present a thermodynamic, pyrolytic, and kinetic study of PVC degradation in the presence of  $\text{ZnFe}_2\text{O}_4$ . It was found that,  $\text{ZnFe}_2\text{O}_4$  decomposed to its associated halides. Additionally, the kinetics data confirmed the catalytic activity of  $\text{ZnFe}_2\text{O}_4$ , dropping the de-hydrochlorination onset temperature of PVC from 272 to 235 °C. The distribution of the activation energy with conversion suggests the presence of several competitive reactions each with a different energy barrier. In such a case, reaction channelling can take place leading to selective zinc chlorination.

Moreover, since the reduction of  $\text{Fe}_2\text{O}_3$  is slow at low temperatures, it is recommended to operate at a temperature as low as 235 °C which can promote the chlorination selectivity towards zinc leaving iron bearing compounds in their stable form ( $\text{Fe}_2\text{O}_3$ ).

Keywords: non-isothermal kinetics, zinc iron oxide, TGA, activation energy

## 1. Introduction

During steel manufacturing, hazardous electric arc furnace dust (EAFD) is generated as a waste by-product. About 7.5 million tons of EAFD is globally produced annually from steel manufacturing (Teo et al., 2018). The chemistry of the generated EAFD strongly depends on the quality of the scrap being employed in the smelting and the composition of other input materials (KiranKumar and Roy, 2022). Despite the variation in EAFD chemistry, the presence of toxic heavy metals such as Pb and Cd has been reported (Al-Harashsheh, 2017; Laubertova et al., 2020). Hence, the large production rate of this material along with the toxic nature of some of its constituents, poses a huge environmental threat. This, in turn, puts a huge pressure on steel manufacturers who resort to landfilling as their major disposal strategy.

Aside to landfilling, the scientific community has directed significant endeavour towards the utilisation of EAFD as a source of zinc by means of hydrometallurgical (Al-Makhadmeh et al., 2018; Laubertova et al., 2020; Oustadakis et al., 2010; Teo et al., 2018) and pyrometallurgical (Omran et al., 2019; Sinaga et al., 2019; Ye et al., 2020; Zhang et al., 2019) treatment routes. Currently, the latter has reached an industrial level. About 83% of EAFD is recycled in the Waelz kiln process (Yakornov et al., 2017). However, the pyrometallurgical approach is only capable of increasing the zinc concentration in EAFD (zinc enrichment) by means of volatilisation, oxidation, and then collection without a complete separation of the metal at a high purity. The furnace utilised in the Waelz process also operates at a temperature of 1200 °C (Suetens et al., 2014) which makes this process highly energy intensive. Industrial uptake of hydrometallurgical treatment methods, in contrast, is limited due to the resistive nature of franklinite ( $ZnFe_2O_4$ ) which prevents the complete extraction of zinc and highlights the importance of rejecting iron from the leaching liquor when acidic reagents are used.

Plastics are also accumulated in large quantities. Polyvinyl chloride (PVC) is a versatile thermoplastic and is classified an industrial polymer with high importance (Marcilla and

Beltrán, 1995). PVC is ranked the third (after polypropylene and high and low density Polyethylene) in terms of converters plastic demand in Europe at 4.7 million tons in 2020 (Plastics-Europe, 2021). This could be assigned to the superior properties and the high versatility of this material. Nonetheless, PVC is considered one of the most troublesome wastes as it is difficult to treat in an environmentally benign manner (Kim, 2001) which can be attributed to the high chlorine content in PVC. Upon thermal treatment, large amounts of hydrogen chloride (HCl) are evolved along with undesirable chlorinated hydrocarbons (dioxins) (Miranda et al., 1999). Due to these issues, the most prevalent route for the disposal of PVC is landfilling. However, the study conducted by (Mersiowsky et al., 1999) suggests a high stability of PVC in landfills. Hence, landfilling results in the indefinite accumulation of PVC which will lead to the occupation of vast dumping areas. Therefore, it is suggested that the most suitable way for recycling PVC would be pyrolysis with mitigation of the emissions accompanied by the thermal decomposition using additives such as metal oxides.

Recent research has focused on the co-thermal treatment of PVC with metallurgical wastes such as EAFD and with metal oxides (Al-Harashsheh, 2017; Al-Harashsheh et al., 2021a; Al-Harashsheh et al., 2021b; Altarawneh et al., 2021; Ji et al., 2020; Lee and Song, 2007; Meng et al., 2021; Ye et al., 2021). The reason behind these studies is to show the capability of metal oxides for mitigating the harmful emissions evolved from decomposing PVC, which would allow recycling via pyrolysis/incineration. (Lee and Song, 2007) confirmed the formation of zinc, lead, and cadmium chlorides upon the thermal treatment of EAFD with PVC. A series of papers published by Al-Harashsheh et al. studied the kinetics (Al-Harashsheh et al., 2015), thermodynamics (Al-Harashsheh, 2017), and zinc and lead extraction possibility (Al-Harashsheh et al., 2022; Al-Harashsheh et al., 2021a; Al-harashsheh et al., 2014; Al-Harashsheh et al., 2021b) upon the co-thermal treatment of EAFD with PVC. However, none of these papers identified the specific effect of each EAFD constituent on the kinetics of the decomposing PVC. Such an

aspect is important since the chemistry of EAFD varies greatly from one country to another making it difficult to extrapolate the results from one specific EAFD from a certain country to all other EAFD generated world-wide. Hence, there has been a focus on establishing a solid foundation on the pyrolysis of PVC with each metal oxide separately. (Ye et al., 2021) studied the effect of magnetite ( $\text{Fe}_3\text{O}_4$ ) on the emissions of decomposing PVC and its ability to capture HCl. (Meng et al., 2021) studied the effect of seven metal oxides: CaO, ZnO (two types), CuO, MgO,  $\text{Al}_2\text{O}_3$  and  $\text{Fe}_2\text{O}_3$  on the thermal degradation of PVC including the onset and maximum rate temperature and their ability to capture HCl. (Altarawneh et al., 2021) studied the effect of ZnO on the kinetics of degrading PVC and the capability of ZnO to capture HCl. To the best of our knowledge, the only study addressed the effect of  $\text{ZnFe}_2\text{O}_4$  on the decomposition of PVC was that conducted by (Zhang et al., 2000). However, that study focused on characterising the gaseous emissions from PVC degradation in the presence of  $\text{ZnFe}_2\text{O}_4$  without a deep consideration of the kinetics aspect of the decomposition.

Since  $\text{ZnFe}_2\text{O}_4$  is considered one of the main sources of zinc in EAFD; reported at 20.27 wt% of EAFD (Al-Harashseh, 2017), we believe that a comprehensive systematic non-isothermal kinetic study of  $\text{ZnFe}_2\text{O}_4$ -PVC (ZF-PVC) mixture should provide researchers in this field with valuable information regarding reaction rates. This contributes towards process optimisation in terms of optimum operating temperatures, holding times, and reactor sizing to achieve a certain extraction/conversion levels. Herein, an attempt is made to study the thermal behaviour of PVC and its mixture with  $\text{ZnFe}_2\text{O}_4$  along with a complete characterisation of the solid products generated from their pyrolysis. The kinetic data associated with the thermal degradation of PVC and its mixture with  $\text{ZnFe}_2\text{O}_4$  were extracted. The kinetic data was then used for the assessment of the chemical stability of PVC and how it reflects on the selective extraction of zinc.

## **2. Non-isothermal kinetics**

## 2.1. The overall rate equation

The reaction rate of thermally stimulated processes is usually represented by the extent of conversion  $X$ , which is given as follows:

$$X = \frac{W_o - W}{W_o - W_f} \quad (1)$$

Where  $W_o$  is the initial weight% at the beginning of the mass loss,  $W_f$  is the final weight% at the end of the mass loss, and  $W$  is the weight% at any time  $t$ . The kinetic rate equation can be represented by the temperature dependent rate constant  $k(T)$  and the temperature independent reaction model  $f(X)$  (Al-Harahsheh et al., 2018):

$$\frac{dX}{dt} = k(T)f(X) \quad (2)$$

The temperature dependency of the reaction rate can be represented through the Arrhenius function (Vyazovkin et al., 2011):

$$k(T) = A. \exp\left(-\frac{E}{RT}\right) \quad (3)$$

Where  $A$  is the frequency factor ( $\text{min}^{-1}$ ),  $E$  is the activation energy (J/mol),  $R$  is the universal gas constant (8.314 J/mol.K), and  $T$  is the temperature (K).

The mathematical formula for the reaction model  $f(X)$  depends on the controlling mechanism of the overall mass loss. A generalised empirical model was introduced by (Šesták and Berggren, 1971) for the mathematical expression of  $f(X)$  as follows:

$$f(X) = X^m(1 - X)^n[-\ln(1 - X)]^p \quad (4)$$

A different combination of  $m$ ,  $n$ , and  $p$  resemble different reaction models (Vyazovkin et al., 2011). Substituting Equations 3 and 4 in 2 yields the following:

$$\frac{dX}{dt} = A. \exp\left(-\frac{E}{RT}\right) (X^m(1 - X)^n[-\ln(1 - X)]^p) \quad (5)$$

Equation 5 represents the rate equation in the differential form. For non-isothermal kinetics at a fixed heating rate of  $\beta = \frac{dT}{dt}$ , the differentiation of the conversion  $X$  can be represented with respect to temperature  $T$  as follows:

$$\frac{dX}{dt} = \frac{dT}{dt} \cdot \frac{dX}{dT} = \beta \cdot \frac{dX}{dT} \quad (6)$$

Substituting Equation 6 in 5 yields:

$$\beta \cdot \frac{dX}{dT} = A \cdot \exp\left(-\frac{E}{RT}\right) (X^m(1-X)^n[-\ln(1-X)]^p) \quad (7)$$

Re-arranging Equation 7 and integrating both sides generates the integral form of the rate equation, which can be written as:

$$\int_0^X \frac{dX}{(X^m(1-X)^n[-\ln(1-X)]^p)} = \frac{A}{\beta} \int_{T_0}^T \exp\left(-\frac{E}{RT}\right) dT \quad (8)$$

Where  $T_0$  is the temperature corresponding to a conversion of zero. At low temperatures, the reaction rate is very low (Ozawa, 1965) making the replacement of  $T_0$  by zero a valid assumption:

$$\int_0^X \frac{dX}{(X^m(1-X)^n[-\ln(1-X)]^p)} = \frac{A}{\beta} \int_0^T \exp\left(-\frac{E}{RT}\right) dT \quad (9)$$

The right hand side of Equation 9 has no exact integration (Coats and Redfern, 1964). Hence, different approaches were followed to either utilise the differential form of the rate equation (Equations 5 or 7) or the integral form (Equation 9) whereby the temperature integration is approximated.

## 2.2. Calculation of the activation energy

### 2.2.1. Iso-conversional kinetic methods

The iso-conversional principle gained its strength from the fact that the activation energy can be obtained without assuming a reaction model. This, in turn, allows the change in the

activation energy with conversion for complicated multi-stage decompositions to be tracked. The iso-conversional principle suggests that the reaction rate is a function of temperature only at a fixed conversion value which can be visualised by taking the logarithmic derivative of the rate with respect to the reciprocal of temperature (Vyazovkin et al., 2011):

$$\left[ \frac{\partial \ln \left( \frac{dX}{dt} \right)}{\partial T^{-1}} \right]_X = \left[ \frac{\partial \ln f(X)}{\partial T^{-1}} \right]_X + \left[ \frac{\partial \ln(k(T))}{\partial T^{-1}} \right]_X = \frac{-E_X}{R} \quad (10)$$

Equation 10 suggests that the change in the rate depends on temperature only at a fixed value of conversion. Thus, when the mass loss curve shows a lateral shift towards a higher temperature at a higher heating rate, this phenomenon can be exploited for extracting the activation energy without needing to assume a reaction model.

#### 2.2.1.1. Integral iso-conversional method

The Kissinger-Akahira-Sunose (KAS) integral equation (Akahira and Sunose, 1971; Kissinger, 1957) can be written as follows:

$$\ln \left( \frac{\beta_i}{T^2_{x,i}} \right) = \ln \left( \frac{A_x R}{E_x g(X)} \right) - \frac{E_x}{RT_{x,i}} \quad (11)$$

This method should ideally be used in cases where the change in the activation energy with conversion is small. A plot of  $\ln \left( \frac{\beta_i}{T^2_{x,i}} \right)$  against  $\frac{1}{T_{x,i}}$  should produce a straight line with a slope of  $-\frac{E_x}{R}$  from which the activation energy is extracted.

#### 2.2.1.2 Differential iso-conversional method

By taking the natural logarithm on both sides of Equation 7, one arrives at the Friedman model (Friedman, 1964):

$$\ln \left[ \beta_i \cdot \frac{dX}{dT} \right]_{X,i} = \ln \left[ \frac{dX}{dt} \right]_{X,i} = \ln[A \cdot f(X)]_{X,i} - \frac{E_x}{RT_{x,i}} \quad (12)$$

For a mass loss with a smooth (non-noisy) derivative thermogravimetric (DTG) signal, the Friedman method can be used to extract activation energies at a higher accuracy compared to the KAS method. This is because unlike the KAS method, the Friedman method does not use any approximation, but instead, it uses the rate equation in its raw form, and hence yielding the most accurate kinetic data. Plotting  $\ln \left[ \frac{dX}{dt} \right]_{X,i}$  against  $\frac{1}{T_{x,i}}$  must yield a straight line with a slope of  $-\frac{E_x}{R}$  from which the activation energy is obtained.

### 2.3. Calculation of the frequency factor

#### 2.3.1. The compensation effect

Calculation of the frequency factor with high accuracy can be achieved using the compensation effect (Vyazovkin, 2021). This method relies on the principle that the values of  $\ln(A)$  and  $E$  are linearly related regardless of being correct or not (Vyazovkin, 2021). The linear dependency maybe presented as:

$$\ln(A)_i = aE_i + b \quad (13)$$

Such that  $a$  and  $b$  are constants. A set of values of  $\ln(A)$  and  $E$  can be produced by fitting the experimental rate against the reciprocal of temperature using different sets of  $f(X)$  as shown in Equation 15. The experimental rate can be estimated by differentiating Equation 1 with respect to time which yields Equation 14:

$$\frac{dX}{dt} = \frac{-1}{w_o - w_f} \cdot \frac{dW}{dt} \quad (14)$$

Such that  $\frac{dW}{dt}$  is the value of the experimental DTG signal obtained from the Thermogravimetric analysis. The kinetic models used for generating the compensation data are presented in Table 1.

Table 1: Kinetic models in the differential  $f(X)$  and the integral  $g(X)$  form (Georgieva et al., 2013) used to generate the  $\ln(A)$  and  $E$  data for the compensation effect.

No.	Kinetic model	$f(X)$	$g(X)$
-----	---------------	--------	--------

Chemical process			
1	One-third order	$\frac{3}{2}(1-X)^{\frac{1}{3}}$	$1 - (1-X)^{\frac{2}{3}}$
2	Three-quarters order	$4(1-X)^{\frac{3}{4}}$	$1 - (1-X)^{\frac{1}{4}}$
3	One and half order	$2(1-X)^{\frac{3}{2}}$	$(1-X)^{-\frac{1}{2}} - 1$
4	Second order	$(1-X)^2$	$(1-X)^{-1} - 1$
5	Third order	$\frac{1}{2}(1-X)^3$	$(1-X)^{-2} - 1$
6	$n^{\text{th}}$ order, $n > 1$	$\frac{1}{n-1}(1-X)^n$	$(1-X)^{-n+1} - 1$

Once a set of  $\ln(A)$  and  $E$  are obtained, a plot is constructed, and the data is fitted with a straight line. The resulting linear equation should have the form presented in Equation 13 from which the values of  $a$  and  $b$  are obtained. The extracted activation energies using the KAS and the Friedman methods are then inserted into Equation 13 to obtain conversion dependent frequency factor values  $\ln(A)_X$ . Further illustration on the compensation effect is presented in detail elsewhere (Vyazovkin, 2021).

#### 2.4. Prediction of the kinetic model

The rearrangement of the differential form of the rate equation (Equation 7) into the form shown in Equation 15 allows for the prediction of the controlling reaction model in the studied conversion range by constructing a plot of  $\ln \left[ \frac{dX}{f(X)} \right]$  against  $\frac{1}{T}$ . Only the correct mathematical expression of  $f(X)$  yields a straight line. The criteria followed for this approach is that the chosen reaction model is the one which yields a straight line and an activation energy as close as possible to that produced from the Friedman model on the studied conversion range.

$$\ln \left[ \frac{dX}{f(X)} \right] = \ln(A) - \frac{E}{RT} \quad (15)$$

### 3. Materials and method

#### 3.1. Thermogravimetric and differential scanning calorimetry analysis

ZnFe<sub>2</sub>O<sub>4</sub> used in this work was obtained from Alfa Aesar with a purity of 99% <, while powdered pure PVC was obtained from Sigma-Aldrich. A stoichiometric mixture of ZnFe<sub>2</sub>O<sub>4</sub> and PVC (ZF-PVC) was prepared in which the amount of PVC added to ZnFe<sub>2</sub>O<sub>4</sub> would be enough to chlorinate it completely to ZnCl<sub>2</sub> and FeCl<sub>3</sub>; the calculation was based on the theoretical content of HCl in the PVC monomer. This yielded a mixture containing 32.5 wt% ZnFe<sub>2</sub>O<sub>4</sub>. The two powders were tumbled in a glass vial containing stainless steel balls for 15 minutes. The homogeneity of the mixture was confirmed using scanning electron microscopy (SEM) technique and is shown in Figure S1 (supplementary material).

The instrument used for the thermal analysis was the simultaneous TGA/DSC analyser (TA SDT Q600) which is capable of generating simultaneous mass loss and heat flow signals. Prior to the thermal analysis, an empty ceramic crucible was loaded to generate a base line for the heat flow signal. A mass of  $9.9 \pm 0.07$  and  $10.2 \pm 0.30$  mg of PVC and ZF-PVC mixture, respectively were then loaded in a ceramic crucible and the thermal analysis was performed in the temperature window 25 – 900 °C under a nitrogen flow of 100 mL/min. Using a small sample mass can help in reducing the thermal gradient between the furnace and the sample for more reliable data. The repeatability of the thermogravimetric scan for the dehydrochlorination stage has been tested on the degradation of ZF-PVC mixture at a heating rate of 10 °C/min (Figure S8). Three heating rates of 10, 30, and 50 °C/min were used during the analysis which are essential for the model-free (iso-conversional) kinetic calculations.

### **3.2. Particle size analysis**

The contact surface area can have a significant impact on the reaction efficiency between solid reactants. The particle sizes for both ZnFe<sub>2</sub>O<sub>4</sub> and PVC were analysed using Beckman Coulter LS13320MW laser diffraction analyser with an Aqueous Liquid Module (ALM). The particle sizes for both ZnFe<sub>2</sub>O<sub>4</sub> and PVC are presented in Table 2.

### **3.3. Pyrolysis of ZF-PVC mixture**

A sample of  $0.31 \pm 0.0001$  g of the ZF-PVC mixture was loaded into a 4 mm quartz tube on top of a porous ceramic fibre disk. The ceramic fibre disk acts as a sample holder and helps in distributing the gas flowing through the sample. Another ceramic fibre disk was loaded on top to prevent the powder from fluidising. The tube with the powder was purged with N<sub>2</sub> (99.9992% pure) for at least 15 minutes before starting the heating. This ensured that the reactants were completely surrounded by a nitrogen blanket. Three pyrolysis temperatures were studied: 260, 420, and 650 °C. The choice of these temperatures was based on the plateau temperature after each stage on the TGA scans. The furnace was heated to the desired temperature, the reactants were then inserted and held at that temperature for 30 minutes. The products generated from the pyrolysis were isolated as fast as possible and transferred to a glass vial. The glass vial was then purged with nitrogen and stored in a desiccator for further analysis.

#### **3.4. Mineralogy of the pyrolysis residue**

The mineralogy of the pyrolysis residues was studied using the X-Ray diffraction (XRD) technique. Due to the hygroscopic nature of the powders, each pyrolysis residue was analysed individually (i.e., they were not loaded into the XRD instrument at the same time). Moreover, the powder on the sample holder was covered with a piece of tape to prevent air from being in contact with the powder which can potentially alter the mineralogical phase. The X-Ray tube on the Bruker D8 Advance XRD instrument was operated at a current and voltage of 40 mA and 40 kV, respectively and the analysis was performed in the  $2\theta$  range 5 – 90°, step size of 0.02° with a scanning time of 1.7 sec/step. Qualitative interpretation of the XRD patterns was performed using DIFFRAC.EVA V5.2 software which utilises the PDF-2 database.

#### **3.5. Morphology and chemistry of the pyrolysis residue**

The morphology and the chemistry of the pyrolysis residue were studied using scanning electron microscopy (SEM) coupled with energy dispersive spectroscopy (EDS) techniques. Powders generated from the pyrolysis were sprinkled on a stub covered with an adhesive

carbon layer. Due to the poor electrical conductivity of the powders, they were coated with a conductive layer of carbon with a thickness of 6 nm. Stubs with the powder on them were then inserted into an FEI Quanta600 MLA SEM instrument where an electron beam with a spot size of 5.0 and an accelerating voltage of 15.0 kV were used for the analysis. The choice of these parameters generated an electron beam with a sufficient energy to perform EDS analysis which allowed studying the chemistry of the generated crystals.

### **3.6. Thermodynamic simulation**

The equilibrium amounts of the expected species during the pyrolysis in the temperature range 200 to 1000 °C were studied using FACT-SAGE 7.3 software. FACT-SAGE software implements the Gibbs free energy minimisation method (Bale et al., 2016; Bale et al., 2002) to calculate the amounts of chemical species when the specified compounds react partially or totally to achieve a state of chemical equilibrium. The chlorine in PVC was added in the simulation as gaseous HCl such that its molar amount was calculated from its stoichiometry in the PVC monomer. The carbon added to the system was based on the final char amount in the crucible after the TGA experiments, while H<sub>2</sub> was assumed to constitute half of the 6.7% excess mass loss from the de-hydrochlorination stage (6.7% over the theoretical HCl content). The molar amounts of ZnFe<sub>2</sub>O<sub>4</sub>, HCl, H<sub>2</sub>, and C were added based on their respective amounts in the mixture prepared experimentally which gave the following molar values: 13.48, 107.9, 115.3, and 34.3 mol, respectively. The simulation was carried out in two stages: the first stage extending from 200 to 430 °C which represents the de-hydrochlorination stage while the latter extends from 430 to 1000 °C representing the polyene thermal cracking stage. In the second stage, N<sub>2</sub> gas was introduced to the system with an amount of 69.91 mol which serves as a medium for mass transfer (volatilisation of formed chlorides). This amount was based on the amount of gaseous emissions in the second stage (which were inert) and hence was substituted

as  $N_2$  to act as a medium for mass transfer. Products from the first stage were added to the second stage except for gaseous ones which were assumed to escape from the reaction system.

The purpose of these calculations is to support the experimental observations obtained in the pyrolysis residues and to help predicting certain chemical and physical processes (reactions, volatilisation, etc.). This, in turn, makes the interpretation of the kinetic data easier since the dominant chemical species and reactions are known versus temperature.

## 4. Results and Discussion

### 4.1. Thermodynamic speciation of ZF-PVC pyrolysis

The equilibrium amounts from the pyrolysis of ZF-PVC mixture are presented in Figure 1 (a) and (b). From a temperature of 200 °C both  $ZnCl_2$  and  $FeCl_2$  appear in their solid form with a complete absence of  $ZnFe_2O_4$ ,  $ZnO$ , and  $Fe_2O_3$  (Figure 1 (a)). This suggests that  $ZnFe_2O_4$  was completely chlorinated yielding  $ZnCl_2$ ,  $Fe_2O_3$  and  $H_2O_{(g)}$ .  $Fe_2O_3$  is then immediately reduced by  $H_2$  to  $Fe^{2+}$  bearing oxide ( $Fe_3O_4$ ) which is then chlorinated into  $FeCl_2$ . Solid  $ZnCl_2$  then starts transforming into the liquid form at a temperature of 310 °C which subsequently starts evaporating to the gaseous form at a temperature of 430 °C and becomes almost entirely present in the gaseous form at a temperature of 630 °C (Figure 1 (b)). Liquid  $FeCl_2$ , in contrast, starts appearing at a temperature of 680 °C and immediately starts volatilising above that temperature until is entirely present in the gaseous form at a temperature of 880 °C. The carbon in Figure 1 (b) remains inert over the entire temperature range in the absence of any zinc or iron oxide species.

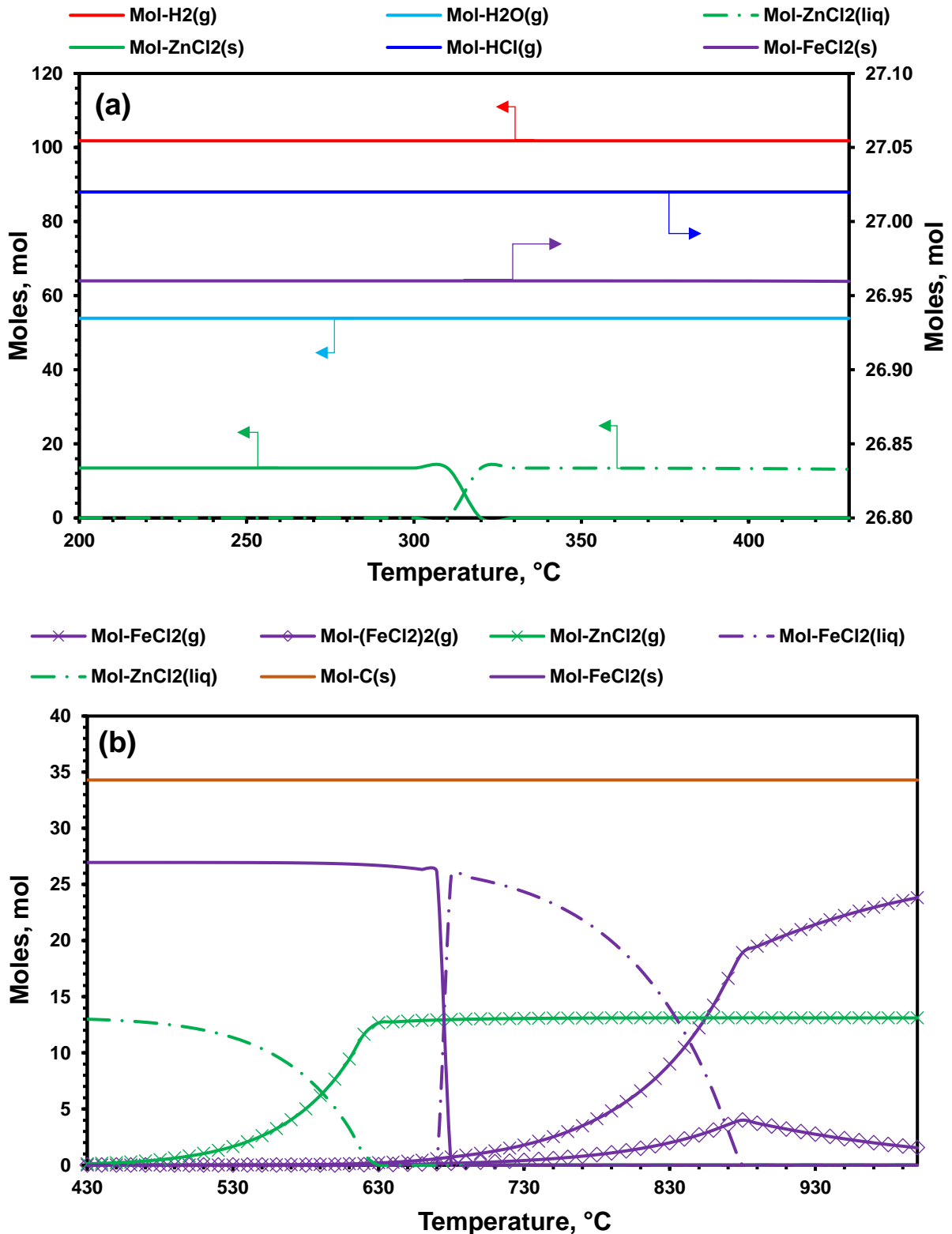


Figure 1: Thermodynamic simulation of the reactants/products from the pyrolysis of the ZF-PVC mixture (32.5 wt% ZnFe<sub>2</sub>O<sub>4</sub>) in the temperature window 200 – 430 °C (a) and 430 – 1000 °C (b).

Overall, the thermodynamic data suggests that ZnFe<sub>2</sub>O<sub>4</sub>, a major zinc source in EAFD, should be completely removed and transformed into chloride forms of zinc and iron upon thermal

treatment with a stoichiometric quantity of PVC. The kinetic barriers contributing towards selective zinc chlorination will be shown in later sections.

#### 4.2. Experimental thermal behaviour of PVC and ZF-PVC mixture

The thermal degradation profiles of pure PVC and ZF-PVC mixture at different heating rates are presented in Figure 2 (a) and (b). The decomposition of pure PVC occurs in three stages, while that of ZF-PVC follows four stages. The first two overlapped stages for pure PVC start at a temperature of 272 °C and produce a mass loss of about 65%. These stages involve the de-hydrochlorination of PVC through the evolution of HCl along with volatiles (Jordan et al., 2001) and the evolution of small amounts of H<sub>2</sub> (Ye et al., 2021). The de-hydrochlorination of PVC absorbs a large amount of energy which is evident from the large endothermic peak extending from 250 to 320 °C (Figure 3). The occurrence of the de-hydrochlorination in the form of a two overlapped stages for pure PVC is discussed in more detail in the kinetics section 4.3. At the end of these stages, most of the chlorine in the PVC was stripped out of the polymer chain (Yu et al., 2016) and the remaining solid was reported to be a conjugated polyene structure (Marcilla and Beltrán, 1995).

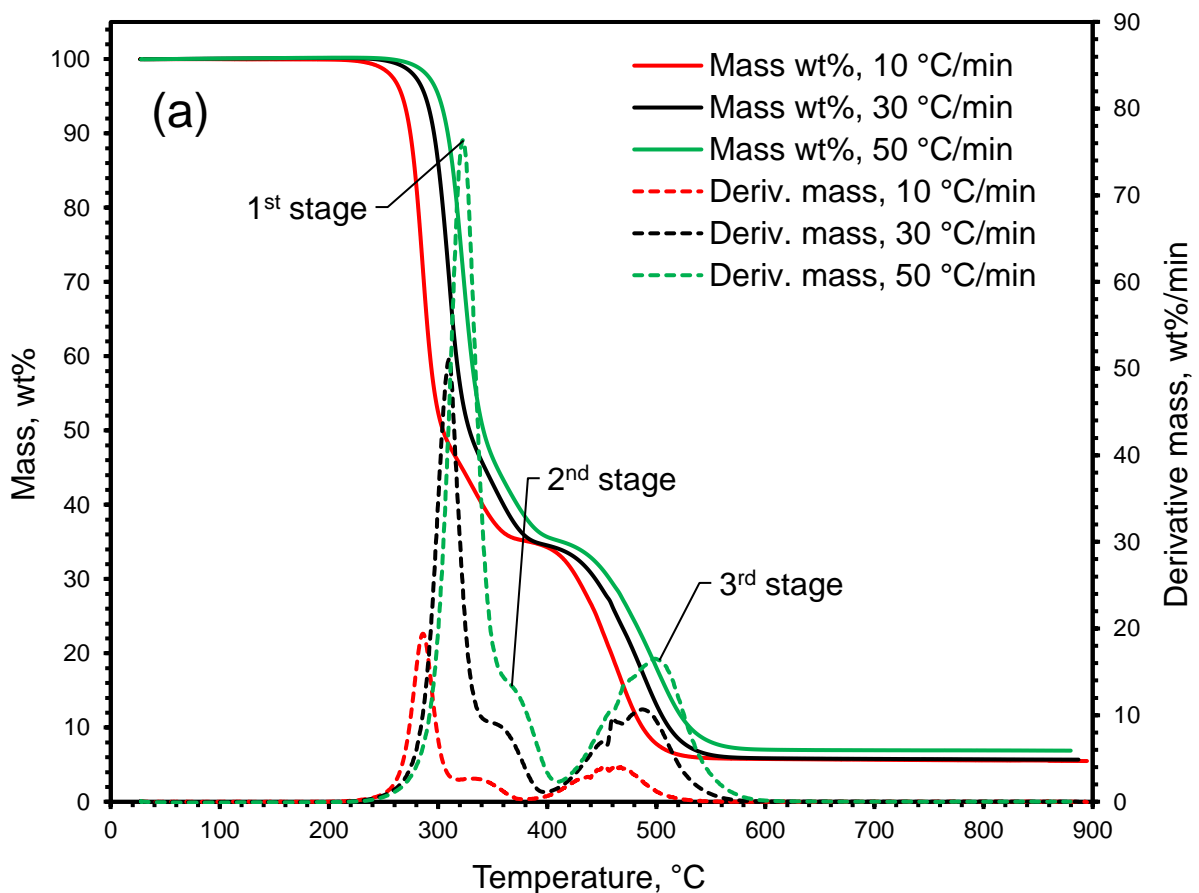
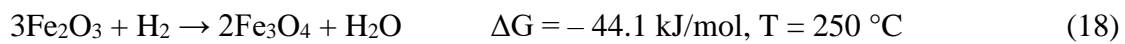
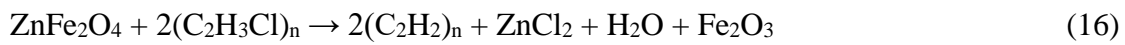
Table 2: The mean particle sizes of PVC and ZnFe<sub>2</sub>O<sub>4</sub> measured using the laser diffraction technique.

Material	Mean particle size, μm <sup>a</sup>
PVC	158.8 ± 18.5
ZnFe <sub>2</sub> O <sub>4</sub>	13.2 ± 4.2

a: Mean ± SD

When a stoichiometric quantity of ZnFe<sub>2</sub>O<sub>4</sub> was added to PVC, the onset de-hydrochlorination temperature of PVC dropped appreciably to a value of 235 °C suggesting a catalytic effect of ZnFe<sub>2</sub>O<sub>4</sub> on PVC degradation. A similar effect was reported before by (Altarawneh et al., 2021) for ZnO such that the addition of a stoichiometric quantity of ZnO resulted in an even larger drop in the de-hydrochlorination onset temperature to a value of 214 °C (compared to 272 °C

for pure PVC). Such behaviour for both ZnO and ZnFe<sub>2</sub>O<sub>4</sub> can be attributed to the direct reaction of these oxides with the chlorine atom in the PVC monomer forming metallic chlorides/oxychlorides while simultaneously generating gaseous H<sub>2</sub>O. The mass spectrometric data reported by (Zhang et al., 2000) of the emissions generated from ZF-PVC mixture is also in line with the results presented here. In their work, H<sub>2</sub>O mass peaks were detected which can be assigned to the chlorination of ZnFe<sub>2</sub>O<sub>4</sub> by PVC. These chlorination reactions can be written according to the following sequence:



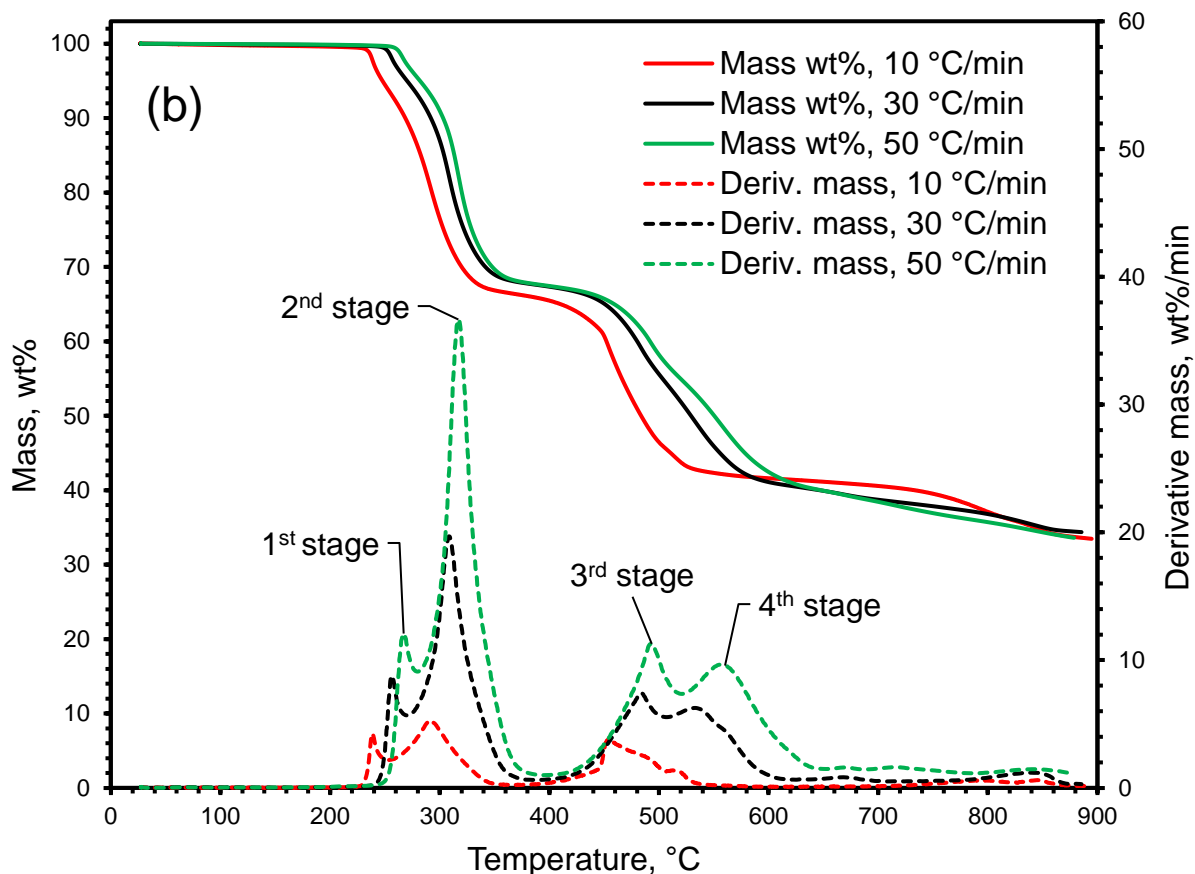


Figure 2: Thermal degradation of pure PVC (Altarawneh et al., 2021) (a) and ZF-PVC (32.5 wt%  $\text{ZnFe}_2\text{O}_4$ ) mixture (b) at heating rates of 10, 30 and 50 °C/min and under a nitrogen flow of 100 mL/min.

Evidence for the chlorination reaction can be seen from the exothermic peak associated with the ZF-PVC mixture (absent for pure PVC) as shown in Figure 3. Additionally, this exothermic peak starts appearing at 227 °C which is much lower than the de-hydrochlorination onset temperature of pure PVC suggesting a direct reaction of  $\text{ZnFe}_2\text{O}_4$  with PVC. Likewise, the addition of  $\text{ZnFe}_2\text{O}_4$  also changed the DTG signal drastically into a doublet peak such that the first peak is associated with the direct reaction of  $\text{ZnFe}_2\text{O}_4$  with PVC ( $\text{H}_2\text{O}$  evolution) while the second one is attributed to the normal de-hydrochlorination of PVC ( $\text{HCl}$  evolution) along with  $\text{H}_2\text{O}$  evolved from the reduction of  $\text{Fe}_2\text{O}_3$  by  $\text{H}_2$  and its consecutive chlorination.

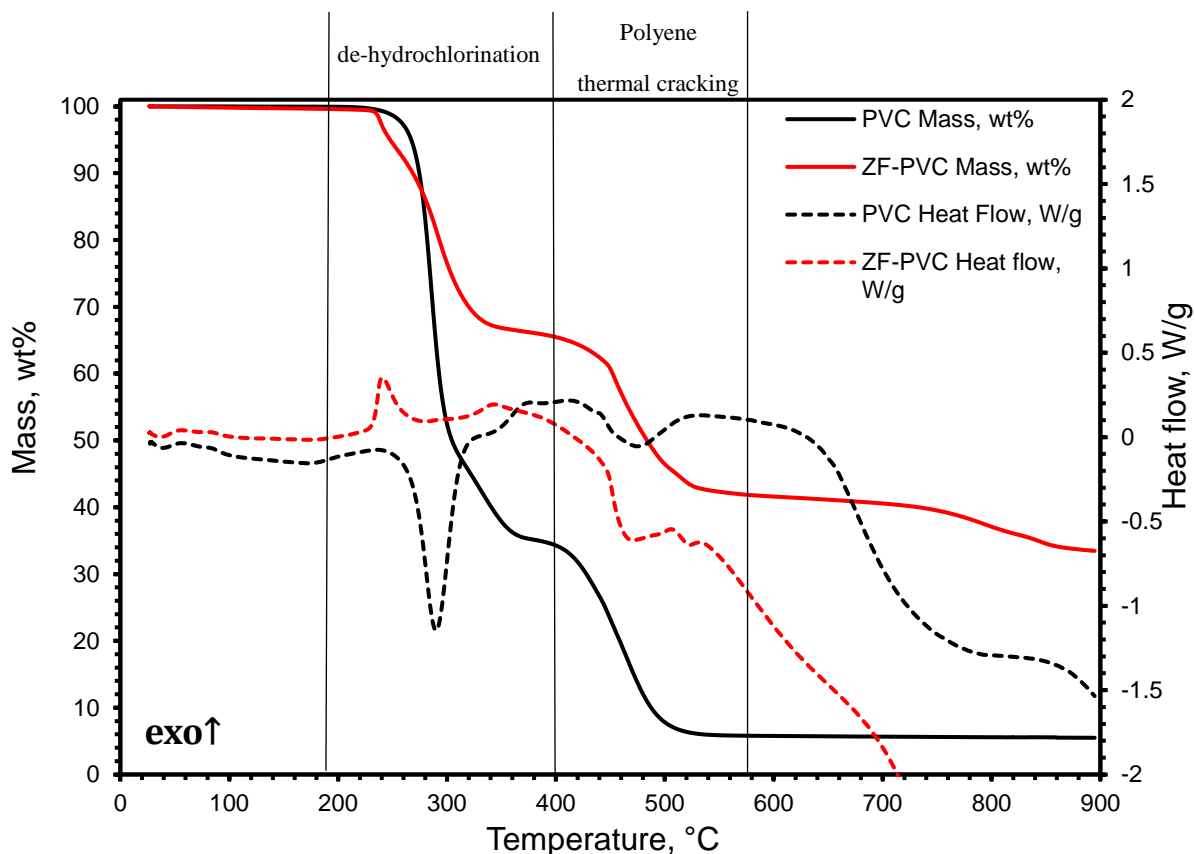


Figure 3: TGA/DSC profiles of pure PVC and ZF-PVC (32.5 wt%  $\text{ZnFe}_2\text{O}_4$ ) under a nitrogen flow of 100 mL/min and a heating rate of 10 °C/min.

The occurrence of Reactions 16, 18 and 19 is confirmed from the XRD patterns presented in Figure 4 which are related to the pyrolysis residues of ZF-PVC at temperatures of 260, 420, and 650 °C. At a temperature as low as 260 °C,  $\text{ZnFe}_2\text{O}_4$ , which is known for its chemical stability (Havlík et al., 2006), was completely destroyed, and transformed into Lawrencite ( $\text{FeCl}_2$ ), Rokuhnite ( $\text{FeCl}_2 \cdot 2\text{H}_2\text{O}$ ), and Hematite ( $\text{Fe}_2\text{O}_3$ ). This result is in agreement with the thermodynamic data presented earlier. The presence of  $\text{Fe}_2\text{O}_3$  here and its absence in the thermodynamics section might be assigned to kinetics whereby the reduction of  $\text{Fe}_2\text{O}_3$  by  $\text{H}_2$  was not fast enough to make it completely disappear at 260 °C. This result is in agreement with the work done by (Pineau et al., 2006) where at a temperature of 258 °C the reduction of  $\text{Fe}_2\text{O}_3$  by  $\text{H}_2$  was very slow needing up to 500 minutes to reach a conversion of ~88%. The slow reduction kinetics at low temperatures is also confirmed from the XRD data shown in Figure 4 where  $\text{Fe}_2\text{O}_3$  is completely reduced and chlorinated only at a higher temperature of 420 °C.

Despite the complete disappearance of  $\text{ZnFe}_2\text{O}_4$  in the 260 °C pattern, no  $\text{ZnCl}_2$  peaks could be detected. In a previous study conducted by (Altarawneh et al., 2021) for the co-pyrolysis of  $\text{ZnO}$  with PVC, peaks of  $\alpha\text{-ZnCl}_2$ ,  $\text{ZnCl}_2 \cdot 1.33\text{H}_2\text{O}$  and  $\text{Zn}(\text{OH})\text{Cl}/\text{Zn}_2\text{OCl}_2 \cdot 2\text{H}_2\text{O}$  were detected, however, with small intensities.  $\text{ZnCl}_2$  is also known to be a deliquescent material which tends to dissolve itself in in-situ solution when a sufficient amount of water is absorbed to the surface. In fact, (Altarawneh et al., 2021) reported that  $\text{ZnCl}_2$  completely disappeared and recrystallised in the form of Simonkolleite ( $\text{Zn}_5(\text{OH})_8\text{Cl}_2 \cdot \text{H}_2\text{O}$ ) when exposed to the atmosphere for long period of times (~ 6 hours). This means that at some point,  $\text{ZnCl}_2$  dissolves into an aqueous solution which upon saturation, recrystallises as  $\text{Zn}_5(\text{OH})_8\text{Cl}_2 \cdot \text{H}_2\text{O}$ . Such behaviour makes the detection of crystalline  $\text{ZnCl}_2$  very difficult to achieve.

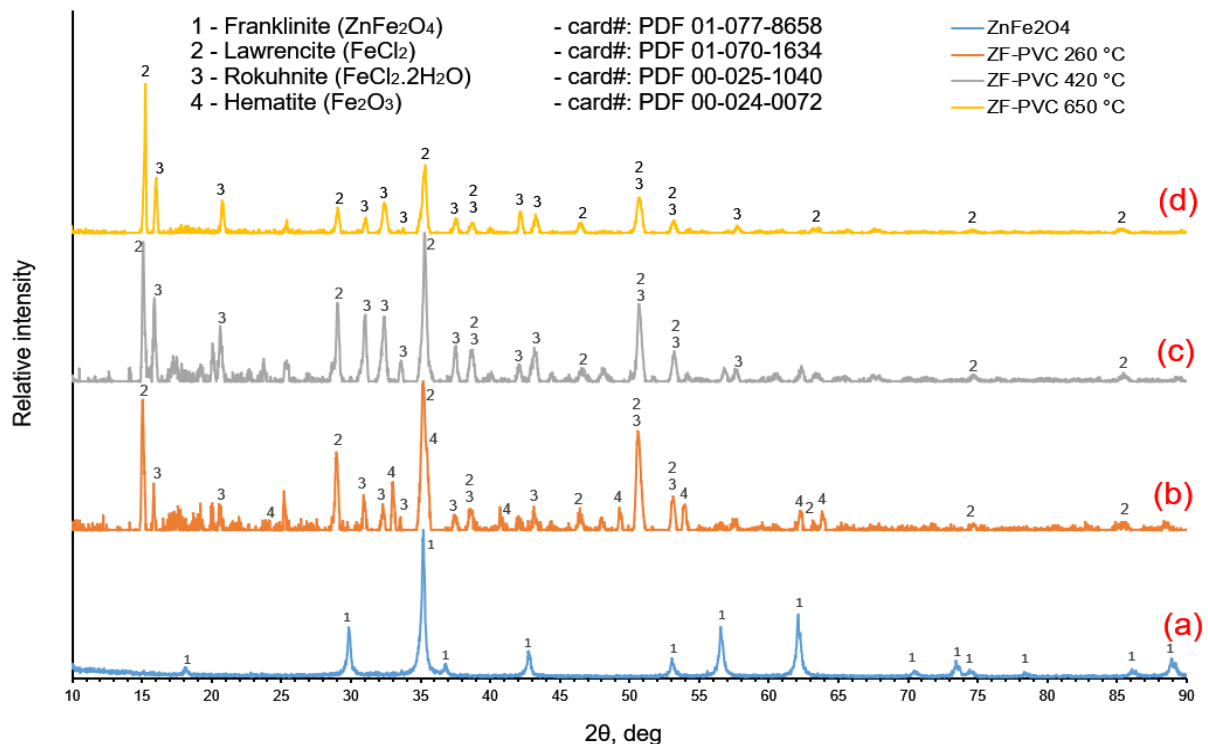


Figure 4: XRD patterns of the pyrolysis residues of ZF-PVC (32.5 wt%  $\text{ZnFe}_2\text{O}_4$ ) mixture under an inert (nitrogen) environment for 30 minutes at different temperatures of (a) room temperature ( $\text{ZnFe}_2\text{O}_4$  alone), (b) 260, (c) 420, and (d) 650 °C.

The formation of  $\text{ZnCl}_2$ , however, can be confirmed from the SEM analysis at a temperature of 650 °C (Figure 5). According to the thermodynamic simulation presented earlier, at a temperature of 650 °C,  $\text{ZnCl}_2$  can only be present in its gaseous form. Such behaviour explains

the absence of zinc upon EDS scanning of a large surface area of the pyrolysis residue at 650 °C for two minutes (Figure 5). The spectra presented under the maps in Figure 5 also shows that zinc has almost zero counts per second suggesting a complete chlorination of  $\text{ZnFe}_2\text{O}_4$  followed by the evaporation of formed  $\text{ZnCl}_2$ . In Figure S7 in the supplementary material, it is shown that  $\text{ZnFe}_2\text{O}_4$  remains stable up to 900 °C. Hence, the only way zinc would disappear from the SEM/EDS images, is that  $\text{ZnFe}_2\text{O}_4$  was completely chlorinated and formed  $\text{ZnCl}_2$  was then volatilised. This result is in a good agreement with the thermodynamics section presented above.

At 260 °C, incomplete chlorination of iron takes place which is evident from the  $\text{Fe}_2\text{O}_3$  peaks appearing in Figure 4 (pattern (b)). When the pyrolysis temperature is increased to 420 °C, all  $\text{Fe}_2\text{O}_3$  peaks disappear giving rise to  $\text{FeCl}_2$  and  $\text{FeCl}_2 \cdot 2\text{H}_2\text{O}$  peaks with higher intensities. Contrary to zinc, the maps in Figure 5 show the presence of iron which is associated with chlorine. Such a result is in line with the XRD pattern (d) in Figure 4 with peaks of both  $\text{FeCl}_2$  and  $\text{FeCl}_2 \cdot 2\text{H}_2\text{O}$ . This result also agrees with the thermodynamics data presented earlier.

The effect of temperature on the degree of chlorination of iron bearing compounds is important for the optimisation and the proper selection of temperature to yield high zinc extraction while simultaneously leaving iron in non-leachable form (oxide form). Further illustration on this is presented in the kinetics section 4.3.

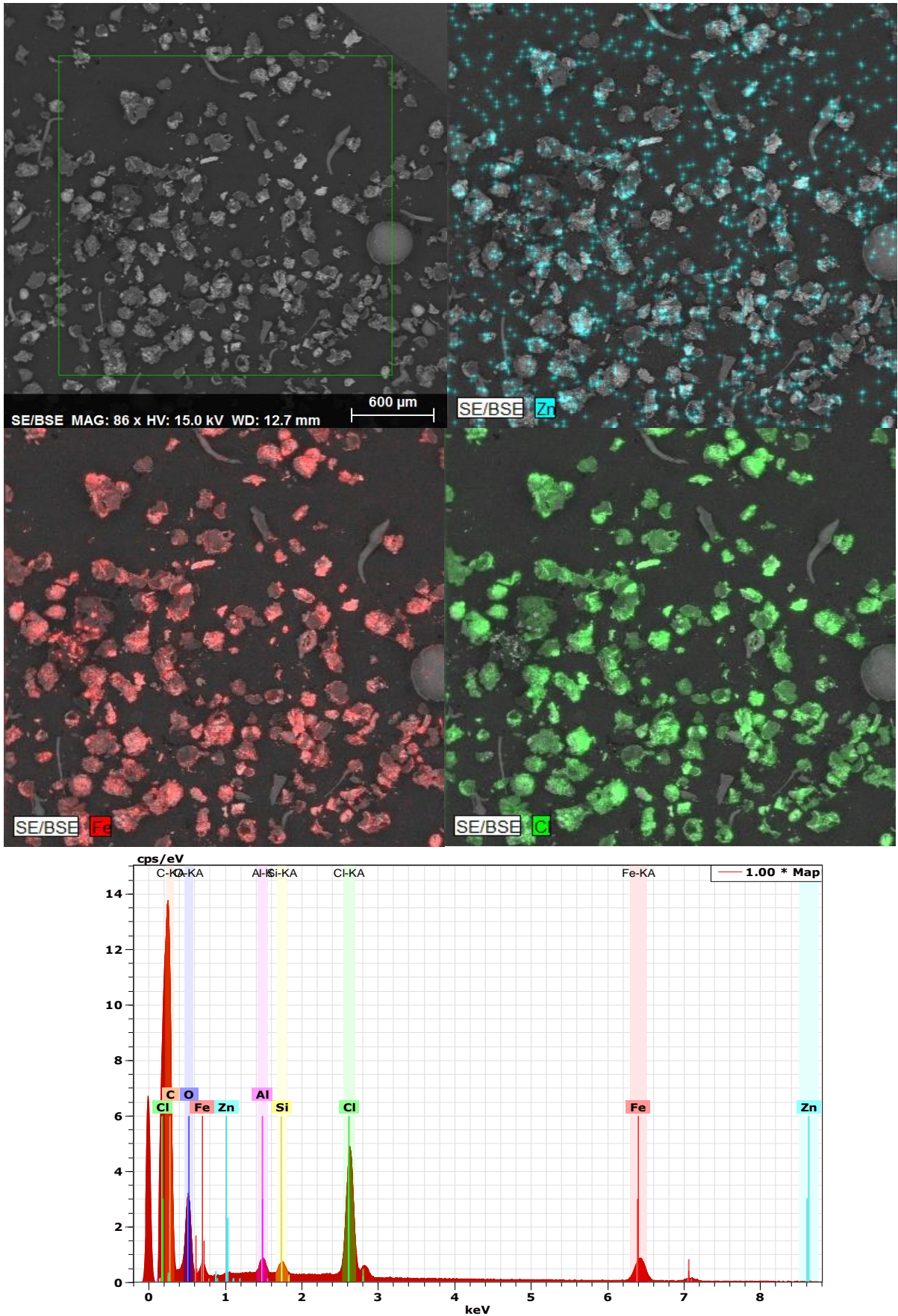


Figure 5: SEM/EDS scans of the pyrolysis residue of ZF-PVC (32.5 wt%  $\text{ZnFe}_2\text{O}_4$ ) at a temperature of 650 °C under an inert (nitrogen) environment for 30 minutes.

The third decomposition stage for pure PVC extending from 400 to 520 °C is associated with the thermal cracking of polyene formed from the de-hydrochlorinated PVC into volatiles such as polyenyl aromatics, alkyl aromatics, and polyaromatics (Blazso and Jakab, 1999). About 6% of the initial weight of the sample was left in the crucible which is characterised as char. The formation of char is confirmed from its oxidation when PVC is heated under air showing a large exothermic peak and a drop of the wt% to zero (Figure S2). Under pyrolytic conditions, however, the cracking of polyene is endothermic as shown in Figure 3.

For a ZF-PVC mixture, the polyene thermal cracking stage extending from 400 to 540 °C appears as a doublet. This is attributed to the simultaneous polyene thermal cracking and the volatilisation of formed ZnCl<sub>2</sub>. This is also evident from the heat flow signals appearing in Figure 3 for ZF-PVC showing endothermic doublet which is absent in the case of pure PVC. The evaporation of ZnCl<sub>2</sub> in that stage has a large kinetic effect which will be discussed in the next section.

### **4.3. Non-isothermal kinetics of PVC and ZF-PVC degradation**

#### **4.3.1. Kinetics of the de-hydrochlorination stage**

In this section, the kinetic parameters associated with the de-hydrochlorination stage resembled by the first two stages for both pure PVC and ZF-PVC mixture (Figure 2 (a) and (b)) are presented. Figure 6 shows a comparison of the activation energy associated with the de-hydrochlorination of pure PVC and ZF-PVC mixture at different conversion levels. The activation energy for pure PVC de-hydrochlorination starts at 109.9 kJ/mol at a conversion of 0.004 and remains almost constant up to a conversion of 0.7 after which an increase to an average value of 167.1 kJ/mol occurs at conversions of 0.8 – 0.9. Such behaviour indicates that two mechanisms control the degradation of pure PVC as presented in Table 3 where two different reaction models ( $f(X)$ ) could fit different conversion ranges. Initially, the truncated Šesták and Berggren function  $f(X) = X(1 - X)^{2.13}$  fits the experimental data in the

conversion range 0.1 – 0.6 (all experimental data fitting are presented in the supplementary material section 3). This type of function is considered an example of an auto catalytic model (Vyazovkin et al., 2011). This agrees with the work done by (Starnes and Ge, 2004) where it was confirmed that the de-hydrochlorination of PVC is auto catalysed by the emitted HCl from PVC decomposition. At a conversion above 0.7, the decomposition becomes controlled by a different reaction model  $f(X) = (1 - X)^2$  which is also accompanied by an increase in the activation energy. This could be assigned to the lean amount of HCl present at the end of the de-hydrochlorination which ceases its catalytic effect. Overall, there is a great degree of agreement between the average activation energy calculated in this work for the pure PVC de-hydrochlorination at 122.6 kJ/mol compared to that calculated and reported in the ICTAC kinetic committee recommendations (Vyazovkin et al., 2020) at 128.5 kJ/mol (both calculated using Friedman model). This confirms the validity of the followed procedure for calculating the kinetic data.

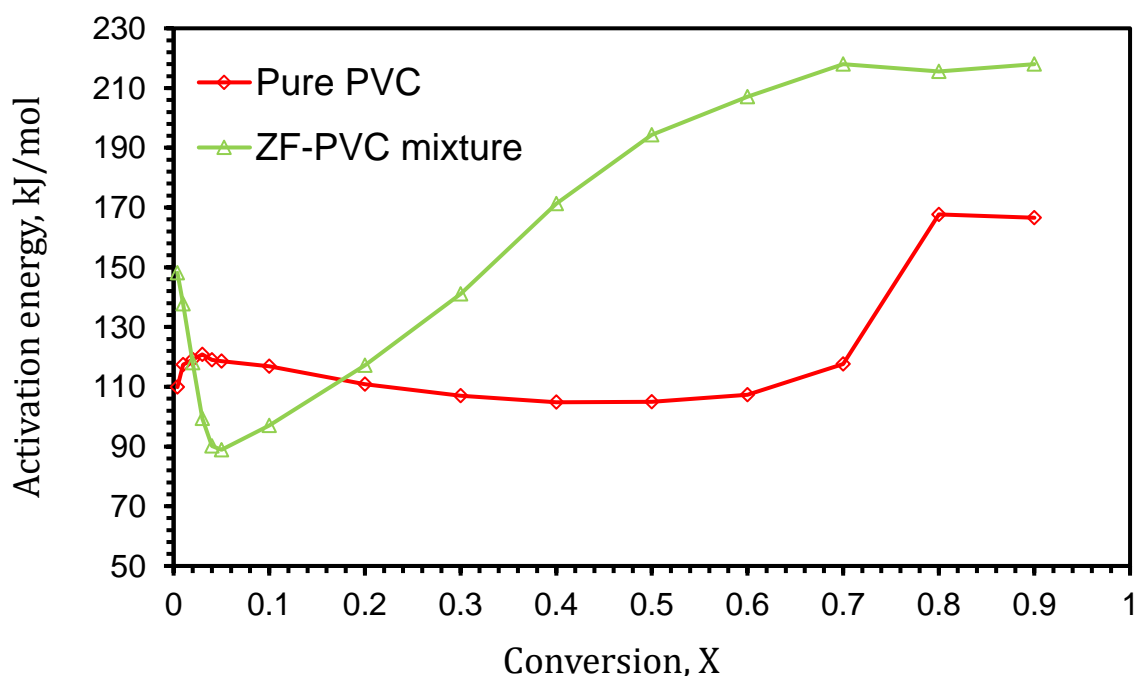


Figure 6: Iso-conversional activation energies associated with the de-hydrochlorination (first and second stages for both pure PVC and ZF-PVC) in the conversion range 0.004 – 0.9 using Friedman model.

The addition of a stoichiometric quantity of  $\text{ZnFe}_2\text{O}_4$  to PVC resulted in a drastic variation in the activation energy of de-hydrochlorination with conversion. The activation energy at  $X = 0.004$  increased from 109.9 to 148.2 kJ/mol (Figure 6). This result means that the initiation mechanism for the de-hydrochlorination of PVC significantly changes in the presence of  $\text{ZnFe}_2\text{O}_4$ , such that for pure PVC, the de-hydrochlorination proceeds via the well-known zipper elimination mechanism (Levchik and Weil, 2005) by which small amounts of HCl initially evolves followed by the formation of labile allylic chlorine sites from which the decomposition proceeds at a fast rate. When  $\text{ZnFe}_2\text{O}_4$  is added, it abstracts chlorine directly from the PVC monomer forming  $\text{ZnCl}_2$  and  $\text{Fe}_2\text{O}_3$ , hence the change in the activation energy.

The catalytic activity of  $\text{ZnFe}_2\text{O}_4$  can be shown in the schematic illustration presented in Figure 7 where the rate constant was calculated at the same temperature of 230 °C (503 K) for both mechanisms A and B. The addition of  $\text{ZnFe}_2\text{O}_4$  accelerated the de-hydrochlorination despite the increase in the activation energy (Figure 7). It can be seen that the combined activation energy and frequency factor at a temperature of 230 °C yielded a rate constant for ZF-PVC mixture (mechanism B) 4.1 times higher than that associated with pure PVC with values of 0.016 and 0.0039  $\text{min}^{-1}$  for ZF-PVC and pure PVC, respectively. Such a result supports what was observed in the thermogravimetric scans where a drop in the onset temperature of the de-hydrochlorination was seen when  $\text{ZnFe}_2\text{O}_4$  was added to PVC. This also means that reaction channelling towards mechanism B over A can potentially take place when low temperature (e.g., 230 °C) is used in the ZF-PVC mixture.

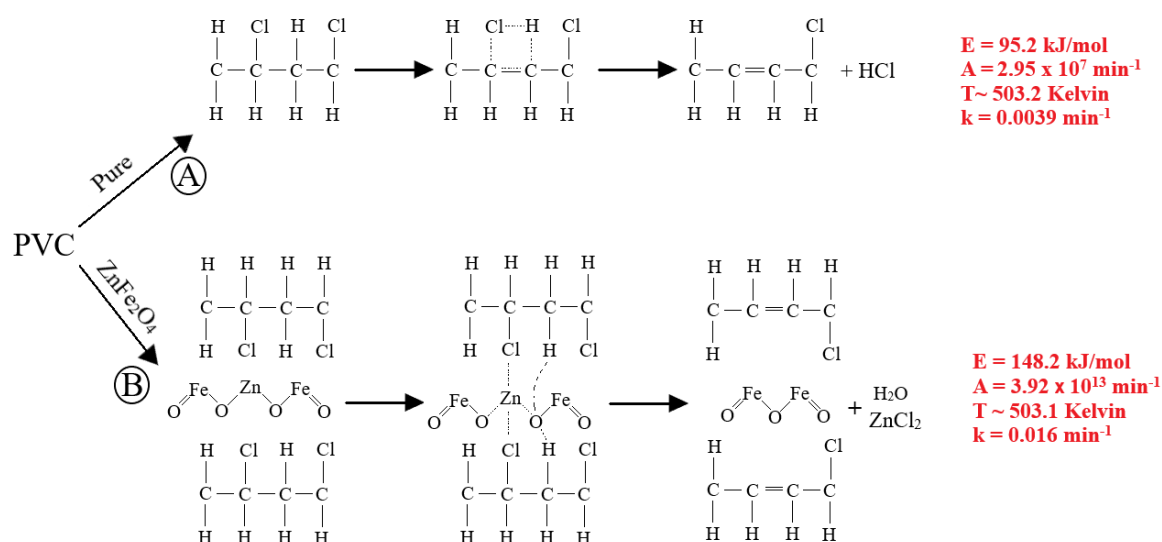


Figure 7: The de-hydrochlorination of PVC with and without ZnFe<sub>2</sub>O<sub>4</sub> along with the kinetic parameters associated with the de-hydrochlorination calculated at a temperature of ~ 503 K showing the higher rate constant (*k*) for ZF-PVC mixture compared to pure PVC; equivalent conversion values for PVC and ZF-PVC at that temperature at a heating rate of 10 °C/min are 0.00044 and 0.004, respectively.

From conversions extending from 0.03 to 0.1 (Figure 6) a significant drop in the activation energy to a value as low as 88.9 kJ/mol is seen followed by a continuous increase reaching a maximum of 218 kJ/mol at a conversion of 0.9. The drop in activation energy between conversions 0.03 – 0.1 (corresponds to temperatures 237 – 243 °C) was previously reported by (Altarawneh et al., 2021) for the co-pyrolysis of ZnO with PVC. This drop was assigned to the decomposition of the formed Zn<sub>2</sub>OCl<sub>2</sub>·2H<sub>2</sub>O/Zn(OH)Cl into ZnCl<sub>2</sub>, ZnO and H<sub>2</sub>O (Altarawneh et al., 2021), which was also reported in a simulation study conducted by (Ahmed et al., 2018).

An increase in the activation energy above a conversion of 0.2 can be assigned to the start of normal PVC de-hydrochlorination, however, this time, in the absence of HCl due to its capturing by Fe<sub>3</sub>O<sub>4</sub> formed from the reduction of Fe<sub>2</sub>O<sub>3</sub> by H<sub>2</sub>. This can be confirmed from the XRD patterns presented in Figure 4 showing large peaks of FeCl<sub>2</sub>/FeCl<sub>2</sub>·2H<sub>2</sub>O suggesting HCl capturing. Fe<sub>3</sub>O<sub>4</sub>, in this case, works as a HCl scavenger, preventing HCl from catalysing the de-hydrochlorination which is the reason behind the increase in the activation energy.

According to the evidence in literature (Pineau et al., 2006) on the reduction of Fe<sub>2</sub>O<sub>3</sub> by H<sub>2</sub>, it is believed that operating at low temperatures (230 – 235 °C) for the ZF-PVC mixture will

result in iron being left in its stable form (Fe<sub>2</sub>O<sub>3</sub>), while simultaneously zinc is being chlorinated into its chloride counterparts. This is because the reduction of Fe<sub>2</sub>O<sub>3</sub> by H<sub>2</sub> was found to be kinetically slow at low temperatures (Pineau et al., 2006).

Table 3: Kinetic parameters associated with the de-hydrochlorination of pure PVC (Figure 3) (Altarawneh et al., 2021).

Conversion, X	KAS		Friedman			Linear model fitting		
	Activation energy, kJ/mol	Frequency factor, ln(A) <sup>a</sup>	Activation energy, kJ/mol	ln(A.f(X))	Frequency factor, ln(A) <sup>a</sup>	Activation energy, kJ/mol	Frequency factor, ln(A) <sup>a</sup>	f(X)
0.1	118.2	25.03	116.9	23.52	24.74	110.5	24.60	$X(1 - X)^{2.13}$
0.2	116.0	24.53	110.9	22.59	23.37			
0.3	114.3	24.14	107.0	21.88	22.48			
0.4	113.5	23.96	104.8	21.38	21.98			
0.5	112.6	23.76	105.0	21.28	22.03			
0.6	112.1	23.64	107.3	21.41	22.55			
0.7	112.9	23.83	117.6	22.88	24.89			
<i>Transition region (no fitting)</i>								
0.8	125.2	26.62	167.7	31.54	36.28	158.3	32.65	$(1 - X)^2$
0.9	153.2	32.99	166.6	29.84	36.03			
Average <sup>b</sup>	119.8 ± 12.4	25.39 ± 2.83	122.6 ± 24.2	24.04 ± 3.65	26.04 ± 5.50	—		

a: Unit of frequency factor (A) is min<sup>-1</sup>

b: Average = mean ± SD

Table 4: Kinetic parameters associated with the de-hydrochlorination of ZF-PVC mixture (Figure 3).

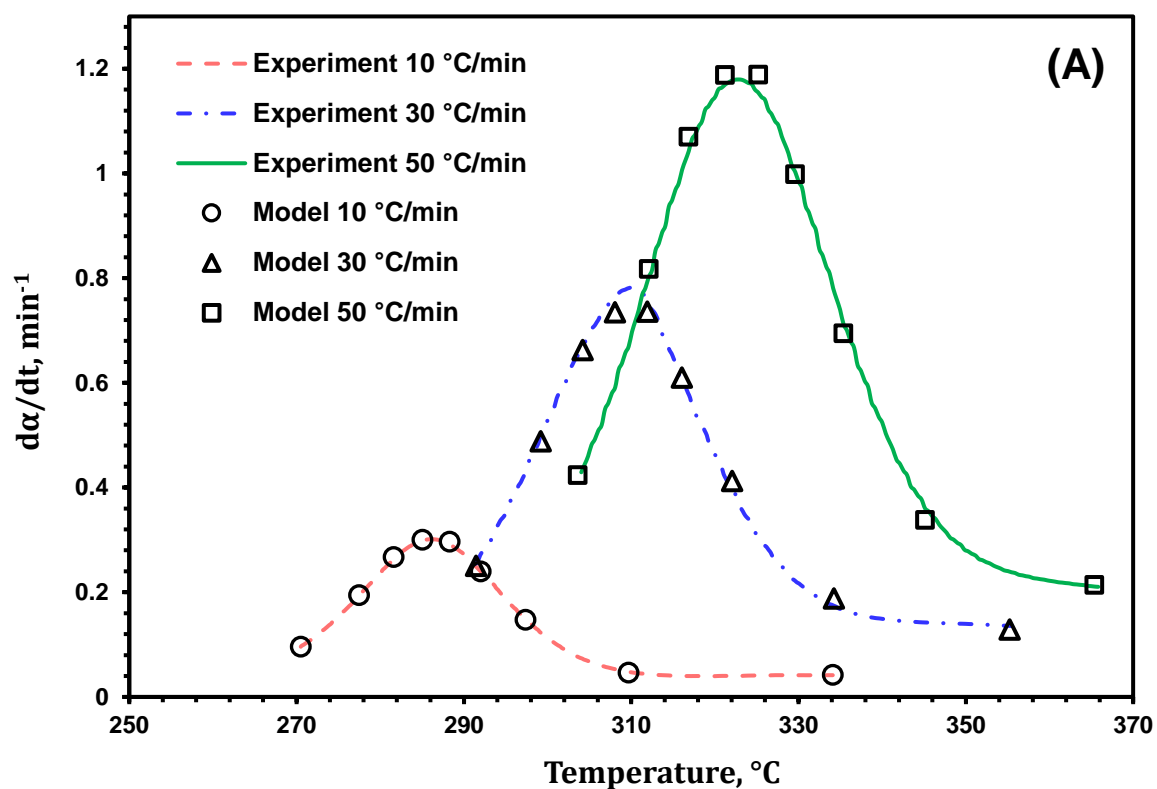
Conversion, X	KAS		Friedman			Linear model fitting		
	Activation energy, kJ/mol	Frequency factor, ln(A) <sup>a</sup>	Activation energy, kJ/mol	ln(A.f(X))	Frequency factor, ln(A) <sup>a</sup>	Activation energy, kJ/mol	Frequency factor, ln(A) <sup>a</sup>	f(X)
0.1	115.8	23.63	97.0	20.17	19.16	----	----	----
0.2	109.7	22.18	117.2	23.92	23.96	177.4	37.66	$(1 - X)^2$
0.3	117.6	24.06	141.1	28.84	29.64			
0.4	130.1	27.03	171.3	35.15	36.83			
0.5	146.5	30.93	194.3	39.83	42.29			
0.6	160.3	34.21	207.1	42.14	45.33			
0.7	178.8	38.60	218.0	43.75	47.92			
0.8	192.2	42.03	215.6	42.34	47.35			
0.9	206.2	45.12	218.0	41.50	47.92			
Average <sup>b</sup>	150.8 ± 33.5	31.98 ± 8.00	175.5 ± 43.89	35.29 ± 8.34	37.82 ± 10.43	—		

a: Unit of frequency factor (A) is min<sup>-1</sup>

b: Average = mean ± SD

Despite the continuous increase in the activation energy for ZF-PVC, the de-hydrochlorination experimental data for that mixture was fit using a second order reaction model  $f(X) = (1 - X)^2$  in the conversion range 0.2 – 0.9 (Table 4). The reliability of the kinetic data associated with the de-hydrochlorination of pure PVC and ZF-PVC mixture can be confirmed

by comparing the experimental rates with the rates calculated using the extracted kinetic parameters (Figure 8). Clearly, a very good agreement between the model generated data and the experimental data can be seen. The comparison was also performed at different heating rates to confirm that the kinetic parameters can be used to predict reaction rates at different temperatures.



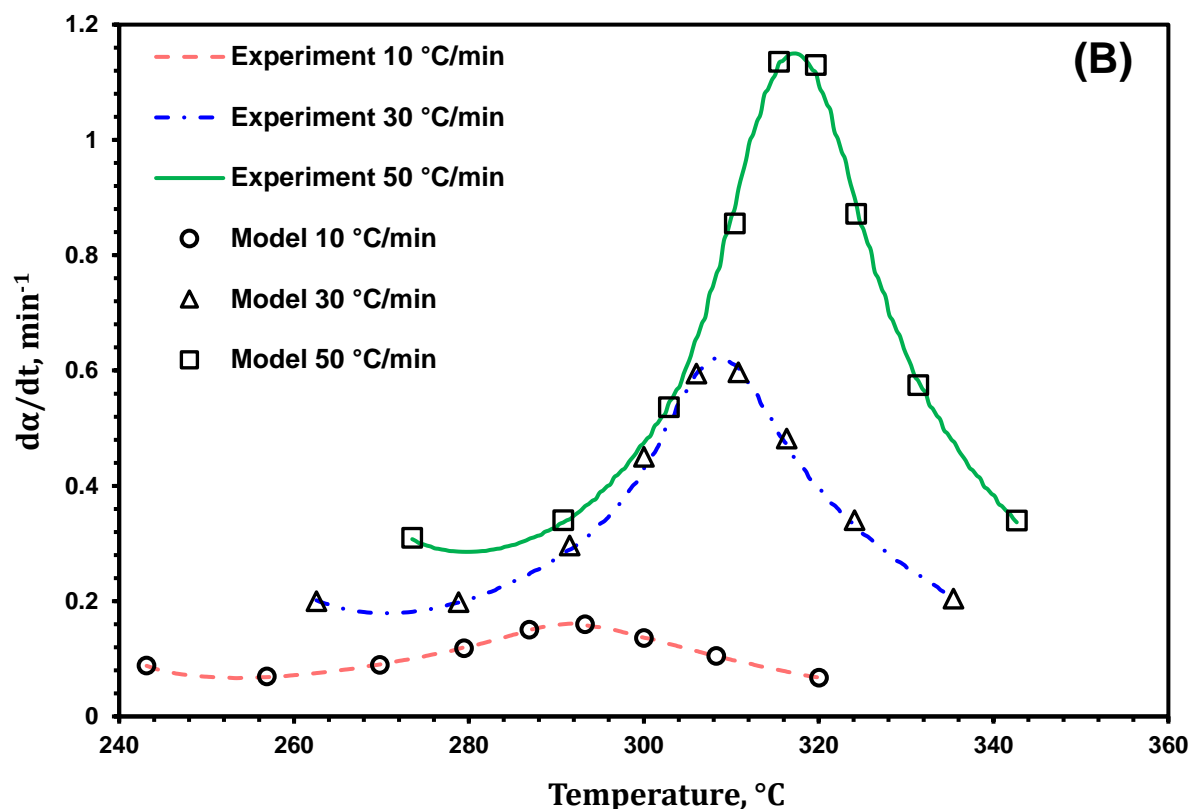


Figure 8: A comparison between experimental and model generated de-hydrochlorination rates of pure PVC (A) and ZF-PVC mixture (B) at heating rates of 10, 30, and 50  $^{\circ}\text{C}/\text{min}$  in the conversion range 0.1 – 0.9 (kinetic data from Friedman model).

#### 4.3.2. Kinetics of the polyene thermal cracking stage

In this section, the kinetic parameters of the polyene thermal cracking stage for pure PVC and ZF-PVC mixture are reported. The activation energy associated with the polyene thermal cracking for both PVC and ZF-PVC is presented in Figure 9. The activation energy for the polyene thermal cracking is significantly higher than that associated with the de-hydrochlorination of PVC; it starts at 300.6 kJ/mol at a conversion of 0.004 compared with 109.9 kJ/mol for the de-hydrochlorination. Such a result is in agreement with the experimental results where the thermal cracking of the polymer backbone takes place at the significantly higher temperature of 422  $^{\circ}\text{C}$  compared to 272  $^{\circ}\text{C}$  for the de-hydrochlorination. The activation energy then keeps dropping with conversion averaging at  $205.8 \pm 13.9$  kJ/mol in the conversion range 0.1 – 0.9. The rate of mass loss could be fitted with one reaction model ( $f(X) =$

$2(1 - X)^{\frac{3}{2}}$  (Table 5) in the conversion range 0.1 – 0.9 which suggests that the process is chemically controlled over the entire range.

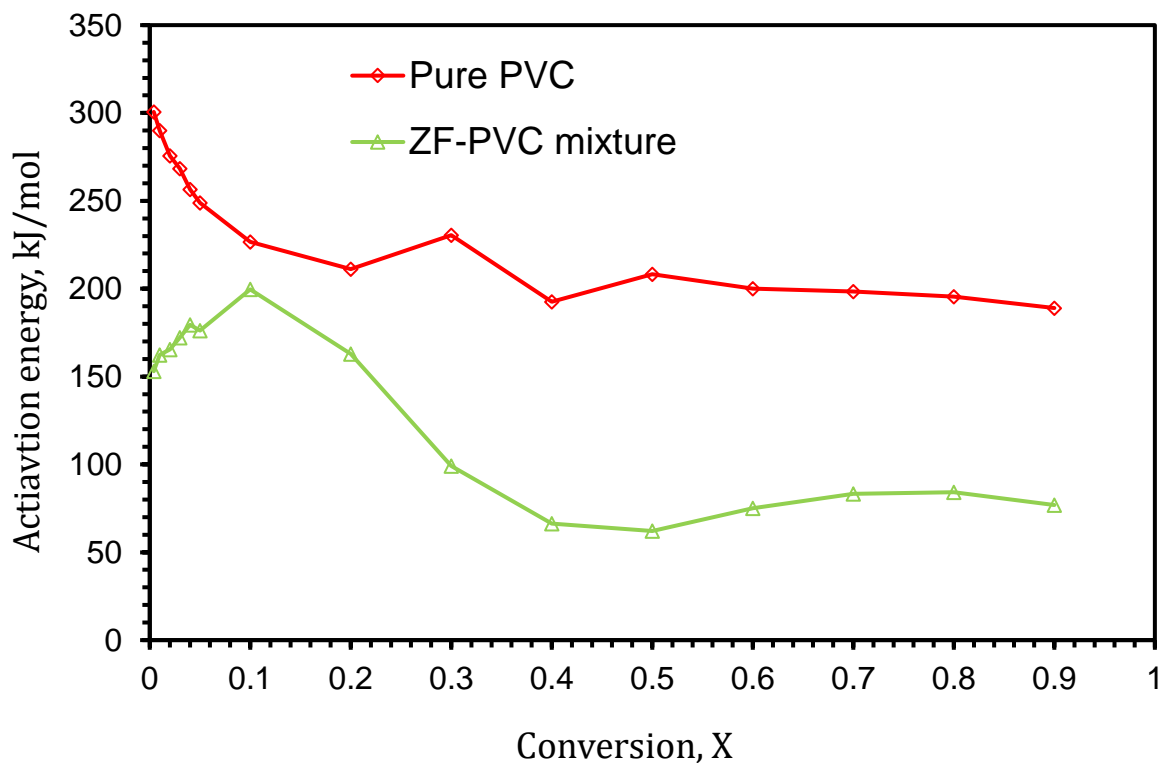


Figure 9: Iso-conversional activation energies associated with polyene thermal cracking (third stage for pure PVC and third and fourth stages for ZF-PVC) in the conversion range 0.004 – 0.9 using Friedman model.

Table 5: Kinetic parameters associated with the polyene thermal cracking of pure PVC (Figure 3) (Altarawneh et al., 2021).

Conversion, $\alpha$	KAS		Friedman			Linear model fitting		
	Activation energy, kJ/mol	Frequency factor, $\ln(A)^a$	Activation energy, kJ/mol	$\ln(A.f(X))$	Frequency factor, $\ln(A)^a$	Activation energy, kJ/mol	Frequency factor, $\ln(A)^a$	$f(X)$
0.1	256.2	41.56	226.7	36.66	36.37	201.8	31.67	$2(1 - X)^{\frac{3}{2}}$
0.2	235.7	37.95	211.1	33.67	33.62			
0.3	227.9	36.58	230.5	36.58	37.04			
0.4	219.6	35.12	192.6	30.04	30.36			
0.5	212.5	33.87	208.2	32.24	33.11			
0.6	208.8	33.21	200.0	30.64	31.66			
0.7	205.8	32.69	198.4	30.00	31.38			
0.8	202.4	32.09	195.4	28.99	30.85			
0.9	197.2	31.17	189.0	27.03	29.73			
Average <sup>b</sup>	218.4 ± 17.7	34.92 ± 3.11	205.8 ± 13.9	31.76 ± 3.14	32.68 ± 2.45			

a: Unit of frequency factor (A) is  $\text{min}^{-1}$

b: Average = mean ± SD

The addition of ZnFe<sub>2</sub>O<sub>4</sub> to PVC resulted in a drop in the activation energy for the polyene thermal cracking stage. The initiation activation energy at a conversion of 0.004 was 153 kJ/mol compared to 300.6 kJ/mol for pure PVC. This suggests that the presence of different chloride forms (FeCl<sub>2</sub>/FeCl<sub>2</sub>.2H<sub>2</sub>O and ZnCl<sub>2</sub>) can possibly alter the initiation mechanism associated with the cracking of the polymer backbone lowering the activation energy. As the reaction progresses, the activation energy increases to a value of 199.6 kJ/mol at  $X = 0.1$  then drops with conversion reaching an average value of 78.1 kJ/mol in the conversion range 0.3 – 0.9. Similar behaviour was previously seen in (Altarawneh et al., 2021) for the polyene thermal cracking of a mixture of ZnO and PVC where the activation energy dropped to an average value of 75.2 kJ/mol between conversions from 0.1 and 0.9. This drop in activation energy is assigned to the volatilisation of ZnCl<sub>2</sub> in that temperature range. This is because physical processes (e.g., volatilisation) are known to exhibit lower activation energies compared to chemical ones. Since lumped activation energies are given using Equation 20 (Vyazovkin et al., 2020) for multi-step processes (parallel processes), the evaporation of ZnCl<sub>2</sub> in the same range of the polyene thermal cracking can greatly affect the overall value of the apparent activation energy associated with the mass loss.

$$E_{\alpha} = \frac{E_1 k_1(T) f_1(\alpha) + E_2 k_2(T) f_2(\alpha)}{k_1(T) f_1(\alpha) + k_2(T) f_2(\alpha)} \quad (20)$$

Where numbers 1 and 2 in Equation 20 represent two parallel steps. The thermal cracking for ZF-PVC is controlled by a similar reaction model to that of pure PVC ( $f(X) = 2(1 - X)^{\frac{3}{2}}$ ) between conversions 0.1 and 0.2. However, from conversion 0.3 up to 0.8 the mass loss becomes controlled by a first order equation ( $f(X) = 1 - X$ ) (Table 6).

Table 6: Kinetic parameters associated with the polyene thermal cracking of ZF-PVC mixture (Figure 3)

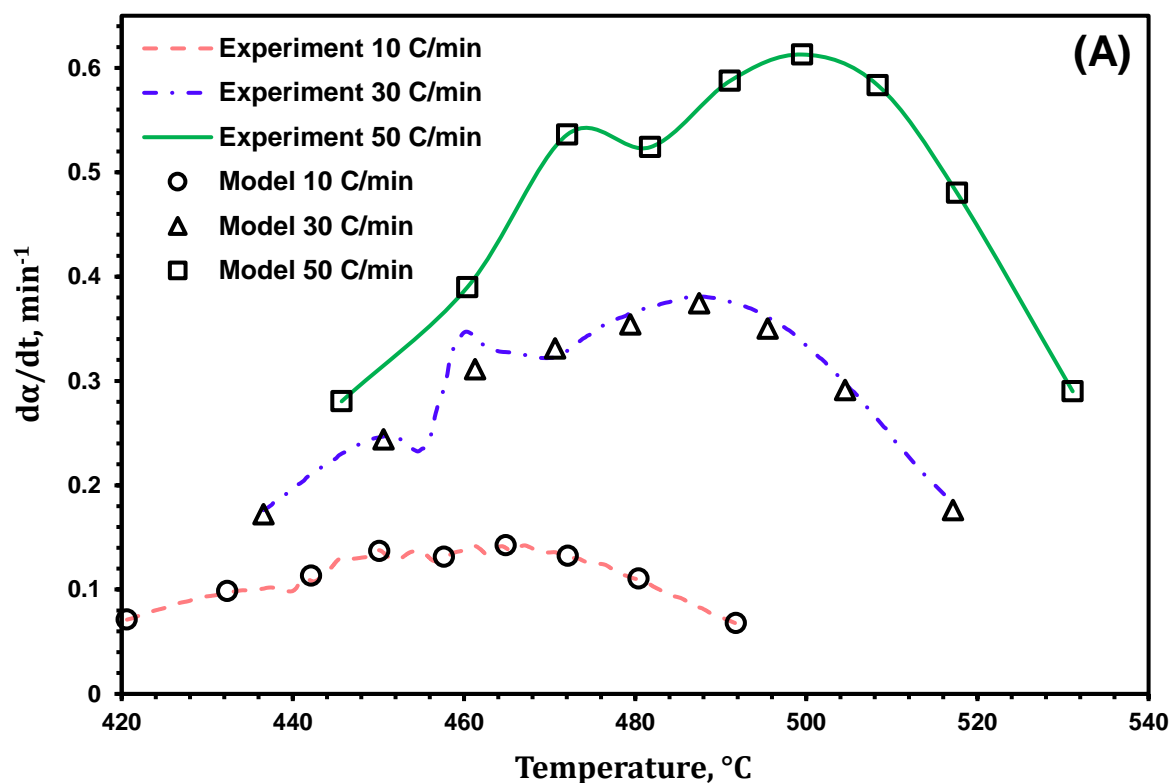
Conversion, $\alpha$	KAS		Friedman			Linear model fitting		
	Activation energy, kJ/mol	Frequency factor, $\ln(A)^a$	Activation energy, kJ/mol	$\ln(A.f(X))$	Frequency factor, $\ln(A)^a$	Activation energy, kJ/mol	Frequency factor, $\ln(A)^a$	$f(X)$
0.1	182.2	27.92	199.6	30.96	30.94			

0.2	191.9	29.60	162.9	24.80	24.58	189.8	28.68	$2(1 - X)^{\frac{3}{2}}$
0.3	167.6	25.39	99.2	14.54	13.53	76.90	11.16	1 - X
0.4	142.1	20.97	66.4	8.93	7.84			
0.5	117.6	16.72	62.1	8.03	7.10			
0.6	105.7	14.66	75.1	9.92	9.35			
0.7	99.7	13.62	83.2	10.94	10.76			
0.8	95.3	12.85	84.2	10.70	10.93			
0.9	93.3	12.51	76.8	8.97	9.64	Did not fit in model		
Average <sup>b</sup>	132.8 ± 36.9	19.36 ± 6.40	101.0 ± 44.9	14.20 ± 7.66	13.85 ± 7.78	—		

a: Unit of frequency factor (A) is  $\text{min}^{-1}$

b: Average = mean ± SD

The reliability of the kinetic data for the polyene thermal cracking stage was checked by comparing the experimental rate with the rate generated from the extracted kinetic parameters (Figure 10). It can be seen that there is a very good agreement between the rate generated from the extracted kinetic data (dotted) and the experimental rate at different heating rates. Making the comparison at different heating rates show that the kinetic data is able to predict the reaction rates at different temperatures.



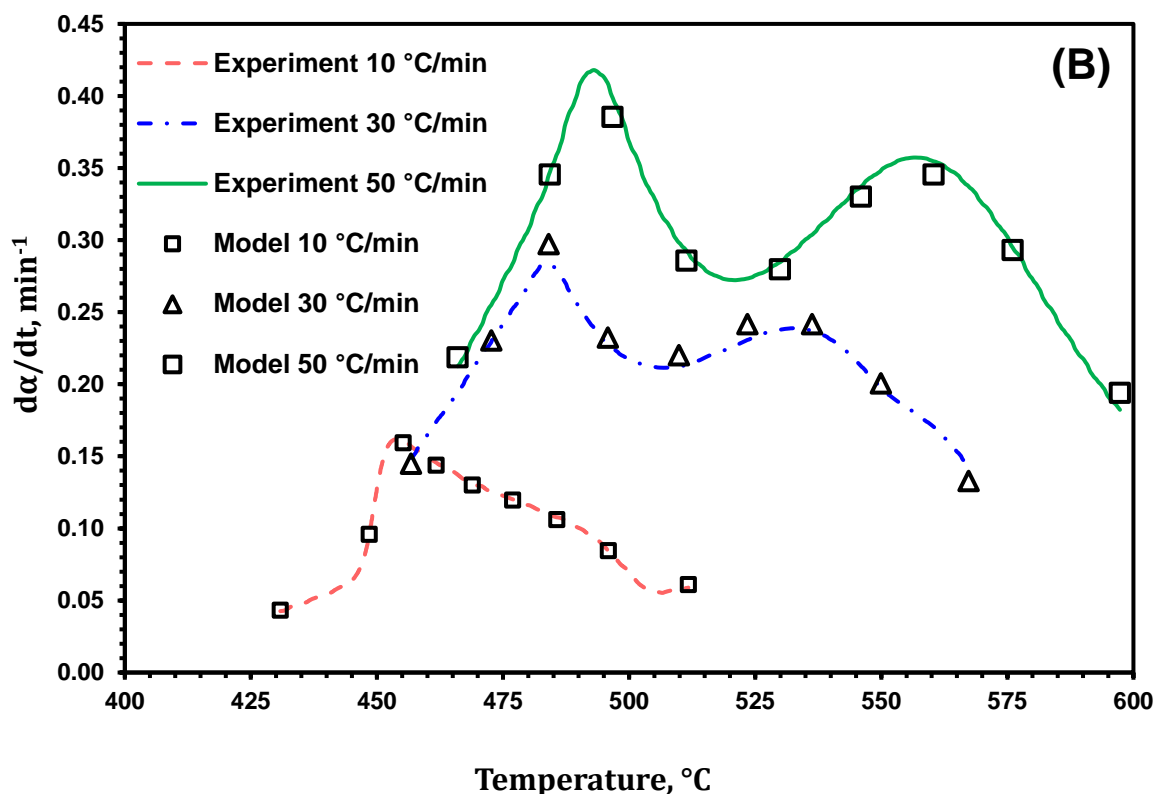


Figure 10: A comparison between experimental and model generated polyene thermal cracking rates of pure PVC (A) and ZF-PVC mixture (B) at heating rates of 10, 30, and 50 °C/min in the conversion range 0.1 – 0.9 (kinetic data from Friedman model).

## 5. Conclusions

In this work, the thermal behaviour, and the kinetic parameters of PVC degradation alone and in the presence of  $\text{ZnFe}_2\text{O}_4$  have been studied. The de-hydrochlorination of PVC resulted in a complete conversion of  $\text{ZnFe}_2\text{O}_4$  into its chloride species ( $\text{ZnCl}_2$  and  $\text{FeCl}_2/\text{FeCl}_2 \cdot 2\text{H}_2\text{O}$ ). Since  $\text{ZnFe}_2\text{O}_4$  is stable up to 900 °C, the formation of  $\text{ZnCl}_2$  was confirmed from the disappearance of zinc in the pyrolysis residue at 650 °C suggesting the complete chlorination of  $\text{ZnFe}_2\text{O}_4$  and the evaporation of formed  $\text{ZnCl}_2$ .

The addition of  $\text{ZnFe}_2\text{O}_4$  catalysed the degradation lowering the de-hydrochlorination onset temperature from 272 °C (pure PVC) to 235 °C (ZF-PVC mixture) despite the increase in the initiation activation energy from 109.9 kJ/mol (pure PVC) to 148.2 kJ/mol (ZF-PVC). This can be assigned to the increase in the frequency factor which compensated for the increase in the

activation energy yielding a higher overall rate constant at a lower temperature. The dehydrochlorination in the presence of  $\text{ZnFe}_2\text{O}_4$  initially proceeds via a direct reaction between  $\text{ZnFe}_2\text{O}_4$  with the PVC monomer eventually yielding  $\text{ZnCl}_2$  and  $\text{Fe}_2\text{O}_3$ .  $\text{Fe}_2\text{O}_3$  is then reduced to  $\text{Fe}_3\text{O}_4$  by reacting with  $\text{H}_2$  from PVC degradation which eventually chlorinates to  $\text{FeCl}_2$  and  $\text{FeCl}_2 \cdot 2\text{H}_2\text{O}$  both of which were detected by XRD.

The kinetic data exhibited different energy barriers and frequency factors for different parallel reactions. This, in turn, yielded different values of rate constant for different reaction pathways. Such a phenomenon can be used to channel the chlorine in the PVC towards the direct chlorination of  $\text{ZnFe}_2\text{O}_4$  instead of it being released as  $\text{HCl}$  which would subsequently be captured by  $\text{Fe}_3\text{O}_4$  (reduced from  $\text{Fe}_2\text{O}_3$ ) to form  $\text{FeCl}_2/\text{FeCl}_2 \cdot 2\text{H}_2\text{O}$ . Moreover, since the reduction of  $\text{Fe}_2\text{O}_3$  by  $\text{H}_2$  is kinetically slow, the chlorination selectivity of zinc over iron can be maximised by operating at temperatures below  $260\text{ }^\circ\text{C}$  which would leave iron in its stable form  $\text{Fe}_2\text{O}_3$ . The evidence in this study showed that  $\text{Fe}_2\text{O}_3$  can be detected by XRD with the complete absence of  $\text{ZnFe}_2\text{O}_4$  when the pyrolysis was performed at a low temperature ( $260\text{ }^\circ\text{C}$ ) suggesting that selectivity can be maximised with proper controlling of the temperature.

## 6. Future work

While the kinetic parameters extracted in this work can describe the thermal behaviour of PVC and ZF-PVC accurately, in some cases they might not reflect the chemical/physical processes fundamentally. The values reported here are lumped values which take into account several consecutive/parallel processes. Moreover, to build a model for the kinetic effect EAFDs of varying composition and chemistries on the thermal degradation of PVC, one needs to study the kinetic effect of the other major EAFD components such as  $\text{Fe}_2\text{O}_3$ ,  $\text{Fe}_3\text{O}_4$ ,  $\text{PbO}$ , and in some cases  $\text{MgO}$ . Hence, in future work, the kinetic effect of the other major EAFD components contributing to a model describing the overall effect of these components combined should be

addressed. This, in turn, would reflect the effect of EAFDs with different chemistries world-wide on the thermal degradation of PVC.

For now, the extracted kinetic data produced a very good fit when compared with experimental reaction rate suggesting that the extracted kinetic parameters can be used to predict the thermal behaviour of PVC and ZF-PVC at different temperatures.

## Acknowledgment

The authors would like to thank Sabrin Samad from the Nanoscale and Microscale Research Centre (nmRC) at the University of Nottingham for providing aid with the SEM analysis.

## References

- Ahmed, O.H., Altarawneh, M., Al-Harshsheh, M., Jiang, Z.-T., Dlugogorski, B.Z., 2018. Recycling of zincite (ZnO) via uptake of hydrogen halides. *Physical Chemistry Chemical Physics* 20, 1221-1230.
- Akahira, T., Sunose, T., 1971. Res. Report Chiba Inst. Technol. Sci. Technol 16, 22.
- Al-Harshsheh, M., 2017. Thermodynamic Analysis on the Thermal Treatment of Electric Arc Furnace Dust-PVC Blends. *Arabian Journal for Science and Engineering*, 1-13.
- Al-Harshsheh, M., Al-Otoom, A., Al-Makhadmeh, L., Hamilton, I.E., Kingman, S., Al-Asheh, S., Hararah, M., 2015. Pyrolysis of poly(vinyl chloride) and—electric arc furnacedust mixtures. *Journal of Hazardous Materials* 299, 425-436.
- Al-Harshsheh, M., Aljarrah, M., Al-Otoom, A., Altarawneh, M., Kingman, S., 2018. Pyrolysis kinetics of tetrabromobisphenol a (TBBPA) and electric arc furnace dust mixtures. *Thermochimica Acta* 660, 61-69.
- Al-Harshsheh, M., Altarawneh, S., Al-Omari, M., 2022. Selective dissolution of zinc and lead from electric arc furnace dust via oxidative thermolysis with polyvinyl chloride and water-leaching process. *Hydrometallurgy*, 105898.
- Al-Harshsheh, M., Altarawneh, S., Al-Omari, M., Altarawneh, M., Kingman, S., Dodds, C., 2021a. Leaching behavior of zinc and lead from electric arc furnace dust–Poly (vinyl) chloride residues after oxidative thermal treatment. *Journal of Cleaner Production* 328, 129622.
- Al-harshsheh, M., Kingman, S., Al-Makhadmeh, L., Hamilton, I.E., 2014. Microwave treatment of electric arc furnace dust with PVC: Dielectric characterization and pyrolysis-leaching. *Journal of Hazardous Materials* 274, 87-97.
- Al-Harshsheh, M., Orabi, Y., Al-Asheh, S., 2021b. Comparative study on the pyrolysis and leachability of washed/unwashed electric arc furnace dust-PVC mixtures and their residues. *Journal of Environmental Chemical Engineering*, 105410.
- Al-Makhadmeh, L.A., Batiha, M.A., Al-Harshsheh, M.S., Altarawneh, I.S., Rawadieh, S.E., 2018. The Effectiveness of Zn Leaching from EAFD Using Caustic Soda. *Water, Air, & Soil Pollution* 229, 33.
- Altarawneh, S., Al-Harshsheh, M., Dodds, C., Buttress, A., Kingman, S., 2021. Thermal degradation kinetics of polyvinyl chloride in presence of zinc oxide. *Thermochimica Acta*, 179105.

Bale, C.W., Bélisle, E., Chartrand, P., Decterov, S.A., Eriksson, G., Gheribi, A.E., Hack, K., Jung, I.H., Kang, Y.B., Melançon, J., Pelton, A.D., Petersen, S., Robelin, C., Sangster, J., Spencer, P., Van Ende, M.A., 2016. Reprint of: FactSage thermochemical software and databases, 2010–2016. *Calphad* 55, 1-19.

Bale, C.W., Chartrand, P., Decterov, S.A., Eriksson, G., Hack, K., Ben Mahfoud, R., Melançon, J., Pelton, A.D., Petersen, S., 2002. FactSage thermochemical software and databases. *Calphad* 26, 189-228.

Blazso, M., Jakab, E., 1999. Effect of metals, metal oxides, and carboxylates on the thermal decomposition processes of poly (vinyl chloride). *Journal of Analytical and Applied Pyrolysis* 49, 125-143.

Coats, A.W., Redfern, J., 1964. Kinetic parameters from thermogravimetric data. *Nature* 201, 68-69.

Friedman, H.L., 1964. Kinetics of thermal degradation of char-forming plastics from thermogravimetry. Application to a phenolic plastic, *Journal of polymer science part C: polymer symposia*. Wiley Online Library, pp. 183-195.

Georgieva, V., Zvezdova, D., Vlaev, L., 2013. Non-isothermal kinetics of thermal degradation of chitin. *Journal of thermal analysis and calorimetry* 111, 763-771.

Havlík, T., Souza, B.V.e., Bernardes, A.M., Schneider, I.A.H., Miškuřová, A., 2006. Hydrometallurgical processing of carbon steel EAF dust. *Journal of Hazardous Materials* 135, 311-318.

Ji, M., Chen, L., Que, J., Zheng, L., Chen, Z., Wu, Z., 2020. Effects of transition metal oxides on pyrolysis properties of PVC. *Process Safety and Environmental Protection* 140, 211-220.

Jordan, K.J., Suib, S.L., Koberstein, J.T., 2001. Determination of the Degradation Mechanism from the Kinetic Parameters of Dehydrochlorinated Poly(vinyl chloride) Decomposition. *The Journal of Physical Chemistry B* 105, 3174-3181.

Kim, S., 2001. Pyrolysis kinetics of waste PVC pipe. *Waste management* 21, 609-616.

KiranKumar, T., Roy, G.G., 2022. A Review on Processing of Electric Arc Furnace Dust (EAFD) by Pyro-Metallurgical Processes. *Transactions of the Indian Institute of Metals*, 1-12.

Kissinger, H.E., 1957. Reaction kinetics in differential thermal analysis. *Analytical chemistry* 29, 1702-1706.

Laubertova, M., Havlik, T., Parilak, L., Derin, B., Trpcevska, J., 2020. The effects of microwave-assisted leaching on the treatment of electric arc furnace dusts (EAFD). *Archives of Metallurgy and Materials* 65.

Lee, G.-S., Song, Y.J., 2007. Recycling EAF dust by heat treatment with PVC. *Minerals engineering* 20, 739-746.

Levchik, S.V., Weil, E.D., 2005. Overview of the recent literature on flame retardancy and smoke suppression in PVC. *Polymers for Advanced Technologies* 16, 707-716.

Marcilla, A., Beltrán, M., 1995. Thermogravimetric kinetic study of poly(vinyl chloride) pyrolysis. *Polymer Degradation and Stability* 48, 219-229.

Meng, T.-T., Zhang, H., Lü, F., Shao, L.-M., He, P.-J., 2021. Comparing the effects of different metal oxides on low temperature decomposition of PVC. *Journal of Analytical and Applied Pyrolysis* 159, 105312.

Mersiowsky, I., Stegmann, R., Ejlertsson, J., 1999. Long term behaviour of poly (vinyl chloride) products under soil buried and landfill conditions. *Plastics, rubber and composites* 28, 321-326.

Miranda, R., Pakdel, H., Roy, C., Darmstadt, H., Vasile, C., 1999. Vacuum pyrolysis of PVCII: Product analysis. *Polymer Degradation and Stability* 66, 107-125.

Omran, M., Fabritius, T., Heikkinen, E.-P., 2019. Selective Zinc Removal from Electric Arc Furnace (EAF) Dust by Using Microwave Heating. *Journal of Sustainable Metallurgy* 5, 331-340.

Oustadakis, P., Tsakiridis, P.E., Katsiapi, A., Agatzini-Leonardou, S., 2010. Hydrometallurgical process for zinc recovery from electric arc furnace dust (EAFD): Part I: Characterization and leaching by diluted sulphuric acid. *Journal of Hazardous Materials* 179, 1-7.

Ozawa, T., 1965. A new method of analyzing thermogravimetric data. *Bulletin of the chemical society of Japan* 38, 1881-1886.

Pineau, A., Kanari, N., Gaballah, I., 2006. Kinetics of reduction of iron oxides by H<sub>2</sub>: Part I: Low temperature reduction of hematite. *Thermochimica acta* 447, 89-100.

Plastics-Europe, 2021. *Plastics – the Facts 2021*.

Šesták, J., Berggren, G., 1971. Study of the kinetics of the mechanism of solid-state reactions at increasing temperatures. *Thermochimica Acta* 3, 1-12.

Sinaga, G., Wismogroho, A., Fitroturokhmah, A., Kusumaningrum, R., Widayatno, W., Hadiko, G., Amal, M., 2019. The pyrometallurgical recovery of zinc from electric arc furnace dust (EAFD) with active carbon, *IOP Conference Series: Materials Science and Engineering*. IOP Publishing, p. 012068.

Starnes, W.H., Ge, X., 2004. Mechanism of autocatalysis in the thermal dehydrochlorination of poly (vinyl chloride). *Macromolecules* 37, 352-359.

Suetens, T., Klaasen, B., Van Acker, K., Blanpain, B., 2014. Comparison of electric arc furnace dust treatment technologies using exergy efficiency. *Journal of cleaner production* 65, 152-167.

Teo, Y.Y., Lee, H.S., Low, Y.C., Choong, S.W., Low, K.O., 2018. Hydrometallurgical extraction of zinc and iron from electric arc furnace dust (EAFD) using hydrochloric acid. *Journal of Physical Science* 29, 49-54.

Vyazovkin, S., 2021. Determining Preexponential Factor in Model-Free Kinetic Methods: How and Why? *Molecules* 26, 3077.

Vyazovkin, S., Burnham, A.K., Criado, J.M., Pérez-Maqueda, L.A., Popescu, C., Sbirrazzuoli, N., 2011. ICTAC Kinetics Committee recommendations for performing kinetic computations on thermal analysis data. *Thermochimica acta* 520, 1-19.

Vyazovkin, S., Burnham, A.K., Favergeon, L., Koga, N., Moukhina, E., Pérez-Maqueda, L.A., Sbirrazzuoli, N., 2020. ICTAC Kinetics Committee recommendations for analysis of multi-step kinetics. *Thermochimica Acta* 689, 178597.

Yakornov, S.A., Pan'shin, A.M., Kozlov, P.A., Ivakin, D.A., 2017. Development of Charge Pelletizing Technology Based on Electric Arc Furnace Dust for Pyrometallurgical Processing in Rotary Kilns. *Metallurgist* 61, 529-534.

Ye, L., Li, T., Hong, L., 2021. Co-pyrolysis of Fe<sub>3</sub>O<sub>4</sub>-poly (vinyl chloride)(PVC) mixtures: Mitigation of chlorine emissions during PVC recycling. *Waste Management* 126, 832-842.

Ye, Q., Li, G., Peng, Z., Augustine, R., Pérez, M.D., Liu, Y., Liu, M., Rao, M., Zhang, Y., Jiang, T., 2020. Microwave-assisted self-reduction of EAF dust-biochar composite briquettes for production of direct reduced iron. *Powder Technology* 362, 781-789.

Yu, J., Sun, L., Ma, C., Qiao, Y., Yao, H., 2016. Thermal degradation of PVC: A review. *Waste Management* 48, 300-314.

Zhang, B., Yan, X.-Y., Shibata, K., Uda, T., Tada, M., Hirasawa, M., 2000. Thermogravimetric-mass spectrometric analysis of the reactions between oxide (ZnO, Fe<sub>2</sub>O<sub>3</sub> or ZnFe<sub>2</sub>O<sub>4</sub>) and polyvinyl chloride under inert atmosphere. *Materials Transactions, JIM* 41, 1342-1350.

Zhang, M., Li, J., Zeng, Q., Mou, Q., 2019. An Experimental Study on the Reduction Behavior of Dust Generated from Electric Arc Furnace. *Applied Sciences* 9, 3604.

## Appendix 4: A thermo-kinetic investigation on the thermal degradation of polyvinyl chloride in the presence of magnetite and hematite

Sanad Altarawneh<sup>1,\*</sup>, Mohammad Al-Harahsheh<sup>2</sup>, Adam Buttress<sup>1</sup>, Chris Dodds<sup>1</sup>, Sam Kingman<sup>1</sup>

\*corresponding author: [sanad.altarawneh@nottingham.ac.uk](mailto:sanad.altarawneh@nottingham.ac.uk)

<sup>1</sup> Faculty of Engineering, University of Nottingham, Nottingham, NG7 2RD, UK

<sup>2</sup> Chemical Engineering Department, Jordan University of Science and Technology, Irbid, 22110, Jordan

### Abstract

Electric arc furnace dust (EAFD) which is accumulated in large amounts world-wide contains hematite ( $\text{Fe}_2\text{O}_3$ ) and significant quantities of magnetite ( $\text{Fe}_3\text{O}_4$ ). Waste polyvinyl chloride (PVC) also poses a great environmental threat aside to accumulated EAFD. Both of these wastes have shown a great potential for their co-thermal treatment for metal extraction, thus minimising their environmental footprint. Herein, an investigation on the thermal degradation behaviour, reaction products, thermodynamics and the decomposition kinetics of PVC and its stoichiometric mixtures with  $\text{Fe}_3\text{O}_4$  and  $\text{Fe}_2\text{O}_3$  was conducted using non-isothermal thermogravimetric scans. The kinetic data suggests a significant increase in the average activation energy of PVC de-hydrochlorination from  $122.6 \pm 24.2$  kJ/mol (pure PVC) to  $177.0 \pm 28.0$  and  $199.0 \pm 77.0$  kJ/mol when stoichiometric quantities of  $\text{Fe}_3\text{O}_4$  and  $\text{Fe}_2\text{O}_3$  were mixed with PVC. The inhibiting effect of both  $\text{Fe}_3\text{O}_4$  and  $\text{Fe}_2\text{O}_3$  on the degradation of PVC might be assigned to the capturing of emitted gaseous HCl which is known for its catalytic effect. This result suggests that EAFDs containing both  $\text{Fe}_3\text{O}_4$  (in large amounts) and  $\text{Fe}_2\text{O}_3$  can have an inhibiting effect on the de-hydrochlorination of PVC resulting in longer processing times or the requirement of higher processing temperatures for achieving reasonable reaction rates.

Keywords: PVC;  $\text{Fe}_3\text{O}_4$ ;  $\text{Fe}_2\text{O}_3$ ; pyrolysis; iron oxide; non-isothermal kinetics

## 1. Introduction

Economic development and advancement is accompanied by a rise in the rate of waste generation [1]. Among a wide array of different industries, steel manufacturing can be considered as one of the largest industrial sectors in terms of production rate. The global annual crude steel production was 189 million tons in 1950 which increased to 850 and 1809 million tons in 2000 and 2018, respectively [2]. Electric arc furnaces (EAFs) accounted for 28% of the total steel production in 2018 [2]. This large production rate from EAFs is accompanied by harmful emissions in the form of small particle size dust which is referred to as electric arc furnace dust (EAFD). The overall hazard associated with EAFD lies in its large production rate (1–2% of EAF steel charge) [3], the presence of toxic heavy metals such as Cd and Pb [3], and the absence of a sustainable and an environmentally benign recycling route of the material.

Parallel to accumulated EAFD, there has been a significant increase in the generation rate of plastic wastes due to its extensive use in all life applications [4]. Among thermoplastics, Polyvinyl Chloride (PVC) is considered one of the most commonly used [5]. A simulation study performed by Zhou et al. [6] suggests that in China alone, the accumulated PVC waste will reach up to 600 million tons by the end of year 2050. The disposal of this waste has been the concern of many environmental engineers. Conventionally, landfilling and incineration of PVC are the most prevalent routes for disposal. Due to the stable nature of PVC [7], the former approach can result in the indefinite accumulation of PVC in landfills. The latter, on the other hand, results in the formation of hazardous emissions such as hydrogen chloride (HCl) and chlorinated hydrocarbons (dioxins) [8-12]. The adoption of an incineration approach requires finding a sustainable solution to the emissions that accompany decomposing PVC. This can involve using resistive material for the construction of the handling equipment, or the co-thermal treatment of PVC with other materials that can act as emission fixators [9, 12-14]. EAFD has been identified as an excellent candidate for the fixation of the harmful emissions

evolved from decomposing PVC [4, 10-13]. Lee and Song [13], confirmed the formation of zinc, lead, and cadmium chlorides upon thermal treatment with PVC with recovery percentages up to 96.2, 97.4 and 98.8% respectively. A series of papers published by Al-Harashsheh et al. [10-12, 14, 15], tackled the metal extraction, kinetics, and thermodynamics aspects of the co-thermal treatment of PVC with EAFD. The limitation of these studies is that they were unable to elucidate the individual contribution of each metal oxide in EAFD to the fixation of emissions as well as their effect on the kinetics of PVC degradation. Knowledge of the individual kinetic effect of each metal oxide phase is important. This is because the chemistry of EAFD can vary greatly from one site to another and from one country to another. Thus, establishing a kinetic database for the effect of each metal oxide present in EAFD on the kinetics of PVC degradation helps in making kinetic predictions for PVC decomposition mixed with EAFD from different sources with different chemistries based on their mineralogical composition.

In this study, we present a systematic non-isothermal kinetic study of the thermal dehydrochlorination of PVC mixed with stoichiometric amounts of  $\text{Fe}_3\text{O}_4$  and  $\text{Fe}_2\text{O}_3$ ; the former is present in EAFD at high concentrations. The thermal scans were generated at different heating rates which allows the calculation of the apparent activation energy, the apparent frequency factor, and the apparent reaction model associated with the dehydrochlorination using model free methods. A detailed identification of the solid pyrolysis products of  $\text{Fe}_3\text{O}_4$ -PVC and  $\text{Fe}_2\text{O}_3$ -PVC mixtures at different temperatures was undertaken using different solid analytical techniques.

## **2. Materials and method**

### **2.1. Thermogravimetric analysis and Differential scanning calorimetry**

$\text{Fe}_3\text{O}_4$  and PVC powders were obtained from Sigma-Aldrich, while  $\text{Fe}_2\text{O}_3$  was obtained from Fisher scientific.  $\text{Fe}_3\text{O}_4$  and  $\text{Fe}_2\text{O}_3$  powders had purities of 99.99% and 99.999%, respectively.

Iron oxide-PVC mixtures were prepared based on the stoichiometric amount of HCl in the PVC monomer to fully chlorinate  $\text{Fe}_3\text{O}_4$  and  $\text{Fe}_2\text{O}_3$  into their corresponding chloride forms ( $\text{FeCl}_2$  and  $\text{FeCl}_3$  for  $\text{Fe}_3\text{O}_4$  and  $\text{FeCl}_3$  for  $\text{Fe}_2\text{O}_3$ ). Hence, mixtures of 31.6 and 29.9 wt% of  $\text{Fe}_3\text{O}_4$  and  $\text{Fe}_2\text{O}_3$  with PVC were prepared. The instrument used for the simultaneous TGA/DSC analysis was a SDT Q600. Before the analysis, an experiment with an empty sample holder (ceramic crucible) was performed to produce a baseline for the heat flow signal. Accurate amounts ( $10.7 \pm 0.39$  mg ( $\text{Fe}_3\text{O}_4$ -PVC) and  $10.3 \pm 0.49$  mg ( $\text{Fe}_2\text{O}_3$ -PVC)) were loaded into the ceramic crucibles and the thermal analysis was performed under a nitrogen flow of 100 mL/min. Different heating rates of 10, 30 and 50 K/min for PVC and  $\text{Fe}_3\text{O}_4$ -PVC were used. For  $\text{Fe}_2\text{O}_3$ -PVC, however, heating rates of 5, 10, and 30 K/min were used. This is because the 50 K/min accentuated the effect of a certain parallel reaction resulting in a larger mass loss at 50 K/min thus preventing the usage of model free kinetic approach. The temperature range used in the analysis was 25 to 900 °C.

## **2.2. Pyrolysis of iron oxides-PVC mixtures**

A sample of  $0.32 \pm 0.0075$  g of each mixture was loaded in a 4 mm diameter quartz tube. The powder was pre-purged with nitrogen (purity: 99.9992%) for at least 15 minutes to allow the formation of a nitrogen blanket around the reactants, after which the flow was held at ~5 mL/min. The pyrolysis temperatures were 400, 550, 650, and 850 °C for  $\text{Fe}_3\text{O}_4$ -PVC and 400, 600, and 850 °C for  $\text{Fe}_2\text{O}_3$ -PVC. The different temperature choice for each mixture was made because of their distinct TGA profiles such that each temperature resembles a plateau after every stage. The reactants were loaded into the furnace and were held at the desired temperature for 30 minutes. The pyrolysis products were taken out of the reactor, purged with nitrogen, and stored in a desiccator for further analysis.

## **2.3. Mineralogy characterisation**

The pyrolysis residues were characterised using X-Ray Diffraction (XRD). Due to the hygroscopic nature of the generated powder, the sample was covered with plastic tape during the analysis to prevent it from being exposed to the ambient atmosphere. The analysis was conducted on a Bruker D8 Advance XRD machine. The mineralogy of the generated phases were studied in the  $2\theta$  range of  $5 - 90^\circ$  at a step size of  $0.02^\circ$  with a scan time of 1.7 sec/step. The radiation source was Cu  $k\alpha$  and the X-ray tube was operated at a current and voltage of 40 mA and 40 kV, respectively.

#### **2.4. Morphology and chemistry characterisation**

The pyrolysis residues were characterised for morphology and chemistry using FEI Quanta600 MLA scanning electron microscope (SEM) coupled with energy dispersive spectroscopy (EDS). A small amount of the pyrolysis residue was sprinkled on a stub covered with a carbon adhesive layer. Powders on stubs were coated with an  $8.2 \pm 1.4$  nm layer of carbon to enhance the electrical conductivity during the analysis to prevent electron charging. The operating conditions of the SEM instrument were: spot size of 5.00 and an accelerating voltage of 15.0 kV.

#### **2.5. Particle size analysis**

Since the particle size can have an impact on the contact surface area between reactants, the particle sizes of the materials used in this work were measured. The instrument used for the analysis was the Beckman Coulter LS13320MW laser diffraction analyser with an Aqueous Liquid Module (ALM). The particle size was measured for the as received materials used in this work (PVC,  $\text{Fe}_3\text{O}_4$ , and  $\text{Fe}_2\text{O}_3$ ) and are reported in Table 2.

#### **2.6. Thermodynamics simulation**

Due to the presence of a large amount of possible reduction reactions, the interpretation of the kinetic data becomes easier with the presence of thermodynamics data. FACTSAGE software package was used to calculate the change in the Gibbs free energy associated with the relevant

reactions during the course of PVC degradation in the presence of Fe<sub>3</sub>O<sub>4</sub> and Fe<sub>2</sub>O<sub>3</sub> in the temperature window 20 – 1000 °C. Based on this data, one can know if a certain reaction lies majorly forward or backwards (i.e., its equilibrium status).

### 3. Non-isothermal kinetics and modelling

#### 3.1. Kinetic rate equation

In non-isothermal kinetics, the mass of the sample is monitored while being heated at a fixed heating rate  $\beta$ . The loss/gain in mass is represented by the conversion ( $\alpha$ ) which is given by:

$$\alpha = \frac{M_o - M}{M_o - M_f} \quad (1)$$

Where  $M_o$  is the initial mass%,  $M_f$  is the final mass%, and  $M$  is the mass% at any time  $t$ .

The rate ( $r_A$ ) of mass loss/gain is thus represented by the derivative of the conversion with respect to time  $\left(\frac{d\alpha}{dt}\right)$  which is given as the product of the temperature dependent rate constant  $k(T)$  and the temperature independent conversion function  $f(\alpha)$  [16]:

$$r_A = \frac{d\alpha}{dt} = k(T) \cdot f(\alpha) \quad (2)$$

The rate constant dependency on temperature can be described by the Arrhenius function:

$$k(T) = A \exp\left(\frac{-E}{RT}\right) \quad (3)$$

In which,  $A$  is the frequency factor in  $\text{min}^{-1}$ ,  $E$  is the activation energy J/mol, and  $R$  is the universal gas constant (8.314 J/mol .K).

The general expression of the conversion function is given by the empirical equation introduced by Šesták and Berggren [17]:

$$f(\alpha) = \alpha^m (1 - \alpha)^n [-\ln(1 - \alpha)]^p \quad (4)$$

Such that, m, n, and p, are empirically obtained exponents, and different combinations of them yield different reaction models [18]. Substituting the values of  $f(\alpha)$ ,  $k(T)$ , and the heating rate

$\beta = \frac{dT}{dt}$  in Equation 2, we obtain the following equation:

$$\frac{r_A}{\beta} = \frac{d\alpha}{dT} = \frac{A}{\beta} \exp\left(\frac{-E}{RT}\right) \cdot (\alpha^m(1-\alpha)^n[-\ln(1-\alpha)]^p) \quad (5)$$

Equation 5 shows the derivative form of the rate equation. By rearranging and integrating both sides, we reach at the integral form:

$$g(\alpha) = \int_0^\alpha \frac{d\alpha}{\alpha^m(1-\alpha)^n[-\ln(1-\alpha)]^p} = \int_{T_0}^T \frac{A}{\beta} \exp\left(\frac{-E}{RT}\right) dT \quad (6)$$

The most reliable techniques that are able to track the variation in the apparent activation energy and the frequency factor with conversion are the model free kinetic methods [19, 20].

## 3.2. Calculation of the activation energy

### 3.2.1. Model free kinetic methods

Model free methods rely on the principle that at a fixed conversion level, the rate of degradation is a function of temperature only [18]. This can be visualised by taking the logarithmic derivative of Equation 2 with respect to the reciprocal of temperature at a constant conversion [18]:

$$\left[\frac{\partial \ln\left(\frac{d\alpha}{dt}\right)}{\partial T^{-1}}\right]_\alpha = \left[\frac{\partial \ln f(\alpha)}{\partial T^{-1}}\right]_\alpha + \left[\frac{\partial \ln(k(T))}{\partial T^{-1}}\right]_\alpha = 0 + \frac{-E\alpha}{R} \quad (7)$$

Equation 7 tells us that knowledge of the iso-conversional activation energy can be achieved without assuming any reaction model, hence comes the name model-free [18].

#### 3.2.1.1. Differential model free method

The Friedman method [19] utilises the differential form (Equation 5) of the rate equation with slight adjustment to the following form:

$$\ln\left(\beta \frac{d\alpha}{dT}\right)_{\alpha,i} = \ln\left(\frac{d\alpha}{dt}\right)_{\alpha,i} = \ln(Af(\alpha)) - \frac{E\alpha}{RT_{\alpha,i}} \quad (8)$$

At a specific conversion at a certain heating rate, specific values of  $\ln\left(\frac{d\alpha}{dt}\right)$  and  $\frac{1}{T}$  are obtained.

Hence, a plot of  $\ln\left(\frac{d\alpha}{dt}\right)$  against  $\frac{1}{T}$  at a minimum of three different heating rates, yields a straight line with a slope of  $-\frac{E\alpha}{R}$  from which the apparent activation energy is calculated.

### 3.2.1.2. Integral model free method

Instead of performing the integration on the conversion function from 0 to  $\alpha$ , performing it on small segments between  $\alpha_0$  and  $\alpha_1$  (such that  $\alpha_1 - \alpha_0 = 0.02$ ) allows numerical integrations to be performed accurately. A numerical integration method was applied by Ortega [20] leading to the following final equation:

$$\ln\left(\frac{\beta_i}{T_1 - T_0}\right) = \ln\left(\frac{A}{F(\alpha_1) - F(\alpha_0)}\right) - \frac{E\alpha}{RT_{avg}} \quad (9)$$

Such that  $F(\alpha)$  is the indefinite anti-derivative of  $\frac{1}{f(\alpha)}$ , and  $T_0$  and  $T_1$  are the temperatures corresponding to conversions  $\alpha_0$  and  $\alpha_1$ , respectively.  $T_{avg}$  is the average temperature and is given as follows:

$$T_{avg} = \frac{T_1 + T_0}{2} \quad (10)$$

Using thermograms recorded at a minimum of three different heating rates, a plot of  $\ln\left(\frac{\beta_i}{T_1 - T_0}\right)$  against  $\frac{1}{T_{avg}}$  yields a straight line with a slope of  $-\frac{E\alpha}{R}$  from which the apparent activation energy can be calculated.

### 3.3. Calculation of the frequency factor using the compensation effect

This method relies on the principle that values of  $\ln(A)$  and  $E$ , whether they are correct or not are linearly correlated [21]. This relation can be built by fitting the experimental rate data to

different reaction models  $f(\alpha)$  (differential) or  $g(\alpha)$  (integral). In this case, Equation 11 was used and hence the differential form  $f(\alpha)$  of the reaction model was used.

$$\ln\left(\frac{d\alpha}{dt} \cdot \frac{1}{f(\alpha)}\right) = \ln(A) - \frac{E}{RT} \quad (11)$$

The most common reaction models are presented in Table 1. When a set of  $\ln(A)$  is obtained against a set of  $E$ , these values are plotted against each other. The mathematical formula of the linear regression line should correspond to this equation:

$$\ln(A)_i = aE_i + b \quad (12)$$

Such that,  $a$  and  $b$  are constants, while  $\ln(A)_i$  and  $E_i$  are each value generated using each reaction model. When the compensation chart is built, iso-conversional values of  $E_\alpha$  obtained from the model free methods mentioned earlier can be substituted in Equation 12 to extract their corresponding iso-conversional values of  $\ln(A)_\alpha$ . More elaboration on this method is presented in detail in Vyazovkin [21].

### 3.4. Prediction of the reaction model $f(\alpha)$

Extracting the mathematical formula of the reaction model for complex mass loss where many concurrent and sequential reactions are taking place is difficult. Since apparent activation energy and frequency factor are reported here, the reaction models reported for the dehydrochlorination stage with and without  $\text{Fe}_3\text{O}_4$  and  $\text{Fe}_2\text{O}_3$  will also be apparent ones. Rearranging the intercept  $I_\alpha = \ln(Af(\alpha))$  generated from the Friedman model to Equation 13 allows calculating the value of  $f(\alpha)$  at each conversion level. The value of  $\ln A_\alpha$  can be substituted from those obtained from the compensation effect presented above.

$$f(\alpha) = \exp(I_\alpha - \ln A_\alpha) \quad (13)$$

The calculated  $f(\alpha)$  values are then plotted against conversion with all the reaction models shown in Table 1 thus allowing tracking the change in  $f(\alpha)$  with conversion. A schematic

diagram showing how the  $f(\alpha)$  function was predicted by combining the Friedman model and the compensation effect is presented in Figure 1.

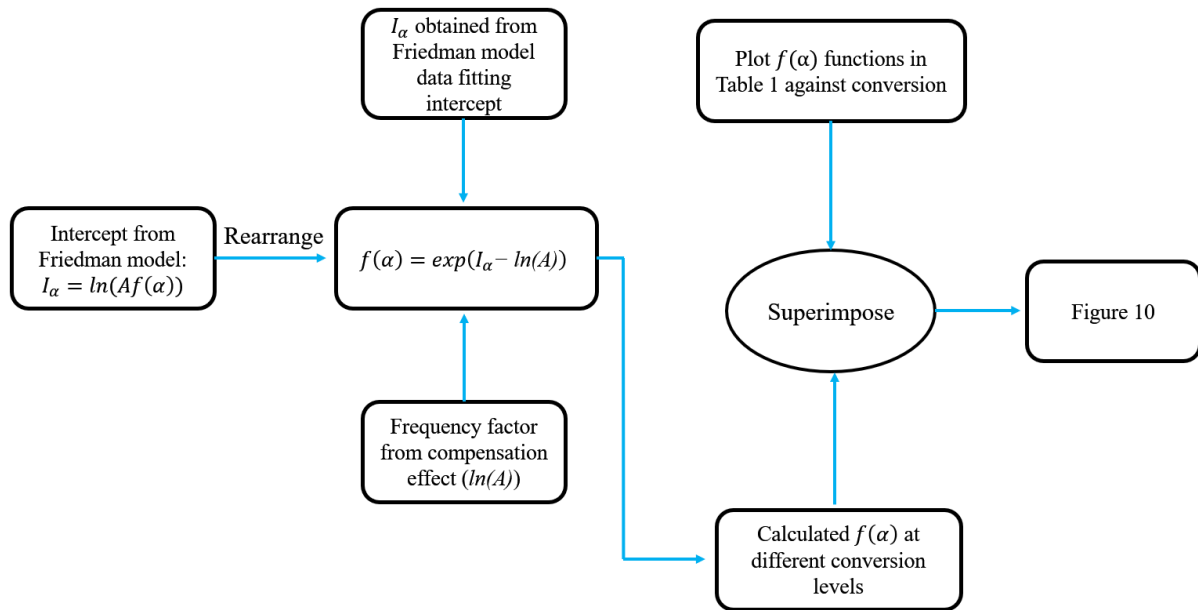


Figure 1: A schematic diagram showing how the  $f(\alpha)$  model is predicted using a combined Friedman-compensation effect approach.

Table 1: The most important kinetic models in the differential  $f(\alpha)$  and integral  $g(\alpha)$  forms [22].

No.	Symbol	Kinetic model	$f(\alpha)$	$g(\alpha)$
<b>Chemical process</b>				
1	F <sub>1/3</sub>	One-third order	$\frac{3}{2}(1-\alpha)^{\frac{1}{3}}$	$1 - (1-\alpha)^{\frac{2}{3}}$
2	F <sub>3/4</sub>	Three-quarters order	$4(1-\alpha)^{\frac{3}{4}}$	$1 - (1-\alpha)^{\frac{1}{4}}$
3	F <sub>3/2</sub>	One and half order	$2(1-\alpha)^{\frac{3}{2}}$	$(1-\alpha)^{-\frac{1}{2}} - 1$
4	F <sub>2</sub>	Second order	$(1-\alpha)^2$	$(1-\alpha)^{-1} - 1$
5	F <sub>3</sub>	Third order	$\frac{1}{2}(1-\alpha)^3$	$(1-\alpha)^{-2} - 1$
6	F <sub>n</sub>	n <sup>th</sup> order, n > 1	$\frac{1}{n-1}(1-\alpha)^n$	$(1-\alpha)^{-n+1} - 1$
<b>Acceleratory rate equations</b>				
7	P <sub>3/2</sub>	Mampel power law	$\frac{2}{3}\alpha^{-\frac{1}{2}}$	$\alpha^{\frac{3}{2}}$
8	P <sub>1/2</sub>	Mampel power law	$2\alpha^{\frac{1}{2}}$	$\alpha^{\frac{1}{2}}$
9	P <sub>1/3</sub>	Mampel power law	$3\alpha^{\frac{2}{3}}$	$\alpha^{\frac{1}{3}}$
10	P <sub>1/4</sub>	Mampel power law	$4\alpha^{\frac{3}{4}}$	$\alpha^{\frac{1}{4}}$
11	P <sub>1</sub>	Exponential law	$\alpha$	$\ln\alpha$
<b>Sigmoidal rate equations</b>				
12	A <sub>1</sub> , F <sub>1</sub>	Avrami–Erofeev equation	$(1-\alpha)$	$-\ln(1-\alpha)$

13	$A_{3/2}$	Avrami–Erofeev equation	$\frac{3}{2}(1-\alpha)(-\ln(1-\alpha))^{\frac{1}{3}}$	$[-\ln(1-\alpha)]^{\frac{2}{3}}$
14	$A_2$	Avrami–Erofeev equation	$2(1-\alpha)(-\ln(1-\alpha))^{\frac{1}{2}}$	$[-\ln(1-\alpha)]^{\frac{1}{2}}$
15	$A_3$	Avrami–Erofeev equation	$3(1-\alpha)(-\ln(1-\alpha))^{\frac{2}{3}}$	$[-\ln(1-\alpha)]^{\frac{1}{3}}$
16	$A_4$	Avrami–Erofeev equation	$4(1-\alpha)(-\ln(1-\alpha))^{\frac{3}{4}}$	$[-\ln(1-\alpha)]^{\frac{1}{4}}$
17	$A_u$	Prout-Tomkins equation	$\alpha(1-\alpha)$	$\ln\left[\frac{\alpha}{1-\alpha}\right]$
Phase boundary reaction				
18	$R_1, F_0, P_1$	Power law	$(1-\alpha)^0$	$\alpha$
19	$R_2, F_{1/2}$	Power law	$2(1-\alpha)^{\frac{1}{2}}$	$1-(1-\alpha)^{\frac{1}{2}}$
20	$R_3, F_{2/3}$	Power law	$3(1-\alpha)^{\frac{2}{3}}$	$1-(1-\alpha)^{\frac{1}{3}}$
Diffusion mechanism				
21	$D_1$	Parabola law	$\frac{1}{2}\alpha$	$\alpha^2$
22	$D_2$	Valensi equation	$[-\ln(1-\alpha)]^{-1}$	$\alpha + (1-\alpha)\ln(1-\alpha)$
23	$D_3$	Jander equation	$\frac{3}{2}(1-\alpha)^{\frac{2}{3}}\left[1-(1-\alpha)^{\frac{1}{3}}\right]^{-1}$	$\left[1-(1-\alpha)^{\frac{1}{3}}\right]^2$

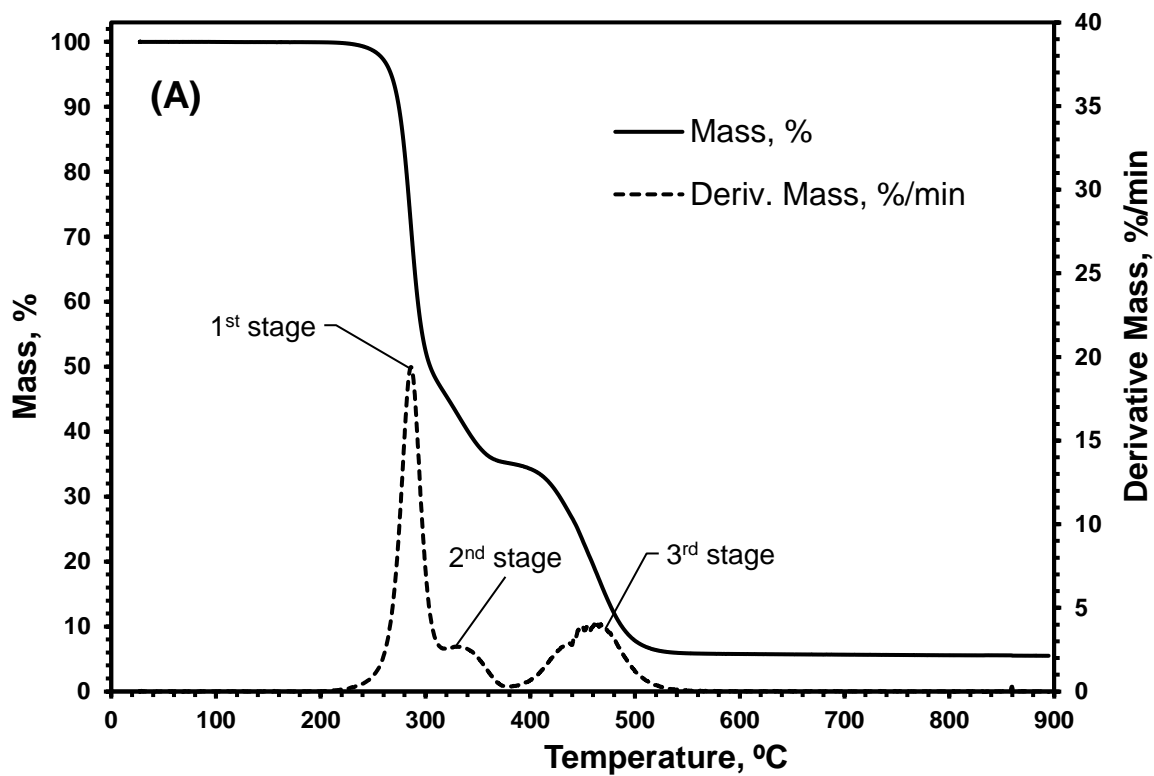
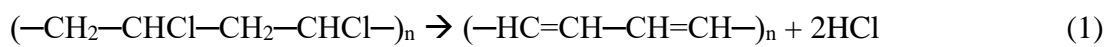
## 4. Results and discussion

### 4.1. Thermal behaviour of PVC and iron oxides-PVC mixtures

#### 4.1.1. Thermal behaviour of pure PVC pyrolysis

The TGA and differential thermogravimetric (DTG) profiles of pure PVC degradation are presented in Figure 2 (A). PVC decomposes following three degradation stages. The first two overlapped stages having an onset temperature of 272 °C and a mass loss of 65% are mainly attributed to the de-hydrochlorination of PVC and the emission of gaseous HCl [23]. However, a portion of this loss is also associated with the evolution of H<sub>2</sub> [24], benzene, toluene, and other hydrocarbons [25]. This accounts for the increased mass loss above the theoretical content of HCl (58.3 wt%) in the PVC monomer. After the first two stages, the PVC chain is

almost entirely stripped from its chlorine content [25]. The reaction describing the first two stages might thus be written as follows:



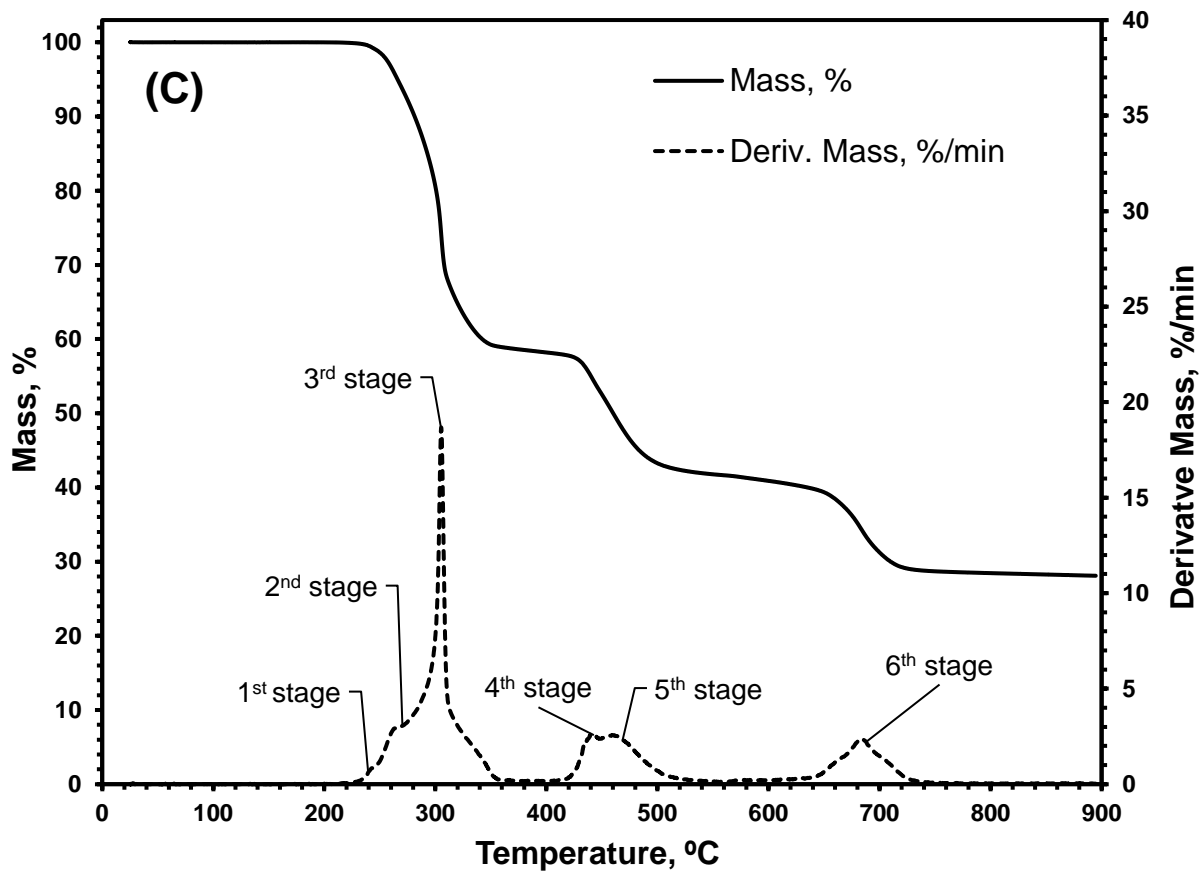
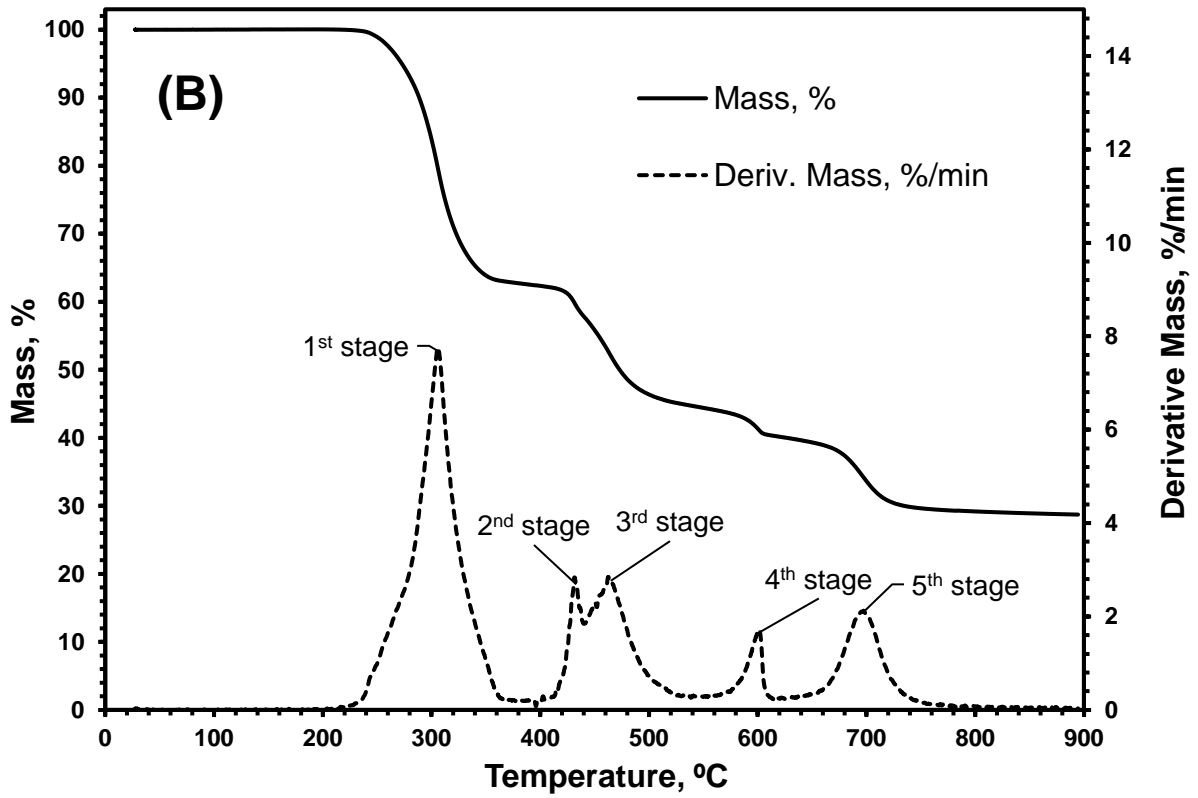


Figure 2: TGA/DTG profiles of pure PVC (A), Fe<sub>3</sub>O<sub>4</sub>-PVC (31.6 wt% Fe<sub>3</sub>O<sub>4</sub>) (B) and Fe<sub>2</sub>O<sub>3</sub>-PVC (29.9 wt% Fe<sub>2</sub>O<sub>3</sub>) (C) degradation under a nitrogen flow of 100 mL/min and at a heating rate of 10 K/min.

The solid residue left after the first two stages is polyene [23]. Formed polyene sequences then start degrading at 423 °C (third stage) into unsubstituted aromatics, alkyl aromatics and solid char [26]. H<sub>2</sub> has also been reported to evolve from this stage as well [24]. The third stage could be written according to the following chemical reaction [24]:



A residual mass of about 6% remains in the crucible after the thermal cracking of the PVC backbone, which as mentioned earlier, is characterised to be char [26]. Both the PVC dehydrochlorination and the polyene thermal cracking stages show endothermic events with the former showing larger one (Figure 3, peaks 1 and 4).

Table 2: The mean particle size of the feed materials used in this work before any processing (e.g., mixing, tumbling etc.).

Material	Particle size, $\mu\text{m}$
PVC	$158.8 \pm 18.5$
Fe <sub>3</sub> O <sub>4</sub>	$31.7 \pm 5.0$
Fe <sub>2</sub> O <sub>3</sub>	$36.6 \pm 4.8$

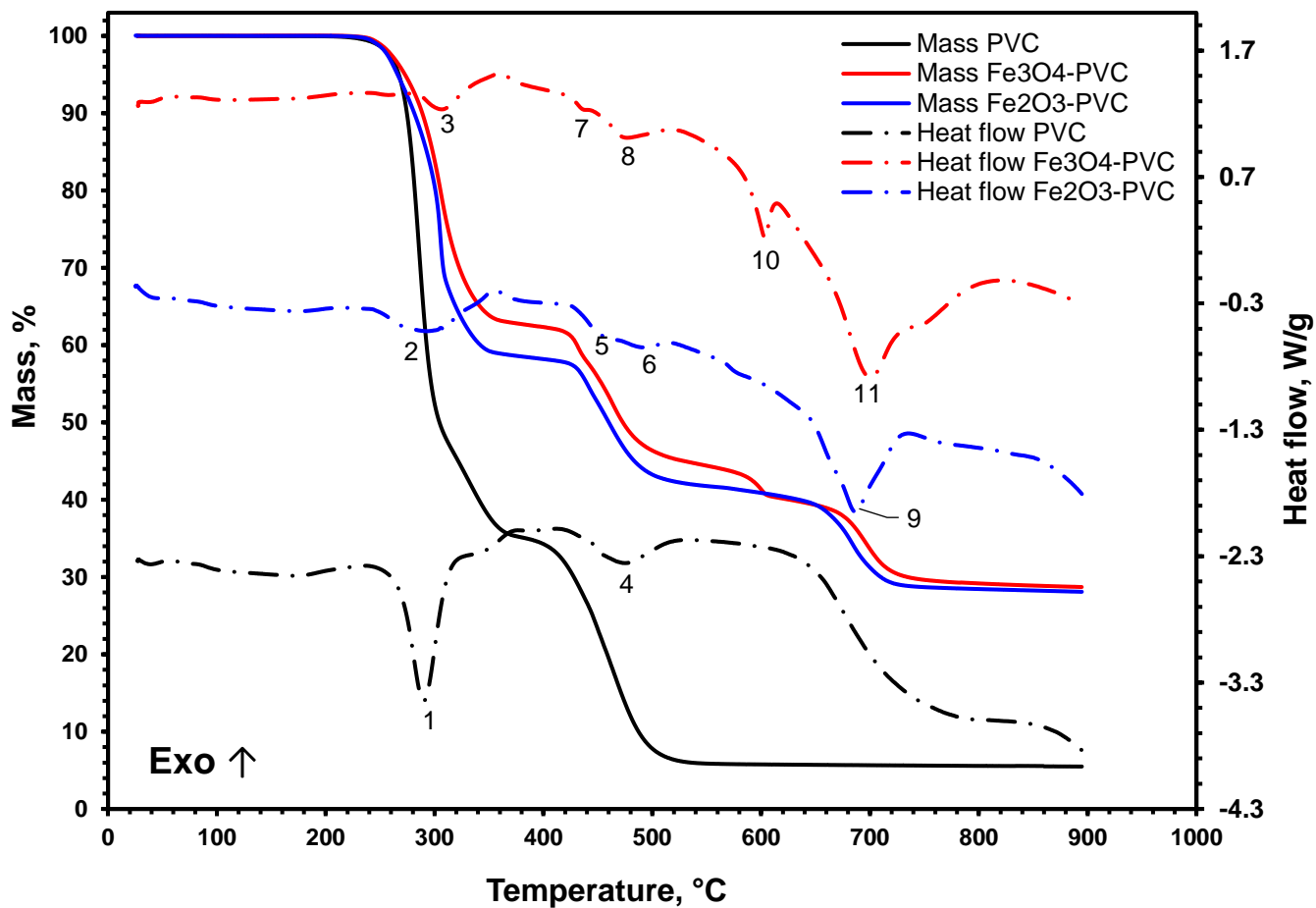


Figure 3: TGA/DSC profiles of pure PVC,  $\text{Fe}_3\text{O}_4$ -PVC (31.6 wt%  $\text{Fe}_3\text{O}_4$ ), and  $\text{Fe}_2\text{O}_3$ -PVC (29.9 wt%  $\text{Fe}_2\text{O}_3$ ) under nitrogen flow of 100 mL/min and a heating rate of 10 K/min.

#### 4.1.2. Thermal behaviour and reaction products of $\text{Fe}_3\text{O}_4$ -PVC pyrolysis

The addition of a stoichiometric amount of  $\text{Fe}_3\text{O}_4$  to PVC resulted in a significant change to the thermogravimetric profile of the PVC degradation. The decomposition of the  $\text{Fe}_3\text{O}_4$ -PVC mixture follows five degradation/reduction stages, instead of three as in the case of pure PVC (Figure 2 (B)).

The first stage starting at 274 °C is attributed to the de-hydrochlorination of PVC (HCl evolution) and the emission of  $\text{H}_2\text{O}$  from the chlorination of  $\text{Fe}_3\text{O}_4$  (Reaction 3) [24]. It is evident from the profile presented in Figure 5 (D) that the chlorination of  $\text{Fe}_3\text{O}_4$  by HCl is thermodynamically favourable where it shows negative Gibbs free energy values up to a temperature of 580 °C. The profiles presented in Figure 3 suggest that the addition of  $\text{Fe}_3\text{O}_4$  to PVC did not significantly affect the onset de-hydrochlorination temperature. However, this

addition did hamper the decomposition speed thus creating higher stability than in the case of pure PVC. Further evidence of this hampering effect is presented in the kinetic section 4.2.1.

The chlorination reaction can be written as follows:



Despite the exothermic nature of this reaction, no exothermic peak was detected from the DSC measurement (Figure 3). This can be assigned to the highly endothermic nature of PVC dehydrochlorination which could mask the exothermic chlorination event (Figure 3, peak 1). Nonetheless, the chlorination of  $\text{Fe}_3\text{O}_4$  by HCl is confirmed from the XRD pattern presented in Figure 4 for the pyrolysis of the  $\text{Fe}_3\text{O}_4$ -PVC mixture at different pyrolysis temperatures. It is clear that the iron chloride species appears in the hydrate form (Rokuehnite;  $\text{FeCl}_2 \cdot 2\text{H}_2\text{O}$ ) with low intensity peaks, while no Lawrencite ( $\text{FeCl}_2$ ) peaks can be seen at 400 °C (Pattern B). However, as the temperature of the pyrolysis increases to 550 and 650 °C, more prominent peaks of  $\text{FeCl}_2 \cdot 2\text{H}_2\text{O}$  are seen and the peaks associated with  $\text{FeCl}_2$  start to appear showing very high intensity at 650 °C (Figure 4, Pattern D). The formation of  $\text{FeCl}_2$  was also detected under the SEM for the 650 °C residue where  $\text{FeCl}_2$  crystals appeared in the form of thin cylindrical discs (Figure S1 supplementary material). These discs could not be seen in the residue at a temperature of 400 °C which agrees with the absence of  $\text{FeCl}_2$  peaks in the 400 °C XRD pattern in Figure 4. In the works performed by Kanungo [27] and Louvain et al. [28] the de-hydration behaviour of  $\text{FeCl}_2 \cdot 4\text{H}_2\text{O}$  was studied. Kanungo [27] reported that the de-hydration takes place in three steps where two water moles are lost in the first step followed by losing one mole in each of the following steps such that the material is completely de-hydrated at a temperature of 183 °C at a heating rate of 6 °C/min under flowing nitrogen. A similar behaviour was reported by Louvain et al. [28] whereby the mass loss associated with the de-hydration of  $\text{FeCl}_2 \cdot 4\text{H}_2\text{O}$  was completed at about 180 °C under nitrogen and at a heating rate of 5 °C/min. Louvain et al. [28] even managed to isolate  $\text{FeCl}_2 \cdot 2\text{H}_2\text{O}$  and exposed it to a thermogravimetric

scan. In that work [28],  $\text{FeCl}_2 \cdot 2\text{H}_2\text{O}$  showed a clear mass loss which peaked at 134 °C. Such a mass loss can potentially be also assigned to the de-hydration. Hence, the peaks associated with  $\text{FeCl}_2 \cdot 2\text{H}_2\text{O}$  appearing at high temperatures in Figure 4 can potentially be regarded to the hydration of  $\text{FeCl}_2$  present in the post pyrolysis residue; the increased amount of  $\text{FeCl}_2 \cdot 2\text{H}_2\text{O}$  with temperature can be attributed to the increased amount of formed  $\text{FeCl}_2$  which is then hydrated.

Reaction 3 suggests that aside to the formed  $\text{FeCl}_2$ , hematite ( $\text{Fe}_2\text{O}_3$ ) should also be seen in the 400 °C pattern (Figure 4, pattern B). The absence of  $\text{Fe}_2\text{O}_3$  peaks in Figure 4 is attributed to the direct reduction of  $\text{Fe}_2\text{O}_3$  into  $\text{Fe}_3\text{O}_4$  by the emitted  $\text{H}_2$  gas during the de-hydrochlorination stage according to Reaction 4. This reaction shows a negative Gibbs free energy over the entire temperature range suggesting that it is thermodynamically favourable. Moreover, the reduction of  $\text{Fe}_2\text{O}_3$  by  $\text{H}_2$  was previously reported to take place at a temperature as low as 218 °C, however, it showed slow kinetics up to 309 °C [29].

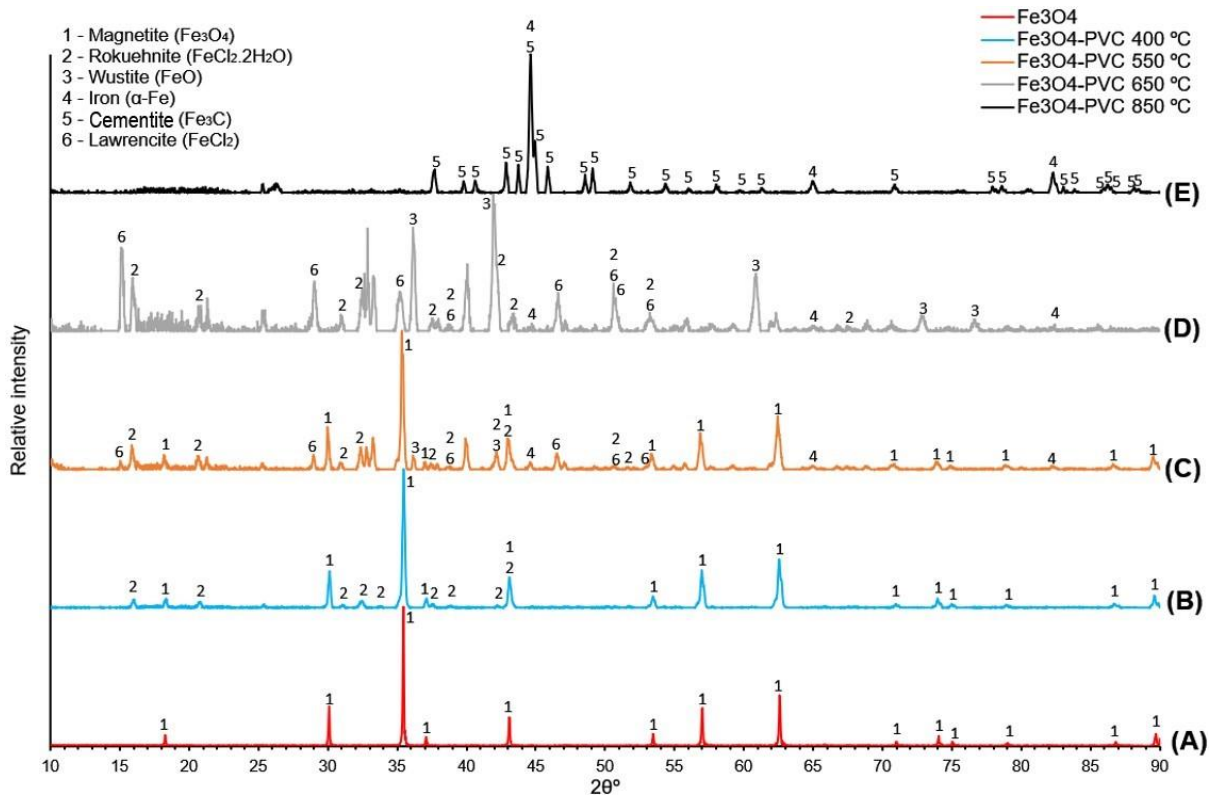
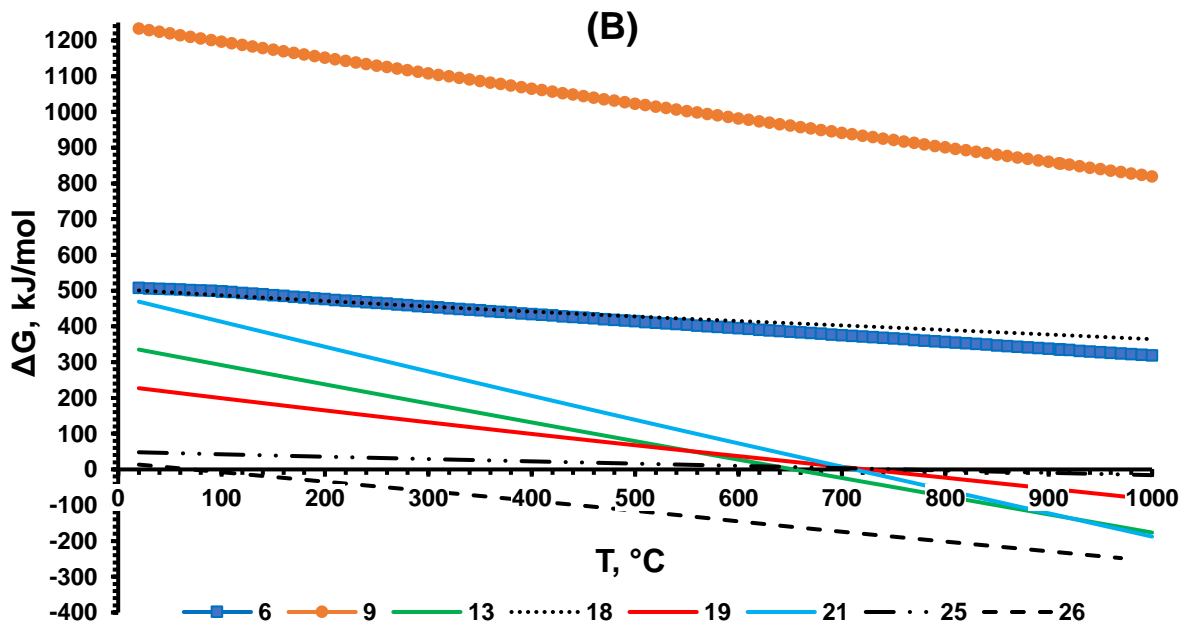
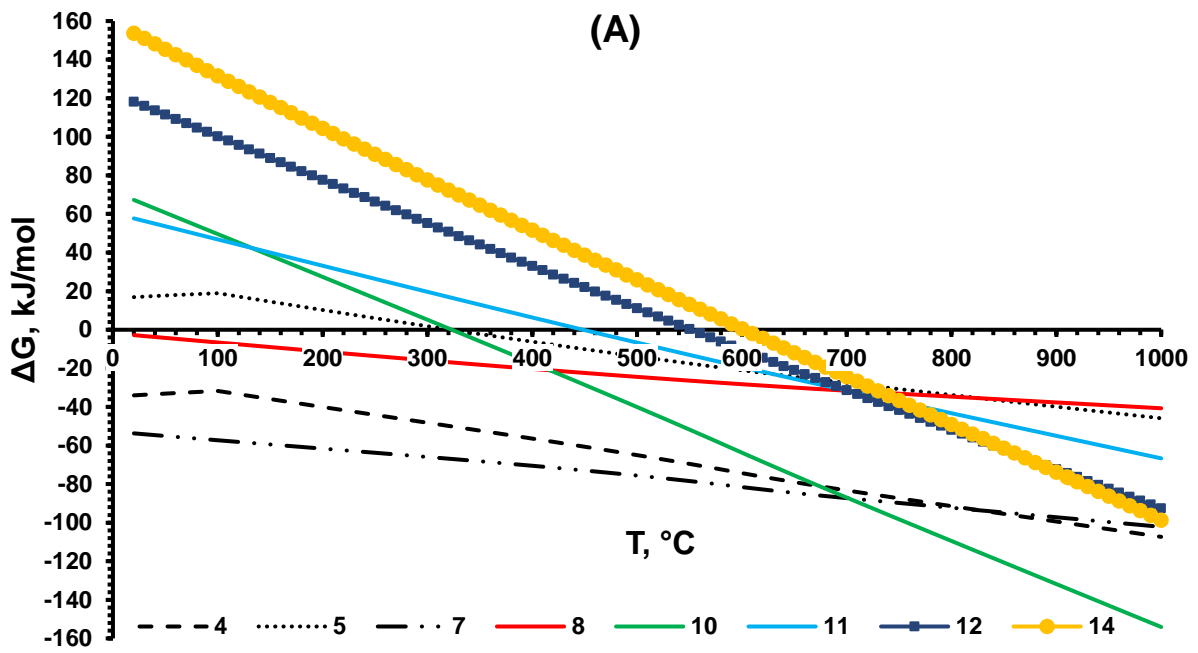


Figure 4: XRD patterns for the pyrolysis of  $\text{Fe}_3\text{O}_4$ -PVC mixture (31.6 wt%  $\text{Fe}_3\text{O}_4$ ) at different temperatures.

In the second stage ranging from 410 – 440 °C (Figure 2 (B)), polyene sequences decompose to form char, volatiles, and H<sub>2</sub> [24]. In the presence of Fe<sub>3</sub>O<sub>4</sub>, (CO)<sub>x</sub> was reported to form as well [24]. In stage 3 (440 – 520 °C), formed char, H<sub>2</sub>, and CO (from reduction) can then partially react with Fe<sub>3</sub>O<sub>4</sub> to form small amounts of FeO which is then partially reduced into α-Fe according to reactions 15, 17, 20, and 22. The peaks of both FeO and α-Fe can be seen in Figure 4 (Pattern C) confirming these reactions. The thermodynamics of these reactions, while being endergonic ( $0 < \Delta G$ ), they can still be driven forward since  $\Delta G$  has small positive values of 14.5, 2.5, 23.8, and 45.1 kJ/mol at a temperature of 460 °C for reactions 15, 17, 20 and 22, respectively. The positive value of  $\Delta G$  also explains why the peaks of FeO and α-Fe are very small as these reactions are majorly directed backwards. In literature, the in situ XRD analysis performed by Pineau et al. [30] also suggested the possibility of the co-existence of Fe<sub>3</sub>O<sub>4</sub>, FeO, and Fe for the reduction system of Fe<sub>3</sub>O<sub>4</sub> under H<sub>2</sub> in the temperature window 390 – 570 °C. This temperature range overlaps with the range reported here. After that, the reduction of FeO to Fe by CO (reaction 24) is thermodynamically possible up to a temperature of 550 °C leading to the formation of α-Fe.

The overlapping between polyene cracking and the partial reduction of Fe<sub>3</sub>O<sub>4</sub> is reflected in the thermal data as DTG and heat flow doublets (Figures 2 (B) and 3).



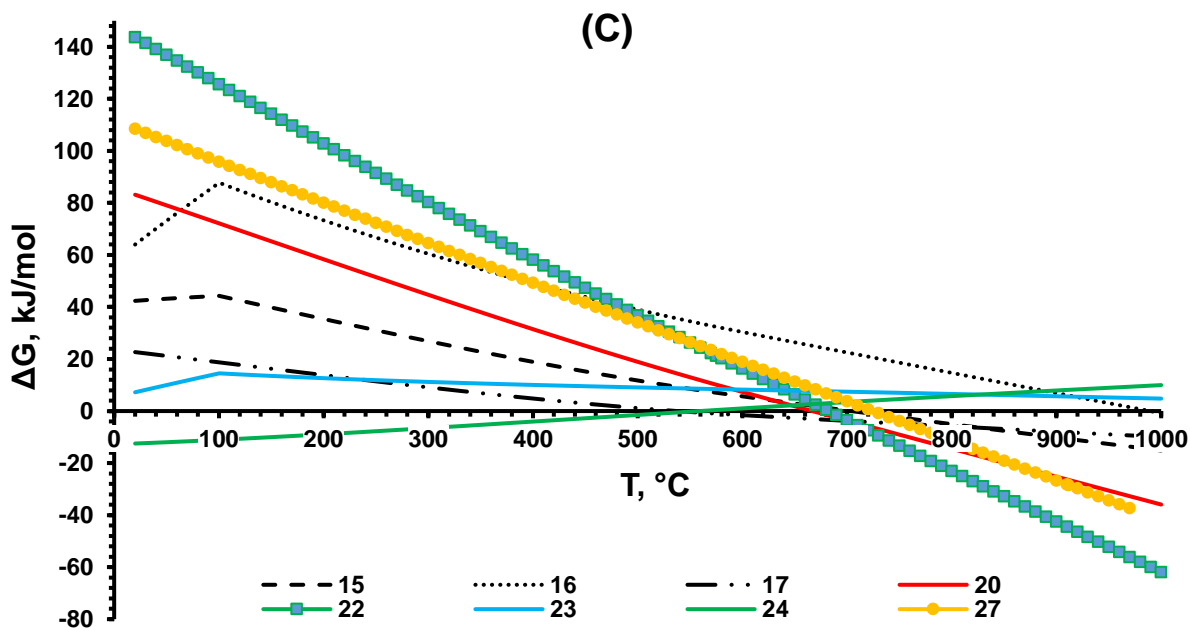
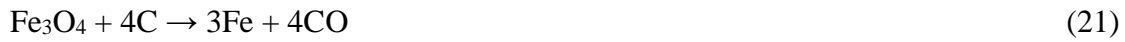
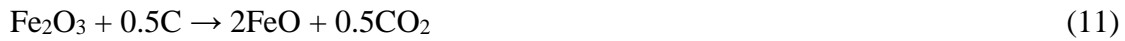


Figure 5: The change in the Gibbs free energy for the major chlorination and reduction reactions (4 – 28) occurring during the thermal degradation of PVC in the presence of  $\text{Fe}_3\text{O}_4$  and  $\text{Fe}_2\text{O}_3$ .





In the temperature range 575 – 615 °C, a mass loss of about 4.0% can be seen (Figure 2 (B)).

In that range, the reduction of Fe<sub>3</sub>O<sub>4</sub> by char starts yielding FeO according to reactions 20 and 22. The change in the Gibbs free energy for these reactions is close to zero in that range at 7.4 and 16.3 kJ/mol for reactions 20 and 22, respectively suggesting that Fe<sub>3</sub>O<sub>4</sub> and FeO can co-exist and hence FeO peaks intensity increase. However, released CO from reaction 22 can then react with Fe<sub>3</sub>O<sub>4</sub> and transform it further into FeO at higher temperatures (650 °C) such as that seen in Figure 4 Pattern D with the thermodynamically favourable reaction 17 (Figure 5 (C)). The formation of FeO in large amounts is confirmed from the intense XRD peaks (Figure 4, pattern D). This reduction is also associated with the appearance of a sharp endothermic heat

flow in Figure 3 (peak 10). This endotherm is in line with the thermodynamics data since the enthalpy change for reactions 20 and 22 are +104.0 and +189.9 kJ/mol, respectively.

A further increase in temperature in the range 655 – 750 °C yields another mass loss of about 9.9% (Figure 2 (B)). At that point, formed FeO is reduced to  $\alpha$ -Fe by char as shown in reactions 25 and 27. Both reactions 25 and 27 are almost at equilibrium ( $\Delta G = 3.6$  and  $3.7$  kJ/mol) at a temperature of 700 °C which suggests that  $\alpha$ -Fe should start appearing alongside FeO. The results in the XRD, however, were collected at 850 °C, a temperature at which the presence of  $\alpha$ -Fe is more favoured which explains the large  $\alpha$ -Fe peaks. This mass loss is accompanied with a very large endothermic peak (Figure 3 peak 11) which is in agreement with the enthalpy change of reactions 25 and 27 at +65.8 and +151.3 kJ/mol, respectively at a temperature of 700 °C. A similar mass loss was reported by Ye et al. [24] for a Fe<sub>3</sub>O<sub>4</sub>-PVC mixture in which both CO and CO<sub>2</sub> gases were detected by a mass spectrometer in that temperature range. This is in line with reactions 25 and 27 containing CO and CO<sub>2</sub> as products. The formation of  $\alpha$ -Fe is shown in Figure 4 Pattern E and is also confirmed in the SEM/EDS maps and spot analysis presented in Figure S2.

A portion of the formed  $\alpha$ -Fe then reacts with the residual char to form cementite (Fe<sub>3</sub>C) according to reaction 28 which is thermodynamically favourable above 820 °C. Fe<sub>3</sub>C peaks are clearly shown in the XRD pattern (Figure 4 Pattern E).

#### 4.1.3. Thermal behaviour and reaction products of Fe<sub>2</sub>O<sub>3</sub>-PVC pyrolysis

The TGA/DTG profiles of the Fe<sub>2</sub>O<sub>3</sub>-PVC mixture (29.9 wt% Fe<sub>2</sub>O<sub>3</sub>) are presented in Figure 2 (C). The degradation follows six stages instead of three and five as in the cases of pure PVC and Fe<sub>3</sub>O<sub>4</sub>-PVC, respectively. The initial large mass loss (first three stages) is attributed to the de-hydrochlorination of PVC starts at about 275 °C with a mass loss of 41.0%. This mass loss is also associated with the evolution of H<sub>2</sub>O along with HCl. In the work done by Zhang et al. [31] it was reported that H<sub>2</sub>O fragments start to appear in a mass spectrometer connected to a

Fe<sub>2</sub>O<sub>3</sub>-PVC mixture at a temperature of about 277 °C. This H<sub>2</sub>O emission can be related to the reduction of Fe<sub>2</sub>O<sub>3</sub> by H<sub>2</sub> (Reaction 4) into Fe<sub>3</sub>O<sub>4</sub> and the subsequent chlorination of formed Fe<sub>3</sub>O<sub>4</sub> by HCl into FeCl<sub>2</sub> (Reaction 3). The occurrence of these reactions is confirmed from the XRD patterns presented in Figure 6 (Pattern B) where peaks of both FeCl<sub>2</sub>.2H<sub>2</sub>O and Fe<sub>3</sub>O<sub>4</sub> can be seen.

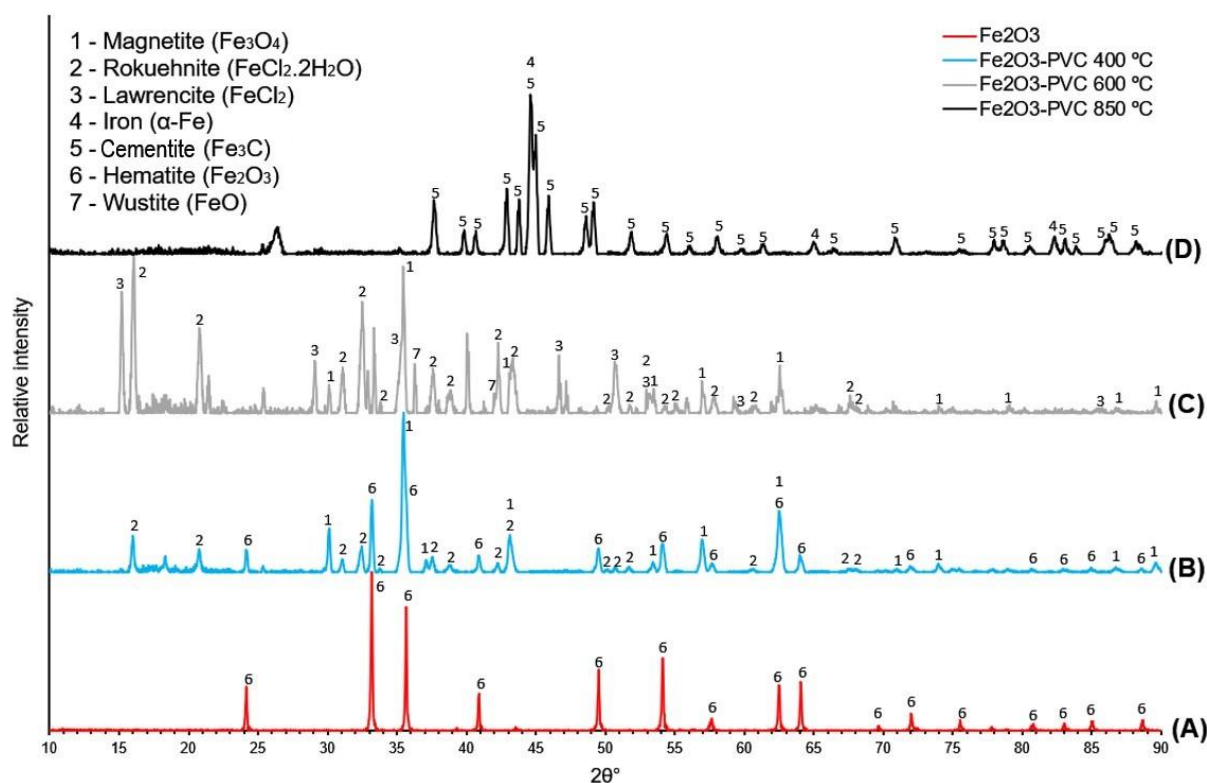


Figure 6: XRD patterns for the pyrolysis of Fe<sub>2</sub>O<sub>3</sub>-PVC mixture (29.9 wt% Fe<sub>2</sub>O<sub>3</sub>) at different temperatures.

When the temperature increases up to 600 °C, peaks of FeCl<sub>2</sub> start to appear and this temperature increase also results in a significant increase in the intensity of FeCl<sub>2</sub>.2H<sub>2</sub>O XRD peaks. Likewise, it is believed that more FeCl<sub>2</sub> is formed at higher temperatures (which could be attributed to enhanced chlorination kinetics) after which it is hydrated into FeCl<sub>2</sub>.2H<sub>2</sub>O when cooled down. The increase in the peak intensity of FeCl<sub>2</sub>.2H<sub>2</sub>O can also be seen in the SEM scans of the pyrolysis residue of Fe<sub>2</sub>O<sub>3</sub>-PVC at 600 °C which confirm the growth of a large Monoclinic crystal of FeCl<sub>2</sub>.2H<sub>2</sub>O (Figure 7). Spot analysis of this crystal is presented in Figure S3. The spot analysis shows atomic percentages of 37.6, 37.8, and 24.6% for iron, oxygen, and chlorine, respectively suggesting their co-existence in one crystal. The deviation from the

theoretical percentages present in the  $\text{FeCl}_2 \cdot 2\text{H}_2\text{O}$  molecule is due to contamination of the crystal by other minerals which is clearly shown in the secondary electron image of this crystal (Figure S4). The presence of crystals of this size in the 600 °C residue and their absence in the 400 °C residue explains the huge increase in the intensity of  $\text{FeCl}_2 \cdot 2\text{H}_2\text{O}$  with temperature in the XRD patterns (Figure 6).

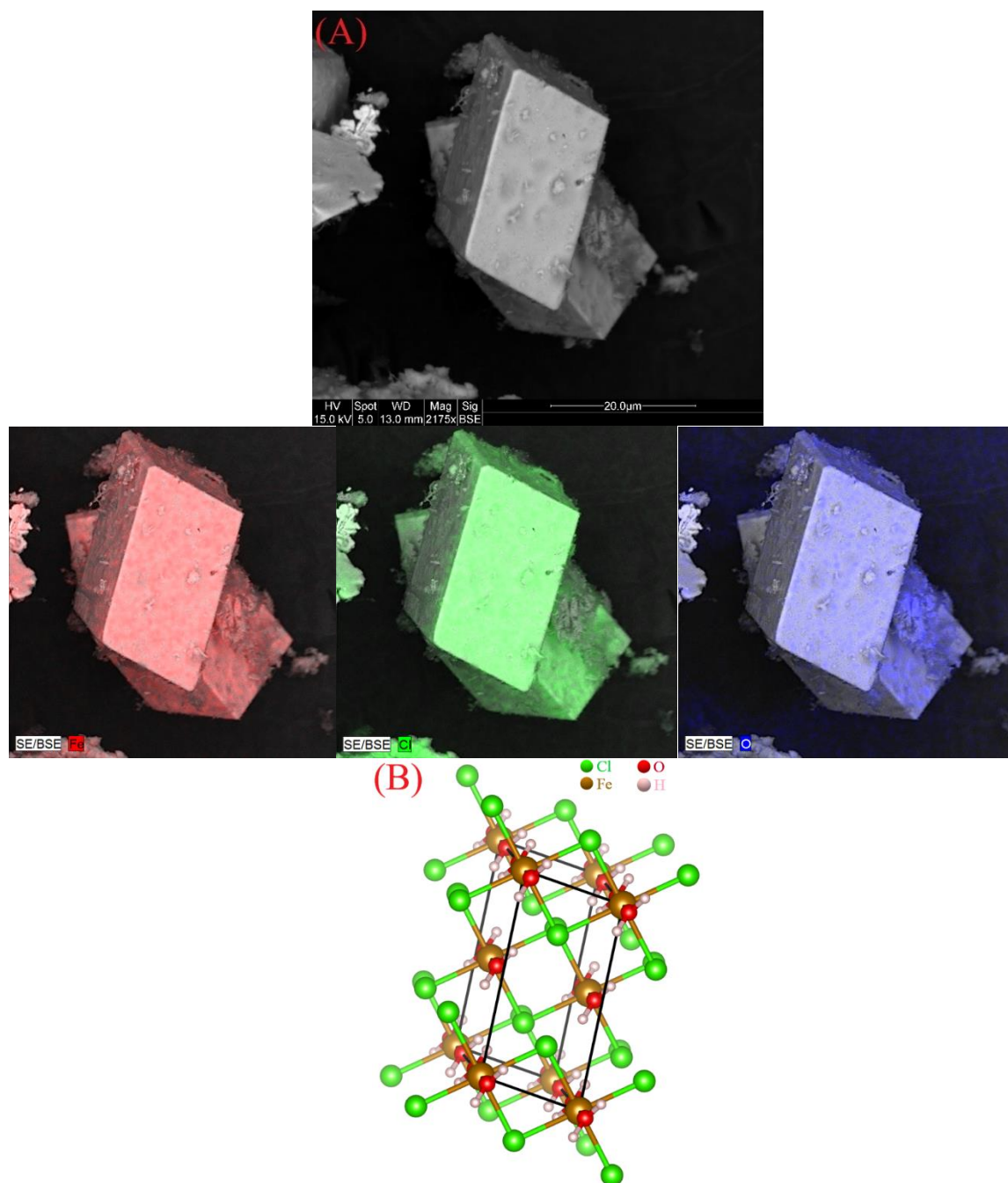


Figure 7: (A) Back scattered image of a large Monoclinic crystal of Rokuehnite ( $\text{FeCl}_2 \cdot 2\text{H}_2\text{O}$ ) along with EDS mapping formed in the post pyrolysis residue of  $\text{Fe}_2\text{O}_3$ -PVC mixture at 600 °C and (B) Monoclinic crystal lattice of Rokuehnite ( $\text{FeCl}_2 \cdot 2\text{H}_2\text{O}$ ) obtained from Crystallography Open Database (COD) and graphed using VESTA software [32, 33].

The de-hydrochlorination of PVC in presence of  $\text{Fe}_2\text{O}_3$  showed an endothermic peak (Figure 3, peak 2). The intensity of this peak is much lower than that seen for pure PVC. This could be assigned to the exothermic nature of the reduction of  $\text{Fe}_2\text{O}_3$  by  $\text{H}_2$  occurring in the same temperature range resulting in a flatter endotherm.

The fourth and fifth overlapped stages extending from 415 to 512 °C (Figure 2 (C)) are associated with the simultaneous polyene thermal cracking and the reduction of  $\text{Fe}_2\text{O}_3$  into  $\text{Fe}_3\text{O}_4$  and  $\text{FeO}$ . The reduction into  $\text{Fe}_3\text{O}_4$  occurs according to reactions 4, 7, 10, and 26 all of which have a negative  $\Delta G$  in this temperature range. In these reactions,  $\text{H}_2$ ,  $\text{C}_{(s)}$ , and  $\text{CO}$  react with  $\text{Fe}_2\text{O}_3$  to form  $\text{Fe}_3\text{O}_4$ . The formation of  $\text{FeO}$ , in contrast, is majorly attributed to the reduction of  $\text{Fe}_2\text{O}_3$  by gaseous  $\text{H}_2$  and  $\text{CO}$  as shown in reactions 5 and 8 which are spontaneous in this temperature range. The reduction by  $\text{C}_{(s)}$  can also contribute mildly to the formation of  $\text{FeO}$  in that range as well (reaction 11). All of these reactions are endothermic in this temperature range except reaction 7. The heat flow from these reactions can be seen in the endothermic doublet (peaks 5 and 6) appearing in Figure 3 such that the former peak is associated with polyene thermal cracking while the latter is associated with the reduction reactions.

After stages four and five, the residue does not contain  $\text{Fe}_2\text{O}_3$  anymore, and  $\text{FeO}$  peaks started to appear (Figure 6, Pattern C). The final stage (sixth stage) extending in the temperature span 630 – 740 °C and showing a mass loss of 11.6% is associated with the carbothermic reduction of  $\text{Fe}_3\text{O}_4$  and  $\text{FeO}$ .  $\text{Fe}_3\text{O}_4$  is reduced to  $\text{FeO}$  according to reactions 20 and 22 which show values of  $\Delta G$  that are very close to zero after which they shift to negative values with increase in temperature. A portion of  $\text{Fe}_3\text{O}_4$  might also be reduced directly into  $\text{Fe}$  following reactions 19 and 21 (showing small positive  $\Delta G$  values). The reduction of  $\text{FeO}$  by  $\text{C}_{(s)}$  shown in reactions 25 and 27 have very small positive  $\Delta G$  suggesting that  $\text{FeO}$  can transform into  $\text{Fe}$ .  $\text{CO}$  emitted from the reactions above can also reduce  $\text{Fe}_3\text{O}_4$  to  $\text{FeO}$  and  $\text{FeO}$  to  $\text{Fe}$  as shown in reactions 17

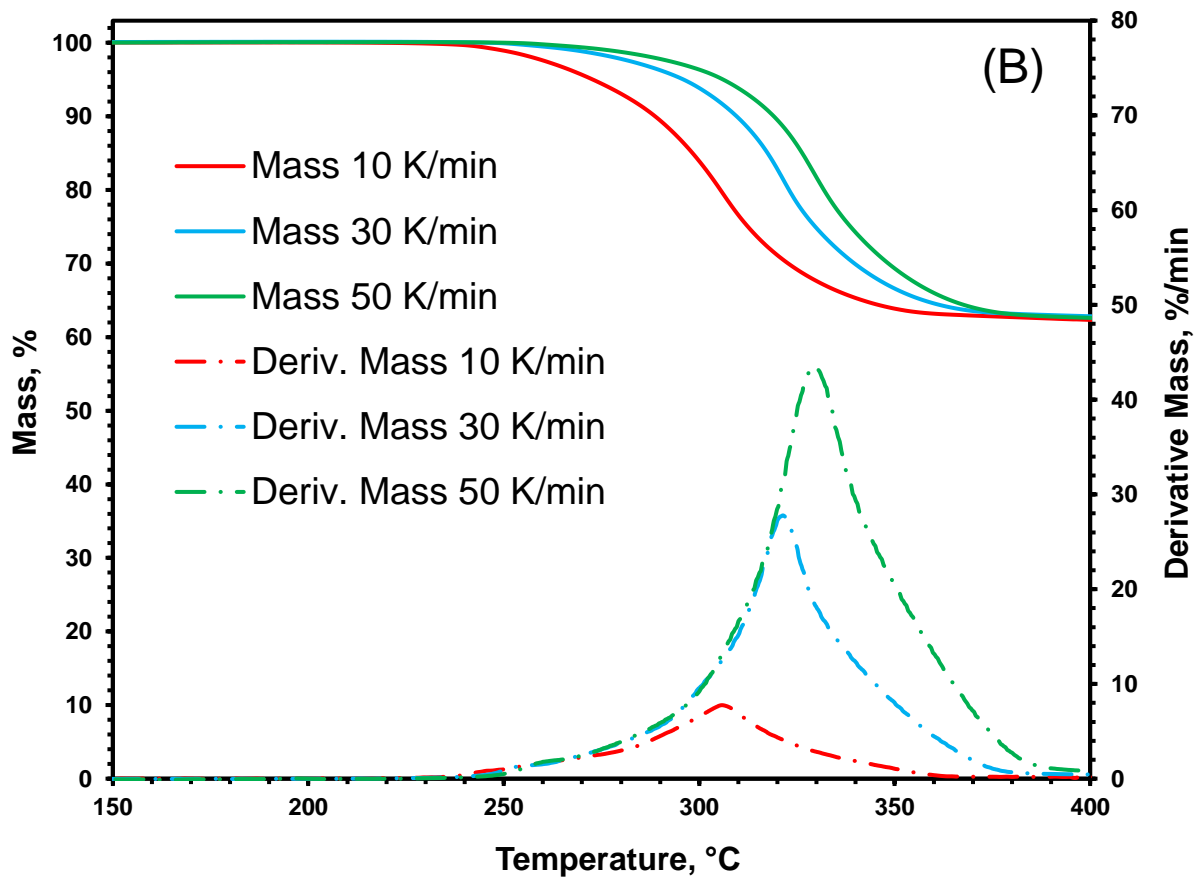
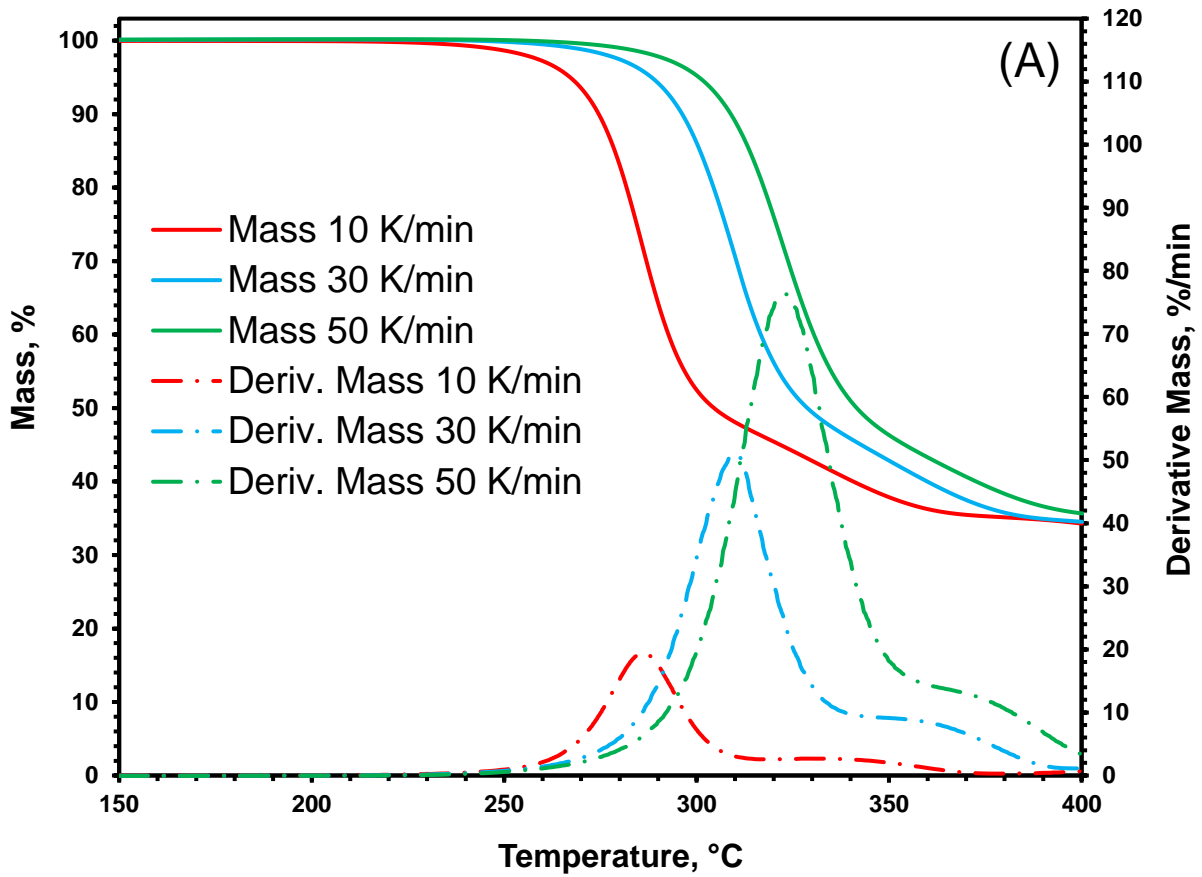
and 24 where the former exhibit negative  $\Delta G$  values in that range while the latter has very small positive (close to zero)  $\Delta G$ .

This stage is accompanied by a large endothermic peak (peak 9, Figure 3) and the formation of  $\alpha$ -Fe is clearly seen in Figure 6 (Pattern D). Having an endothermic heat flow in Figure 3 is in line with the thermodynamics data in which all these reactions exhibit a positive  $\Delta H$  except for reaction 24. The reactions suggested here that are associated with the sixth stage are in a very good agreement with the results reported by Zhang et al. [31]. In that work, large peaks of CO and CO<sub>2</sub> appeared on a mass spectrometer in the same temperature range for a mixture of Fe<sub>2</sub>O<sub>3</sub>-PVC [31]. Finally, formed  $\alpha$ -Fe reacts with excess char to form Fe<sub>3</sub>C (Figure 6 Pattern D) according to reaction 28.

## **4.2. Non-isothermal pyrolysis kinetics**

### **4.2.1. De-hydrochlorination kinetics of pure PVC, Fe<sub>3</sub>O<sub>4</sub>-PVC, and Fe<sub>2</sub>O<sub>3</sub>-PVC**

In this section, stages one and two for pure PVC, stage one for Fe<sub>3</sub>O<sub>4</sub>-PVC and the first three stages for Fe<sub>2</sub>O<sub>3</sub>-PVC will be referred to as the “de-hydrochlorination stage”. The usage of three different heating rates allows the calculation of the apparent activation energy using the model free approach. The de-hydrochlorination stages for PVC, Fe<sub>3</sub>O<sub>4</sub>-PVC, and Fe<sub>2</sub>O<sub>3</sub>-PVC at different heating rates are presented in Figures 8 (A), (B), and (C), respectively.



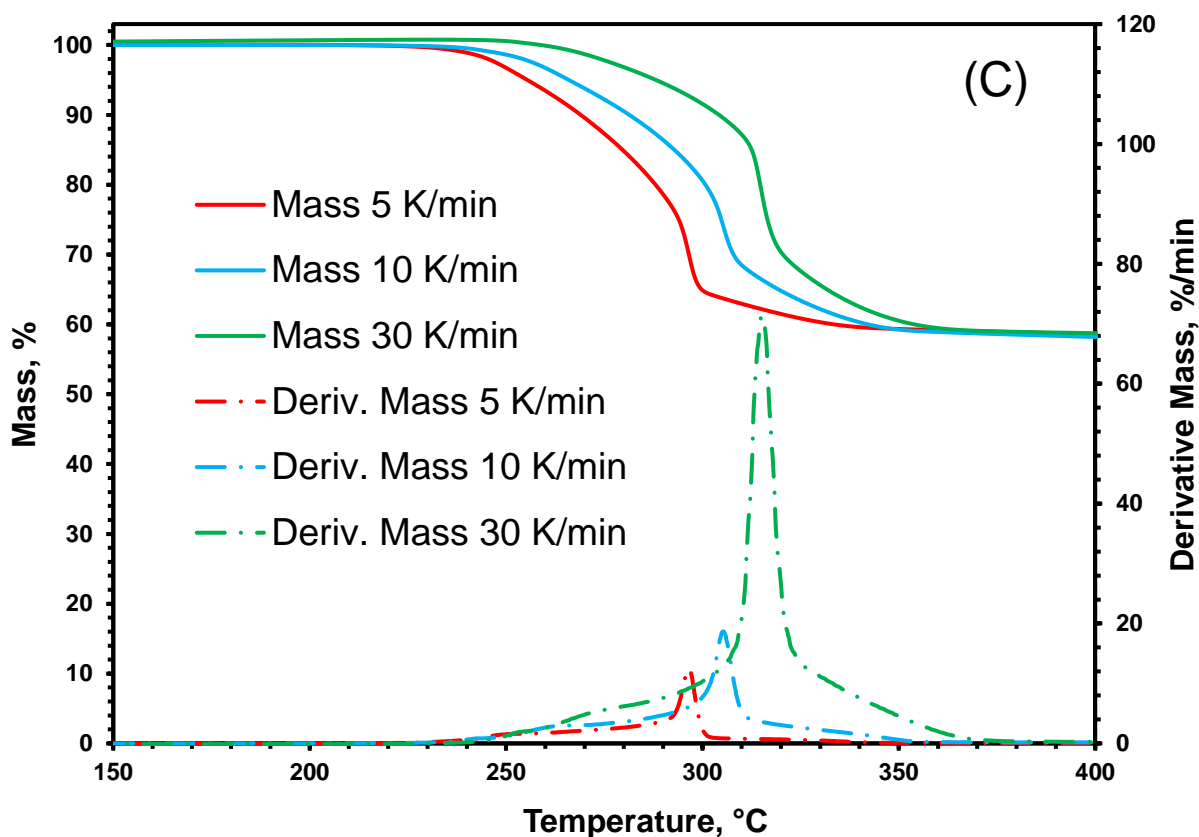


Figure 8: The de-hydrochlorination of pure PVC (A),  $\text{Fe}_3\text{O}_4$ -PVC (31.6 wt%  $\text{Fe}_3\text{O}_4$ ) (B), and  $\text{Fe}_2\text{O}_3$ -PVC (29.9 wt%  $\text{Fe}_2\text{O}_3$ ) (C) under nitrogen flow of 100 mL/min and different heating rates.

All the decomposition profiles in Figure 8 (A), (B), and (C) show a systematic lateral shift to a higher temperature at a fixed conversion level with an increase in the heating rate. Such a behaviour allows the utilisation of the iso-conversional principle mentioned earlier (section 3.2) for the determination of the apparent activation energy. Data obtained from these curves were fitted in the conversion range 0.1 – 0.9. Kinetic data fitting for PVC and its mixtures with  $\text{Fe}_3\text{O}_4$  and  $\text{Fe}_2\text{O}_3$  are presented in the supplementary material (Section 2).

The kinetic parameters associated with the de-hydrochlorination of pure PVC under an inert environment ( $\text{N}_2$ ) are presented in Figures 9 (A) and (B).

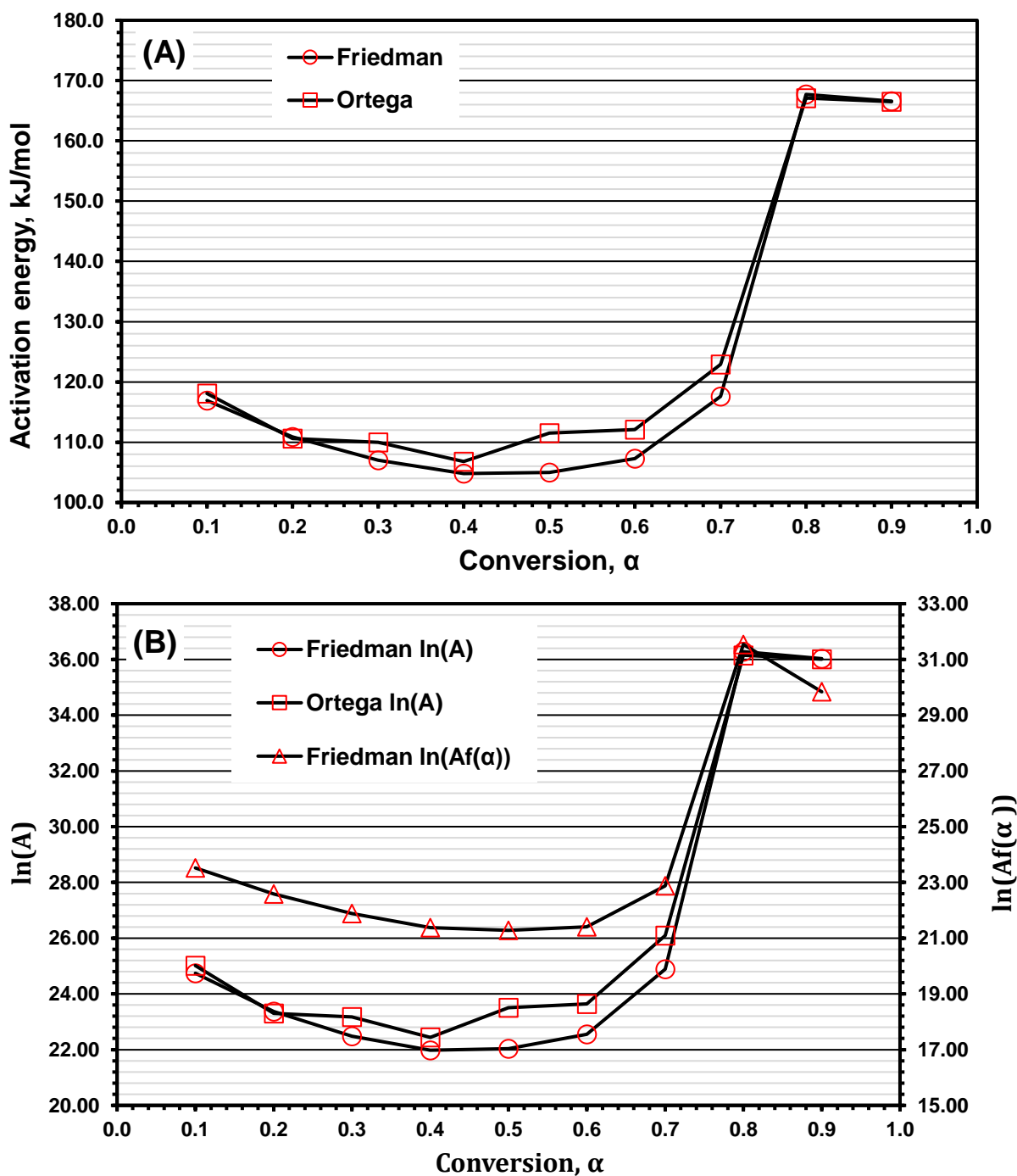


Figure 9: The apparent activation energy (A) and frequency factor (B) (unit of A and  $A_f(\alpha)$  is  $\text{min}^{-1}$ ) associated with the de-hydrochlorination of PVC (first two stages in Figure 2 (A)).

Clearly from Figures 9 (A) and (B), a great agreement of the apparent activation energy and frequency factor calculated from Friedman (differential) and Ortega (integral) methods can be seen. The activation energies associated with the de-hydrochlorination of pure PVC in the conversion range 0.1 – 0.9, averaged at  $122.6 \pm 24.2$  and  $125.1 \pm 22.8$  kJ/mol calculated from Friedman and Ortega models, respectively. An insignificant variation in the value of the

activation energy in the conversion range 0.1 – 0.7 is observed suggesting a single controlling mechanism in that range.

Figure 10 shows some of the conversion functions (lines) along with data points generated for  $f(\alpha)$  using the model free kinetic parameters (Equation 13; dots) at different conversions. For pure PVC, the  $f(\alpha)$  obtained from the model free parameters (squares) overlaps with the reaction model “C” given as  $f(\alpha) = 3.7\alpha(1 - \alpha)^2$  in the conversion range 0.1 – 0.6 (Figure 10).

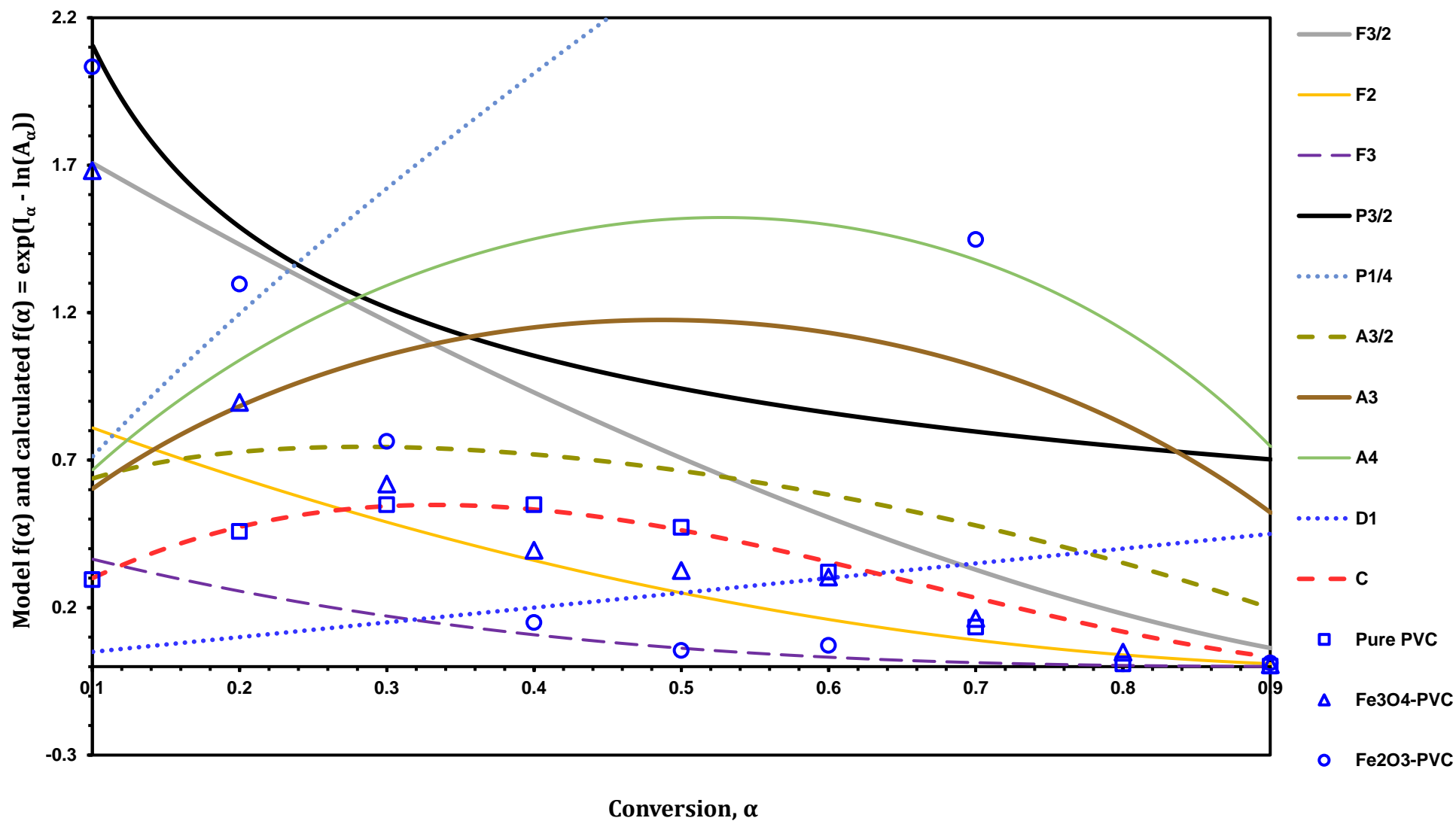


Figure 10: A plot of the reactions models presented in Table 1 against conversion and the corresponding  $f(\alpha)$  values generated for the de-hydrochlorination stage of pure PVC, Fe<sub>3</sub>O<sub>4</sub>-PVC and Fe<sub>2</sub>O<sub>3</sub>-PVC using iso-conversional data (mechanism "C" is  $f(\alpha) = 3.7\alpha(1 - \alpha)^2$ ).

At a conversion of 0.7, experimental  $f(\alpha)$  becomes very close to F<sub>2</sub> model and then overlaps with F<sub>3</sub> at  $\alpha = 0.8$  and 0.9. Previously [34], linear data fitting approach was used and the best fit obtained for PVC de-hydrochlorination was achieved using  $f(\alpha) = \alpha(1 - \alpha)^{2.13}$  in the conversion range 0.1 – 0.6 (A model very similar to the one obtained here from the model free kinetic data). The reaction model reported in this work (Figure 10) follows the truncated form of the Šesták and Berggren [17, 18] which is also known as the extended Prout-Tomkins model ( $f(\alpha) = \alpha^m(1 - \alpha)^n$ ) [18]. The truncated Šesták and Berggren model is considered an example of an auto-catalytic model [18]. This agrees with the fact that the de-hydrochlorination of PVC was characterised as an auto-catalytic process where released HCl was found to contribute to accelerating the de-hydrochlorination process [35]. This effect eventually disappears which is evident from the increase in the activation energy at  $0.7 < \alpha$  along with the change in the reaction model towards mechanisms F<sub>2</sub> and F<sub>3</sub>.

The addition of a stoichiometric amount of Fe<sub>3</sub>O<sub>4</sub> to PVC (31.6 wt% Fe<sub>3</sub>O<sub>4</sub>) resulted in a significant increase in the apparent activation energy for the de-hydrochlorination Figures 11 (A) and (B).

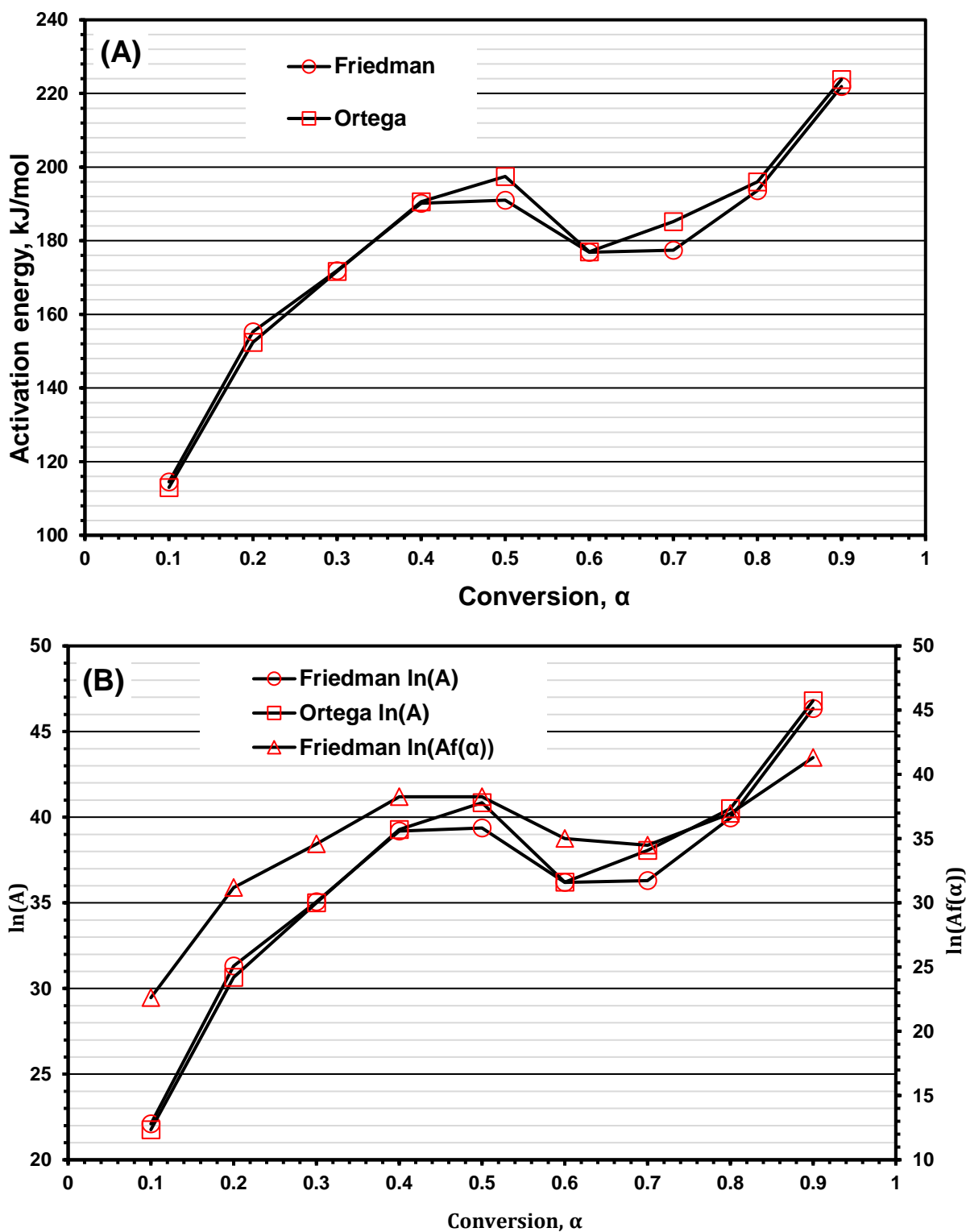
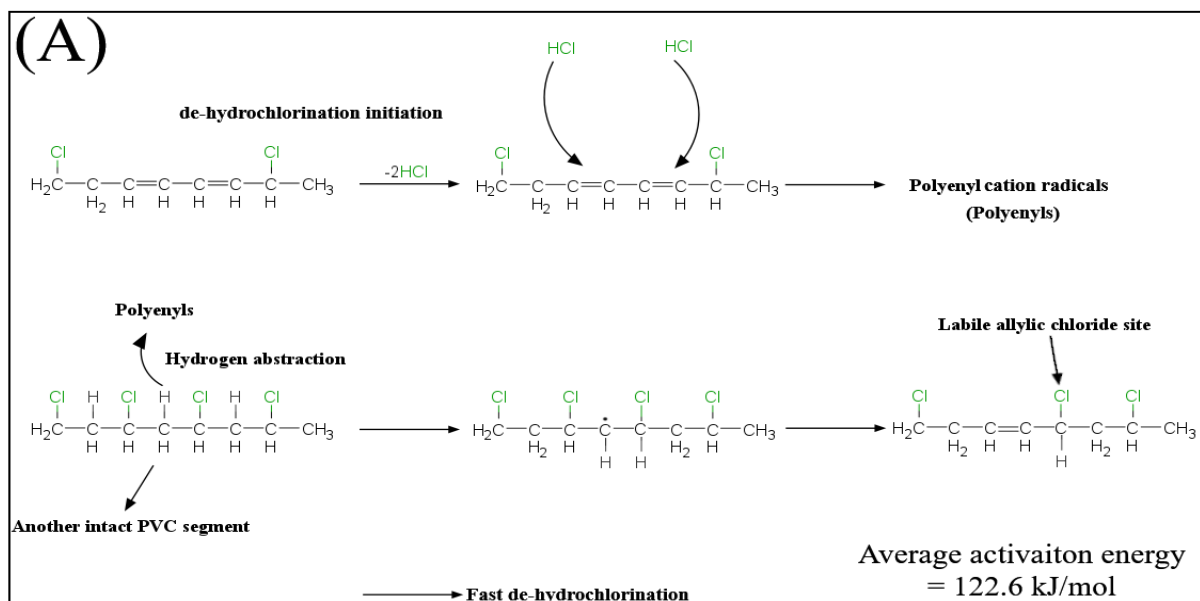


Figure 11: The apparent activation energy (A) and frequency factor (B) (unit of A and  $Af(\alpha)$  is  $\text{min}^{-1}$ ) associated with the de-hydrochlorination of  $\text{Fe}_3\text{O}_4$ -PVC (first stage in Figure 2 (B)).

At a conversion of 0.1, the apparent activation energy starts at a value that is very similar to that seen for pure PVC at 114.5 and 113.0 kJ/mol calculated from Friedman and Ortega, respectively. However, at lower conversion values associated with the initiation of the de-

hydrochlorination ( $\alpha = 0.004$ ), the activation energy for  $\text{Fe}_3\text{O}_4$ -PVC mixture is much higher than that of pure PVC at 204.2 kJ/mol ( $\text{Fe}_3\text{O}_4$ -PVC) compared to 109.9 kJ/mol (pure PVC) at the same conversion. This suggests that a significant change in the initiation mechanism of the de-hydrochlorination has taken place when  $\text{Fe}_3\text{O}_4$  was added to PVC. As the reaction progresses above 0.1, a significant increase appears in the activation energy with it subsequently reaching a value of 191.0 kJ/mol at a conversion of 0.5 compared to 105.0 kJ/mol for pure PVC (Friedman) at the same conversion. Judging from the XRD and SEM data presented in earlier sections, the change in the apparent activation energy can be assigned to the capturing of released HCl by  $\text{Fe}_3\text{O}_4$  to form  $\text{FeCl}_2$  which can prohibit the auto-catalytic effect of HCl on the degradation of PVC. In this case,  $\text{Fe}_3\text{O}_4$  works as a HCl scavenger which can fully or at least partially prevent the emitted HCl from forming polyenyl cation radicals which have been shown to be necessary for increasing the decomposition rate (Figure 12 (A)) [35]. Such an effect can translate in the form of an increase in the activation energy. A mechanism illustrating the inhibiting effect of  $\text{Fe}_3\text{O}_4$  in capturing emitted gaseous HCl is presented in Figure 12 (B).



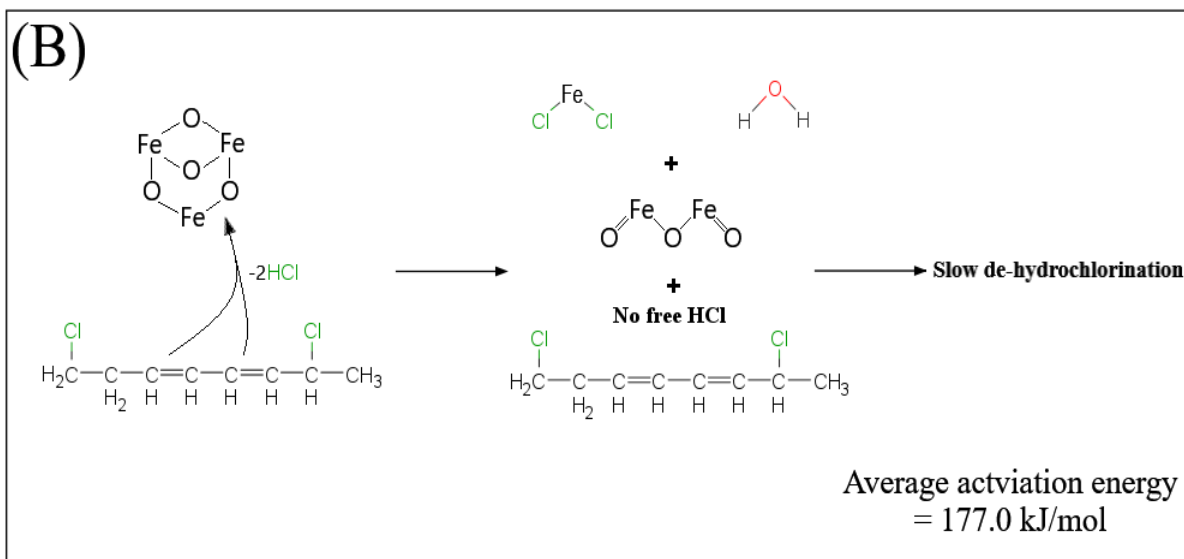


Figure 12: (A) Auto-catalysis mechanism of PVC de-hydrochlorination suggested by Starnes and Ge [35] and (B) The role of  $\text{Fe}_3\text{O}_4$  in inhibiting the catalytic activity of HCl.

The complexity of the degradation of  $\text{Fe}_3\text{O}_4$ -PVC mixture can be seen from the continuous shift of the reaction model from one mechanism to another (Figure 10; triangles). Such behaviour can be assigned to the occurrence of many concurrent/sequential mass losses during the de-hydrochlorination where  $f(\alpha)$  overlaps with more than one mechanism below  $\alpha = 0.4$  then settles at values close to  $F_2$  model between  $0.4 < \alpha < 0.9$  except for  $\alpha = 0.6$  where it overlaps with  $D_1$ .

$\text{Fe}_2\text{O}_3$  showed a larger impact on the apparent activation energy of PVC de-hydrochlorination compared to  $\text{Fe}_3\text{O}_4$ . Likewise, the initiation activation energy increased from 109.9 to 215.1 kJ/mol when  $\text{Fe}_2\text{O}_3$  was added ( $\alpha = 0.004$ ). The variation of the apparent activation energy and frequency factor for  $\text{Fe}_2\text{O}_3$ -PVC de-hydrochlorination are shown in Figures 13 (A) and (B). Due to very poor data fitting at  $\alpha = 0.8$ , the kinetic parameters at that conversion were not included.

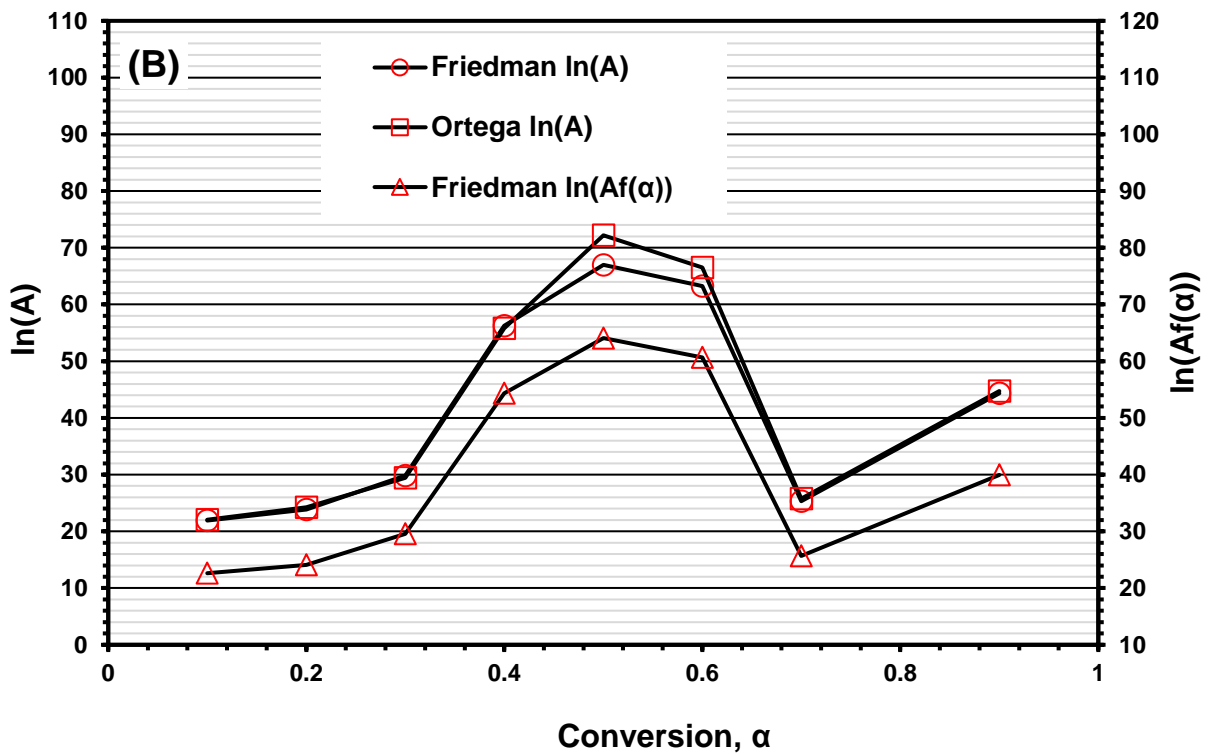
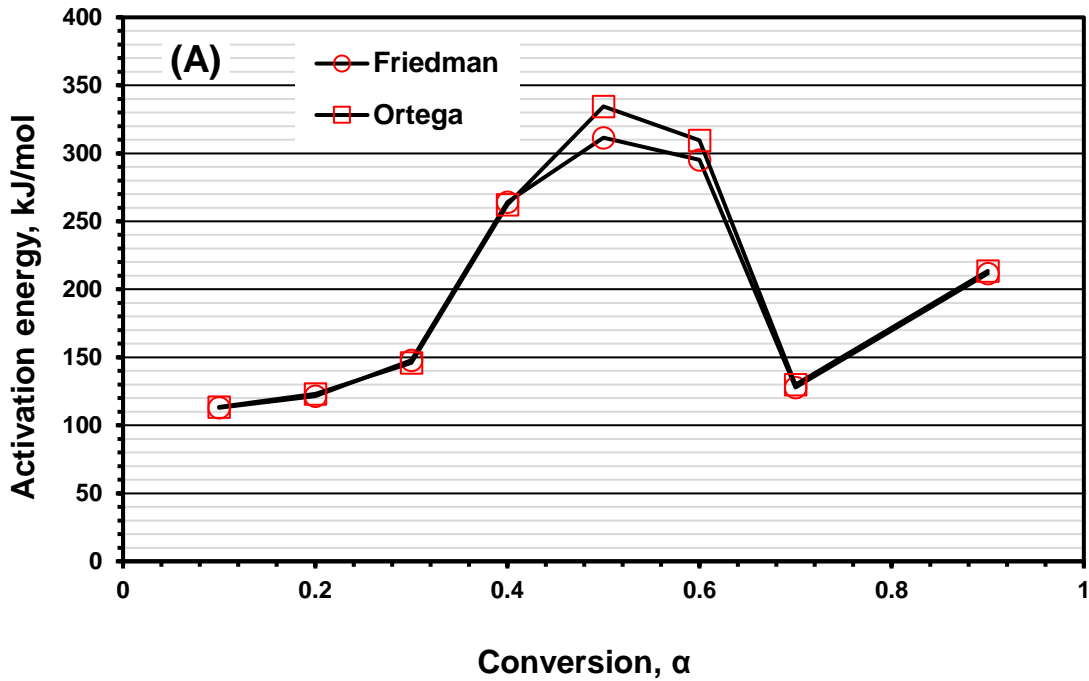
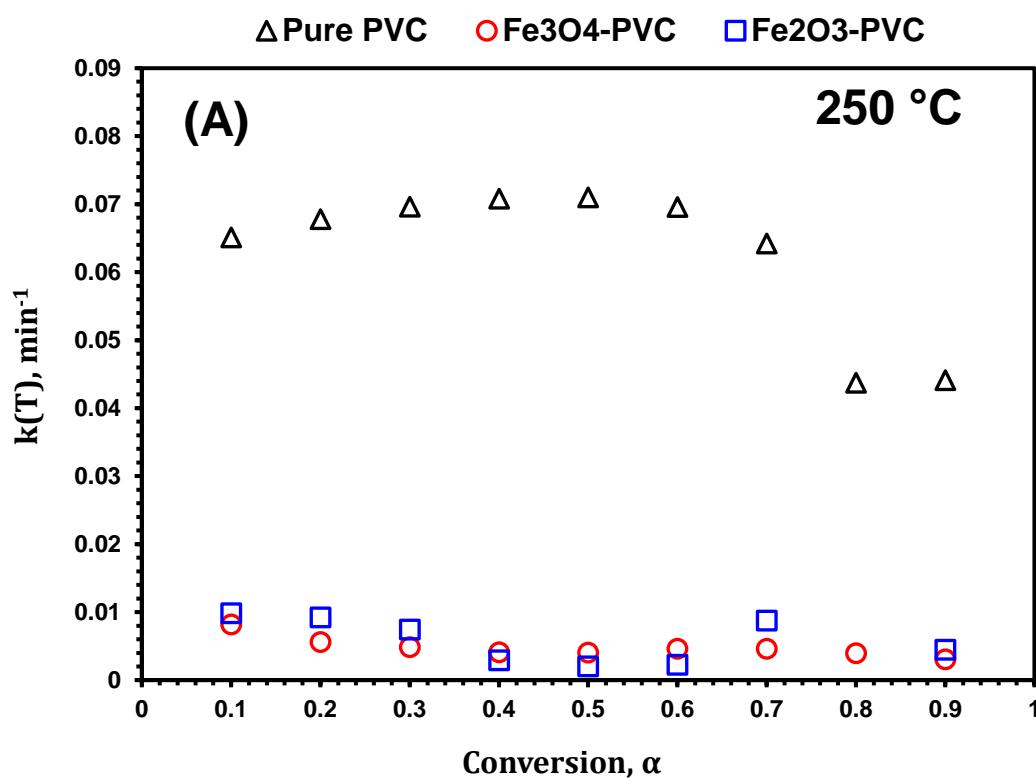


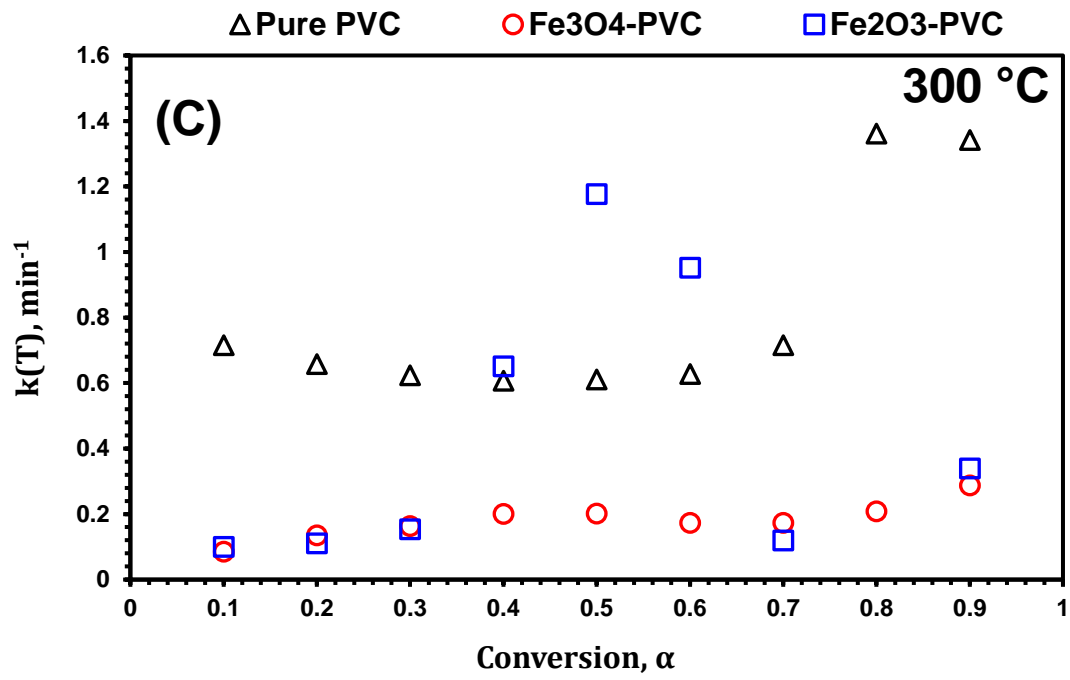
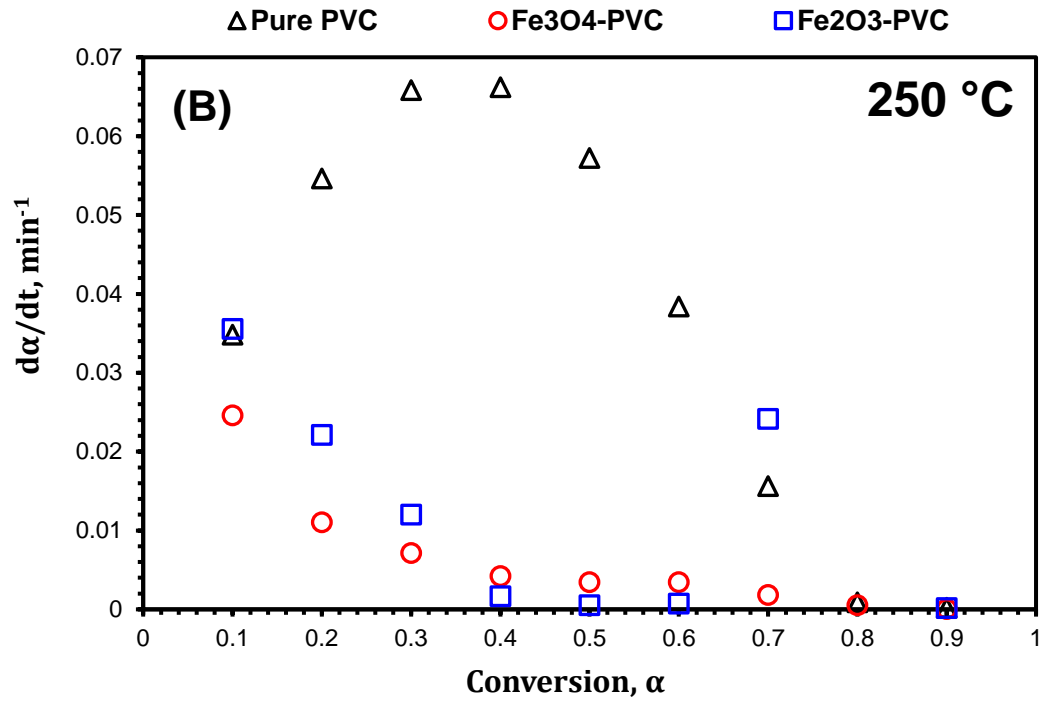
Figure 13: The apparent activation energy (A) and frequency factor (B) (unit of A and  $A_f(\alpha)$  is  $\text{min}^{-1}$ ) associated with the de-hydrochlorination of  $\text{Fe}_2\text{O}_3$ -PVC (third stage in Figure 2 (C)).

The apparent activation energy changes greatly with conversion starting at 112.9 kJ/mol at a conversion of 0.1 and reaching a maximum of 311.5 kJ/mol (Friedman) at a conversion of 0.5. It is believed that the capturing of emitted HCl by the  $\text{Fe}_3\text{O}_4$  formed from the reduction of  $\text{Fe}_2\text{O}_3$  can affect the value of the activation energy. This is because HCl was reported to catalyse the

de-hydrochlorination [35]. This can be confirmed by the prominent XRD peaks of  $\text{FeCl}_2$  and  $\text{FeCl}_2 \cdot 2\text{H}_2\text{O}$  seen in Figure 6. The apparent reaction model describing  $\text{Fe}_2\text{O}_3$ -PVC de-hydrochlorination is best described by mechanism  $F_3$  between  $0.4 < \alpha < 0.9$  except for  $\alpha = 0.7$  ( $A_4$  model had a better fit). Different reaction models described the degradation below  $\alpha = 0.4$ .

To compare the effect of  $\text{Fe}_3\text{O}_4$  and  $\text{Fe}_2\text{O}_3$  on the de-hydrochlorination rate of PVC, the effect of the frequency factors shown in Figures 9, 11 and 13 must also be taken into account. This is achieved by comparing the rate and the rate constant for each system against the conversion at fixed temperatures of 250 and 300 °C (Figure 14).





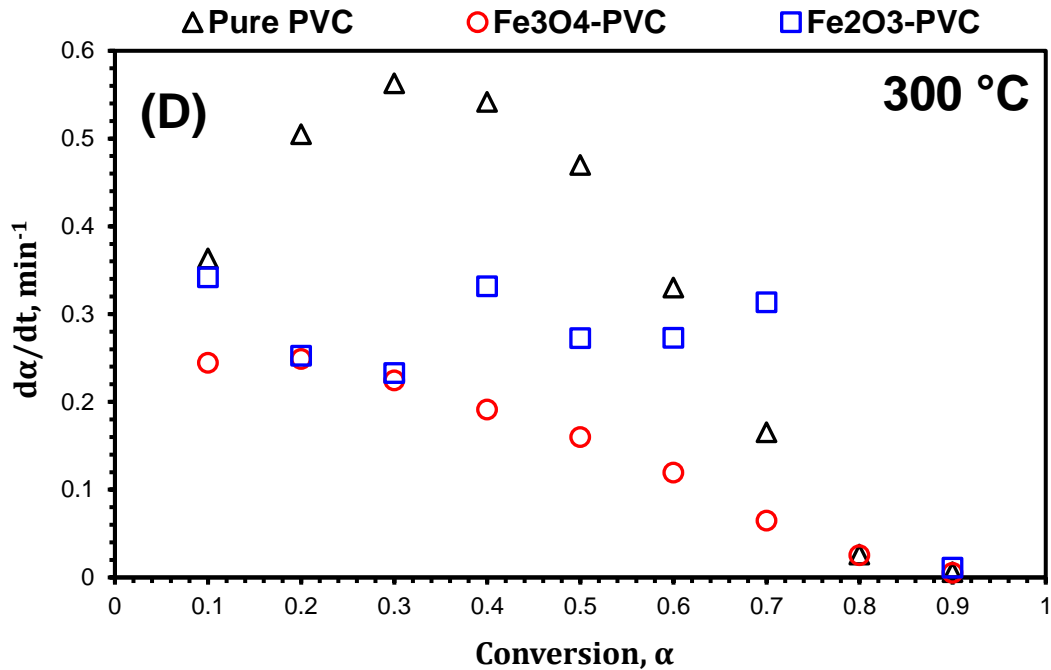
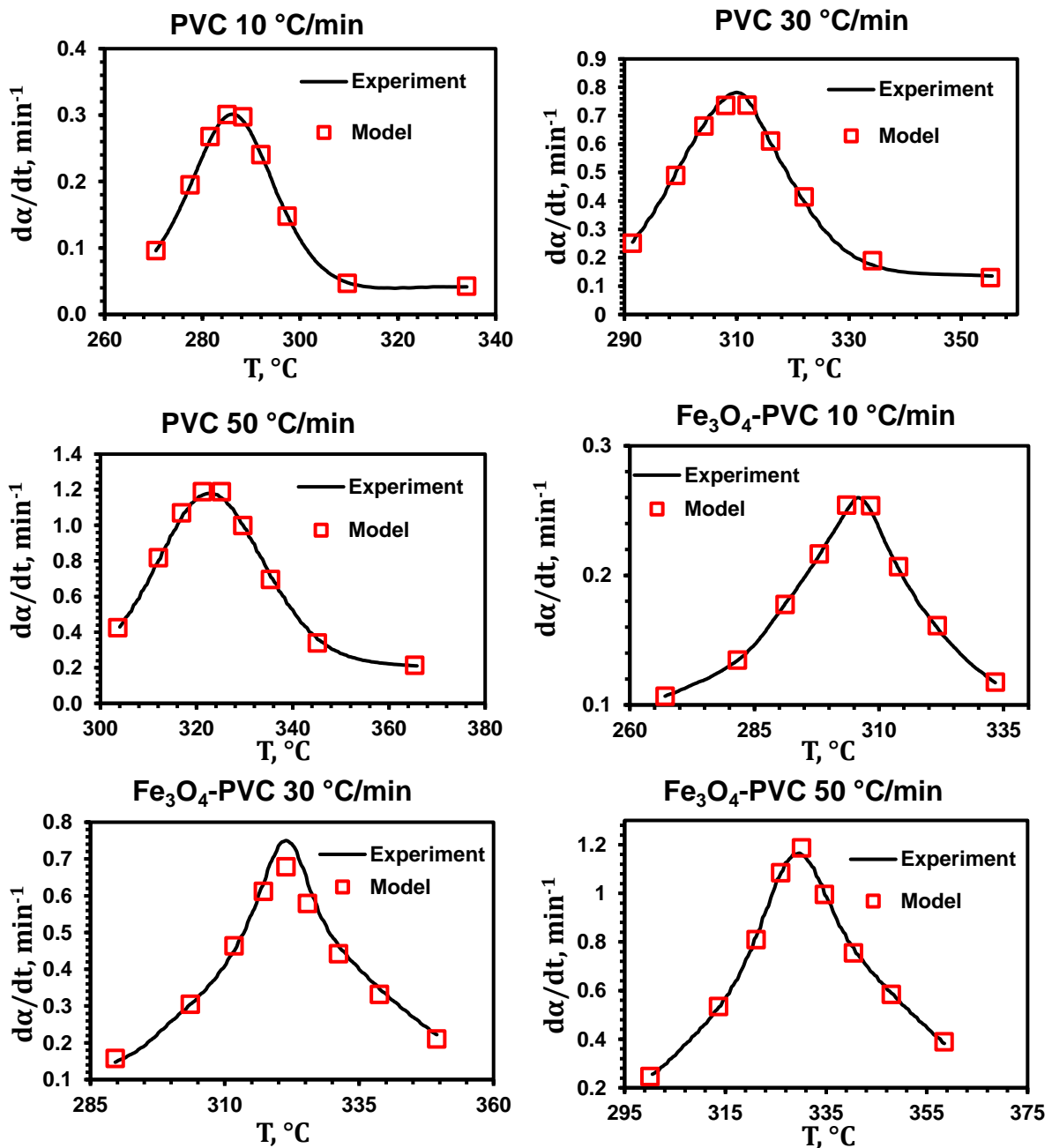


Figure 14: de-hydrochlorination rate (B) and (D) and rate constant (A) and (C) calculated using data from Freidman model of pure PVC, Fe<sub>3</sub>O<sub>4</sub>-PVC (31.6 wt% Fe<sub>3</sub>O<sub>4</sub>), and Fe<sub>2</sub>O<sub>3</sub>-PVC (29.9 wt% Fe<sub>2</sub>O<sub>3</sub>) at different conversion levels and at constant temperatures of 250 and 300 °C.

It is clear that the addition of both Fe<sub>3</sub>O<sub>4</sub> and Fe<sub>2</sub>O<sub>3</sub> to PVC yields a drop in the rate of mass loss associated with the de-hydrochlorination stage as shown in Figures 14 (B) and (D). Since the decomposition of Fe<sub>3</sub>O<sub>4</sub>-PVC and Fe<sub>2</sub>O<sub>3</sub>-PVC mixtures exhibit high activation energies, they can be described as strongly temperature dependent. Hence, it can be seen that the difference in the degradation rate between pure PVC and Fe<sub>3</sub>O<sub>4</sub>-PVC/Fe<sub>2</sub>O<sub>3</sub>-PVC becomes smaller when the temperature is increased from 250 to 300 °C. This is evident from the behaviour of the rate constant presented in Figures 14 (A) and (C), where, for instance, at a conversion of 0.5, the rate constant for pure PVC degradation is 17.8 and 35.5 times that of Fe<sub>3</sub>O<sub>4</sub>-PVC and Fe<sub>2</sub>O<sub>3</sub>-PVC at 250 °C while it is 3.0 and 0.52 times the rate constant of Fe<sub>3</sub>O<sub>4</sub>-PVC and Fe<sub>2</sub>O<sub>3</sub>-PVC at 300 °C. This means, at high temperatures, the activation energy barrier is overcome, and the high frequency factor associated with the de-hydrochlorination of Fe<sub>3</sub>O<sub>4</sub>-PVC/Fe<sub>2</sub>O<sub>3</sub>-PVC compensates for their high energy barrier leading to higher reaction rates.

The reliability of the extracted kinetic data can be confirmed from comparing the mass loss rates calculated from the kinetic parameters extracted here with the experimental rates (Figure

15). An excellent agreement between experimental and model generated rates of dehydrochlorination can be seen in Figure 15 for the three different systems (PVC, Fe<sub>3</sub>O<sub>4</sub>-PVC, and Fe<sub>2</sub>O<sub>3</sub>-PVC). Presenting the data in Figure 15 at different heating rates was done to confirm that the generated kinetic parameters from Friedman model can produce correct mass loss rate values at different temperatures. The results in Figure 15 suggest the reliability of the kinetic parameters at temperatures in the vicinity of the temperatures used to generate these profiles.



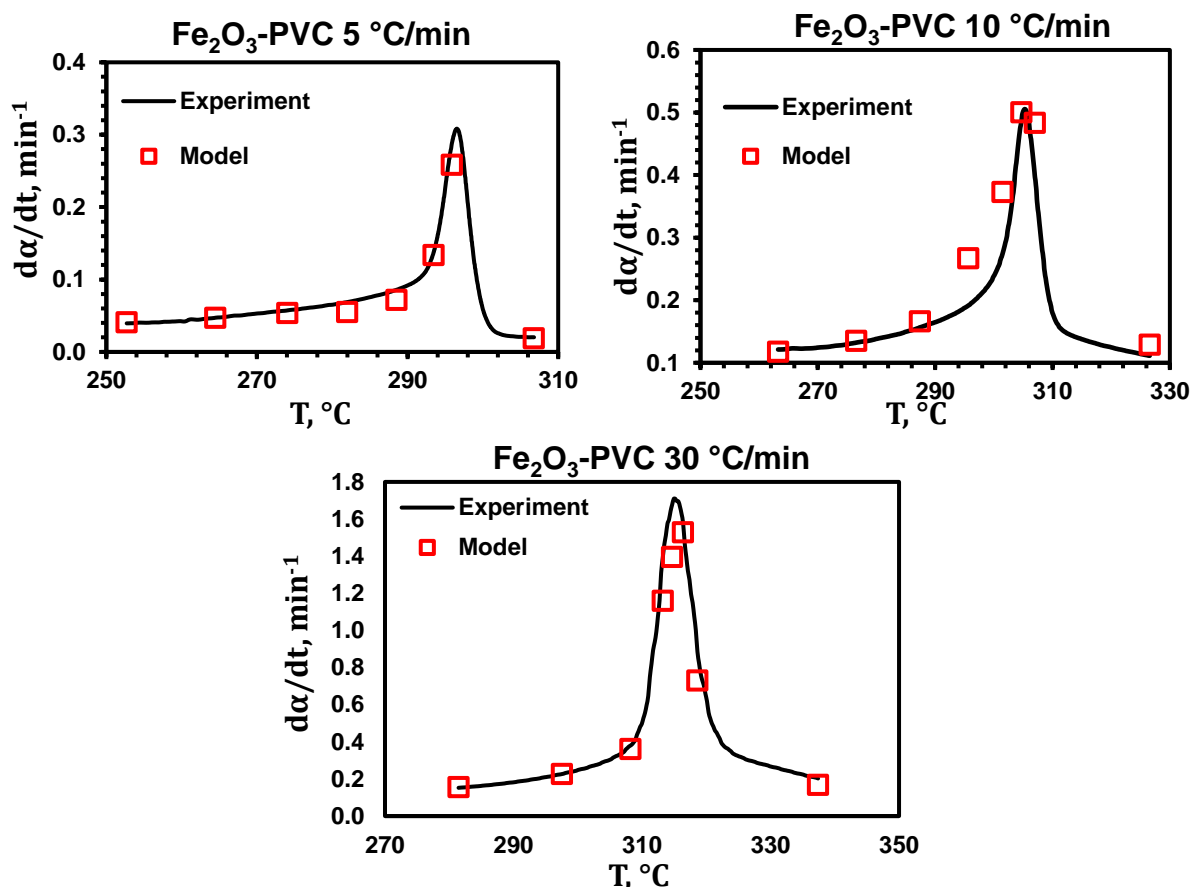


Figure 15: de-hydrochlorination experimental rates against the rate calculated using kinetic data obtained from Friedman method for Pure PVC,  $\text{Fe}_3\text{O}_4$ -PVC, and  $\text{Fe}_2\text{O}_3$ -PVC at different heating rates.

The thermo-kinetic study presented in this work provide answers to essential questions regarding the effect of individual components of EAFD ( $\text{Fe}_3\text{O}_4$  and  $\text{Fe}_2\text{O}_3$ ) on the decomposition kinetics of PVC. This work is part of an ongoing study addressing the effect of each EAFD component on the degradation kinetics of PVC. Previously, the effect of  $\text{ZnO}$  and  $\text{ZnFe}_2\text{O}_4$  on the degradation kinetics of PVC was considered [34, 36]. The overall objective is to establish a kinetic database based on which the reaction rates of PVC with EAFD from different plants/countries with different mineral composition can be predicted. The utilisation of the kinetic parameters presented here contributes greatly to the optimisation of the co-thermal treatment of EAFD-PVC mixtures by selecting the optimal reaction temperatures which should make a balance between reaction times and process economics. Further investigation needs to be performed on other EAFD constituents such as litharge/massicot ( $\text{PbO}$ ) under pyrolytic conditions. At the end, all these studies combined should be collected in

one work and a simulation study based on these parameters should be made to predict the kinetic effect of EAFD with different chemistries on PVC degradation.

## 5. Conclusions

This work reports the thermo-kinetic behaviour of PVC in the presence of  $\text{Fe}_3\text{O}_4$  (a major EAFD component) and  $\text{Fe}_2\text{O}_3$ . The chlorination of  $\text{Fe}_3\text{O}_4$  at a temperature of 400 °C was confirmed by the XRD peaks of  $\text{FeCl}_2 \cdot 2\text{H}_2\text{O}$ . Despite the fact that the chlorination of  $\text{Fe}_2\text{O}_3$  by HCl is thermodynamically unfavourable, the presence of reducing agents (such as  $\text{H}_2$ ) during the de-hydrochlorination transformed  $\text{Fe}_2\text{O}_3$  into  $\text{Fe}_3\text{O}_4$  which was then chlorinated into  $\text{FeCl}_2$  which was evaporated when the temperature was increased up to 850 °C. Performing the pyrolysis of  $\text{Fe}_3\text{O}_4$ -PVC and  $\text{Fe}_2\text{O}_3$ -PVC at a temperature of 850 °C yielded elemental iron  $\alpha$ -Fe, suggesting that PVC can also be used as a reducing agent aside to being a source for chlorination.

The thermogravimetric scans under pyrolytic conditions ( $\text{N}_2$ ) were used along with the model-free methods of Friedman and Ortega to calculate the kinetic parameters associated with the de-hydrochlorination of pure PVC and its mixtures with  $\text{Fe}_3\text{O}_4$  and  $\text{Fe}_2\text{O}_3$ . The extracted kinetic data suggests that both  $\text{Fe}_3\text{O}_4$  and  $\text{Fe}_2\text{O}_3$  have an inhibiting effect on the de-hydrochlorination of PVC resulting in a significant increase in the value of the apparent activation energy along with an insufficient increase in the frequency factor. This, in turn, results in lower values of the overall rate of degradation for these mixtures compared to pure PVC at the common PVC pyrolysis temperatures of 250 and 300 °C.

## Acknowledgment

The authors would like to thank Sabrin Samad from the Nanoscale and Microscale Research Centre (nmRC) at the University of Nottingham for helping with the SEM analysis.

## References

- [1] H. Zhu, X. Jiang, J. Yan, Y. Chi, K. Cen, TG-FTIR analysis of PVC thermal degradation and HCl removal, *Journal of analytical and applied pyrolysis*, 82 (2008) 1-9.
- [2] W.S. Association, *Steel Facts. A collection of amazing facts about steel*. Worldsteel, in, 2018.
- [3] M. Sebag, C. Korzenowski, A. Bernardes, A. Vilela, Evaluation of environmental compatibility of EAFD using different leaching standards, *Journal of hazardous materials*, 166 (2009) 670-675.
- [4] M. Al-Harashsheh, J. Al-Nu'airat, A. Al-Otoom, H. Al-jabali, M. Al-zoubi, Treatments of electric arc furnace dust and halogenated plastic wastes: A review, *Journal of Environmental Chemical Engineering*, (2018) 102856.
- [5] M. Sadat-Shojai, G.-R. Bakhshandeh, Recycling of PVC wastes, *Polymer Degradation and Stability*, 96 (2011) 404-415.
- [6] Y. Zhou, N. Yang, S. Hu, Industrial metabolism of PVC in China: A dynamic material flow analysis, *Resources, Conservation and Recycling*, 73 (2013) 33-40.
- [7] I. Mersiowsky, R. Stegmann, J. Ejlerthsson, Long term behaviour of poly (vinyl chloride) products under soil buried and landfill conditions, *Plastics, rubber and composites*, 28 (1999) 321-326.
- [8] S. Kim, Pyrolysis kinetics of waste PVC pipe, *Waste management*, 21 (2001) 609-616.
- [9] Y. Masuda, T. Uda, O. Terakado, M. Hirasawa, Pyrolysis study of poly (vinyl chloride)–metal oxide mixtures: quantitative product analysis and the chlorine fixing ability of metal oxides, *Journal of Analytical and Applied Pyrolysis*, 77 (2006) 159-168.
- [10] M. Al-harashsheh, S. Kingman, L. Al-Makhadmah, I.E. Hamilton, Microwave treatment of electric arc furnace dust with PVC: Dielectric characterization and pyrolysis-leaching, *Journal of Hazardous Materials*, 274 (2014) 87-97.
- [11] M. Al-Harashsheh, A. Al-Otoom, L. Al-Makhadmah, I.E. Hamilton, S. Kingman, S. Al-Asheh, M. Hararah, Pyrolysis of poly(vinyl chloride) and—electric arc furnace dust mixtures, *Journal of Hazardous Materials*, 299 (2015) 425-436.
- [12] M. Al-Harashsheh, Thermodynamic Analysis on the Thermal Treatment of Electric Arc Furnace Dust-PVC Blends, *Arabian Journal for Science and Engineering*, (2017) 1-13.
- [13] G.-S. Lee, Y.J. Song, Recycling EAF dust by heat treatment with PVC, *Minerals engineering*, 20 (2007) 739-746.
- [14] M. Al-Harashsheh, Y. Orabi, S. Al-Asheh, Comparative study on the pyrolysis and leachability of washed/unwashed electric arc furnace dust-PVC mixtures and their residues, *Journal of Environmental Chemical Engineering*, (2021) 105410.
- [15] M. Al-Harashsheh, S. Altarawneh, M. Al-Omari, M. Altarawneh, S. Kingman, C. Dodds, Leaching behavior of zinc and lead from electric arc furnace dust–Poly (vinyl) chloride residues after oxidative thermal treatment, *Journal of Cleaner Production*, 328 (2021) 129622.
- [16] M. Al-Harashsheh, M. Aljarrah, A. Al-Otoom, M. Altarawneh, S. Kingman, Pyrolysis kinetics of tetrabromobisphenol a (TBBPA) and electric arc furnace dust mixtures, *Thermochimica Acta*, 660 (2018) 61-69.
- [17] J. Šesták, G. Berggren, Study of the kinetics of the mechanism of solid-state reactions at increasing temperatures, *Thermochimica Acta*, 3 (1971) 1-12.
- [18] S. Vyazovkin, A.K. Burnham, J.M. Criado, L.A. Pérez-Maqueda, C. Popescu, N. Sbirrazzuoli, ICTAC Kinetics Committee recommendations for performing kinetic computations on thermal analysis data, *Thermochimica acta*, 520 (2011) 1-19.
- [19] H.L. Friedman, Kinetics of thermal degradation of char-forming plastics from thermogravimetry. Application to a phenolic plastic, in: *Journal of Polymer Science Part C: Polymer Symposia*, Wiley Online Library, 1964, pp. 183-195.

- [20] A. Ortega, A simple and precise linear integral method for isoconversional data, *Thermochimica Acta*, 474 (2008) 81-86.
- [21] S. Vyazovkin, Determining Preexponential Factor in Model-Free Kinetic Methods: How and Why?, *Molecules*, 26 (2021) 3077.
- [22] V. Georgieva, D. Zvezdova, L. Vlaev, Non-isothermal kinetics of thermal degradation of chitin, *Journal of thermal analysis and calorimetry*, 111 (2013) 763-771.
- [23] A. Marcilla, M. Beltrán, Thermogravimetric kinetic study of poly(vinyl chloride) pyrolysis, *Polymer Degradation and Stability*, 48 (1995) 219-229.
- [24] L. Ye, T. Li, L. Hong, Co-pyrolysis of Fe<sub>3</sub>O<sub>4</sub>-poly (vinyl chloride)(PVC) mixtures: Mitigation of chlorine emissions during PVC recycling, *Waste Management*, 126 (2021) 832-842.
- [25] J. Yu, L. Sun, C. Ma, Y. Qiao, H. Yao, Thermal degradation of PVC: A review, *Waste Management*, 48 (2016) 300-314.
- [26] A. Ballistreri, S. Foti, P. Maravigna, G. Montaudo, E. Scamporrino, Effect of metal oxides on the evolution of aromatic hydrocarbons in the thermal decomposition of PVC, *Journal of Polymer Science: Polymer Chemistry Edition*, 18 (1980) 3101-3110.
- [27] S.B. Kanungo, Kinetics of thermal dehydration and decomposition of hydrated chlorides of 3d transition metals (Mn-Cu series). Part-II. Dehydration of FeCl<sub>2</sub>.4H<sub>2</sub>O, *Journal of India Chemical Society*, 81 (2004) 750-756.
- [28] N. Louvain, A. Fakhry, P. Bonnet, M. El-Ghozzi, K. Guérin, M.-T. Sougrati, J.-C. Jumas, P. Willmann, One-shot versus stepwise gas–solid synthesis of iron trifluoride: investigation of pure molecular F<sub>2</sub> fluorination of chloride precursors, *CrystEngComm*, 15 (2013) 3664-3671.
- [29] J. Zieliński, I. Zglinicka, L. Znak, Z. Kaszukur, Reduction of Fe<sub>2</sub>O<sub>3</sub> with hydrogen, *Applied Catalysis A: General*, 381 (2010) 191-196.
- [30] A. Pineau, N. Kanari, I. Gaballah, Kinetics of reduction of iron oxides by H<sub>2</sub>: Part II. Low temperature reduction of magnetite, *Thermochimica Acta*, 456 (2007) 75-88.
- [31] B. Zhang, X.-Y. Yan, K. Shibata, T. Uda, M. Tada, M. Hirasawa, Thermogravimetric-mass spectrometric analysis of the reactions between oxide (ZnO, Fe<sub>2</sub>O<sub>3</sub> or ZnFe<sub>2</sub>O<sub>4</sub>) and polyvinyl chloride under inert atmosphere, *Materials Transactions, JIM*, 41 (2000) 1342-1350.
- [32] B. Morosin, E.J. Graeber, Crystal structures of manganese (II) and iron (II) chloride dihydrate, *The Journal of Chemical Physics*, 42 (1965) 898-901.
- [33] K. Momma, F. Izumi, VESTA: a three-dimensional visualization system for electronic and structural analysis, *Journal of Applied crystallography*, 41 (2008) 653-658.
- [34] S. Altarawneh, M. Al-Harashseh, C. Dodds, A. Buttress, S. Kingman, Thermal degradation kinetics of polyvinyl chloride in presence of zinc oxide, *Thermochimica Acta*, (2021) 179105.
- [35] W.H. Starnes, X. Ge, Mechanism of autocatalysis in the thermal dehydrochlorination of poly (vinyl chloride), *Macromolecules*, 37 (2004) 352-359.
- [36] S. Altarawneh, M. Al-Harashseh, C. Dodds, A. Buttress, S. Kingman, Thermodynamic, pyrolytic, and kinetic investigation on the thermal decomposition of polyvinyl chloride in the presence of franklinite, *Process Safety and Environmental Protection*, (2022).